Efficient Synthetic Receptors for Endotoxin Detection using Molecular Imprinting

Thesis presented for the degree of

Doctor of Philosophy

March 2019

Danielle Louise Huckle

Institute of Infection and Immunity

Cardiff University

Declaration

This work has not been submitted in substance for any other degree or award at this or any other university or place of learning, nor is being submitted concurrently in candidature for any degree or other award.

Signed (candidate) Date ……

STATEMENT 1

This thesis is being submitted in partial fulfillment of the requirements for the degree of …PhD…

Signed (candidate) Date ……

STATEMENT 2

This thesis is the result of my own independent work/investigation, except where otherwise stated.

Other sources are acknowledged by explicit references. The views expressed are my own.

Signed (candidate) Date ……

STATEMENT 3

I hereby give consent for my thesis, if accepted, to be available for photocopying and for inter-library loan, and for the title and summary to be made available to outside organisations.

Signed (candidate) Date ……

STATEMENT 4: PREVIOUSLY APPROVED BAR ON ACCESS

I hereby give consent for my thesis, if accepted, to be available for photocopying and for inter-library loans **after expiry of a bar on access previously approved by the Academic Standards & Quality Committee.**

Signed (candidate) Date ……

Final word count: 35,382 (59,082 including prelim pages, refs, captions, contents)

Dedication

This thesis is dedicated to my husband Ed.

Nothing I have done during the course of this work would have been possible without you.

Acknowledgements

Interminable thanks to my initial supervisor team Professor Judith Hall, Dr. Chris Allender and Dr. Jenna Bowen. Vast gratitude is also extended for the invaluable help provided by Professor Adrian Porch who kindly came on board at a later stage.

Many thanks to fellow MRRU lab members Dr. Nick Williams and Dr. Vibha Tamboli; I'm confident we will all remain in touch and enjoy good meals over the coming years. Thanks to Dr. Erica Loizidou with organic chemistry help for work in chapter three.

Members of the Centre for High Frequency Engineering, Cardiff School of Engineering were incredibly patient, knowledgeable and helpful. Thanks are extended to Dr. Nick Clark, Dr. Jerome Cuena, Nick Inoue, Professor David Barrow and Professor Adrian Porch. Thanks also to Professor Philip Davies from Cardiff University School of Chemistry for use of equipment during the course of this work.

Thanks are also extended to the Welsh Deanery and the Royal College of Anaesthetists. It is the flexibility you granted me in my anaesthesia training programme that ultimately afforded me the opportunity to undertake a PhD. As an NHS consultant, I would also like to extend thanks to my anaesthesia department and especially Dr. Anthony Turley, Dr. Abraham Theron and Dr. Caryl Taylor for understanding the challenges associated with completion of this work.

Finally thanks to my family for support and encouragement over the years (especially my cousin Duncan for invaluable help with chapter four). Ed- the dedication is enough; you were more than vital to proceedings.

Presentations and publications

Work from this thesis has been presented at the following national conferences:

Jan 2019: Association of Anaesthetists of Great Britain and Ireland, Winter Scientific Meeting**,** London UK

April 2017: Anaesthetic Research Society, Spring Scientific Meeting, London UK

Jan 2017: Association of Anaesthetists of Great Britain and Ireland, Winter Scientific Meeting, London UK

March 2014: Society of Anaesthetists in Wales, Spring Scientific Meeting, Brecon, Wales UK

August 2013: Graduate Student Symposium on Molecularly Imprinted Polymers, Belfast, Ireland

Oct 2013: Anaesthetic Research Society, Winter Scientific Meeting, London UK

Work from this thesis has been presented at the following international conferences:

June 2017: Euroanaesthesia, Geneva, Switzerland

May 2015: 4th International Conference on Bio-sensing Technology, Lisbon, Portugal

Conference abstract publications:

Huckle D, Bowen J, Allender C, Hall J. Novel approaches to biosensor development for endotoxin detection: e-Supplement of the European Journal of Anaesthesiology, Volume 34, Supplement 55, June 2017

Huckle D, Loizidou E, et al. Structure manipulation of polymyxin B and subsequent integration into polymer capable of endotoxin detection and sequestration. *Anaesthesia.* 2015; 70 (Supp S4).

Huckle D, Hall J, Bowen J, Allender C, Cuenca J, Porch A. Towards an efficient biosensor for the detection of lipopolysaccharide in sepsis using molecularly imprinted polymers. *BJA.* 2014 Jan; 112 (1): 199.

Summary

Sepsis remains a poorly understood and potentially devastating medical syndrome. Unlike other medical emergencies there is no definitive, measureable biomarker. Lipopolysaccharide (LPS) is widely implicated in the pathogenesis of sepsis. It is not routinely measured owing to a lack of reliable diagnostic assay.

Molecular imprinting is a novel approach to LPS detection. It describes the generation of synthetic, polymeric receptors through the polymerisation of monomers around a template molecule. The resultant polymers possess recognition properties akin to an antibody with the ability to recognise the original target molecule. LPS is not a suitable template for conventional molecular imprinting techniques, therefore, techniques that circumvent problems associated with the imprinting of biological macromolecules are needed. Modified approaches that localise the template at a surface via chemical immobilisation at a solid-solvent interface (surface imprinting on a solid support) or via self-assembly at a solvent-solvent interface (microfluidic techniques plus microwave-assisted polymerisation) have been investigated. Polymyxin B (PMB), a peptide antibiotic, has high affinity for LPS and was utilised in this study to help localise LPS at an interface under a variety of experimental conditions; including the synthesis of a polymerisable PMB (p-PMB).

A synthesised p-PMB polymer was subsequently found able to bind LPS from solution with an apparent K_d of 0.327 µM. Furthermore, using a bespoke microfluidic/microwave hybrid system, with benzethonium chloride (BC) used as a LPS surrogate, BC imprinted polymer beads were produced. Subsequent binding experiments demonstrated ability of the imprinted bead to bind to the original template with a B_{max} of 0.014 nmol/mg and an apparent K_d of 0.536 µM.

List of Abbreviations

µTAS	Micro Total Analysis Systems
AAm	Acrylamide
AAPH	2’2’ Azo (2-methyl-propionamide) dihydrochloride
ACN	Acetonitrile
AIBN	Azobisisobutyronitrile
ATRP	Atom Transfer Radical Polymerisation
BC	Benzethonium Chloride
Ca	Capillary number
CA-125	Ovarian cancer antigen 125
CAC	Critical Aggregation Concentration
CAD	Computer Aided Design
CD-14	Cluster Differentiation-14
CMC	Critical Micelle Concentration
CRP	C Reactive Protein
CVVH	Continuous Veno-Venous Haemofitration
Dab	3,3'-Diaminobenzidine
dBM	Power ratio in decibels
DCM	Dichloromethane
DI	De-ionised
DMF	Dimethylformamide
EAA	Endotoxin Activity Assay
ETFE	Ethylene tetrafluoroethylene
FITC	Fluorescein Isothiocyanate
FTIR	Fourier-transform Infrared Spectroscopy
GlcN	1,4- bisphosphorylated β1,6- linked D-glucosamine
GMA	Glycidyl Methacrylate
HCl	Hydrogen Chloride
HDL-C	High-density Lipoprotein Cholesterol
Hep	L-glycerol-D-manno-heptose
HPLC	High-performance Liquid Chromatography

IF	Interfacial Tension
IgM	Immunoglobulin M
IL	Interleukin
IR	Infrared
JAMA	Journal of the American Medical Association
Kdo	2-keto-3-deoxyoctamate
LAL	Limulus Amebocyte Lysate
LBP	Lipopolysaccharide Binding Protein
Leu	Leukocytes
LICI	Limulus Intracellular Coagulation Inhibitor
LPS	Lipopolysaccharide
LTA	Lipoteichoic Acid
M/Z	Mass/charge
MBAam	N,N'-methylene-bisacrylamide
MC	Methacryloyl Chloride
MD-2	Lymphocyte antigen 96
MEMS	Micro-electro-mechanical Systems
MeOH	Methanol
MF	Microfluidics
MIP	Molecularly Imprinted Polymer
MIT	Molecular Imprinting Technology
mLSI	Microfluidic Large Scale Integration
MS	Mass Spectroscopy
MyD88	Myeloid Differentiation gene primary product 88
NFκB	Nuclear Factor kappa B
NICE	National Institute for Clinical Excellence
NMP-22	Nuclear matrix protein 22
NMR	Nuclear Magnetic Resonance
PAAm	Polyacrylamide
PAF	Platelet Activating Factor
PAI-1	Plasminogen Activator Inhibitor-1
PAMPs	Pathogen Associated Molecular Patterns
PDMS	Polydimethylsiloxane

PEEK	Polyether Ether Ketone
PET	Positron Emission Tomography
PFA	Perfluoralkoxy Alkane
Phe	Phenylalanine
PMB	Polymyxin B
PMBN	Polymyxin B Nonapeptide
pNA	*p* Nitroaniline
p-PMB	Polymerisable polymyxin B
p-PMB	Polymerisable PMB
$p\text{-}PMB_{GMA}$	Polymerisable PMB via glycidyl methacrylate reaction
$p\text{-}PMB_{MC}$	Polymerisable PMB via methacryloyl chloride reaction
PSA	Prostate Specific Antigen
PTFE	Polytetrafluroethene
PTX3	Pentraxin-related protein
RAFT	Reversible Addition Fragmentation (chain) Transfer
RDRP	Reversible-deactivation Radical Polymerisation
Re	Reynold's number
rFC	Recombinant Factor C
SPR	Surface Plasmon Resonance
SPPS	Solid Phase Peptide Synthesis
sTREM	Soluble Triggering Receptor found on Myeloid cells
suPAR	Soluble urokinase Plasminogen Activator Receptor
TE	Transverse Electric
TEM	Transverse Electric and Magnetic
TFA	Trifluoroacetic Acid
Thr	Threonine
TIR	Toll/Interleukin 1 Receptor
TIRAP	TIR domain-containing Adaptor Protein
TLR	Toll-like Receptor
TM	Transverse Magnetic
TRIF	TIR domain-containing Inducing Interferon β
WCC	White Cell Count
WFI	Water for Injection

Contents

Figures

Tables

Chapter 1. General Introduction

1.1 General overview

1.1.1 Background

Sepsis, the overwhelming result of severe infection, is a leading cause of mortality globally (1,2). It remains a poorly understood and potentially devastating medical syndrome and, unlike other medical emergencies, there is no definitive collection of diagnostic parameters, including measureable biomarker. Lipopolysaccharide (LPS) is widely implicated in the pathogenesis of significant physiological disturbance in sepsis (3–6). It is not currently routinely measured owing to a lack of reliable diagnostic assay. The overarching aim of this work therefore was the synthesis of an efficient biosensor for the detection of LPS. Each experimental chapter describes a distinct investigative pathway, utilising a variety of techniques; all contributing to this aim.

1.1.2 General overview of thesis

The thesis will demonstrate a stepwise approach towards the molecular imprinting of a complex biomacromolecule. It will show novel use of the antibiotic polymyxin B (PMB; chapters two and three) and will also describe the integration of two technologies (microfluidics and microwave-initiated polymerisation; chapters four and five) in a specifically designed system for the manufacture of polymer beads. A schematic overview is shown in figure 1.1.

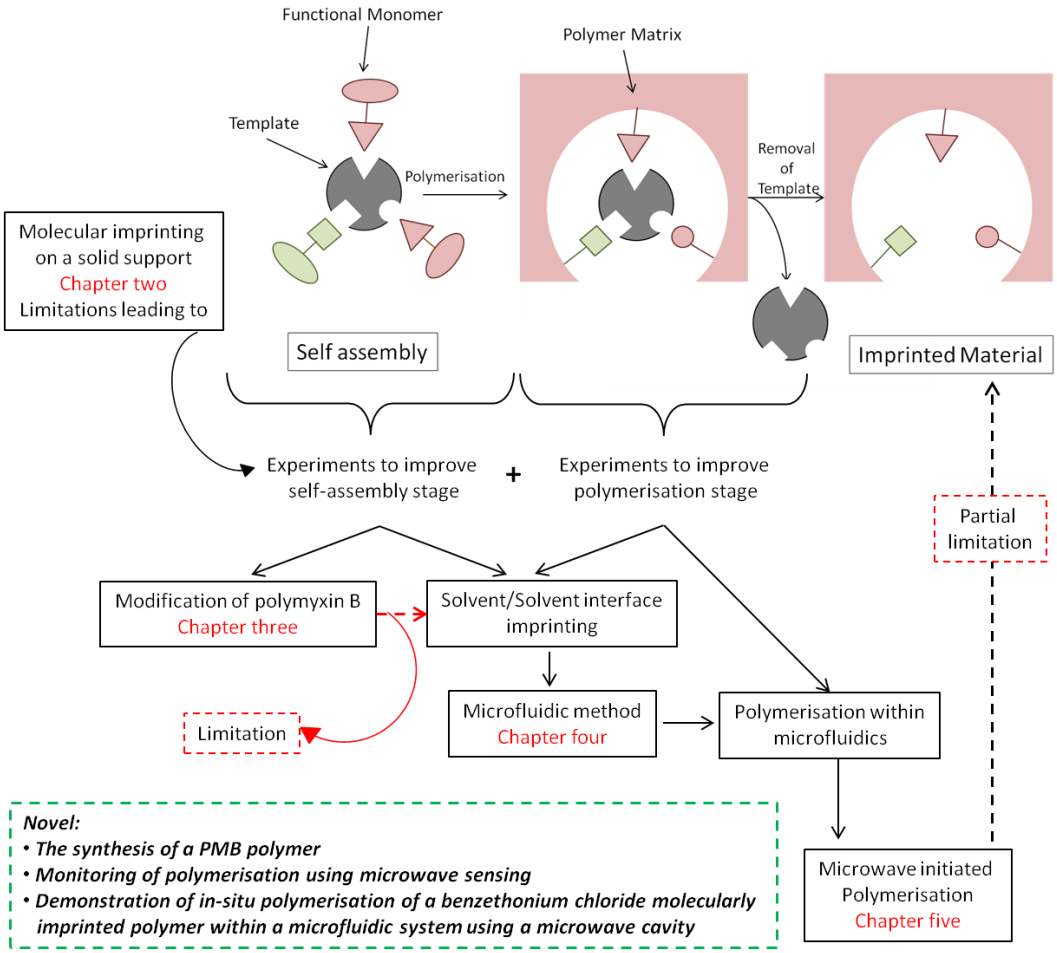

Figure 1.1: Overview of thesis. Also indicated are the key novel findings of this work.

Molecular imprinting is a novel approach to LPS detection, it describes the generation of synthetic, polymeric receptors through the polymerisation of monomers around a template molecule. The resultant polymers possess recognition properties akin to an antibody with the ability to recognise the original target molecule. Molecular imprinting is reviewed in this chapter (section 1.4). Chapter two describes development of surface modification strategies on chloromethyl polystyrene resin (Merrifield resin) to facilitate the attachment of PMB and subsequent imprinting of LPS.

Chapter three explores PMB further with experiments that negate the need for a solid, Merrifield resin support. This chapter describes methods

of PMB structure manipulation to render it polymerisable (p-PMB) with subsequent synthesis of a polymyxin B polymer.

Thereafter, chapter four describes the initial stages of a microfluidic system development for the production of polymer beads. The system was also designed to incorporate *in-situ* bead polymerisation and this chapter describes iterations of a microfluidic system tested prior to eventual use of microwave-initiated polymerisation.

Chapter five describes the integration of microwave delivery into an established microfluidic system in order to polymerise molecularly imprinted polymer beads. In addition, microwave technology is used to characterise individual reactants to guide experimental design and to provide insight into the polymerisation process. Chapter five therefore describes proof-of-concept work on a small scale indicating the potential of microfluidic and microwave technology integration in molecular imprinting strategies. Moreover, this application of microwave technology has not been described previously and offers a novel method of monitoring polymerisation.

1.2 Sepsis and critical illness

1.2.1 Introduction

Sepsis is a common cause for admission to critical care units in the UK (7) and carries a significant economic cost worldwide (8). There is also a growing wealth of evidence indicating the detrimental effects on ongoing health for sepsis survivors, both physical and psychological (9–11). Furthermore, secondary infection and development of sepsis subsequent to admission to critical care is also a major cause of morbidity and mortality. Conditions such as ventilator associated pneumonia (12), fungal infection (13), severe gastrointestinal infection (14) and infection associated with indwelling medical devices (15,16) can detrimentally affect critical care patients.

The definition of sepsis has recently been revised and has been generally well received (17). The revision was necessary to clarify the descriptive difficulty surrounding this syndrome and improve understanding of its prevalence and virulence (18). Therefore, in February 2016, a consensus definition of sepsis and septic shock was published in JAMA, superseding the standing definition from 2001 (19). In this paper, sepsis is succinctly defined as 'a life threatening organ dysfunction caused by a dysregulated host response to infection' (20). Septic shock is also given a clear set of diagnostic criteria: a vasopressor requirement to maintain mean arterial blood pressure of 65 mmHg (or greater) and a serum lactate level of greater than 2 $mmolL^{-1}$ (in a normovolaemic patient) (20).

The early recognition and correct initial diagnosis of sepsis are key concepts that govern the effective treatment of the syndrome. Both may seem eminently achievable, however, they are not always straightforward. Sepsis is a time critical medical condition with outcome for patients improving when diagnosis and institution of treatment is achieved quickly (21–24). Furthermore, emphasis on timely recognition and delivery of

therapy is an overarching theme of sepsis treatment guidelines such as those from the Surviving Sepsis Campaign (SSC) (25) and the National Institute of Clinical Excellence (NICE) (26). Care 'bundles', a compendium of guidelines from evidence based practice, are used by many institutions for the treatment of sepsis and compliance with these guidelines has repeatedly been shown to improve patient outcome (27,28). In 2010 Levy *et al.* investigated the impact of SSC guidelines and included data from over 15,000 patients from 162 hospitals. The authors demonstrated improvement in the compliance of several time critical interventions, including early intervention administration of antibiotics (OR- 0.70 ($p < 0.001$)). Moreover, a sustained improvement in patient outcome was highlighted along with improved guideline compliance (30.8% mortality to 27 % ($p < 0.01$)) (21).

Early recognition of sepsis can be difficult as patients will often present late to community physicians and even later to tertiary centres. Symptoms are brushed off and coped with, preventing the necessary medical intervention. When a patient does present to medical services, correct diagnosis of infective conditions may still be troublesome. Adjuvant diagnostic tools within community pharmacies or primary care would be highly beneficial to supplement clinical acumen. Furthermore, standard diagnostic tests, blood cultures for example, may not be reliable (29). In the 2009 EPIC II study, investigators looking at infection prevalence data from 14,414 patients from 1265 worldwide intensive care units found 30% of patients with suspected sepsis had negative blood culture results (30). Moreover, blood culture techniques also have practical limitations. Results can often take days, possibly causing initial diagnostic delay and could prevent stewardship of broad spectrum antibiotics (31). Furthermore, using larger volumes of sampled blood improves accuracy of blood culture results and this can be practically difficult in certain patients (32). Needless culturing of blood is also a problem and recent guidance designed to help

streamline the ordering of blood cultures have been published, in a bid to prevent the culture of blood samples from very low risk patients (33).

1.2.2 Biomarkers of sepsis

Considering sepsis is a 'deregulated host response to infection' (20) focus on circulating biomarkers (indicative of this host response) could hold the key to an earlier, accurate diagnosis of sepsis. Subsequently, many biomarkers have gained research focus and have also been the subject of many comprehensive reviews (34–39). Pierrakos and Vincent in their 2010 review classify circulating biomarkers of sepsis into the following categories: cytocine/chemokines, cell markers, receptors, biomarkers related to vascular endothelial damage, biomarkers related to vasodilatation, acute phase proteins and 'other' (over 50 potential biomarkers are in this category (36)). Figure 1.2 shows a variety of biomarkers that could be clinically significant in patients with suspected sepsis.

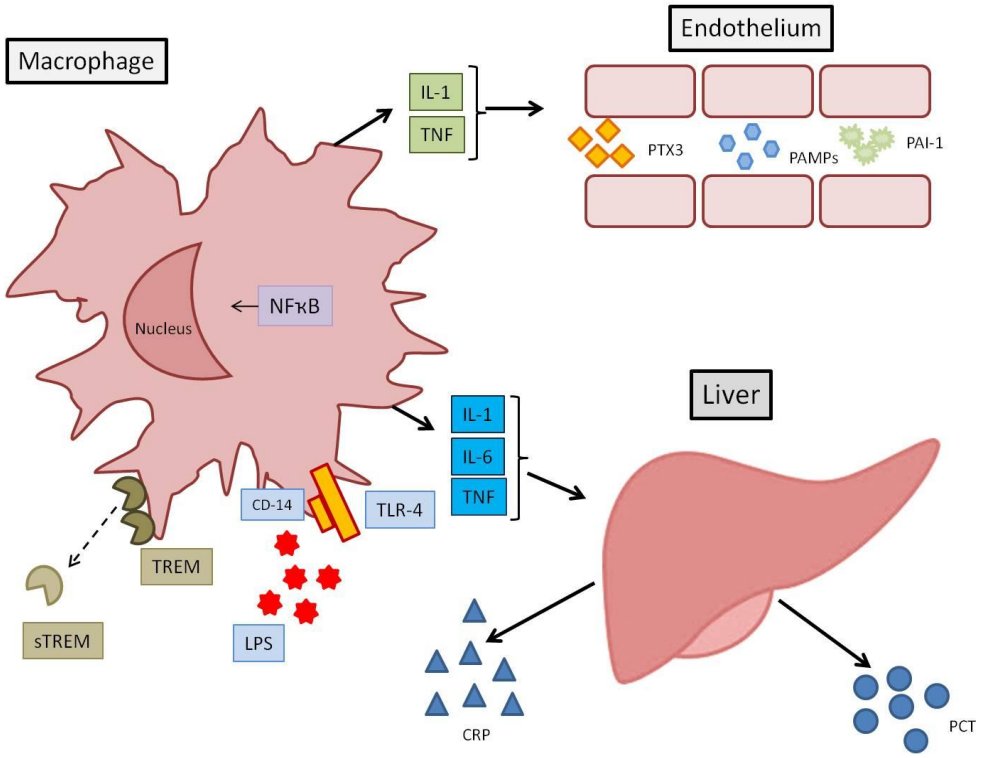

Figure 1.2: Schematic representation of selected key circulating biomarkers involved in the pathophysiology of sepsis. NFκB: Nuclear Factor kappa B; TREM: Triggering Receptor Expressed on Myeloid cells; sTREM: soluble Triggering Receptor found on Myeloid cells; LPS: Lipopolysaccharide; CD-14: Cluster Differentiation-14; TLR-4: Toll-like Receptor type 4; IL-1: Interleukin-1; IL-6: Interleukin- 6; TNF: Tumour Necrosis Factor; CRP: C Reactive Protein; PCT: Procalcitonin; PTX3: Pentraxin-related protein; PAMPs: Pathogen Associated Molecular Patterns; PAI-1: Plasminogen Activator Inhibitor-1. Adapted from (38).

Blood serum levels of C-reactive protein (CRP) and white cell count (WCC) are routinely checked in the clinical setting in patients with suspected sepsis, but the true potential of lesser-known biological markers remains elusive (40). The latest Surviving Sepsis Campaign guidelines (2016) recommend measurement of serum procalcitonin (PCT) in patients with

suspected sepsis in the context of antibiotic stewardship. However, this is classed as a 'weak recommendation' with 'low quality evidence' (25). PCT, a hormone used for the regulation of serum calcium, has received much attention in recent years and many studies have shown promise, including large randomised controlled trials (41). Studies continue to emerge that support the use of routine PCT measurement and conclude PCT should be used to guide diagnosis and treatment of sepsis (41,42). However, other authors have highlighted the problem of the non-specific nature of serum PCT fluctuations (38), highlighting that elevated PCT is also seen following trauma (43), severe burns (44) and certain neoplasms (45). Other potentially useful circulating biomarkers include the Soluble Triggering Receptor Expressed on Myeloid cells (s-TREM), a member of the immunoglobulin family (46). The non-soluble receptor TREM was identified by Bouchon and colleagues in 2000, who demonstrated significant upregulation of TREM in the presence of the pathogens *Pseudomonas aeruginosa* and *Staphylococcus aureus*. Increased expression was also seen in the presence of both LPS and Gram-positive derived lipoteichoic acid (LTA) (46,47). A recent prospective study found significantly higher levels of s-TREM in patients with sepsis who had a poorer outcome. However, the study included 63 patients, only 24 of which had documented blood borne infection (48). Soluble urokinase Plasminogen Activator Receptor (suPAR) is another circulating biomarker that has been the subject of review (49,50). This circulating protein is released from the membrane bound urokinase plasminogen activator receptor upon immune system activation (50). In agreement with other papers on the subject, a 2012 review by Backes *et al.* concluded that suPAR detection may be useful in the prognosis of patients with sepsis, however, it is of limited use in the initial diagnosis of sepsis (49). In recent work from Cirstea *et al.* in Canada, the detection of high-density lipoprotein cholesterol (HDL-C) levels as a prognosticator in sepsis was investigated. Results from Cristea *et a.* showed that low HDL-C levels

were independently associated with the development of multi organ failure in patients with sepsis and had a high predictive value for poor outcome compared to other measured markers such as lactate and WCC (51).

In more recent years, sepsis biomarker researchers have increasing interest in genomics (52), pharmacogenomics (53), lipidomics (54,55) and metabolomics (56,57). These less 'conventional' marker subsets refer to the study of the genome; known cellular drug pathways for biomarker discovery; cellular lipids; and cell metabolites, respectively. Taking metabolomics as an example, several promising studies have highlighted the potential clinical value of obtaining a metabolomic profile for patients with sepsis. Seymour and colleagues, publishing results from the GenIMS study cohort (Genetic and Inflammatory Markers of Sepsis), investigated differences in the plasma metabolomic profile of surviving and non-surviving patients with community acquired pneumonia who developed sepsis. Albeit a small sample size (15 in each group), the difference in metabolomic profile between 90 day survivors and non-survivors was clearly evident and furthermore, metabolomes identified within the profile belonged to molecular patterns of known importance in sepsis (56). Similarly, Langley *et al.* investigated the metabolomic profile of 1,152 patients with sepsis and demonstrated a markedly different metabolomic profile between survivors and non-survivors. However, they were not able to delineate survivors dependent on the severity of sepsis or causative pathogen (57). Using a metabolomic profile to reliably prognosticate and stratify patients with sepsis remains an elusive technique (58).

The answer may be in monitoring a combination of different circulating biomarkers, combining conventional and non-conventional marker detection in a bid to diagnose and prognosticate in sepsis. This approach is also the subject of many recent reviews, with numerous combinations of

biomarkers investigated (59–63). The focus of investigative work described in this thesis was lipopolysaccharide (LPS; also known as endotoxin) and its potential as a sepsis marker.

1.3 Lipopolysaccharide

1.3.1 Structure of LPS

Gram-negative bacteria cells, unlike eukaryotic cells, have dual level protection from the surrounding environment with two cell membranes (64). A phospholipid bilayer constitutes the inner membrane, whereas the outer membrane has two distinct bilayers (64). The inner leaflet is also a layer of zwitterionic phospholipids similar to the layers of the inner membrane. However, in contrast to the neighbouring layers, the outer leaflet of the outer membrane is littered with lipopolysaccharide (LPS) (65) (figure 1.3).

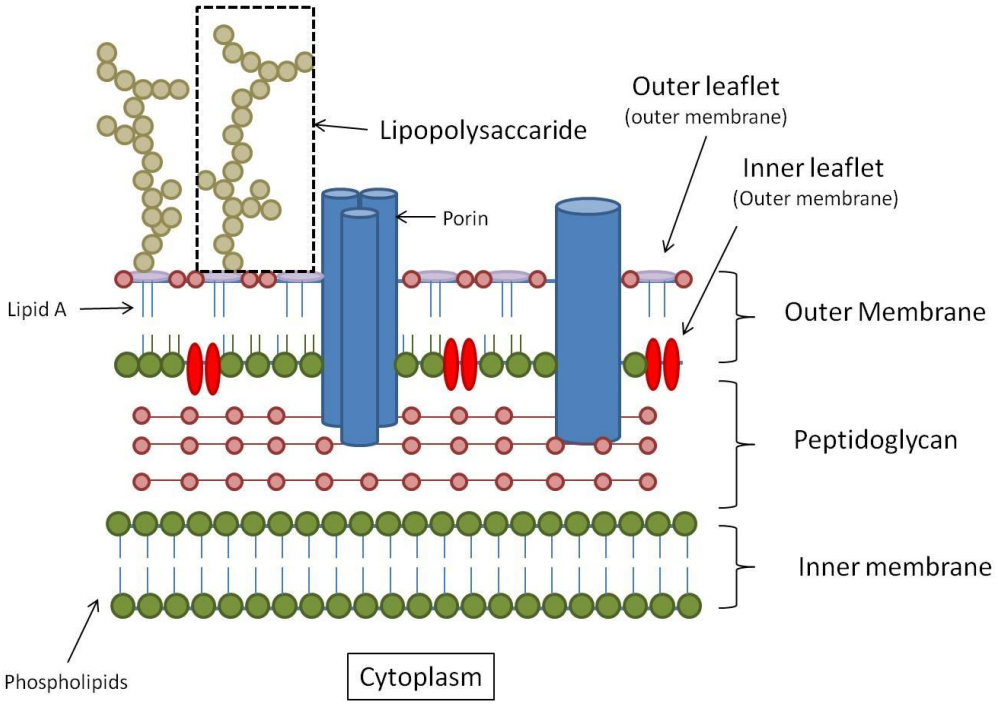

Figure 1.3: Schematic of the Gram-negative cell membrane structure demonstrating the placement of LPS on its outer membrane of the outer cell wall. Adapted from (66).

Figure 1.4 shows the general architecture of LPS, demonstrating three distinct regions: Lipid A region, a core oligosaccharide region and the O-specific antigen chain (polysaccharide region).

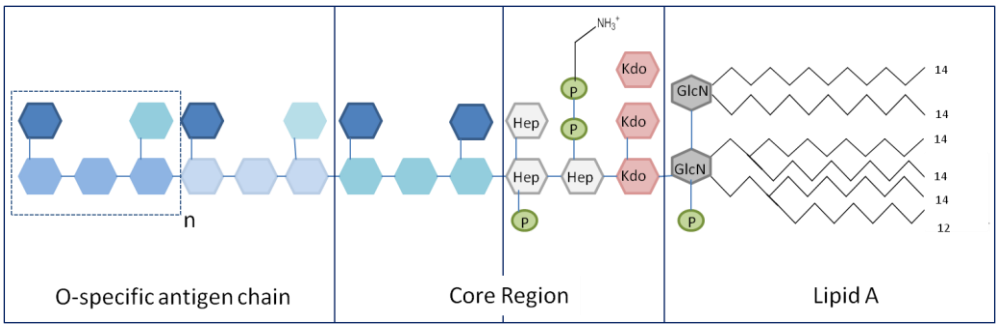

Figure 1.4: The architecture of *Escherichia coli* LPS. Hep: L-glycerol-D-manno-heptose; P: Phosphate residue; Kdo: 2-keto-3-deoxyoctamate; GlcN: 1,4- bisphosphorylated β1,6-linked D-glucosamine. The number at the end of the carbon chains indicates number of carbons. Adapted from (66), copyright (2003).

1.3.1.1 Lipid A

Lipid A is a glycophospolipid containing fatty acids with chains of 10 to 20 carbons (67) and attaches the long polysaccharide chain to the outer leaflet of the outer cell wall. The inherent toxicity of LPS is thanks to this hydrophobic portion (68,69) and even in picomolar amounts the administration of lipid A can trigger release of pro-inflammatory cytokines (70). The structure of lipid A plays an important role in the outer cell wall barrier functions of Gram-negative bacteria. For example, the physicochemical attribute of outer cell membrane viscosity is due to the close proximity of Lipid A fatty acid arrangement, therefore aiding the impermeable nature of the membrane (71). Moreover, lipid A serves to maintain the overall shape of the bacterium and also further maintains membrane integrity through close approximation to membrane proteins (71,72). Less structural variability between bacterial species is seen in the lipid A portion compared to both the core region and the O-specific antigen

chain. For example, fatty acid chain length varies between *Escherichia coli* and *Pseudomonas aeruginosa*, the latter displaying shorter chain lengths down to 10 carbons compared to the 14 length chains found in *Escherichia coli* (66,73,74).

1.3.1.2 Core region

As demonstrated in figure 1.4, the inner portion of the short core region is composed of repeating 2-keto-3-deoxyoctamate (KDO) and L-glycerol-D-manno-heptoses (heptose) residues (66). The outermost portion of the core region demonstrates interspecies variability; using varied combinations of sugars, phosphates and amino acids (75). Some LPS structures end at this core region and do not have an O-specific antigen chain; these are described as 'rough'. In this case antigenic properties are derived from their core region (LPS is described as 'smooth' if it has an O-specific antigen chain) (74,76).

1.3.1.3 O- Specific chain

The O-specific antigen chain, composed of repeating polysaccharide subunits, is capable of great complexity. It therefore demonstrates significant diversity and varies between Gram-negative species (75,77). The architecture determines the bacterial serotype and is described as providing the bacterial 'fingerprint' by Caroff & Karibian in their extensive 2003 review (76). The O-specific antigen chain has been found responsible for a diverse range of immunogenic roles (75,78–80). For example, bacterial adhesion to mucosal cells and subsequent virulence is facilitated by the O-specific chains of *Actinobacillus pleuropneumoniae* (76,79). Furthermore, this portion of LPS structure can shield bacteria from host defences including complement induced lysis (78) and phagocytosis (80).

1.3.2 Function of LPS

1.3.2.1 Pro- inflammatory

LPS is a potent pro-inflammatory molecule capable of activating the innate immune system at concentrations below 1nM (81). Shown in figure 1.5 is the inflammatory cascade triggered by LPS. The figure is a simplified representation of several highly complex amplification pathways involved in this process. LPS is initially bound to a soluble lipopolysaccharide binding protein (LBP), a 60 kDa glycoprotein (82,83). This LPS/LBP complex is then recognised by the membrane bound Toll-like receptor 4 (TLR-4) (84).

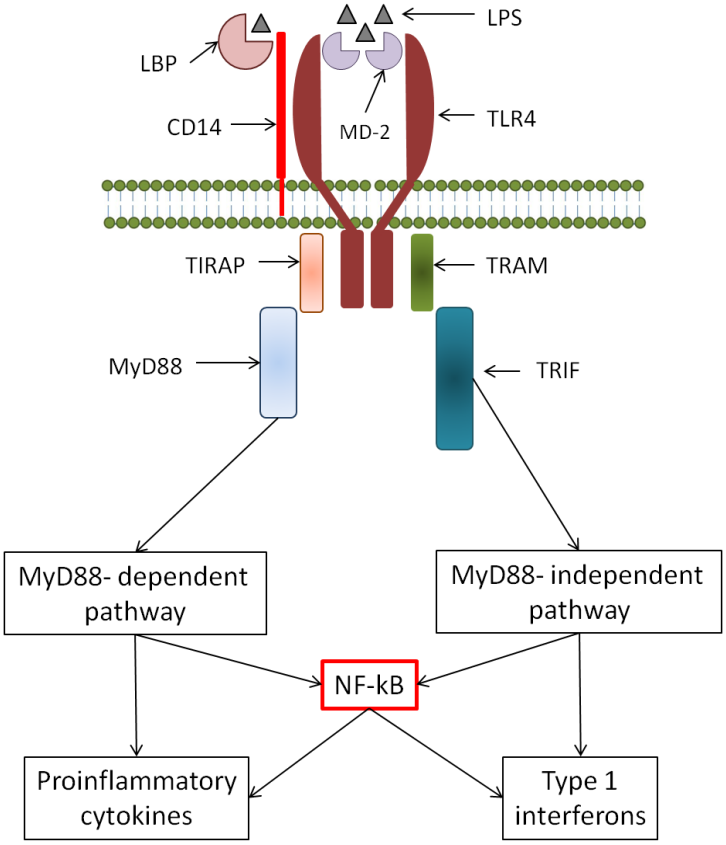

Figure 1.5: Simplified schematic overview of the host inflammatory cascade initiated by endotoxin pathogen invasion. LPS binds to lipopolysaccharide binding protein and the complex recognition is facilitated by TLR4/MD-2 transmembrane complex. The two distinct pathways (MyD88 dependent and independent) constitute the ongoing cascade and represent several complex steps. The end result is the production of inflammatory cytokines that are responsible for the clinical manifestations of sepsis. CD14: cluster of differentiation 14; TLR4: Toll Like Receptor 4; (TIR: Toll/Interleukin 1 Receptor); MD-2: lymphocyte antigen 96; TIRAP: TIR domain-containing Adaptor Protein; TRIF: TIR domain-containing Inducing Interferon β; MyD88: Myeloid Differentiation gene primary product 88; LBP: Lipopolysaccharide Binding Protein; NF-KB: Nuclear Factor-Kappa B. Adapted from (85) with permission.

In 1998, the search for the receptor responsible for initial detection of LPS led Poltorak *et al.* via genomic mapping, to identify an intact gene in the region of the *Lps* ^{d} locus (84). This *Lps* ^{d} locus was previously found to be responsible for an induced endotoxin-unresponsive state in mice (86), mapping of which revealed the gene encoding TLR-4 which is now widely recognised as the LPS recognition receptor. TLR-4 is found primarily on macrophages, activation of which allows LPS to exert its pro-inflammatory action with subsequent generation of several inflammatory mediators such as IL-1β, IL-6, IL-8 and TNFα (87). This sequence of events instigated by LPS is efficient and essential in host clearance of minor, local infection. However, overproduction of these inflammatory mediators can prove detrimental and leads to the clinical manifestations of sepsis (88). In effect, the very systems in place to protect us become our downfall in severe sepsis. However, humans still need to retain the ability to recognise and respond to LPS. Subsequent to identification of the TLR-4 encoding gene, Poltorak *et al.* provided evidence that mice with a deleterious mutation in this TLR-4 gene were unable to respond to LPS and therefore unable to mount an important initial immunogenic response (89).

1.3.2.2 Pro-pathogenic

LPS also has a key role in the promotion of bacterial virulence. Many pathogens (*Neisseria meningitides, Neisseria gonorrhoeae, Haemophilus influenzae,* for example) express LPS on their outer cell membrane that share vital structural elements with human antigens such as lactosyl and platelet activating factor (PAF), effectively providing a level of camouflage (90). This adaptation of 'molecular mimicry' also allows bacteria to take advantage of any host receptor systems for the mimicked antigens, improving entry into host cells and adherence to host tissue (90,91). The LPS of certain pathogenic species have also adapted to allow incorporation of extra chemical groups, such as sialic acid, a move that often confers

resistance to host immune systems and to antimicrobial agents (92,93). Antimicrobial resistance (AMR) refers to this adaptation of pathogens that ultimately renders certain antimicrobials ineffective for that particular pathogen (94). A global action plan for tackling AMR was launched by the World Health Organisation in 2015 (95), furthermore, such is the perceived threat of AMR that a two year review was commissioned by the UK Department of Health and the Wellcome Trust in 2014, with the final report published in 2016. Incidentally, one of the key recommendations of this report is the promotion of new, rapid diagnostics for infection to guide antibiotic use (96).

1.3.2.3 LPS in sepsis

LPS has been widely implicated in the pathophysiology of sepsis (3–5,97). The reaction of both animals (3,98) and humans (99,100) to endotoxin administration consistently and reliably triggers the sepsis-like syndrome and detection of endotoxin in the blood of patients who meet the diagnostic criteria for sepsis has been demonstrated (6,101). However, wide ranges for the percentage of patients diagnosed clinically with sepsis who have endotoxemia are quoted in the literature (20 to 40% (102)). This highlights two main problems for the interpretation of studies measuring serum endotoxin levels. Firstly, the clinical diagnosis of sepsis by even the most experienced of clinicians can be difficult and if a study relies on the accuracy of this initial diagnosis, error is undoubtedly introduced. Secondly, interpretation of studies is problematic considering the problems with commercially available assays for endotoxin. Without a highly sensitive and specific detection test for endotoxin, clinical studies looking to evaluate levels in patients will continue to be contentious. Furthermore, the presence of endotoxin in blood is not unique to sepsis, and not even unique to pathological conditions with evidence of endotoxemia in triatheletes following vigorous exercise (103). Increased endotoxin levels

have been found in patients with liver disease (104), cardiovascular disease (105,106) and also following open heart surgery requiring cardiopulmonary bypass (107). Interestingly, authors have also suggested the usefulness of measuring endotoxin in patients diagnosed with sepsis following cardiopulmonary bypass to predict outcome (108). Furthermore, humans carry as much as 25 grams of endotoxin in the gastrointestinal tract (6,109), representing around 80% of the gut cell wall mass of Gram-negative bacteria (110). During illness the translocation of GI tract endotoxin secondary to increased permeability of the gut mucosa (67,111), or via direct damage to the mucosa caused by trauma, ischemia or ionising radiation (111) can contribute to elevated blood levels. Therefore, interpretation of elevated endotoxin in patients with multiple causative possibilities is potentially complex.

1.3.2.4 Measuring LPS

Currently, LPS detection is not used routinely in the clinical setting; however, it is a vital step in pharmaceutical quality control (112). The ubiquitous nature and associated virulence of LPS (troublesome to patients at picogram levels) is a problem for the pharmaceutical industry and levels in parenteral preparations are tightly regulated (113). Reliable and specific LPS detection is paramount and commonly undertaken with the Limulus Amebocyte Lysate (LAL) assay, which relies on the haematological host clotting response of the horseshoe crab to invading endotoxin (114).

Shown in figure 1.6 is the simplified clotting cascade of the Atlantic horseshoe crab when exposed to endotoxin. This amplification pathway forms the basis of the LAL assay which was first described by Fredrick Bang and Jack Levin in 1968, following their independent observations of the effect of endotoxin pyrogen on the blood cells of the horseshoe crab (114).

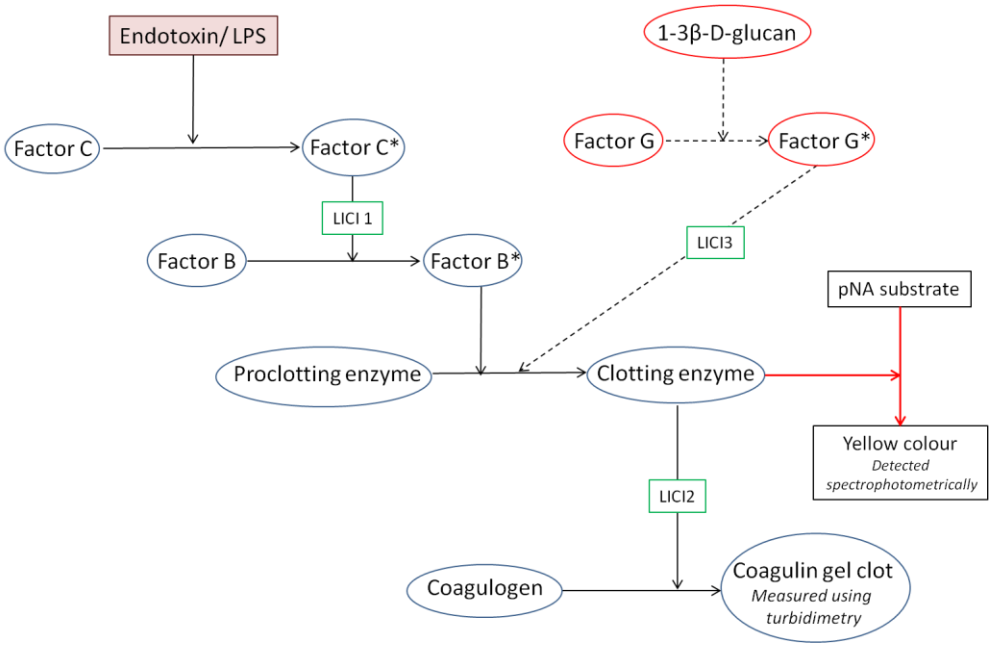

Figure 1.6: Diagram of the horseshoe crab coagulation cascade triggered by endotoxin. The purpose of the final step (coagulin gel production) is to effectively trap the invading Gram-negative bacteria/endotoxin source. 1-3β-D-glucan is a fungal toxin and drives the conversion of Factor G to Factor G*; this in turn can also effect the endotoxin driven cascade. LICI: Limulus Intracellular Coagulation Inhibitor; pNA: *p* Nitroaniline. Diagram adapted from (102,115,116).

However, the LAL assay has limitations. Specificity is a problem and several endogenous factors can trigger the same amplification clotting cascade shown in figure 1.6. For example, 1-3β-D-glucan is a fungal toxin that can also amplify the conversion of pro-clotting enzyme to clotting enzyme and can therefore cause false positive results (115,117). Furthermore, false positives have been demonstrated with the LAL assay from a diverse range of substrates, including: immunglobulins (118), synthetic polyneucleotides (119), thrombin and thromboplastin (120) and gold nanoparticles (121). Moreover, harvested Gram-positive pepdidoglycans can also give false positive results (122). Considering the interference from a variety of substances when using this assay, it is unsurprising that sample

preparation is an important consideration and there are several strategies employed by pharmaceutical companies to compensate (dilution, filtration, dialysis or temperature control for example (123)). Furthermore, there is an ecological consideration secondary to widespread use of this assay. The overharvesting of horseshoe crab is having detrimental effects on the crab's population and it was labelled an endangered species in Japan over 40 years ago (115,124).

Advances in genetic engineering have allowed the successful derivatisation of an enzymatically active recombinant Factor C (rFC), the key factor in the cascade shown in figure 1.6. Based on rFC, Ding and Ho (2001) described an endotoxin assay with impressive LPS sensitivity (125) and the PyroGene (Lonza Inc, USA) detection kit became commercially available in 2004. However, although the ecological considerations for the horseshoe crab are addressed with this innovation, the reliance on the same coagulation cascade will undoubtedly involve the risk of false positives that plague the LAL assay. Using LAL-based assays with clinical samples can be problematic; in his 2000 paper J. Cohen highlighted four key considerations for the clinical use of the LAL assay: contamination (considering the assay is highly sensitive); specificity (results are referenced to a standard endotoxin and may not correlate); confounding substances in plasma; and accuracy (semi-quantitative nature of the assay) (102). Furthermore, if a patient has received antibiotics this may also interfere with the LAL assay (126).

As an alternative to the LAL assay, the Endotoxin Activity Assay (EAA; Spectral Medical Inc, USA) is a chemiluminescent assay reliant on the oxidative burst reaction of neutrophils when they are exposed to LPS-IgM immune complexes (127). The assay gives a semi-quantitative result, grouping endotoxin activity levels as low (< 0.4), intermediate (0.4 – 0.59) or high (>0.6). Several observational studies have commented on the clinical use of the EAA in patients with sepsis (108,128), but a notable

cohort study was the MEDIC trial, published in 2004 (6). This study looked at 857 patients admitted to intensive care units in the USA, Canada, Belgium and the UK. EAA levels were measured on day one and patients stratified according to EAA level (low, intermediate or high). Significant differences in patient outcome and organ dysfunction were found between these groups and high EAA levels were associated with increased mortality, irrespective of the causative organism. However, sensitivity and specificity levels for the detection of Gram-negative infection were poor: 85.3% and 44% respectively (6). More recently, the EAA from Spectral Medic Inc is known more as the detection device used in large multi centre randomised controlled trials investigating extracorporeal LPS removal strategies in sepsis using polymyxin B coated cartridges (Toramyxin) (129,130).

Detection of LPS in this project was investigated using the principles of molecular imprinting, a polymer chemistry discipline that has been used in various detection applications since the 1970s (131).

1.4 Molecular Imprinting

1.4.1 General introduction

The ability to generate synthetic recognition systems to mimic antibodies certainly sounds like an attractive prospect. The synthesis of molecularly imprinted polymers (MIPs) is an approach with the credentials to realise this possibility. Molecular imprinting describes the method of 'imprinting' a target molecule (template) into a polymer matrix (132). This serves to provide the polymer with recognition properties akin to the original target molecule. The individual work of two pioneering scientists, Günter Wulff and Klaus Mosbach, led to the first modern descriptions of molecular imprinting techniques in the 1970s and 1990s, respectively (133–135). A seminal *Nature* publication by Mosbach and colleagues in 1993 catapulted molecular imprinting into the wider scientific community and introduced the use of MIPs in 'antibody mimicry' (135). Writing in 2005, Andrew Mayes highlights the impact of this paper, stating: 'The exponential growth in interest and activity in the field of imprinting can be traced back to the influence of the publication' (136).

1.4.2 Conventional Imprinting

Shown in figure 1.7 is a simplified representation of the conventional bulk imprinting process. This can utilise a covalent approach (covalent bonds between template and monomers) or a non-covalent approach to produce an imprinted material with high affinity for the target molecule (132).

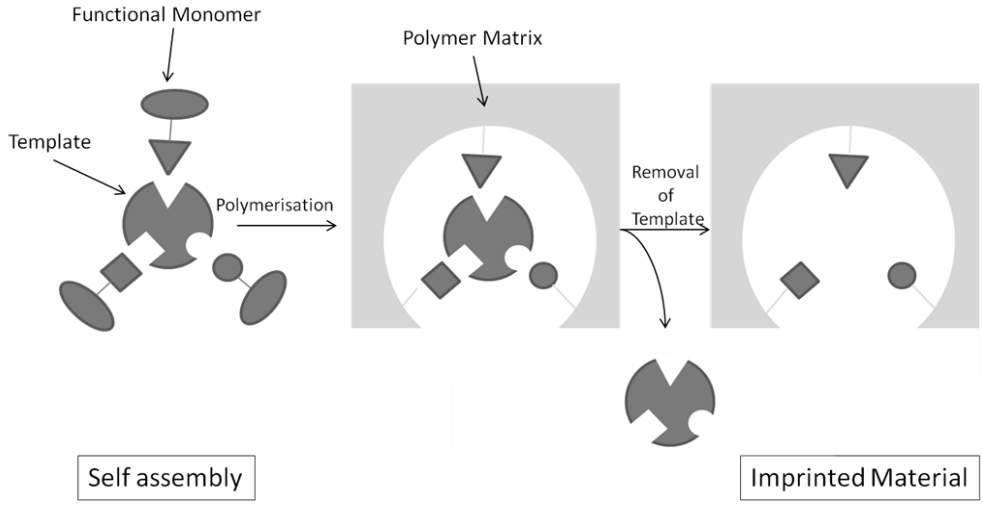

Figure 1.7: Schematic 2D representation of traditional, bulk molecular imprinting method. The self assembly of the template molecule and functional monomers takes place followed by polymerisation. The template molecule is then removed, leaving an imprint of the template molecule within the polymer matrix.

As shown in figure 1.7, the template is imprinted as a whole and thereafter removed from the polymer matrix as a complete molecule, this figure therefore represents an exemplar bulk imprinting process (132). Bulk imprinting is effective for the imprinting of small molecules (137); however, less success has been demonstrated with large, cumbersome templates such as proteins or whole cells (138,139). Therefore, molecular imprinting technology (MIT) has continuously evolved to circumvent issues with the imprinting of macromolecular templates (131,132,139).

1.4.3 Macromolecular imprinting

Macromolecular imprinting is a challenging and complex branch of MIT due to the specific obstacles faced when working with large molecules. In their extensive 2006 review, Turner *et al*. describe these obstacles under the following headings: size, complexity, conformational flexibility and solubility (139). Briefly, these subcategories describe the following

problems with macromolecular imprinting: the logistical issues of large molecules finding, and successfully leaving, binding sites due to their size; the sheer complexity of large molecules such as proteins increases the chances of different areas of the same molecule possessing multiple binding sites and exhibiting differing chemical properties; proteins tend to adopt conformations secondary to any environmental changes, these environmental changes may be necessary for the polymerisation stage; and, as described by Turner 'perhaps the greatest challenge of all is the limited choice of solvent', finding the balance of protein/template stability and conditions suitable for the molecular imprinting processes can prove challenging (139).

Advances in the field of macromolecular imprinting have developed to address the problems outlined above. Surface imprinting, a method used in this study, is one such advance that tackles problems with template size and manoeuvrability (140). Surface imprinting describes the formation of high affinity binding sites located at the surface of the polymer, with binding performance indicative of the ease of accessibility of these binding sites (141,142). An exemplar surface imprinting strategy is shown in figure 1.8.

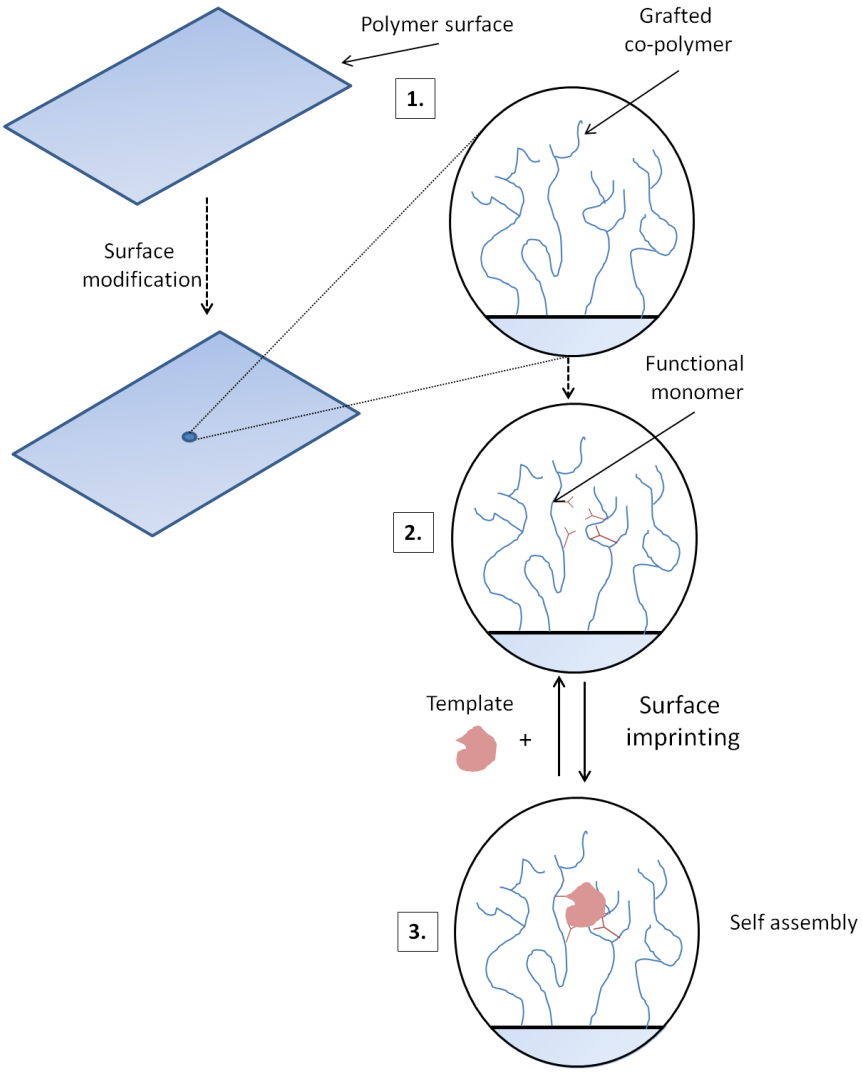

Figure 1.8: Schematic demonstrating the principles of surface imprinting. **1).** A polymer surface (support) is modified with a second, co-polymer grafted onto its surface. **2).** The modified polymer surface is now capable of displaying functional monomers chosen to interact with the desired template. **3).** The template is now introduced to the system and following conventional imprinting methodology, the template and functional monomers self assemble, however, unlike conventional imprinting this only takes place on the support surface. (Diagram adapted from educational material shown on PolyAn® website. All permissions granted).

Surface imprinting strategies fall under two broad headings: the synthesis of a polymer film (143–145) or template immobilisation (using resin for example) with subsequent polymerisation on this support surface. Template immobilisation was branded a 'new approach to molecular imprinting' by Mosbach in a 2000 communication paper (146) and developing suitable immobilisation strategies is now often a key part of the successful imprinting. For example, in Mosbach's 2000 paper a theophylline derivative was immobilised on an amino derivatised silica gel via amide bonds and successfully imprinted (146). Further examples include immobilisation of cholesterol via a carbonate ester to diol-derived carbon chain spacer moiety interaction (147); immobilisation of amlodipine through hydrogen bonding with carboxyl modified silica microspheres (148) and covalent immobilisation of haemoglobin via imine bonds between the haemoglobin amino groups and aldehyde groups on an aminopropyl silica surface (149).

Epitope imprinting represents a bridge between bulk and surface imprinting strategies and describes the imprinting of a larger protein via the imprinting of a representative short polypeptide chain (140,150,151). Rachkov *et al*. published seminal work on epitope imprinting in 2000. The group demonstrated successful recognition of the nonapeptide oxytocin subsequent to the imprinting of a smaller, representative tetrapeptide (150). Subsequently, epitope imprinting strategies have been developed to successfully imprint complex macromolecules such as albumin (143,152), immunoglobulin G (153) and lysozyme (154). Shea's 2006 paper combines the technique of epitope imprinting and surface imprinting (both template immobilisation and polymer film synthesis) (143). Using three key biological proteins (cytochrome c, alcohol dehydrogenase and bovine serum albumin) the group demonstrated covalent epitope attachment to a silicon surface with subsequent MIP film synthesis via surface polymerisation (143).

In 2010, Shea and co-workers pushed MIPs into an exciting biomedical arena. They elegantly demonstrated this use of molecular imprinting to produce 'plastic antibodies' with the ability to neutralise a toxin *in vivo*; work that heralded a sea change in the true potential of MIT. The target was melittin, the active ingredient of bee venom (155,156) and Shea *et al.* demonstrated a significant increase in survival time of mice injected with a MIP nanoparticle following an injection of melittin compared to mice who received an injection of melittin alone. A common reservation concerning the use of synthetic nanoparticles *in vivo* is toxicity (157), however, in this study no toxicity was seen with intravenous administration of the MIP. Shea's work provides an interesting background for the pursuit of generating a MIP with the ability to detect and sequester LPS.

Table 1.1 outlines some of the advantages of developing recognition systems using molecular imprinting compared to using naturally occurring, endogenous recognition systems. Many of these advantages ensure molecular imprinting remains an important research focus in the development of potential 'plastic antibodies'.

Table 1.1: Comparison of naturally occurring recognition elements with synthesised MIPs. Adapted from (140) and (158).

Property	Natural recognition template	MIPs
Binding affinity	High	Variable
Robustness	Limited stability/poor performance in non-aqueous media	Stable under a variety of conditions/ can work in organic solvents
Cost	Expensive synthesis	Inexpensive
Storage	Days at room temp	Long term storage without any loss in performance
Sensor integration	Poor compatibility with transducer surfaces/micromachining /miniaturisation	Polymers are fully compatible with micromachining technology

1.4.4 Molecular imprinting and biosensing

Molecular imprinting has many attributes that make it an attractive technology in the field of biosensing and extensive reviews have been written solely focussed on this application (159–163). Polymer sensors offer advantages such as robustness, reduced cost and increased shelf life when compared to traditional, antibody based sensors and biosensing MIPs have been developed to work with a variety of media including urine (164,165), cerebrospinal fluid (166) and blood (167,168). Imprinted polymer nanoparticles have also been shown to out-perform enzyme-

linked immunosorbent assays for a variety of biologically relevant targets (137).

The detection of drugs by MIPs was first highlighted in 1993 by Mosbach's group (theophylline and diazepam detection (135)) and is now an established field of MIT. With implications for therapeutic drug monitoring and evidence based dosing regimens for antibiotics, the detection of ciprofloxacin (169), metronidazole (167) and tetracycline (170) have been demonstrated by MIPs. Furthermore, well established imprinting methods for a common drug template propranolol have been successfully applied to drug detection in human plasma and urine, utilising strategies for the production of aqueous compatible MIPs (165,171). The detection of beta blockers in urine has relevance for the sports industry, an application highlighted by Santos *et al*. in their 2015 paper describing a water compatible oxprenolol MIP capable of the detection of a variety of beta blockers in urine (165).

Clinically relevant circulating biomarkers have also been successfully imprinted to provide a viable alternative to gold-standard detection methods. MIPs for cancer diagnostics have been successfully synthesised for prostate specific antigen (PSA) (172,173), ovarian cancer antigen 125 (CA-125) (174) and nuclear matrix protein 22 (NMP-22) (175), the latter being a relatively newly discovered biomarker for urethral cancer screening in patients with microscopic haematuria (176). In their 2017 MIP cancer diagnostic sensors review, Selvolini and Marrazza echo sentiments from previous MIP biosensor papers by highlighting advantages such as stability, low cost and high affinity profiles. Furthermore, the authors stress the nanoscale potential of MIPs and hint at the use of MIP sensors in near-patient testing devices (177).

Despite the growing wealth of MIP research concerning biosensors, attention has not been paid to the development of MIPs for potential

biomarkers in sepsis. Considering the global burden and time sensitive nature of the condition, MIT application to sepsis diagnostics is a worthwhile pursuit.

1.5 References

1. Vincent J-L, Marshall JC, Namendys-Silva SA, François B, Martin-Loeches I, Lipman J, et al. Assessment of the worldwide burden of critical illness: the intensive care over nations (ICON) audit. Lancet Respir Med. 2014 May;2(5):380–6.

2. Fleischmann C, Scherag A, Adhikari NKJ, Hartog CS, Tsaganos T, Schlattmann P, et al. Assessment of Global Incidence and Mortality of Hospital-treated Sepsis. Current Estimates and Limitations. Am J Respir Crit Care Med. 2016 Feb 1;193(3):259–72.

3. Morrison DC, Danner RL, Dinarello CA, Munford RS, Natanson C, Pollack M, et al. Bacterial endotoxins and pathogenesis of Gram-negative infections: current status and future direction. J Endotoxin Res. 1994 Jun 1;1(2):71–83.

4. Glauser MP, Zanetti G, Baumgartner JD, Cohen J. Septic shock: pathogenesis. Lancet Lond Engl. 1991 Sep 21;338(8769):732–6.

5. Opal SM. Endotoxins and other sepsis triggers. Contrib Nephrol. 2010;167:14–24.

6. Marshall JC, Foster D, Vincent J-L, Cook DJ, Cohen J, Dellinger RP, et al. Diagnostic and prognostic implications of endotoxemia in critical illness: results of the MEDIC study. J Infect Dis. 2004 Aug 1;190(3):527–34.

7. Padkin A, Goldfrad C, Brady AR, Young D, Black N, Rowan K. Epidemiology of severe sepsis occurring in the first 24 hrs in intensive care units in England, Wales, and Northern Ireland. Crit Care Med. 2003 Sep;31(9):2332–8.

8. Angus DC, Linde-Zwirble WT, Lidicker J, Clermont G, Carcillo J, Pinsky MR. Epidemiology of severe sepsis in the United States: analysis of incidence, outcome, and associated costs of care. Crit Care Med. 2001 Jul;29(7):1303–10.

9. Iwashyna TJ, Ely EW, Smith DM, Langa KM. Long-term cognitive impairment and functional disability among survivors of severe sepsis. JAMA. 2010 Oct 27;304(16):1787–94.

10. Winters BD, Eberlein M, Leung J, Needham DM, Pronovost PJ, Sevransky JE. Long-term mortality and quality of life in sepsis: a systematic review. Crit Care Med. 2010 May;38(5):1276–83.

11. Shankar-Hari M, Rubenfeld GD. Understanding Long-Term Outcomes Following Sepsis: Implications and Challenges. Curr Infect Dis Rep. 2016;18(11).

12. Hunter JD. Ventilator associated pneumonia. BMJ. 2012;344:e3325.

13. Arendrup MC. Epidemiology of invasive candidiasis. Curr Opin Crit Care. 2010 Oct;16(5):445–52.

14. Bobo LD, Dubberke ER, Kollef M. Clostridium difficile in the ICU: the struggle continues. Chest. 2011 Dec;140(6):1643–53.

15. Chant C, Smith OM, Marshall JC, Friedrich JO. Relationship of catheter-associated urinary tract infection to mortality and length of stay in critically ill patients: a systematic review and meta-analysis of observational studies. Crit Care Med. 2011 May;39(5):1167–73.

16. Tacconelli E, Smith G, Hieke K, Lafuma A, Bastide P. Epidemiology, medical outcomes and costs of catheter-related bloodstream infections in intensive care units of four European countries: literature- and registry-based estimates. J Hosp Infect. 2009 Jun;72(2):97–103.

17. Singer M. Interveiw with speaker at ARS/BJA Research Forum, London, UK. 2017.

18. Shankar-Hari M, Deutschman CS, Singer M. Do we need a new definition of sepsis? Intensive Care Med. 2015 May 1;41(5):909–11.

19. Levy MM, Fink MP, Marshall JC, Abraham E, Angus D, Cook D, et al. 2001 SCCM/ESICM/ACCP/ATS/SIS International Sepsis Definitions Conference. Intensive Care Med. 2003 Apr;29(4):530–8.

20. Singer M, Deutschman CS, Seymour CW, Shankar-Hari M, Annane D, Bauer M, et al. The Third International Consensus Definitions for Sepsis and Septic Shock (Sepsis-3). JAMA. 2016 Feb 23;315(8):801–10.

21. Levy MM, Dellinger RP, Townsend SR, Linde-Zwirble WT, Marshall JC, Bion J, et al. The Surviving Sepsis Campaign: results of an international guideline-based performance improvement program targeting severe sepsis. Intensive Care Med. 2010 Feb;36(2):222–31.

22. Levy MM, Artigas A, Phillips GS, Rhodes A, Beale R, Osborn T, et al. Outcomes of the Surviving Sepsis Campaign in intensive care units in the USA and Europe: a prospective cohort study. Lancet Infect Dis. 2012 Dec;12(12):919–24.

23. Westphal GA, Lino AS. Systematic screening is essential for early diagnosis of severe sepsis and septic shock. Rev Bras Ter Intensiva. 2015;27(2):96–101.

24. Rhodes A, Phillips G, Beale R, Cecconi M, Chiche JD, De Backer D, et al. The Surviving Sepsis Campaign bundles and outcome: results from the International Multicentre Prevalence Study on Sepsis (the IMPreSS study). Intensive Care Med. 2015 Sep;41(9):1620–8.

25. Rhodes A, Evans LE, Alhazzani W, Levy MM, Antonelli M, Ferrer R, et al. Surviving Sepsis Campaign: International Guidelines for Management of Sepsis and Septic Shock: 2016. Intensive Care Med. 2017 Mar 1;43(3):304–77.

26. Sepsis: recognition, diagnosis and early management | Guidance and guidelines | NICE [Internet]. Available from: https://www.nice.org.uk/guidance/ng51

27. Gao F, Melody T, Daniels DF, Giles S, Fox S. The impact of compliance with 6-hour and 24-hour sepsis bundles on hospital mortality in patients with severe sepsis: a prospective observational study. Crit Care. 2005;9(6):R764–70.

28. Ferrer R, Artigas A, Levy MM, Blanco J, González-Díaz G, Garnacho-Montero J, et al. Improvement in process of care and outcome after a multicenter severe sepsis educational program in Spain. JAMA. 2008 May 21;299(19):2294–303.

29. Vincent J-L, Rello J, Marshall J, Silva E, Anzueto A, Martin CD, et al. International study of the prevalence and outcomes of infection in intensive care units. JAMA. 2009 Dec 2;302(21):2323–9.

30. Vincent J-L, Rello J, Marshall J, Silva E, Anzueto A, Martin CD, et al. International study of the prevalence and outcomes of infection in intensive care units. JAMA J Am Med Assoc. 2009 Dec 2;302(21):2323–9.

31. Dark PM, Dean P, Warhurst G. Bench-to-bedside review: The promise of rapid infection diagnosis during sepsis using polymerase chain reaction-based pathogen detection. Crit Care. 2009;13(4):217.

32. Mermel LA, Maki DG. Detection of bacteremia in adults: consequences of culturing an inadequate volume of blood. Ann Intern Med. 1993 Aug 15;119(4):270–2.

33. Coburn B, Morris AM, Tomlinson G, Detsky AS. Does this adult patient with suspected bacteremia require blood cultures? JAMA J Am Med Assoc. 2012 Aug 1;308(5):502–11.

34. Herzum I, Renz H. Inflammatory markers in SIRS, sepsis and septic shock. Curr Med Chem. 2008;15(6):581–7.

35. Marshall JC, Reinhart K. Biomarkers of sepsis. Crit Care Med. 2009 Jul;37(7):2290–8.

36. Pierrakos C, Vincent J-L. Sepsis biomarkers: a review. Crit Care Lond Engl. 2010;14(1):R15.

37. Reinhart K, Bauer M, Riedemann NC, Hartog CS. New Approaches to Sepsis: Molecular Diagnostics and Biomarkers. Clin Microbiol Rev. 2012 Oct 1;25(4):609–34.

38. Lichtenstern C, Brenner T, Bardenheuer HJ, Weigand MA. Predictors of survival in sepsis: what is the best inflammatory marker to measure? Curr Opin Infect Dis. 2012 Jun;25(3):328–36.

39. Cho S-Y, Choi J-H. Biomarkers of Sepsis. Infect Chemother. 2014 Mar;46(1):1–12.

40. Faix JD. Biomarkers of sepsis. Crit Rev Clin Lab Sci. 2013 Feb;50(1):23–36.

41. Bouadma L, Luyt C-E, Tubach F, Cracco C, Alvarez A, Schwebel C, et al. Use of procalcitonin to reduce patients' exposure to antibiotics in intensive care units (PRORATA trial): a multicentre randomised controlled trial. The Lancet. 6;375(9713):463–74.

42. Balcl C, Sungurtekin H, Gürses E, Sungurtekin U, Kaptanoglu B. Usefulness of procalcitonin for diagnosis of sepsis in the intensive care unit. Crit Care. 2003;7(1):85–90.

43. Maier M, Wutzler S, Lehnert M, Szermutzky M, Wyen H, Bingold T, et al. Serum procalcitonin levels in patients with multiple injuries including visceral trauma. J Trauma. 2009 Jan;66(1):243–9.

44. von Heimburg D, Stieghorst W, Khorram-Sefat R, Pallua N. Procalcitonin--a sepsis parameter in severe burn injuries. Burns J Int Soc Burn Inj. 1998 Dec;24(8):745–50.

45. Giovanella L, Maffioli M, Suriano S, Dorizzi RM. Elevated calcitonin and procalcitonin levels in nonmedullary benign and malignant thyroid nodules. Clin Endocrinol (Oxf). 2010 Jun;72(6):852–3.

46. Bouchon A, Facchetti F, Weigand MA, Colonna M. TREM-1 amplifies inflammation and is a crucial mediator of septic shock. Nature. 2001 Apr 26;410(6832):1103–7.

47. Bouchon A, Dietrich J, Colonna M. Cutting edge: inflammatory responses can be triggered by TREM-1, a novel receptor expressed on neutrophils and monocytes. J Immunol Baltim Md 1950. 2000 May 15;164(10):4991–5.

48. Jeong SJ, Song YG, Kim CO, Kim HW, Ku NS, Han SH, et al. Measurement of Plasma STREM-1 in Patients With Severe Sepsis Receiving Early Goal-Directed Therapy and Evaluation of Its Usefulness. Shock. 2012 Jun;37(6):574–8.

49. Backes Y, van der Sluijs KF, Mackie DP, Tacke F, Koch A, Tenhunen JJ, et al. Usefulness of suPAR as a biological marker in patients with systemic inflammation or infection: a systematic review. Intensive Care Med. 2012 Sep;38(9):1418–28.

50. Donadello K, Scolletta S, Covajes C, Vincent J-L. suPAR as a prognostic biomarker in sepsis. BMC Med. 2012;10:2.

51. Cirstea M, Walley KR, Russell JA, Brunham LR, Genga KR, Boyd JH. Decreased high-density lipoprotein cholesterol level is an early prognostic marker for organ dysfunction and death in patients with suspected sepsis. J Crit Care. 2017 Apr;38:289–94.

52. Calvano SE, Xiao W, Richards DR, Felciano RM, Baker HV, Cho RJ, et al. A network-based analysis of systemic inflammation in humans. Nature. 2005 Oct 13;437(7061):1032–7.

53. Russell JA. Genomics and pharmacogenomics of sepsis: so close and yet so far. Crit Care [Internet]. 2016;20. Available from: https://www.ncbi.nlm.nih.gov/pmc/articles/PMC4936251/

54. Anthonymuthu TS, Kim-Campbell N, Bayır H. Oxidative lipidomics: applications in critical care. Curr Opin Crit Care. 2017 Aug;23(4):251–6.

55. Stephenson DJ, Hoeferlin LA, Chalfant CE. Lipidomics in translational research and the clinical significance of lipid-based biomarkers. Transl Res J Lab Clin Med. 2017 Nov;189:13–29.

56. Seymour CW, Yende S, Scott MJ, Pribis J, Mohney RP, Bell LN, et al. Metabolomics in pneumonia and sepsis: an analysis of the GenIMS cohort study. Intensive Care Med. 2013 Aug 1;39(8):1423–34.

57. Langley RJ, Tsalik EL, Velkinburgh JC van, Glickman SW, Rice BJ, Wang C, et al. An Integrated Clinico-Metabolomic Model Improves Prediction of Death in Sepsis. Sci Transl Med. 2013 Jul 24;5(195):195ra95-195ra95.

58. Evangelatos N, Bauer P, Reumann M, Satyamoorthy K, Lehrach H, Brand A. Metabolomics in Sepsis and Its Impact on Public Health. Public Health Genomics. 2018 Jan 19;

59. Su L, Han B, Liu C, Liang L, Jiang Z, Deng J, et al. Value of soluble TREM-1, procalcitonin, and C-reactive protein serum levels as biomarkers for detecting bacteremia among sepsis patients with new fever in intensive care units: a prospective cohort study. BMC Infect Dis. 2012;12:157.

60. Kibe S, Adams K, Barlow G. Diagnostic and prognostic biomarkers of sepsis in critical care. J Antimicrob Chemother. 2011 Apr;66 Suppl 2:ii33-40.

61. Gibot S, Béné MC, Noel R, Massin F, Guy J, Cravoisy A, et al. Combination biomarkers to diagnose sepsis in the critically ill patient. Am J Respir Crit Care Med. 2012 Jul 1;186(1):65–71.

62. Tsalik EL, Jaggers LB, Glickman SW, Langley RJ, van Velkinburgh JC, Park LP, et al. Discriminative value of inflammatory biomarkers for suspected sepsis. J Emerg Med. 2012 Jul;43(1):97–106.

63. Meynaar IA, Droog W, Batstra M, Vreede R, Herbrink P. In Critically Ill Patients, Serum Procalcitonin Is More Useful in Differentiating between Sepsis and SIRS than CRP, Il-6, or LBP. Crit Care Res Pract. 2011;2011:594645.

64. Beveridge TJ. Structures of Gram-Negative Cell Walls and Their Derived Membrane Vesicles. J Bacteriol. 1999 Aug;181(16):4725–33.

65. Silhavy TJ, Kahne D, Walker S. The Bacterial Cell Envelope. Cold Spring Harb Perspect Biol [Internet]. Available from: http://www.ncbi.nlm.nih.gov/pmc/articles/PMC2857177/

66. Beutler B, Rietschel ET. Innate immune sensing and its roots: the story of endotoxin. Nat Rev Immunol. 2003 Feb 1;3(2):169–76.

67. Hurley JC. Endotoxemia: methods of detection and clinical correlates. Clin Microbiol Rev. 1995 Apr;8(2):268–92.

68. Marshall JC. Lipopolysaccharide: An Endotoxin or an Exogenous Hormone? Clin Infect Dis. 2005 Nov 15;41(Supplement_7):S470–80.

69. Brandenburg K, Seydel U, Schromm AB, Loppnow H, Koch MHJ, Rietschel ET. Conformation of lipid A, the endotoxic center of bacterial lipopolysaccharide. J Endotoxin Res. 1996 Jun 1;3(3):173–8.

70. Ramachandran G. Gram-positive and gram-negative bacterial toxins in sepsis. Virulence. 2014 Jan 1;5(1):213–8.

71. Rietschel ET, Wollenweber H-W, Zähringer U, Lüderitz O. Lipid A, the lipid component of bacterial lipopolysaccharides: Relation of chemical structure to biological activity. Klin Wochenschr. 1982 Jul 1;60(14):705–9.

72. Yamada H, Mizushima S. Interaction between Major Outer Membrane Protein (O-8) and Lipopolysaccharide in Escherichia coli K12. Eur J Biochem. 1980 Jan 1;103(1):209–18.

73. Raetz CRH, Whitfield C. Lipopolysaccharide Endotoxins. Annu Rev Biochem. 2002;71(1):635–700.

74. Steimle A, Autenrieth IB, Frick J-S. Structure and function: Lipid A modifications in commensals and pathogens. Int J Med Microbiol. 2016 Aug 1;306(5):290–301.

75. Rietschel ET, Kirikae T, Schade FU, Ulmer AJ, Holst O, Brade H, et al. The chemical structure of bacterial endotoxin in relation to bioactivity. Immunobiology. 1993 Apr 1;187(3):169–90.

76. Caroff M, Karibian D. Structure of bacterial lipopolysaccharides. Carbohydr Res. 2003 Nov 14;338(23):2431–47.

77. Wang X, Quinn PJ. Lipopolysaccharide: Biosynthetic pathway and structure modification. Prog Lipid Res. 2010 Apr;49(2):97–107.

78. Lerouge I, Vanderleyden J. O-antigen structural variation: mechanisms and possible roles in animal/plant-microbe interactions. FEMS Microbiol Rev. 2002 Mar;26(1):17–47.

79. Paradis SE, Dubreuil D, Rioux S, Gottschalk M, Jacques M. High-molecular-mass lipopolysaccharides are involved in Actinobacillus pleuropneumoniae adherence to porcine respiratory tract cells. Infect Immun. 1994 Aug;62(8):3311–9.

80. Joiner KA, Schmetz MA, Goldman RC, Leive L, Frank MM. Mechanism of bacterial resistance to complement-mediated killing: inserted C5b-9 correlates with killing for Escherichia coli O111B4 varying in O-antigen capsule and O-polysaccharide coverage of lipid A core oligosaccharide. Infect Immun. 1984 Jul 1;45(1):113–7.

81. Aderem A, Ulevitch RJ. Toll-like receptors in the induction of the innate immune response. Nature. 2000 Aug 17;406(6797):782–7.

82. Pugin J, Schürer-Maly CC, Leturcq D, Moriarty A, Ulevitch RJ, Tobias PS. Lipopolysaccharide activation of human endothelial and epithelial cells is mediated by lipopolysaccharide-binding protein and soluble CD14. Proc Natl Acad Sci. 1993 Apr 1;90(7):2744–8.

83. Wright SD, Ramos RA, Tobias PS, Ulevitch RJ, Mathison JC. CD14, a receptor for complexes of lipopolysaccharide (LPS) and LPS binding protein. Science. 1990 Sep 21;249(4975):1431–3.

84. Poltorak A, Smirnova I, He X, Liu MY, Van Huffel C, McNally O, et al. Genetic and physical mapping of the Lps locus: identification of the toll-4 receptor as a candidate gene in the critical region. Blood Cells Mol Dis. 1998 Sep;24(3):340–55.

85. Lu Y-C, Yeh W-C, Ohashi PS. LPS/TLR4 signal transduction pathway. Cytokine. 2008 May;42(2):145–51.

86. Rosenstreich DL, Vogel SN, Jacques AR, Wahl LM, Oppenheim JJ. Macrophage sensitivity to endotoxin: genetic control by a single codominant gene. J Immunol Baltim Md 1950. 1978 Nov;121(5):1664–70.

87. Holst B, Raby A-C, Hall JE, Labéta MO. Complement takes its Toll: an inflammatory crosstalk between Toll-like receptors and the receptors for the complement anaphylatoxin C5a. Anaesthesia. 2012 Jan;67(1):60–4.

88. Van Amersfoort ES, Van Berkel TJC, Kuiper J. Receptors, Mediators, and Mechanisms Involved in Bacterial Sepsis and Septic Shock. Clin Microbiol Rev. 2003 Jul;16(3):379–414.

89. Poltorak A, He X, Smirnova I, Liu MY, Van Huffel C, Du X, et al. Defective LPS signaling in C3H/HeJ and C57BL/10ScCr mice: mutations in Tlr4 gene. Science. 1998 Dec 11;282(5396):2085–8.

90. Harvey HA, Swords WE, Apicella MA. The mimicry of human glycolipids and glycosphingolipids by the lipooligosaccharides of pathogenic neisseria and haemophilus. J Autoimmun. 2001 May;16(3):257–62.

91. Pier GB, Grout M, Zaidi TS, Olsen JC, Johnson LG, Yankaskas JR, et al. Role of mutant CFTR in hypersusceptibility of cystic fibrosis patients to lung infections. Science. 1996 Jan 5;271(5245):64–7.

92. Guerry P, Ewing CP, Hickey TE, Prendergast MM, Moran AP. Sialylation of lipooligosaccharide cores affects immunogenicity and serum resistance of Campylobacter jejuni. Infect Immun. 2000 Dec;68(12):6656–62.

93. Inzana TJ, Glindemann G, Cox AD, Wakarchuk W, Howard MD. Incorporation of N-acetylneuraminic acid into Haemophilus somnus lipooligosaccharide (LOS): enhancement of resistance to serum and reduction of LOS antibody binding. Infect Immun. 2002 Sep;70(9):4870–9.

94. Tenover FC. Mechanisms of antimicrobial resistance in bacteria. Am J Infect Control. 2006 Jun;34(5 Suppl 1):S3-10; discussion S64-73.

95. WHO | Antimicrobial resistance [Internet]. WHO. Available from: http://www.who.int/mediacentre/factsheets/fs194/en/

96. Publications | AMR Review [Internet]. Available from: https://amr-review.org/Publications.html

97. Marshall JC. Endotoxin in the pathogenesis of sepsis. Contrib Nephrol. 2010;167:1–13.

98. Danek J, Żurek U. Changes in Domestic Animals After Endotoxin Administration a Review. Ann Anim Sci. 2014;14(3):479–489.

99. Michie HR, Manogue KR, Spriggs DR, Revhaug A, O'Dwyer S, Dinarello CA, et al. Detection of circulating tumor necrosis factor after endotoxin administration. N Engl J Med. 1988 Jun 9;318(23):1481–6.

100. Taveira da Silva AM, Kaulbach HC, Chuidian FS, Lambert DR, Suffredini AF, Danner RL. Brief report: shock and multiple-organ dysfunction after self-administration of Salmonella endotoxin. N Engl J Med. 1993 May 20;328(20):1457–60.

101. Opal SM, Scannon PJ, Vincent JL, White M, Carroll SF, Palardy JE, et al. Relationship between plasma levels of lipopolysaccharide (LPS) and LPS-binding protein in patients with severe sepsis and septic shock. J Infect Dis. 1999 Nov;180(5):1584–9.

102. Cohen J. The detection and interpretation of endotoxaemia. Intensive Care Med. 2000 Feb 1;26(1):S051–6.

103. Jeukendrup AE, Vet-Joop K, Sturk A, Stegen JH, Senden J, Saris WH, et al. Relationship between gastro-intestinal complaints and endotoxaemia, cytokine release and the acute-phase reaction during and after a long-distance triathlon in highly trained men. Clin Sci Lond Engl 1979. 2000 Jan;98(1):47–55.

104. Lin C-Y, Tsai I-F, Ho Y-P, Huang C-T, Lin Y-C, Lin C-J, et al. Endotoxemia contributes to the immune paralysis in patients with cirrhosis. J Hepatol. 2007 May;46(5):816–26.

105. Wiedermann CJ, Kiechl S, Dunzendorfer S, Schratzberger P, Egger G, Oberhollenzer F, et al. Association of endotoxemia with carotid atherosclerosis and cardiovascular disease: prospective results from the Bruneck Study. J Am Coll Cardiol. 1999 Dec;34(7):1975–81.

106. Niebauer J, Volk H-D, Kemp M, Dominguez M, Schumann RR, Rauchhaus M, et al. Endotoxin and immune activation in chronic heart failure: a prospective cohort study. The Lancet. 1999 May 29;353(9167):1838–42.

107. Riddington DW, Venkatesh B, Boivin CM, Bonser RS, Elliott TSJ, Marshall T, et al. Intestinal Permeability, Gastric Intramucosal pH, and Systemic Endotoxemia in Patients Undergoing Cardiopulmonary Bypass. JAMA. 1996 Apr 3;275(13):1007–12.

108. Yaroustovsky M, Plyushch M, Popov D, Samsonova N, Abramyan M, Popok Z, et al. Prognostic value of endotoxin activity assay in patients with severe sepsis after cardiac surgery. J Inflamm Lond Engl. 2013 Mar 6;10:8.

109. Van Deventer SJH, Ten Cate JW, Tytgat GNJ. Intestinal endotoxemia. Gastroenterology. 1988 Mar 1;94(3):825–31.

110. Pizzorno J. Toxins From the Gut. Integr Med Clin J. 2014 Dec;13(6):8–11.

111. Van Leeuwen PA, Boermeester MA, Houdijk AP, Ferwerda CC, Cuesta MA, Meyer S, et al. Clinical significance of translocation. Gut. 1994 Jan;35(1 Suppl):S28–34.

112. Suvana K. Endotoxin Detection Methods – Where are we now? [Internet]. Available from: http://www.americanpharmaceuticalreview.com/Featured-Articles/177350-Endotoxin-Detection-Methods-Where-are-we-now/

113. Affairs O of R. Inspection Technical Guides - Bacterial Endotoxins/Pyrogens [Internet]. Available from: https://www.fda.gov/iceci/inspections/inspectionguides/inspectiontechnicalguides/ucm072918.htm

114. Levin J, Bang FB. Clottable protein in Limulus; its localization and kinetics of its coagulation by endotoxin. Thromb Diath Haemorrh. 1968 Mar 31;19(1):186–97.

115. Ding JL, Ho B. Endotoxin detection--from limulus amebocyte lysate to recombinant factor C. Subcell Biochem. 2010;53:187–208.

116. Iwanaga S. Biochemical principle of Limulus test for detecting bacterial endotoxins. Proc Jpn Acad Ser B Phys Biol Sci. 2007 May;83(4):110–9.

117. Vassallo R, Limper AH. FUngal β-glucan can yield false-positive results with the limulus amebocyte lysate endotoxin assay fungal β-glucan can yield false-positive results with the limulus amebocyte lysate endotoxin assay. Chest. 1999 Aug 1;116(2):583–4.

118. Ikemura K, Ikegami K, Shimazu T, Yoshioka T, Sugimoto T. False-positive result in Limulus test caused by Limulus amebocyte lysate-reactive material in immunoglobulin products. J Clin Microbiol. 1989 Sep;27(9):1965–8.

119. Elin RJ, Utter AE. Positive Limulus amoebocyte lysate reactions with polyriboinosinic acid x polyribocytidylic acid. J Clin Microbiol. 1980 Oct;12(4):502–5.

120. Webster CJ. Principles of a quantitative assay for bacterial endotoxins in blood that uses Limulus lysate and a chromogenic substrate. J Clin Microbiol. 1980 Nov;12(5):644–50.

121. Dobrovolskaia MA, Neun BW, Clogston JD, Ding H, Ljubimova J, McNeil SE. Ambiguities in applying traditional Limulus Amoebocyte Lysate tests to quantify endotoxin in nanoparticle formulations. Nanomed. 2010 Jun;5(4):555–62.

122. Wildfeuer A, Heymer B, Schleifer KH, Haferkamp O. Investigations on the specificity of the Limulus test for the detection of endotoxin. Appl Microbiol. 1974 Nov;28(5):867–71.

123. Reich J, Lang P, Grallert H, Motschmann H. Masking of endotoxin in surfactant samples: Effects on Limulus-based detection systems. Biologicals. 2016 Sep;44(5):417–22.

124. Kwan BKY, Cheung JHY, Law ACK, Cheung SG, Shin PKS. Conservation education program for threatened Asian horseshoe crabs: A step towards reducing community apathy to environmental conservation. J Nat Conserv. 2017 Feb;35:53–65.

125. Ding JL, Ho B. A new era in pyrogen testing. Trends Biotechnol. 2001 Aug 1;19(8):277–81.

126. Yamamoto A, Ochiai M, Fujiwara H, Asakawa S, Ichinohe K, Kataoka M, et al. Evaluation of the applicability of the bacterial endotoxin test to antibiotic products. Biol J Int Assoc Biol Stand. 2000 Sep;28(3):155–67.

127. Endotoxin Activity Assay for Researchers [Internet]. Available from: http://www.spectraldx.com/researchers.html

128. Romaschin, Walker. Endotoxin activity in whole blood by neutrophil chemiluminescence-A novel analytical paradigm. Clin Chem. 2000 Sep;46(9):1504–6.

129. Cruz DN, Antonelli M, Fumagalli R, Foltran F, Brienza N, Donati A, et al. Early use of polymyxin B hemoperfusion in abdominal septic shock: the EUPHAS randomized controlled trial. JAMA. 2009 Jun 17;301(23):2445–52.

130. Klein DJ, Foster D, Schorr CA, Kazempour K, Walker PM, Dellinger RP. The EUPHRATES trial (Evaluating the Use of Polymyxin B Hemoperfusion in a Randomized controlled trial of Adults Treated for Endotoxemia and Septic shock): study protocol for a randomized controlled trial. Trials. 2014;15:218.

131. Chen L, Wang X, Lu W, Wu X, Li J. Molecular imprinting: perspectives and applications. Chem Soc Rev. 2016 Apr 18;45(8):2137–211.

132. Vasapollo G, Sole RD, Mergola L, Lazzoi MR, Scardino A, Scorrano S, et al. Molecularly Imprinted Polymers: Present and Future Prospective. Int J Mol Sci. 2011 Sep 14;12(9):5908–45.

133. Wulff G, Vesper W, Grobe-Einsler R, Sarhan A. Enzyme-analogue built polymers, 4. On the synthesis of polymers containing chiral cavities and their use for the resolution of racemates. Makromol Chem. 1977;178(10):2799–2816.

134. WULFF G. The use of polymers with enzyme-analogous structures for the resolution of racemates. Angrew Chem Intern Ed. 1972;11(4):341.

135. Vlatakis G, Andersson LI, Müller R, Mosbach K. Drug assay using antibody mimics made by molecular imprinting. Nature. 1993 Feb 18;361(6413):645–7.

136. Yan M, Ramström O. Molecularly Imprinted Materials: Science and Technology. CRC Press; 2004. 760 p.

137. Smolinska-Kempisty K, Guerreiro A, Canfarotta F, Cáceres C, Whitcombe MJ, Piletsky S. A comparison of the performance of molecularly imprinted polymer nanoparticles for small molecule targets and antibodies in the ELISA format. Sci Rep. 2016 Nov 24;6:37638.

138. Takeuchi T, Hishiya T. Molecular imprinting of proteins emerging as a tool for protein recognition. Org Biomol Chem. 2008 Jul 4;6(14):2459–67.

139. Turner NW, Jeans CW, Brain KR, Allender CJ, Hlady V, Britt DW. From 3D to 2D: a review of the molecular imprinting of proteins. Biotechnol Prog. 2006 Dec;22(6):1474–89.

140. Kryscio DR, Peppas NA. Critical review and perspective of macromolecularly imprinted polymers. Acta Biomater. 2012 Feb;8(2):461–73.

141. Zahedi P, Ziaee M, Abdouss M, Farazin A, Mizaikoff B. Biomacromolecule template-based molecularly imprinted polymers with an emphasis on their synthesis strategies: a review. Polym Adv Technol. 2016 Sep 1;27(9):1124–42.

142. Ertürk G, Mattiasson B. From imprinting to microcontact imprinting—A new tool to increase selectivity in analytical devices. J Chromatogr B. 2016 May 15;1021:30–44.

143. Nishino H, Huang C-S, Shea KJ. Selective Protein Capture by Epitope Imprinting. Angew Chem Int Ed. 2006 Apr 3;45(15):2392–6.

144. Shi F, Liu Z, Wu G-L, Zhang M, Chen H, Wang ZQ, et al. Surface Imprinting in Layer-by-Layer Nanostructured Films. Adv Funct Mater. 2007 Jul 23;17(11):1821–7.

145. Lotierzo M, Henry OYF, Piletsky S, Tothill I, Cullen D, Kania M, et al. Surface plasmon resonance sensor for domoic acid based on grafted imprinted polymer. Biosens Bioelectron. 2004 Sep 15;20(2):145–52.

146. Yilmaz E, Haupt K, Mosbach K. The Use of Immobilized Templates—A New Approach in Molecular Imprinting. Angew Chem Int Ed. 2000 Jun 16;39(12):2115–8.

147. Pérez N, Whitcombe MJ, Vulfson EN. Molecularly imprinted nanoparticles prepared by core-shell emulsion polymerization. J Appl Polym Sci. 2000;77(8):1851–1859.

148. Lai S, Ouyang X, Cai C, Xu W, Chen C, Chen X. Surface-imprinted microspheres prepared by a template-oriented method for the chiral separation of amlodipine. J Sep Sci. 2017 May;40(9):1869–76.

149. Shiomi T, Matsui M, Mizukami F, Sakaguchi K. A method for the molecular imprinting of hemoglobin on silica surfaces using silanes. Biomaterials. 2005 Sep 1;26(27):5564–71.

150. Rachkov A, Minoura N. Towards molecularly imprinted polymers selective to peptides and proteins. The epitope approach. Biochim Biophys Acta. 2001 Jan 12;1544(1–2):255–66.

151. Bossi AM, Sharma PS, Montana L, Zoccatelli G, Laub O, Levi R. Fingerprint-Imprinted Polymer: Rational Selection of Peptide Epitope Templates for the Determination of Proteins by Molecularly Imprinted Polymers. Anal Chem. 2012 May 1;84(9):4036–41.

152. Li M-X, Wang X-H, Zhang L-M, Wei X-P. A high sensitive epitope imprinted electrochemical sensor for bovine serum albumin based on enzyme amplifying. Anal Biochem. 2017 Aug 1;530:68–74.

153. Ertürk G, Uzun L, Tümer MA, Say R, Denizli A. Fab fragments imprinted SPR biosensor for real-time human immunoglobulin G detection. Biosens Bioelectron. 2011 Oct 15;28(1):97–104.

154. Brown ME, Puleo DA. Protein Binding to Peptide-Imprinted Porous Silica Scaffolds. Chem Eng J Lausanne Switz 1996. 2008 Mar 15;137(1):97–101.

155. Hoshino Y, Kodama T, Okahata Y, Shea KJ. Peptide Imprinted Polymer Nanoparticles: A Plastic Antibody. J Am Chem Soc. 2008 Nov 19;130(46):15242–3.

156. Hoshino Y, Koide H, Urakami T, Kanazawa H, Kodama T, Oku N, et al. Recognition, Neutralization, and Clearance of Target Peptides in the Bloodstream of Living Mice by Molecularly Imprinted Polymer Nanoparticles: A Plastic Antibody. J Am Chem Soc. 2010 May 19;132(19):6644–5.

157. De Jong WH, Borm PJA. Drug delivery and nanoparticles:applications and hazards. Int J Nanomedicine. 2008;3(2):133–49.

158. Whitcombe MJ, Chianella I, Larcombe L, Piletsky SA, Noble J, Porter R, et al. The rational development of molecularly imprinted polymer-based sensors for protein detection. Chem Soc Rev. 2011 Mar;40(3):1547–71.

159. Ertürk G, Mattiasson B. Molecular Imprinting Techniques Used for the Preparation of Biosensors. Sensors. 2017 Feb 4;17(2):288.

160. Cieplak M, Kutner W. Artificial Biosensors: How Can Molecular Imprinting Mimic Biorecognition? Trends Biotechnol. 2016 Nov;34(11):922–41.

161. Algieri C, Drioli E, Guzzo L, Donato L. Bio-Mimetic Sensors Based on Molecularly Imprinted Membranes. Sensors. 2014 Jul 30;14(8):13863–912.

162. Uzun L, Turner APF. Molecularly-imprinted polymer sensors: realising their potential. Biosens Bioelectron. 2016 Feb 15;76:131–44.

163. Yano K, Karube I. Molecularly imprinted polymers for biosensor applications. TrAC Trends Anal Chem. 1999 Mar;18(3):199–204.

164. Beltran A, Marcé RM, Cormack P a. G, Borrull F. Synthesis by precipitation polymerisation of molecularly imprinted polymer microspheres for the selective extraction of carbamazepine and oxcarbazepine from human urine. J Chromatogr A. 2009 Mar 20;1216(12):2248–53.

165. Santos MG, Tavares IMC, Boralli VB, Figueiredo EC. Direct doping analysis of beta-blocker drugs from urinary samples by on-line molecularly imprinted solid-phase extraction coupled to liquid chromatography/mass spectrometry. Analyst. 2015 Mar 30;140(8):2696–703.

166. Ji X, Li D, Li H. Preparation and application of a novel molecularly imprinted solid-phase microextraction monolith for selective enrichment of cholecystokinin neuropeptides in human cerebrospinal fluid. Biomed Chromatogr BMC. 2015 Aug;29(8):1280–9.

167. Jafari MT, Rezaei B, Zaker B. Ion Mobility Spectrometry as a Detector for Molecular Imprinted Polymer Separation and Metronidazole Determination in Pharmaceutical and Human Serum Samples. Anal Chem. 2009 May 1;81(9):3585–91.

168. Rezaei B, Mallakpour S, Majidi N. Solid-phase molecularly imprinted pre-concentration and spectrophotometric determination of isoxicam in pharmaceuticals and human serum. Talanta. 2009 Apr 30;78(2):418–23.

169. Yan H, Row KH, Yang G. Water-compatible molecularly imprinted polymers for selective extraction of ciprofloxacin from human urine. Talanta. 2008 Mar 15;75(1):227–32.

170. Chen L, Liu J, Zeng Q, Wang H, Yu A, Zhang H, et al. Preparation of magnetic molecularly imprinted polymer for the separation of tetracycline antibiotics from egg and tissue samples. J Chromatogr A. 2009 May 1;1216(18):3710–9.

171. Hu X, Pan J, Hu Y, Li G. Preparation and evaluation of propranolol molecularly imprinted solid-phase microextraction fiber for trace analysis of β-blockers in urine and plasma samples. J Chromatogr A. 2009 Jan 9;1216(2):190–7.

172. Patra S, Roy E, Madhuri R, Sharma PK. Nano-iniferter based imprinted sensor for ultra trace level detection of prostate-specific antigen in both men and women. Biosens Bioelectron. 2015 Apr 15;66:1–10.

173. Jolly P, Tamboli V, Harniman RL, Estrela P, Allender CJ, Bowen JL. Aptamer-MIP hybrid receptor for highly sensitive electrochemical detection of prostate specific antigen. Biosens Bioelectron. 2016 Jan 15;75:188–95.

174. Viswanathan S, Rani C, Ribeiro S, Delerue-Matos C. Molecular imprinted nanoelectrodes for ultra sensitive detection of ovarian cancer marker. Biosens Bioelectron. 2012 Mar 15;33(1):179–83.

175. Lee M-H, Thomas JL, Chang Y-C, Tsai Y-S, Liu B-D, Lin H-Y. Electrochemical sensing of nuclear matrix protein 22 in urine with molecularly imprinted poly(ethylene-co-vinyl alcohol) coated zinc oxide nanorod arrays for clinical studies of bladder cancer diagnosis. Biosens Bioelectron. 2016 May 15;79:789–95.

176. Miyanaga N, Akaza H, Tsukamoto T, Ishikawa S, Noguchi R, Ohtani M, et al. Urinary nuclear matrix protein 22 as a new marker for the screening of urothelial cancer in patients with microscopic hematuria. Int J Urol Off J Jpn Urol Assoc. 1999 Apr;6(4):173–7.

177. Selvolini G, Marrazza G. MIP-Based Sensors: Promising New Tools for Cancer Biomarker Determination. Sensors. 2017 Mar 29;17(4):718.

Chapter 2. Molecular imprinting studies using a solid support

2.1 Introduction

2.1.1 Chapter outline

This first experimental chapter outlines work with molecular imprinting strategies using a solid support as the first stage of working towards the detection of LPS. The solid support investigated was Merrifield resin and is introduced in section 2.1.2. Thereafter, surface imprinting and polymerisation approaches are explored in sections 2.1.3 and 2.1.4, respectively. Polymyxin B (PMB), a peptide antibiotic, is used in this experimental chapter to facilitate the template and monomer self assembly stage of a surface molecular imprinting process. Chapter three, however, introduces PMB in more detail with an account of PMB/LPS interaction (sections 3.1.2 to 3.1.5).

2.1.2 Merrifield Resin and its modification

Granted the Nobel Prize for chemistry in 1984, Bruce Merrifield's contribution to the science of peptide synthesis is well documented. Commencing in 1959, Merrifield's work on solid phase peptide synthesis (SPPS) provided an historic paradigm shift from the conventional solution phase synthesis of peptides. Bruce Merrifield's namesake resin is a chloromethylated polystyrene resin (figure 2.1) and was first described by Merrifield in 1963 for the synthesis of a tetrapeptide (1). Along with peptide synthesis, Merrifield resin is now used for a variety of applications including oligonucleotide and oligosaccharide synthesis (2,3), biopolymer synthesis and molecular imprinting (4–6).

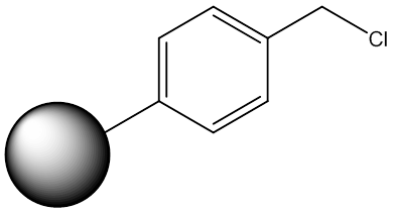

Figure 2.1: Structure of Merrifield resin. Merrifield resin is a cross-linked polystyrene resin that is also known as chloromethyl resin owing to its chloromethyl functional groups.

In 1976 the first description of aminomethyl polystyrene (7) marked the start of investigative work that would lead to the complex multi-functionalisation of resins for organic synthesis reactions. The preparation of aminomethyl polystyrene has itself developed; for example, Arseniyadis and colleagues described the formation of amino-polystyrene from a Merrifield resin and trifluoromethanesulfonic acid reaction (Schmitt rearrangement) (8). The addition of multiple functional groups to Merrifield resin can allow further diversification of coupling reactions (9,10) and can facilitate resin use in the comprehensive testing of small peptide libraries to identify peptides of catalysis interest (10,11). Multi-detachable linkers, for example, allow the preparation of different products during the same reaction (12) and the direct purchase of bi or tri-functionalised resins for a variety of applications is now possible.

Merrifield resin therefore is versatile and can allow functionalisation via attachment chemistries. These properties were exploited in this chapter's work to facilitate surface molecular imprinting of a complex template (lipopolysaccharide).

2.1.3 Surface Molecular imprinting

Surface imprinting is a technique used to optimise molecular imprinting, often of complex molecular targets. It describes the avoidance of steps that create imprinting sites within a matrix and concentrates imprinting efforts

to a functionalised surface. This approach results in re-binding sites with increased exposure to template compared to bulk imprinting. Therefore, the mass transfer of template in and out of binding sites is improved (13,14).

Whether it is though synthesising polymer films or attaching templates to a support surface, surface imprinting strategies are used regularly by many imprinting groups. Molecularly imprinted polymers have been produced for a diverse range of targets using a wide range of solid supports. For example, silica (15–17), quartz crystals (18), quantum dots (19), carbon nanotubes (20,21), and, as in this study, polystyrene resins (6) have all been used to successfully produce MIPs.

Imprinted polymers produced with surface imprinting techniques have also been developed for biomedical application. Recently, Hussain *et al*. synthesised a MIP for platelet aggregation detection, a desirable diagnostic in the detection of HIT (heparin induced thrombocytopenia), a cause of significant bleeding dyscrasias in patients who are administered heparin (18). This was a small study, however, by imprinting platelets on the surface of quartz crystals Hussain *et al*. showed detection of characteristic platelet aggregation in patient serum samples. Additionally, Cumbo *et al*. described, in their 2013 paper, a surface imprinted MIP for virus detection. Named VIPs (Virus Imprinted Particles), Cumbo *et al*. imprinted the surface of silica nanoparticles and demonstrated virus detection in the picomolar range (15).

2.1.4 Polymerisation methods

The control of polymer synthesis is an integral step in any molecular imprinting process. Furthermore, different imprinting strategies may require polymers with differing properties and selection of the polymerisation method is therefore important (22). Typically, chain

polymerisation describes polymerisation of unsaturated monomers via free-radical reactive centres generated on selected monomers (23). It consists of three phases: initiation, propagation and termination and describes the basic strategy for polymerisation in most conventional imprinting methods. An azobisisobutyronitrile (AIBN) free radical initiator is also commonly used in molecular imprinting to initiate and propagate polymerisation and provides an economic and reliable route to polymerisation (24). Moreover, the process is tolerant of many different solvents, can be used for a wide variety of monomers and often only needs mild polymerisation conditions (heat or UV application) (25). However, the process is not controlled and often produces polymers with high molecular weights and high dispersity indices, indicating poor control over polymer growth and resultant polymer architecture (22,25,26).

Reversible-deactivation Radical Polymerisation (RDRP) is a growing polymer chemistry field which is also regularly referred to as controlled/ living polymerisation (27,28). RDRP describes polymerisation un-hindered by a dead-ended polymer chain formation, allowing the development of polymers with ever increasing architectural complexity in a highly controlled reaction (29). The main advantage of these techniques that constitute RDRP for molecular imprinting is the production of a homogenous polymer with a greater correlation between the affinities of binding sites (30). A methodology for synthesis of 'living' polymers was first described by Szwarc in 1956 when he described anionic polymerisation with a slower propagation step allowing for greater control of polymer growth (31). Decades later, RDRP is an established polymerisation technique and describes several mechanistic routes, all of which display greater control over polymer growth than conventional chain polymerisation methods. Two examples of controlled/living polymerisation are Reversible Addition Fragmentation (chain) Transfer (RAFT) polymerisation and Atom Transfer Radical Polymerisation (ATRP) (23). Both

methods involve free radicals, RAFT relies on an agent that is both a chain transfer agent and an initiator (known as a RAFT agent) and ATRP uses a transition metal catalyst (copper complexes for example) (23). These methods, although controlled, both often require undesirable experimental conditions for working with both polymyxin (peptide) and lipopolysaccharide (template molecule). For example, commonly used RAFT agents (trithiocarbonates and dithioesters) require a solution temperature of over 90 degrees to initiate polymerisation (32). Furthermore, despite descriptions of RAFT polymerisation under aqueous conditions (33), typically, organic solvents are required for the process.

This chapter therefore investigates an alternative RDRP approach and describes the synthesis and use of a hydrophilic iniferter in the polymerisation stage of molecular imprinting methods. The term 'iniferter' describes a species that has polymerisation initiator, transfer agent and terminator capability and was first described in the 1980s (34). Iniferter controlled polymerisation involves the insertion of monomers into the iniferter bond itself and produces polymer chains with iniferter fragments at each end, effectively end-capping the polymer chain with a free radical capable of further polymerisation (35). A commonly used iniferter species are dithiocarbamates which, under certain conditions, split into non reactive and reactive radicals; therefore acting as terminators and initiators, respectively (36). Crucially, dithiocarbamate will readily react with chloromethyl groups on the surface of Merrifield resin, giving a reactive radical on the surface. Therefore, greater control of polymer growth on the resin surface could be achieved using this RDRP method. An outline of RDRP methods is shown in figure 2.2.

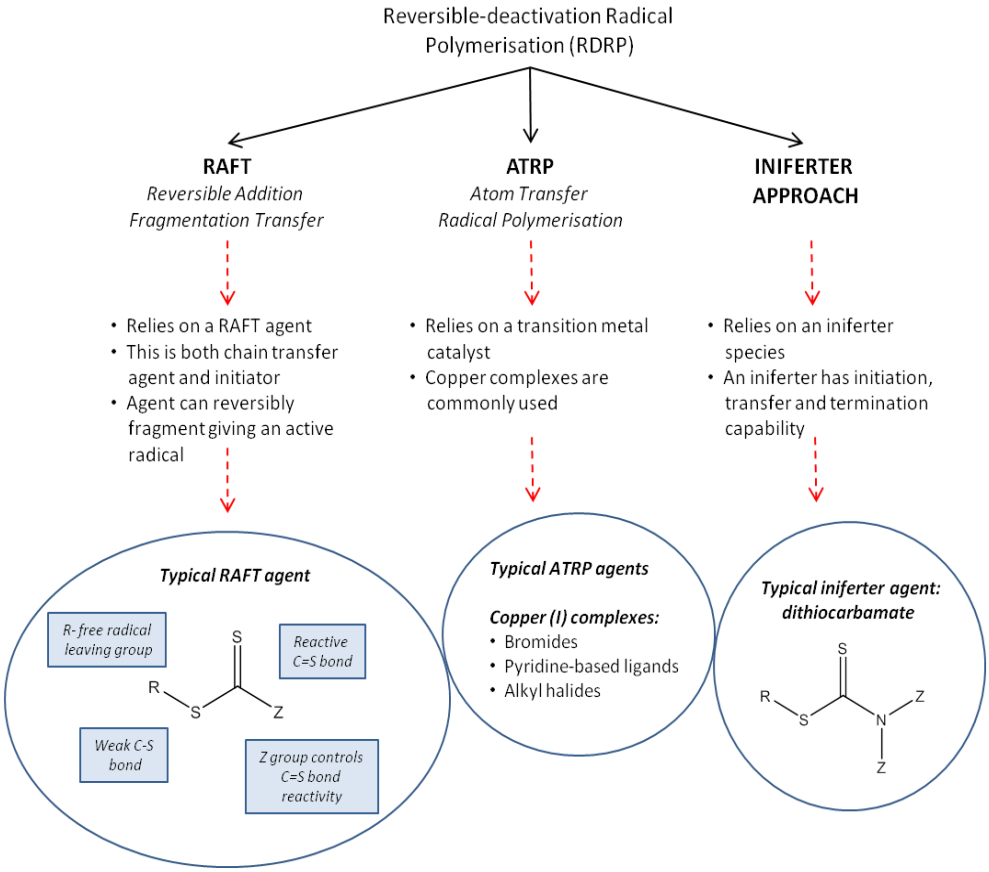

Figure 2.2: Summary of Reversible-deactivation Radical Polymerisation (RDRP) methods.

Many molecular imprinters have used iniferter agents for their RDRP processes (6,36–39), producing a diverse range of MIPs. As a comparison to the complex nature of the template used in this study (lipopolysaccharide), protein MIP synthesis studies have demonstrated success by using iniferter living radical polymerisation. For example, in 2009, Qin *et al*. described the use of iniferter living radical polymerisation for protein MIP synthesis using a dithiocarbamate iniferter species (40). Moreover, imprinters have used iniferter facilitated polymerisation to prepare MIP microspheres (36,41), to prepare molecularly imprinted membranes (37) and to produce cross-linked biomedical polymer film for potential biosensing application (42).

2.2 Chapter aims and objectives

The main aim of this chapter was to generate a solid support capable of accommodating two distinct attachment chemistries to facilitate the molecular imprinting of LPS.

Key objectives were as follows:

1. Controlled modification of chloromethylated polystyrene resin with azide groups to generate solid supports displaying two attachment chemistries.
2. Modification of polymyxin B (PMB) with an alkyne group to enable click chemistry.
3. Demonstrate binding capability of PMB modified resins to LPS.
4. Synthesis and attachment of a hydrophilic iniferter onto the surface of azide functionalised resin and subsequent molecular imprinting of LPS.

2.3 Materials and methods

2.3.1 Materials

Polymyxin B from Enzo (Exeter, UK). All chemicals (including FITC- labelled *Escherichia coli* 0111:B4 LPS) purchased from Sigma-Aldrich (Poole, UK). All organic solvents were of HPLC grade and were obtained from Fisher Scientific (Loughborough, UK).

2.3.2 Analysis

2.3.2.1 FTIR

All FTIR analysis was carried out on a Varian 3100 Excalibur FTIR from Agilent Technologies UK Ltd (Cheshire, UK) and using the Varian Resolutions Pro software.

2.3.2.2 Fluorescence

Fluorescence analysis was undertaken using a FLUOstar OPTIMA platereader (BMG Labtech GmbH, Ortenburg, Germany). The fluorescence properties of the FITC labelled *Escherichia coli* 0111: B4 LPS used in all binding experiments was as follows: excitation wavelength of 485 nm and emission wavelength 520 nm (λ_{ex} 485 nm/ λ_{em} 520 nm). Analysis of binding performance data obtained from fluorescence analysis was carried out with GraphPad Prism® V8 software (B_{max} and apparent K_d values calculated from a single-site specific binding curve fitting algorithm).

2.3.2.3 Elemental

Elemental analysis (carbon, hydrogen, nitrogen and sulphur) was by Medac Ltd. (Surrey, UK).

2.3.3 General method overview

Figure 2.3 summarises the overall resin modification process. Firstly, chloromethylated polystyrene resin was modified with azide groups in a controlled fashion as to allow the preservation of a pre-defined proportion of chloromethyl groups on the resin surface. Secondly, the coexistence of surface azide and chloromethyl groups allowed further modification with iniferter attachment.

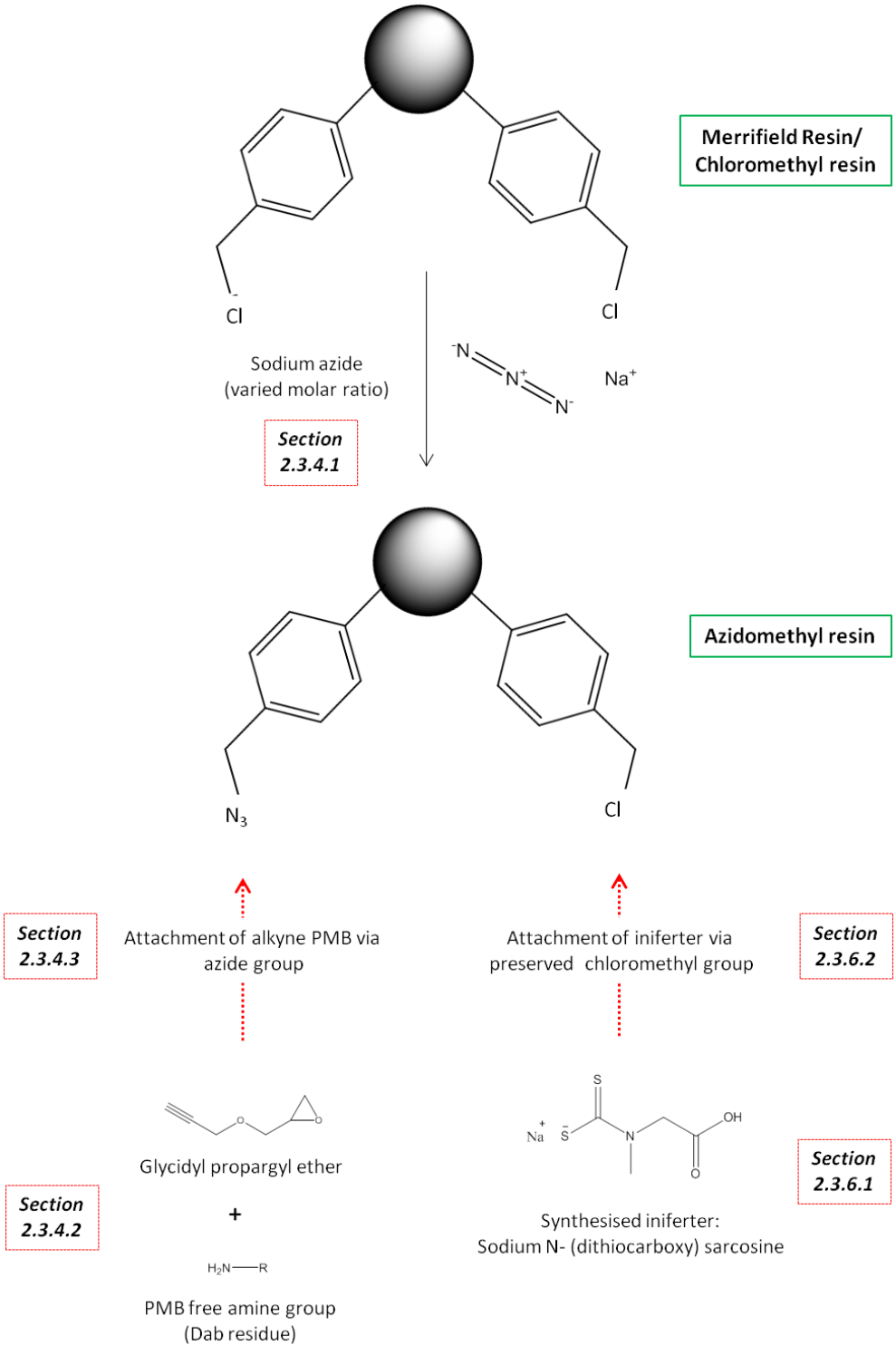

Figure 2.3: Simplified diagram of general method overview.

2.3.4 Preparation of modified Merrifield Resin

2.3.4.1 Azidomethyl resin

A series of azidomethyl resins were synthesised with increasing degrees of chloromethyl to azidomethyl conversion via manipulation of the chloride: azide molar ratio. Following a method described by Arseniyadis *et al*. (8), 250 mg (0.5 mmol chloride) of Merrifield resin was added to 10 ml dry dimethylformamide (DMF) and a pre-defined quantity of sodium azide (dependent on desired conversion percentage) was added. The reaction was gently stirred at 60°C overnight. Resins were then washed with the following through a nylon filter: DMF/water (50/50; 100 ml), DMF, water, ethanol and ether (100 ml each, two cycles). Resins were then dried overnight under vacuum at 40°C and thereafter all synthesised resins were analysed using FTIR. Table 2.1 summarises quantities for azidomethyl resin experiments.

Table 2.1: Reactants for azidomethyl resin synthesis

Azide molar equivalence Mol	Predicted resultant % azide modification	Merrifield resin mg (mmol chloride)	Sodium azide mg (mmol)
0	0	250 (0.5)	0
0.2	20	250 (0.5)	6.5 (0.1)
0.4	40	250 (0.5)	13.0 (0.2)
0.5	50	250 (0.5)	16.25 (0.25)
0.6	60	250 (0.5)	19.8 (0.3)
0.7	70	250 (0.5)	22.75 (0.35)
0.8	80	250 (0.5)	26.0 (0.4)
1	100	250 (0.5)	32.5 (0.5)

2.3.4.2 Preparation of alkyne PMB

Synthesis of an alkyne PMB was necessary to facilitate the coupling of PMB to the surface of azidomethyl polystyrene. PMB 100 mg (72 µmol) was added to 7.76 µl (72 µmol) of glycidyl propargyl ether in 10 ml methanol. This was gently stirred overnight at 40°C. The resultant liquid was rota-evaporated to a dry white powder and re-suspended in DI water (15ml per 100mg).

2.3.4.3 Attachment of alkyne PMB to azidomethyl resin

A metal catalysed alkyne-azide 'click' reaction as described by Sharpless in 1990 (43) was followed for the coupling of alkyne PMB and azidomethyl resin. Alkyne PMB 50 mg (36 µmol) was added to 10 mg of 1 molar equivalent azidomethyl resin in 15 ml DI water. Added to this were sodium ascorbate 88.5 mg (0.45 mmol) and copper (II) sulphate 4.78 mg (0.03 mmol). Following 10 minutes vortex, the reaction was gently stirred overnight at room temperature. The resultant yellow solution was filtered and washed with 100 ml DI water (x3), 100 ml 50/50 DI water/methanol and 50 ml methanol prior to being dried under vacuum at 40°C overnight.

2.3.5 Binding experiments with PMB modified resin

The synthesised series of modified alkyne PMB coupled azidomethyl resins were tested to ascertain LPS binding ability in a binding experiment. All modified resins plus control resins (unmodified chloromethyl resin) were incubated with increasing concentrations of LPS in water for injection (WFI) overnight (5 mg resin per repeat), 3 repeats of each. The LPS concentrations were as follows: 0.1 µg ml^{-1}, 0.5 µg ml^{-1}, 1 µg ml^{-1}, 5 µg ml^{-1} and 10 µg ml^{-1}. Following incubation all samples were filtered through Whatman 1 paper, analysis with fluorescence spectroscopy was then performed on the resultant filtrate.

2.3.6 Polymerisation Experiments

2.3.6.1 Iniferter (Sodium N- (dithiocarboxy) sarcosine) preparation

A method for the synthesis of a hydrophilic iniferter species outlined by previous PhD work in this lab was followed (44,45). Sodium hydroxide 2.25 g (56.2 mmol) was added to 20 ml water which was then cooled to 10°C. Sarcosine 5 g (56.1 mmol) was added to this cooled solution. Carbon disulphide 5.6 ml (93 mmol) was then dissolved in ethanol 15 ml. Whist maintaining the temperature at 10°C, this carbon disulphide/ethanol solution was slowly added to the sarcosine solution. The product was then stirred gently at 10°C for 30 minutes followed by gentle stirring at room temperature for a further 30 minutes. Extraction using chloroform (50 mls x 3) was followed by rota-evaporation until caramel-like oil was formed. This was further rota-evaporated using multiple aliquots of ethanol (10 ml) until it formed a honeycomb-like structural appearance. The product was stored in a desiccator box at -4°C and protected from light.

2.3.6.2 Iniferter attachment to modified Merrifield resin

The iniferter coupling required a 10-20 fold molar excess of the iniferter to resin free chloromethyl groups. For 500 mg of 0.5 mol equivalent resin (0.75 mmol chloride), 3.1 g (15 mmol) of iniferter was used (20 fold excess). The coupling reaction was carried out under three conditions: water 15 ml; water/MeOH (70/30 v/v %) 15 ml; and MeOH/DMF (70/30 v/v %) 15 ml. All reactions were gently stirred overnight at 40°C and protected from light at all times. Samples were washed and filtered with DI water and ethanol and left to dry overnight under vacuum at 40°C. Thereafter, all samples were analysed with FTIR and elemental analysis.

2.3.6.3 Alkyne PMB attachment to iniferter coupled resin

Using the method described in section 2.3.4.3, PMB was attached to iniferter coupled resin. All samples were washed, filtered and dried as described in section 2.3.4.3. The resultant resins therefore had both iniferter and PMB attached to the surface and were therefore used for ongoing polymerisation experiments.

2.3.6.4 Polymerisation of iniferter coupled resin

a. Polymerisation time point experiment

The 0.5 mol equivalent azide converted resin, coupled with iniferter and alkyne PMB, was used in a polymerisation time point experiment. Resin (50 mg) was suspended in 4 ml of DI water in a polymerisation vial. The monomers were then added: AAm 70 mg (1 mmol) plus MBAam 7.5 mg (0.05 mmol). Seven samples were prepared, to correspond with 7 polymerisation time points (0, 20, 40, 60, 80, 100 and 120 minutes), three repeats of each. Samples were sparged with nitrogen for 7 minutes and then stirred gently under UV light of 100 mw/cm^2/325 nm at a distance of 20 cm for the range of irritation times outlined above. Following irradiation all samples were washed and filtered with DI water 100 ml, 100 ml DI water/ methanol (50/50 v/v%), 100 ml and methanol 100 ml. Samples were dried overnight under vacuum at 40 °C. A sample from each time point was analysed by FTIR.

b. Binding Assay

Resins (5 mg) prepared in section 2.3.6.4 (a) were incubated with 1 µg ml^{-1} LPS in WFI overnight (prepared in triplicate). Following incubation all samples were filtered through Whatman 1 paper, the resultant filtrate was analysed with fluoroscopy.

2.3.7 Imprinting Methods

2.3.7.1 Preparation of imprinted and non-imprinted polymer

The resin used for these experiments was the 0.5 mol equivalent azidomethyl resin (50% of chloromethyl groups converted to azide groups), alkyne PMB attached to these azide groups and iniferter species attached to the remaining chloromethyl groups.

The molecularly imprinted polymer (MIP) was prepared as follows: resin (100mg) was suspended in 20ml of DI water, LPS (400 µg /0.04 µmol) was added and the reaction was stirred gently at room temperature for four hours, monomers were then added (AAm 350 mg (5 mmol) and MBAam 37.5 mg (0.25 mmol)) and the reaction was sparged with nitrogen for 7 minutes.

The non-imprinted polymer (NIP) was prepared as follows: resin (100mg) was suspended in 20ml of DI water and this was stirred gently at room temperature for four hours, monomers were then added (AAm 350 mg (5 mmol) and MBAam 37.5 mg (0.25 mmol)) and the reaction was sparged with nitrogen for 7 minutes.

Both MIP and NIP preparations were stirred gently under UV light of 100mw/cm^2/325 nm at a distance of 20 cm for 60 minutes. Following polymerisation, samples were filtered and washed with DI water (100 ml; x3). The samples were then washed with the following (x3): 1% sodium deoxycholate (100 ml), followed by a second wash and filter with DI water (100 ml) and a final wash with 100 ml water/methanol (50/50 v/v %) followed by methanol (100 ml) prior to drying overnight under vacuum at 40°C.

2.3.7.2 Binding assay

The following resins were prepared for overnight incubation with LPS (5 mg each, 1 μg LPS, 4 repeats of each):

- **MIP**: 0.5 mol equivalent azidomethyl resin, iniferter attached, alkyne PMB attached, prior incubation with LPS, polymerisation and washing with sodium deoxycholate;
- **NIP**: 0.5 mol equivalent azidomethyl resin, iniferter species attached, alkyne PMB attached, **no** prior incubation with LPS, polymerisation and washing with sodium deoxycholate;
- **Resin A (RA)**: 0.5 mol equivalent azidomethyl resin, iniferter species attached, alkyne PMB attached;
- **Resin B (RB)**: 0.5 mol equivalent azidomethyl resin, iniferter species attached;
- **Resin C (RC)**: 50% azide modified Merrifield resin, iniferter species attached, and polymerisation.

Polymerisation conditions were standardised for all samples that required it (MIP, NIP and Resin C- stirred gently under UV light of 100mw/cm^2/ 325 nm at a distance of 20 cm for 60 minutes). Following overnight incubation all samples were filtered through Whatman 1 paper, fluorescence spectroscopy was then performed on the resultant filtrate.

2.4 Results and discussion

2.4.1 Preparation of modified Merrifield Resin

2.4.1.1 Azidomethyl resin

Successful generation of azidomethyl resin was demonstrated with FTIR analysis. Shown in figure 2.4 are the transmittance spectra obtained via FTIR analysis of plain (unmodified, black trace) Merrifield resin and 1 mol equivalent azidomethyl resin (red trace). The spectrum obtained by FTIR for 1 mol equivalent azidomethyl resin gave a distinct stretch at ~2100 cm^{-1} which corresponded to presence of an azide group. Spectra of a control resin (unmodified Merrifield resin) lacked this band at 2100 cm^{-1}.

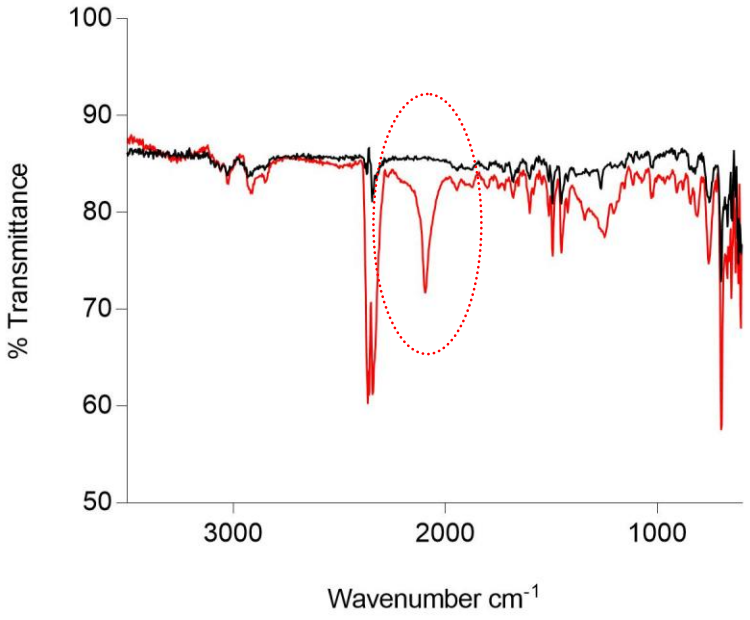

Figure 2.4: FTIR spectra for 1 mol equivalent azidomethyl resin (red) compared to plain (unmodified) Merrifield resin (black). A stretch is seen at V_{max}/ cm^{-1} 2100 (N=N=N; dashed red circle) in the modified azidomethyl resin and is not present in the plain resin.

With evidence of successful substitution of chloride groups with azide functionality, a library of resins with differing azide conversion rates were synthesised. The resultant FTIR spectra for these resins are shown in figure 2.5, where a gradual step-wise increase in the peak area of the stretch at 2100 cm^{-1} is demonstrated.

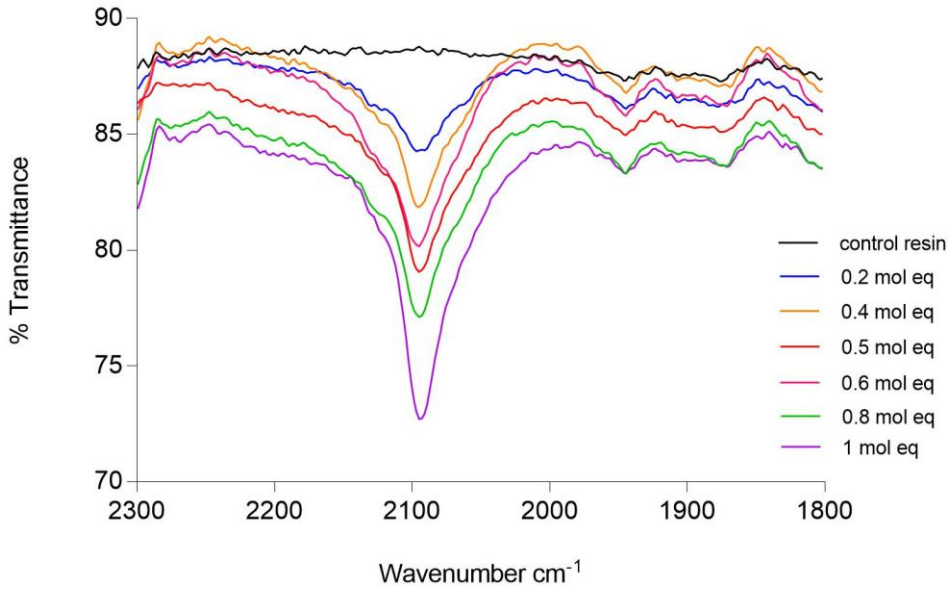

Figure 2.5: FTIR spectra for azidomethyl resins produced through the reaction of Merrifield resin with varying concentrations of sodium azide. The area of interest V_{max}/ cm^{-1} at 2100 is illustrated and representative of azide moiety (N=N=N). Spectra are shown for the following resins: 0.2 mol equivalent (indicates 20% of the molar concentration of chloride groups was added in azide), 0.4; 0.5; 0.6; 0.8 and 1 mol equivalent.

The synthesised resins, the FTIR analysis of which are shown in figures 2.4 and 2.5, were the product of a nucleophilic substitution reaction (figure 2.6). Sodium azide is a water soluble salt of the azide ion, a nucleophilic linear species with high affinity for electrophilic sites (46).

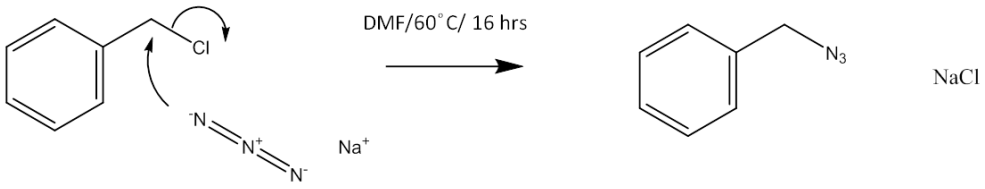

Figure 2.6: Schematic of the nucleophilic substitution reaction of sodium azide and an alkyl halide. Shown is a chloromethyl group (plus aromatic hydrocarbon) representative of the functional group of Merrifield resin. The nucleophilic sodium azide ion attacks the electrophilic species.

In their exhaustive 2005 review, Bräse *et al*. describe the varied reactions of organic azides. Dedicating a section to classic nucleophilic substitution reactions, they indicated sodium azide is the most commonly used azide source (47). Using sodium azide, other groups have synthesised azidomethyl polystyrene for diverse applications. For example, in a recent paper by Slini *et al.*, the synthesis of azidomethyl polystyrene for the preparation of engineered polymers for use in de-pollution applications (attached chelating agents) is described (48). This group achieved a 99% substitution rate (azide groups for chloromethyl groups) using a 1:7.32 molar ratio of chloride to azide. Similarly, Ouerghui *et al*. describe the synthesis of azidomethyl polystyrene in their 2014 paper, again achieving high conversion rates by using a 1:5 molar ratio of chloride to azide (49). However, the graduated, controlled conversion of a selected proportion of chloromethyl groups to azide groups rather than the blanket conversion of

all chloromethyl groups is not heavily represented in the literature. Although, work from this laboratory has shown the controlled azidomethyl resin synthesis as part of Merrifield resin bifunctionalisation technique (9).

Conversely, FTIR analysis can be used to show a reduction in azide groups as a reaction proceeds. In recent work by Albuszis *et al*., effective photo-crosslinking of microspheres via the exploitation of azide functionality was demonstrated with FTIR spectra showing a decrease in the azide stretch as azide groups were consumed during the reaction (50).

2.4.1.2 Preparation of alkyne PMB and coupling to azidomethyl resin

Click Chemistry is an umbrella term to describe a group of neat chemical reactions that generate products efficiently by joining together small units. This study utilises a copper catalysed azide-alkyne cycloaddition reaction, which Sharpless once described as the 'cream of the crop' of Click Chemistry reactions (43). Strictly speaking, this study uses a variant of this reaction as first described by Sharpless; a copper catalyst is employed, and therefore it is not a true Huisgen Cycloaddition. The method using a copper catalyst was first described in 2002 and allows the reaction to continue without the use of extremely high temperatures (51).

Figure 2.7 shows the reaction schematic for the preparation of alkyne PMB. This step was necessary prior to the alkyne 'click' reaction with azide.

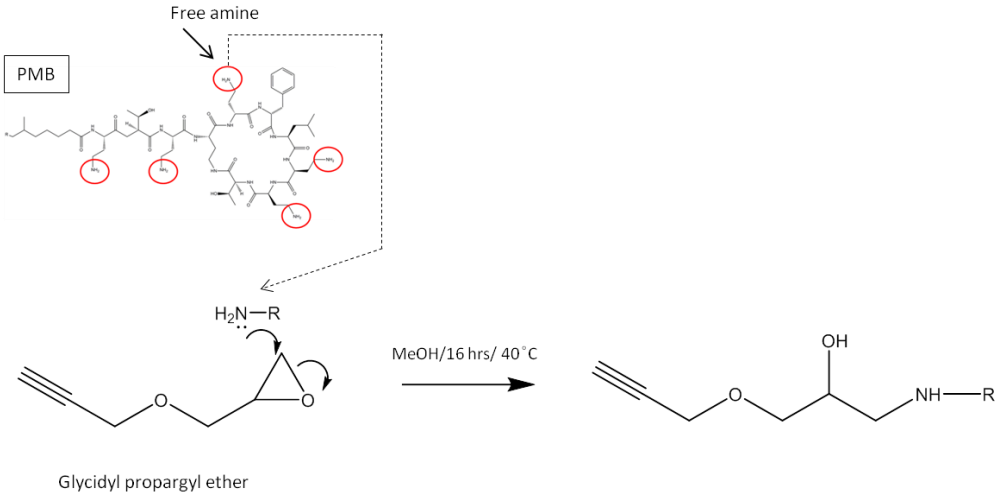

Figure 2.7: Reaction schematic of preparation of alkyne PMB. The epoxide ring of glycidyl propargyl ether comes under nucleophilic attack by a free amine group of PMB (Dab-5 position) leading to opening of the ring and adoption of a more stable bond angle configuration.

Figure 2.8 shows the 'click' reaction between alkyne groups (PMB) and azide (converted Merrifield resin). The azidomethyl resin and modified alkyne PMB react under conditions of copper (II) sulphate catalysis. Therefore using this click method, PMB is successfully anchored to the azidomethyl polystyrene. As the ratios of azide groups are pre-determined, so is the loading of PMB onto the resin.

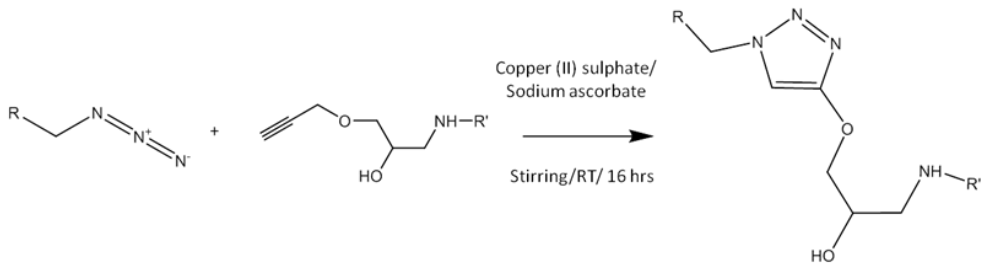

Figure 2.8: Schematic of attachment of alkyne PMB to azide modified resin. R: polystyrene group of Merrifield resin; R': PMB; RT: room temperature.

Figure 2.9 shows FTIR spectra comparing azidomethyl resin (0.5 molar equivalent) with (red) and without (black) PMB coupling. A decrease in the peak area of the azide stretch at ~2100 cm^{-1} is demonstrated in the spectra for PMB- coupled resin compared to the resin lacking PMB.

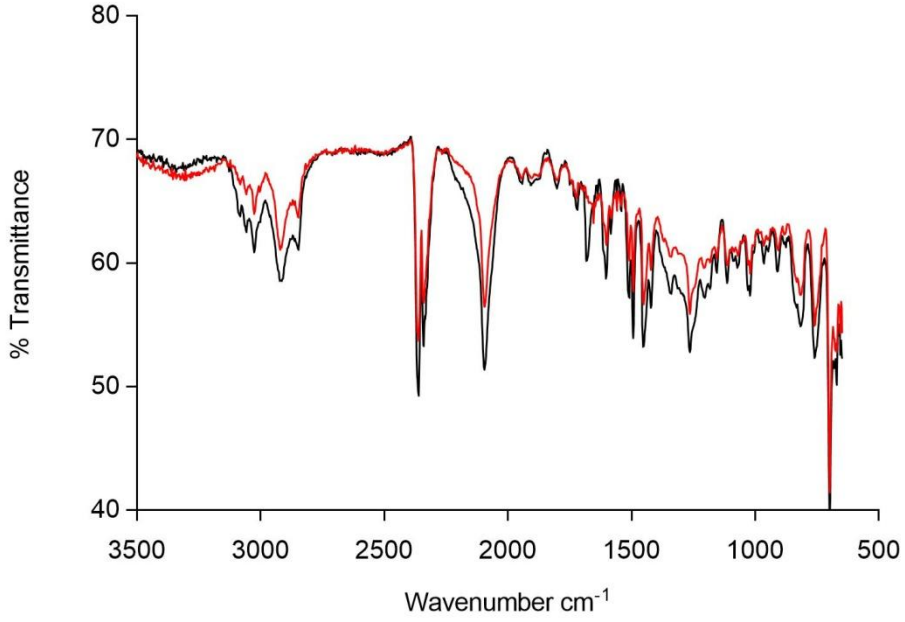

Figure 2.9: Comparison FTIR spectra for 0.5 mol equivalent azidomethyl resin (black) and alkyne PMB derivatised 0.5 mol equivalent azidomethyl resin (red). Reduction in peak area at V_{max}/ cm^{-1} 2100 (azide peak, N=N=N) of red spectra is demonstrated. A small amino stretch is present at ~3200-3400cm^{-1} in red spectra from peptide.

It may be expected that the azide peak would be absent from the PMB resin as the azide groups are used in the azide- alkyne click reaction. This is not the case, although a reduction in peak area of approximately 50% is observed. This is likely due to solvent dependent resin swelling behaviour and the difference between reaction conditions for azide coupling (organic) and those for alkyne PMB coupling (aqueous). To ensure a maximum amount of available azide groups, the coupling reaction to attach alkyne PMB resin took place in DMF; a solvent that encourages significant swelling

of Merrifield resin. However, the attachment of PMB takes place in water where the degree of resin swelling is markedly reduced. Therefore, although a molar excess of PMB is used in the attachment reaction, due to the restricted swelling of the resin, a proportion of azide moieties were likely unavailable for PMB coupling. FTIR results shown in figure 2.9 suggested the continued availability of azide groups despite introduction of alkyne PMB.

The paramount importance of resin swelling in solvents was noted by Merrifield himself (1), who along with others (52,53) reported experimental outcome differences in solid phase peptide synthesis (SPPS) using Merrifield resin dependent on choice of solvent. For example, in their 1998 paper, Santini *et al.* produced swelling data for a library of resins, including Merrifield resin, using a simple method of measuring the volume of swollen resin beads following one hour of solvent submergence. Santini *et al.* showed swelling of Merrifield resin in methanol of 1.8 ml g^{-1}. The authors conclude with proposal of three SPS solvent classifications: swelling greater than 4.0 ml g^{-1} classed as a good solvent; swelling of 2.0 to 4.0 ml g^{-1} a moderate solvent and a swelling volume of less than 2.0 ml g^{-1} is a poor solvent and should not be used for SPPS (54). The swelling of Merrifield resin in DMF has also been reported by several groups. Using the same methods as Santini's group, Vanini and colleagues reported swelling in DMF of three Merrifield resins of increasing chloride loading of 2, 5 and 10 %. Swelling volumes were 4.0 ml g^{-1}, 3.7 ml g^{-1} and 3.0 ml g^{-1} respectively (55). Therefore, by Santini's classifications DMF is a moderate solvent. With a more automated method of investigating swelling, Rodionov *et al.* in their swellographic study paper also report Merrifield resin/DMF swelling volumes that correlate with other authors (56). Therefore, even in methanol the swelling of Merrifield resin is far lower than other solvents. In aqueous environments, however, Merrifield resin

becomes compacted with less binding site availability and those that are reside mainly on the resin surface.

2.4.2 Binding experiments with PMB modified resin

2.4.2.1 Polymyxin loading and LPS binding to PMB resin

A set of azidomethyl resins with a range of azide conversion (0.2, 0.4, 0.6, 0.8 and 1 mol equivalent resins) were coupled with alkyne PMB. These resins were then tested to establish LPS binding performance. In all binding experiments the molar equivalence of the azidomethyl resin relates to a chloride loading of 0.5 mmol (250 mg Merrifield resin). By integrating the data from a FTIC LPS calibration curve (figure 2.10), the amount of LPS bound to the resin under investigation could be plotted against free LPS concentration. Moreover, this allowed the calculation of B_{max} and K_d values for each tested resin; B_{max} refers to the maximum binding capacity of the resin and is expressed in nmol (of LPS) per mg of resin and K_d reflects the concentration of LPS (in μM) at which 50 % of the receptor sites for LPS binding are occupied.

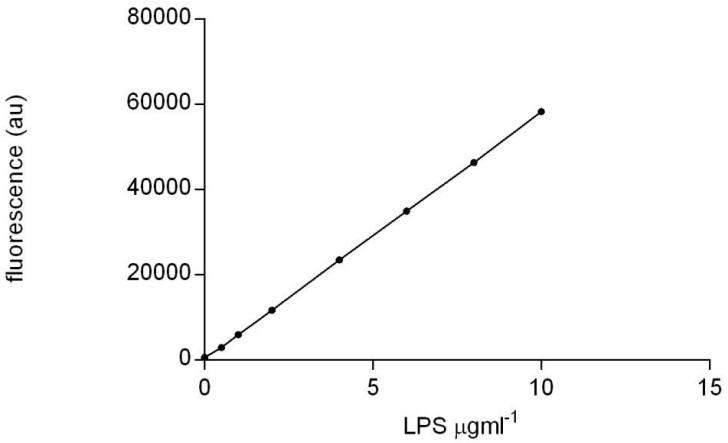

Figure 2.10: Typical FITC-LPS calibration curve. [y= 5787.8x + 274.5. R^2= 0.999].

Figure 2.11 shows results from the first two binding studies using the lower molar equivalent azidomethyl/PMB resins (0.2 and 0.4 mol equivalent).

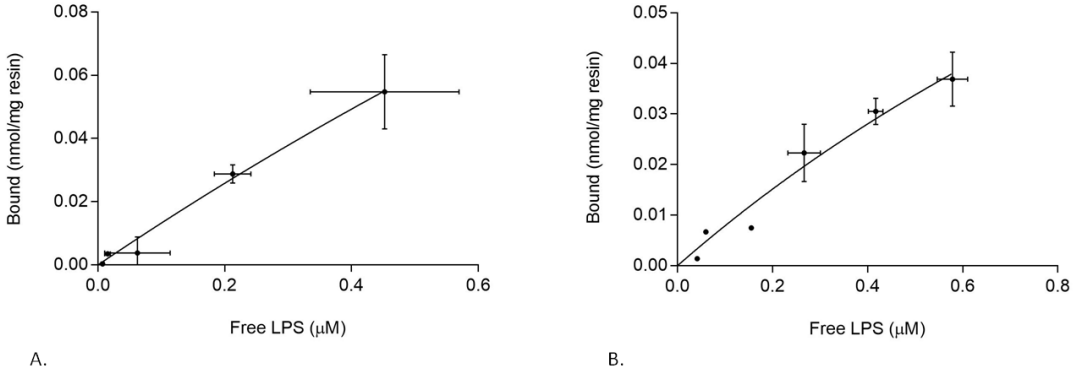

Figure 2.11: Binding curves of 0.2 mol equivalent (A) and 0.4 mol equivalent (B) azidomethyl resin/LPS binding experiment.

Note the lack of distinct curve shown in graph A, indicating a lack of specific binding taking place for this resin/LPS interaction. Error bars are also wide reflecting a wide range of values obtained between replicates, more pronounced for higher free LPS concentrations. The isotherm from analysis of 0.4 mol equivalent azidomethyl resin (graph B) also lacks the morphology of an efficient binding system, however error bars are smaller. Calculating B_{max} and K_d was possible for this isotherm only, however values were magnitudes greater than for other resins (B_{max}: 0.183 nmol mg^{-1}; K_d: 2.325 μM).

Figure 2.12 shows the binding curves for the remainder of the tested resins (PMB resins modified from 0.5, 0.7, 0.8 and 1 molar equivalent resins).

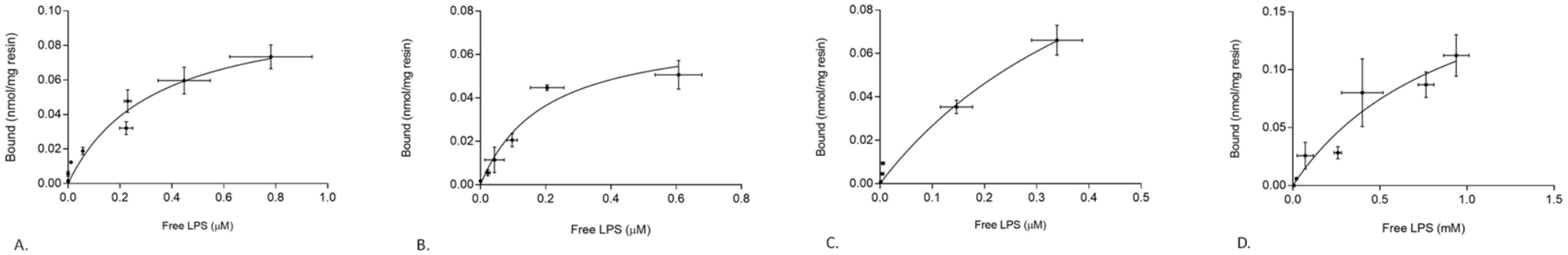

Figure 2.12: Binding isotherms from LPS/PMB modified resin binding experiments. **A:** Binding isotherm from analysis of 0.5 mol equivalent azidomethyl resin/LPS binding experiment (B_{max}: 0.103 nmol mg^{-1}; K_d: 0.328 μM); **B:** 0.7 mol equivalent azidomethyl resin/LPS binding (B_{max}: 0.0722 nmol mg^{-1}; K_d: 0.197 μM); **C:** 0.8 mol equivalent azidomethyl resin/LPS binding (B_{max}: 0.170 nmol mg^{-1}; K_d: 0.534 μM); D: 1 mol equivalent azidomethyl resin/LPS binding (B_{max}: 0.216 nmol mg^{-1}; K_d: 0.95 μM).

Figure 2.13 compares the binding isotherms from analysis of 0.5 mol equivalent azide converted resin/LPS binding experiment (black trace) and 1 mol equivalent azidomethyl resin (red trace).

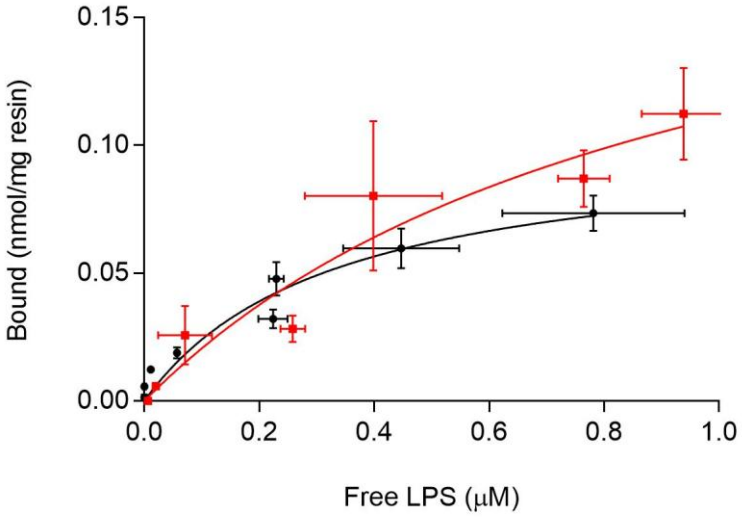

Figure 2.13: Binding isotherm from analysis of 0.5 mol equivalent azidomethyl resin/LPS binding experiment and 1 mol equivalent azide converted resin. Black: 0.5 mol equivalent azidomethyl resin B_{max}: 0.103 nmol/mg; K_d: 0.328 μM. Red: 1 mol equivalent azidomethyl resin B_{max}: 0.216 nmol/mg; K_d: 0.950 μM.

The binding performance data (k_d and B_{max} values) for all tested resins are shown in table 2.2.

Table 2.2: Table of results from binding isotherms of resin library binding to LPS.

Azidomethyl resin (% azide modification)	Apparent B_{max} (nmol/mg resin)	Apparent K_d (μM)
20	N/A	N/A
40	0.183	2.325
50	0.103	0.328
70	0.072	0.197
80	0.170	0.534
100	0.216	0.950

Results from figures 2.11, 2.12 and 2.13, together with binding data shown in table 2.2 show a diverse range of binding performance, suggesting binding to LPS was dependent on azidomethyl resin composition (and hence alkyne PMB loading). At lower rates of azidomethyl conversion (0.2 and 0.4 mol equivalent) data did not form a curved isotherm expected of a single-site specific binding system. The graphs were fitted using non-linear regression modelling (single-site binding). The binding in these systems appeared linear indicating probable nonspecific binding at sites with affinity and capacity for LPS but which are separate from the receptor sites of interest (57). Possible extra sites of interaction include free chloromethyl moieties or uncoupled azide sites.

With the exception of the 0.7 mol equivalent resin, B_{max} values shown in table 2.2 follow an upward trend as the azide conversion increases, with B_{max} for the 1 mol equivalent resin displaying a value around twice that for the 0.5 mol equivalent resin. B_{max} reflects the total density of receptor sites; therefore this doubling of B_{max} as the theoretical number of PMB

binding sites doubles is encouraging. However, K_d values, which represent the concentration of free LPS at which 50 % of the PMB receptor sites are occupied, follow an upward trend. This indicates a possible decrease in affinity as the resins have increased alkyne PMB coupling. The literature reports several methods of investigating the PMB/LPS interaction affinity at equilibrium, however, results broadly correlate. Recent work with a fluorescent probe modified PMB has generated K_d values of 0.3 µM (58) and 0.5 µM (59). These correlate well with earlier work using a slightly different PMB fluorescent modification giving K_d values in the range of 0.4 to 1.5 µM (60). Previous titration calometric studies have also yielded association constants (dependent on LPS type) of 1.8 to 2.3 µM (61). However, results from isothermic titration calorimetry methods reported by Soon and colleagues as part of their work with new fluorescent PMB probes, reported results fitted to a two-site binding system as they failed to sit favourably in a single-site model. In this study the K_d values obtained for the two binding sites were initially 0.5 µM and then 0.08 µM (59). K_d results obtained by this work described in this chapter generally correlate with previous studies which is encouraging. Therefore, that baseline affinity for LPS of PMB has apparently been unhindered by any coupling process when attached to azidomethyl resin, or by prior alkyne attachment processes. The ability to bind LPS with the same level of affinity has, in the most part, been preserved.

2.4.3 Polymerisation Experiments

Iniferter (Sodium N- (dithiocarboxy) sarcosine) synthesis

The synthesis of a hydrophilic iniferter species enabled the progression of polymerisation experiments under aqueous conditions. Aqueous conditions are desirable when working with biological templates and LPS is no exception. LPS tends to form micelles in most solvents secondary to its amphiphilic structure (62). Santos *et al.* investigated the aggregation of LPS

using light scattering spectroscopy and found the LPS serotype *Escherichia coli* 026:B6 begins to aggregate at a concentration of 14 μg ml^{-1} (in water, 37 degrees celsius) (63). However, Santos *et al*. described two stages of LPS behaviour below this concentration. Immediately prior to this aggregation concentration, LPS forms pre-aggregate oligomers and prior to this remains at a monomer arrangement. Therefore, LPS monomers are possible under aqueous conditions at concentrations lower than the CMC (critical micelle concentration).

Figure 2.14 shows the reaction for hydrophilic iniferter synthesis (sodium N-(dithiocarboxy) sarcosine).

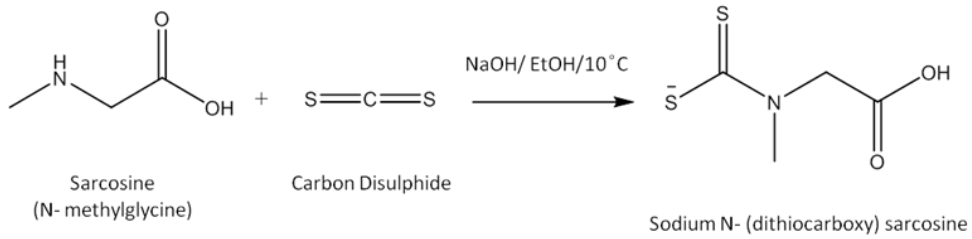

Figure 2.14 Reaction schematic of iniferter synthesis.

2.4.3.1 Iniferter/resin coupling

a. FTIR results

The swelling of Merrifield resin was also a consideration during the attachment of iniferter. Therefore, attachment of iniferter to both plain Merrifield resin and synthesised azidomethyl resin was carried out in aqueous and organic conditions. Resins were then analysed with FTIR.

The IR transmittance spectra obtained for a set of modified 0.5 mol equivalent resins (50 % azide conversion) are shown in figure 2.15. Comparison was made between azidomethyl resin with iniferter attached in water (black spectra, top); azidomethyl resin with iniferter attached in water/methanol (70/30 v/v %, green spectra, middle) and azidomethyl

resin with iniferter attached in methanol/DMF (70/30 v/v %, red spectra, bottom).

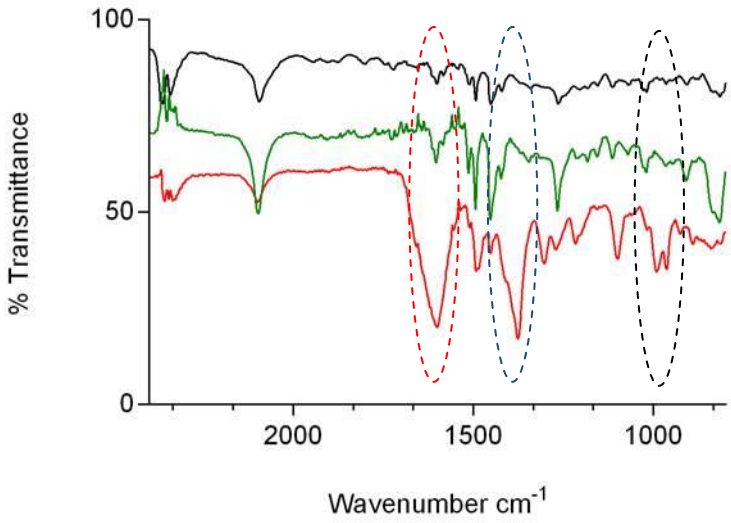

Figure 2.15: FTIR analysis of azidomethyl resin (0.5 mol equivalent resin) with iniferter attached under varied conditions. Black: iniferter attached in water; green: iniferter attached in water/MeOH; red: iniferter attached in MeOH/DMF. There are differences in the spectra obtained from the resin with iniferter attached in methanol/DMF: a greater peak area of stretch seen at V_{max}/cm^{-1} 1610 (C=C; red dashed circle), a significant extra stretch can also be seen at V_{max}/cm^{-1} 1380 (C-H; blue dashed circle), a thiocarbonyl stretch at V_{max}/cm^{-1} 1030 (C=S; red black circle) is also evident and supplemental small extra peaks are demonstrated at V_{max}/cm^{-1} 1220 and V_{max}/cm^{-1} 1106. Spectra off-set for clarity.

b. Elemental analysis

Table 2.3 shows elemental analysis results for iniferter modified resins.

Table 2.3: Elemental analysis results from a series of prepared resins. **A:** 0.5 mol equivalent resin, iniferter attached in water; **B:** 0.5 mol equivalent resin, iniferter attached in water/methanol (70/30 v/v %); **C:** 0.5 mol equivalent resin, iniferter attached in methanol/DMF (70/30 v/v %)

Sample	C % (mmol g^{-1})	H % (mmol g^{-1})	N % (mmol g^{-1})	S % (mmol g^{-1})
A	80.32 (66.93)	7.81 (78.1)	3.02 (2.16)	0 (0)
B	79.92 (66.60)	7.48 (74.8)	2.89 (2.06)	0 (0)
C	60.31 (50.26)	6.64 (66.4)	5.4 (3.86)	8.98 (2.81)

Elemental analysis data shown in table 2.3 partially correlates with FTIR findings. For example, resin C (iniferter attached in DMF/MeOH) shows the greatest sulphur content indicating a greater degree of iniferter coupling. This finding is supported by FTIR spectra (figure 2.15) that shows an increased stretch strength at a V_{max}/cm^{-1} 1030 (C=S) and V_{max}/cm^{-1} 1650 (C=O) compared to other resins.

What is interesting however is the lack of sulphur detection on resins A and resin B. These resins are iniferter coupled resins with iniferter attached in water and water/MeOH respectively. Therefore, it is possible the amounts of iniferter present were below the levels of detection for elemental analysis (detection limit <0.1%). However, it is likely that no iniferter was attached to these resins.

Overall, FTIR and elemental analysis results were mixed. Presence of thiocarbonyl groups on iniferter coupled resins regardless of coupling

reaction conditions was encouraging; however a stronger thiocarbonyl stretch signal was seen from the resin that was coupled with iniferter in a methanol/DMF mix.

2.4.3.2 Polymerisation with iniferter modified resin

a. Polymerisation time point experiment

Once iniferter is coupled to resin, it can be further modified with PMB and following incubation with monomers polymer growth can be evaluated. The monomers used in this study were acrylamide (AAm) and *N-N'*-Methylenebisacrylamide (MBAam), a choice based on extensive work in the imprinting of LPS carried out in this laboratory. Furthermore, several other research groups have demonstrated successful initiation and control of polyacrylamide polymerisation with thiocarbamate based iniferters (37,64,65).

Demonstrating the presence of polymer growth on the modified resins, figure 2.16 shows FTIR spectra from three modified resins that were subjected to polymerisation conditions for 30 minutes (black spectrum) and 90 minutes (red spectrum) compared to a modified resin that was not placed under polymerisation conditions (purple spectrum).

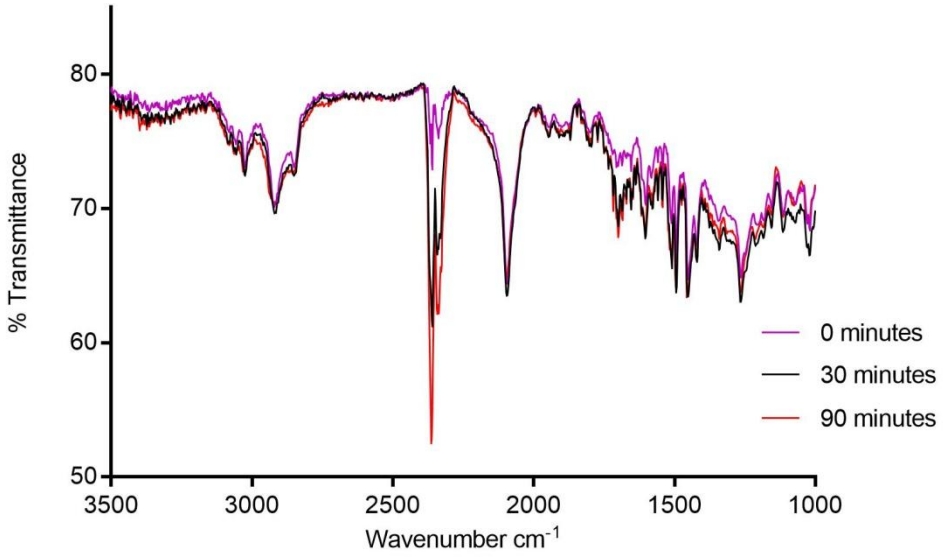

Figure 2.16: FTIR spectra of resins following iniferter attachment different polymerisation times (0, 30 and 90 minutes).

The FTIR spectra in figure 2.16 for resins with polymerisation time of 30 and 90 minutes demonstrated a stretch at ~1690 cm^{-1}. This stretch is absent from the spectra for the resin that was not subjected to polymerisation conditions. Furthermore, a small stretch is seen at 3200-3400 cm^{-1} in the 30 and 90 minutes polymerisation time resins compared to the resin with no polymerisation time. This stretch at ~1690 cm^{-1} is indicative of the carbonyl group of the monomer and the stretch at 3200-3400 cm^{-1} represents amide groups. However, demonstrated by a stretch at ~1030 cm^{-1}, indicative of a thiocarbonyl group, there is evidence of remaining iniferter species on all three resins.

The efficiency of the LPS binding interaction is dependent on the availability of PMB; therefore uncontrolled overgrowth of polymer during the imprinting process would hinder this interaction. Controlled polymer growth during the molecular imprinting process is an important consideration and underpins the choice of polymerisation method. Iniferter driven RDRP has been shown to produce homogenous polymers of

low polydispersity indices and furthermore has been shown to produce MIPs with improved performance compared to those produced with alternative polymerisation techniques (26,30). Shown in figure 2.17 is the theoretical result of polymer overgrowth on LPS binding experiments.

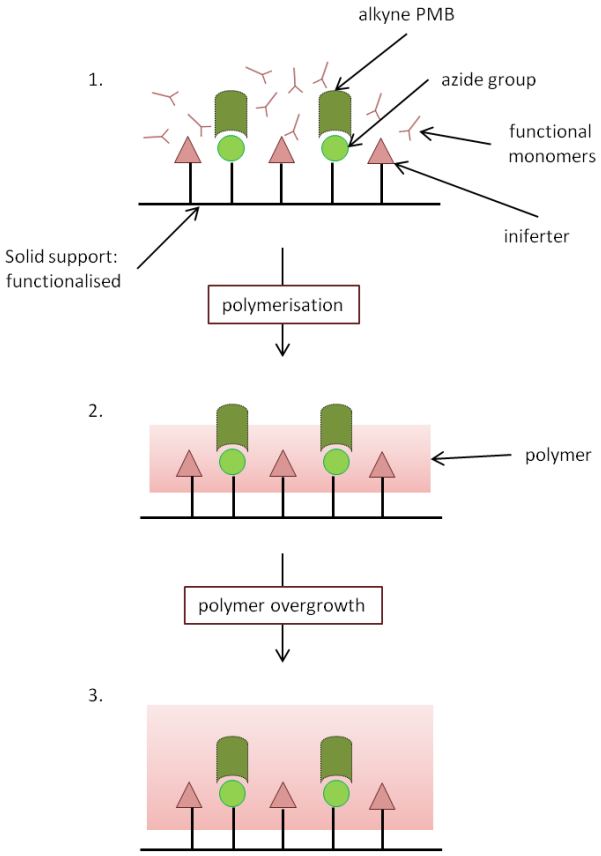

Figure 2.17: Schematic of theoretical result of polymer overgrowth during surface molecular imprinting. **1.)** A functionalised azidomethyl resin is shown with 50% chloromethyl groups converted to azide, and the remainder left to couple with iniferter. Alkyne PMB then attaches to azide functional groups and functional monomers added. **2.)** Polymerisation is initiated by iniferter species and the polymer grows on the surface of the functionalised resin. The polymer has stopped growing to allow sufficient exposure of PMB groups making them available for LPS interaction. **3.)** Polymer overgrowth has occurred. Notice how PMB is now no longer easily accessible for LPS binding.

However, *under* growth of polymer could have also caused issues with LPS binding. Inadequate polymer growth would lead to an ineffective imprinting process as the template/monomer interaction would be hindered and therefore formation of LPS binding sites would become an issue.

b. LPS binding

An LPS binding experiment was carried out to evaluate dependence of resin binding to LPS on the length of time the sample resin was subjected to polymerisation conditions. The resins used in this experiment were 0.5 mol equivalent azidomethyl resins, alkyne PMB coupled, iniferter attached in water and monomers added. Resins were subjected to polymerisation times from zero to 120 minutes.

Figure 2.18 shows the respective binding capability (expressed as percent bound) of prepared resins with differing polymerisation times. If overgrowth did occur it would be expected that binding to LPS would plateau or even decrease as the polymerisation time increased.

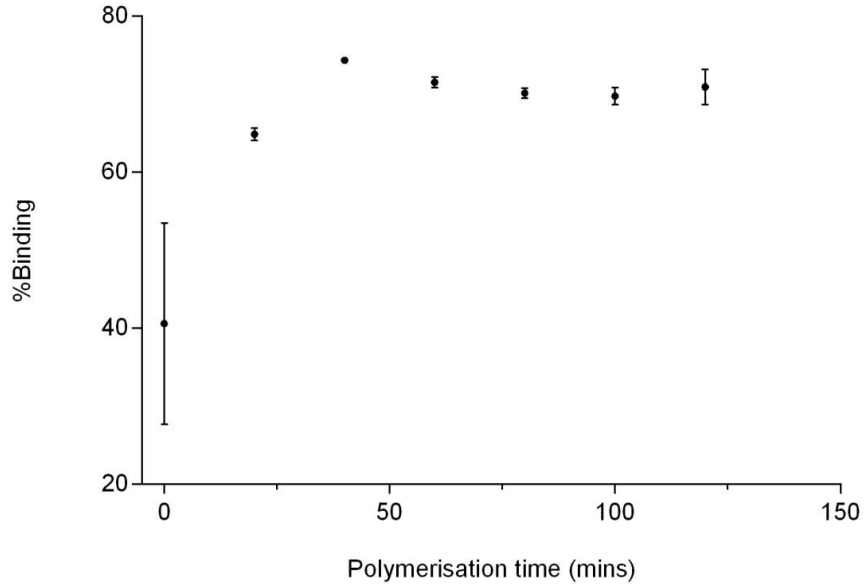

Figure 2.18: Graph showing LPS binding to seven resins which had polymerised for different lengths of time.

Optimal binding capability is demonstrated by the resin that was exposed to polymerisation conditions for 50 minutes. There is then a slight decline in binding capability across the resins that polymerised for 60, 80 and 100 minutes. A marginal increase is then seen (however, wide error bars noted) in binding ability of the resin polymerised for 120 minutes. This may be due to polymer overgrowth preventing the successful binding of available PMB binding sites and LPS. Also clear is the sub-optimal binding demonstrated by the resins with the shortest polymerisation times (0 and 20 minutes), suggesting the presence of polymer itself is advantageous to LPS binding capability.

2.4.4 Imprinting Methods

2.4.4.1 Preparation of imprinted and non-imprinted polymer: binding assay

A typical calibration curve used for the calculation of LPS concentration in resultant binding study filtrate is shown in figure 2.19.

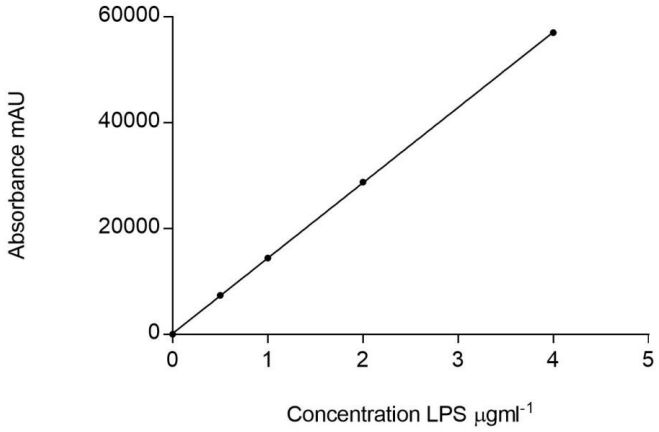

Figure 2.19: Calibration curve for imprinting binding studies. Line fit by linear regression ($y = 14238x + 152.9$; $R^2 = 1$).

Shown in figure 2.20 are the binding study data for a set of modified resins following overnight incubation with known concentrations of FTIC labelled LPS. The tested resins shown in figure 2.20 include imprinted and non imprinted resins, a resin with PMB coupled and no iniferter, a resin with iniferter and no PMB and an iniferter and polymer modified resin.

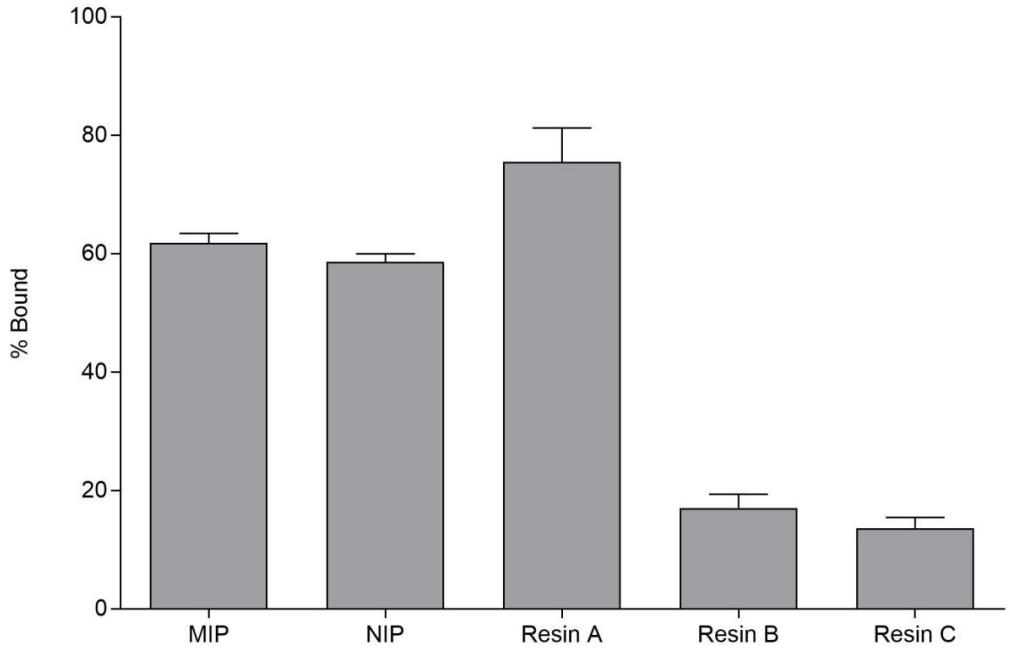

Figure 2.20: Comparison of overall binding ability to LPS of synthesised resins. **MIP:** 0.5 molar eq azidomethyl resin coupled with PMB and iniferter, LPS present during polymerisation process; **NIP**: 0.5 molar eq azidomethyl resin coupled with PMB and iniferter, no LPS present during polymerisation process; **Resin A:** 0.5 molar eq azidomethyl resin with PMB attached; **Resin B:** 0.5 molar eq azidomethyl resin coupled with iniferter; **Resin C:** 0.5 molar eq azidomethyl resin coupled with iniferter and subjected to polymerisation.

Shown in figure 2.20 is a significant difference in binding ability seen between systems that were alkyne PMB coupled and systems that lacked alkyne PMB. It is likely that the measured difference in binding capability of the resins is a result of the mere presence of PMB, regardless of imprinting processes the resin was subjected to.

A disappointing finding is that the best performance is seen in the resin subjected to no imprinting or polymerisation conditions (Resin A). This resin demonstrates similar binding to the resin used on the polymerisation

time point experiment once the polymerisation time had reached 50 minutes (figure 2.18). Furthermore, the composition of the resin used in the time point experiment reflected that of the NIP, apart from the NIP washing stage (1% sodium deoxycholate (100 ml), x3) and at 60 minute polymerisation time (the same polymerisation time used for NIP synthesis) the binding performance of these two resins was similar. However, if the NIP had been subjected to a polymerisation time of 50 minutes it may have achieved binding levels comparable with Resin A. Ten minutes of extra polymer growth time seemed to affect resin LPS binding capability.

2.5 Chapter conclusions

2.5.1 General conclusions

Results from this chapter demonstrated that azidomethyl resin synthesis to a predefined azide: chloride ratio is achievable. A set of resins were produced that demonstrated a stepwise increase in the strength of an indicative azide moiety stretch on FTIR analysis. Peak areas of the azide FTIR stretches increased from 202 (arbitrary units) for the resin with a predicted 0.2 molar equivalent (20% of the molar concentration of the Merrifield resin chloride groups was added in azide) to a peak area of 1005 (arbitrary units) for the predicted 1 molar equivalent resin (indicates 100% of the molar concentration of the Merrifield resin chloride groups was added in azide). Furthermore, the ongoing functionalisation of azidomethyl resin was possible with the attachment of modified PMB to azide moieties. Reflecting successful attachment of PMB to bifunctionalised Merrifield resin, the binding ability of PMB/azidomethyl complexes has also been demonstrated and associated with reasonable binding performance data. For example, LPS binding isotherm analysis of the 0.5 molar equivalent azidomethyl resin (with alkyne PMB attachment) demonstrated an apparent B_{max} and K_d of 0.103 nmol/mg of resin and 0.328 µM, respectively. In comparison, binding data analysis for the 1 molar equivalent azidomethyl resin (with alkyne PMB attachment) showed an apparent B_{max} of 0.216 nmol/mg of resin and an apparent K_d of 0.950 µM. Therefore, improved apparent LPS binding data was produced using functionalised resin with greater PMB attachment.

Imprinting of biological macromolecules is notoriously difficult (66,67). Issues of mass transfer simply due to template size are sometimes an insurmountable problem. The development of surface imprinting has previously led to the successful MIP synthesis for large proteins (68) and other large biological macromolecules (69). However, the successful

imprinting of LPS via surface imprinting methods was not achieved in the experiments described in this chapter. Binding data analysis of produced LPS MIP and NIP were disappointing. Comparison of LPS binding of MIP and NIP did not suggest successful imprinting as binding performance was similar with the MIP binding; therefore, alternative strategies for molecular imprinting were investigated.

2.5.2 Rationale for next chapter

The use of a Merrifield resin solid support was questionable and the behaviour of Merrifield resin (and any modified resin) in solvents was a problem. Organic conditions rendered the resin in a desirable swollen state for coupling and polymerisation stages but aqueous conditions were desirable for any ongoing reactions with LPS. Furthermore, the role of PMB necessitated further investigation.

Chapter three therefore explores the modification of PMB structure that allowed synthesis of a polymerisable PMB (p-PMB) which further facilitated alternative imprinting methods that negated the use of separate solid support.

2.6 References

1. Merrifield RB. Solid Phase Peptide Synthesis. I. The Synthesis of a Tetrapeptide. J Am Chem Soc. 1963 Jul 1;85(14):2149–54.

2. Jonke S, Liu K-G, Schmidt RR. Solid-phase oligosaccharide synthesis of a small library of N-glycans. Chem Weinh Bergstr Ger. 2006 Jan 23;12(4):1274–90.

3. Wu X, Schmidt RR. Solid-phase synthesis of complex oligosaccharides using a novel capping reagent. J Org Chem. 2004 Mar 19;69(6):1853–7.

4. Trotta F, Biasizzo M, Caldera F. Molecularly Imprinted Membranes. Membranes. 2012 Jul 19;2(3):440–77.

5. Yoshikawa M, Fujisawa T, Izumi J, Kitao T, Sakamoto S. Molecularly imprinted polymeric membranes involving tetrapeptide EQKL derivatives as chiral-recognition sites toward amino acids. Anal Chim Acta. 1998 Jun 5;365(1–3):59–67.

6. Rückert B, Hall AJ, Sellergren B. Molecularly imprinted composite materials via iniferter-modified supports. J Mater Chem. 2002 Jan 1;12(8):2275–80.

7. Mitchell AR, Kent SBH, Erickson BW, Merrifield RB. Preparation of aminomethyl-polystyrene resin by direct amidomethylation. Tetrahedron Lett. 1976 Oct 1;17(42):3795–8.

8. Arseniyadis S, Wagner A, Mioskowski C. A straightforward preparation of amino–polystyrene resin from Merrifield resin. Tetrahedron Lett. 2002 Dec 23;43(52):9717–9.

9. Bowen JL, Kelly MA, Gumbleton M, Davies PR, Allender CJ. A simple zero length surface-modification approach for preparing novel bifunctional supports for co-immobilisation studies. Tetrahedron Lett. 2012 Jul 18;53(29):3727–30.

10. Krattiger P, McCarthy C, Pfaltz A, Wennemers H. Catalyst-substrate coimmobilization: a strategy for catalysts discovery in split-and-mix libraries. Angew Chem Int Ed Engl. 2003 Apr 17;42(15):1722–4.

11. Cardno M, Bradley M. A simple multiple release system for combinatorial library and peptide analysis. Tetrahedron Lett. 1996 Jan 1;37(1):135–8.

12. Guillier F, Orain D, Bradley M. Linkers and Cleavage Strategies in Solid-Phase Organic Synthesis and Combinatorial Chemistry. (Chem. Rev. 2000, 100, 2091. Published on the Web May 6, 2000). Chem Rev. 2000 Oct 1;100(10):3859–3859.

13. Lv Y, Tan T, Svec F. Molecular imprinting of proteins in polymers attached to the surface of nanomaterials for selective recognition of biomacromolecules. Biotechnol Adv. 2013 Dec;31(8):1172–86.

14. Balamurugan S, Spivak DA. Molecular imprinting in monolayer surfaces. J Mol Recognit. 2011 Nov 1;24(6):915–29.

15. Cumbo A, Lorber B, Corvini PF-X, Meier W, Shahgaldian P. A synthetic nanomaterial for virus recognition produced by surface imprinting. Nat Commun. 2013 Feb 19;4:1503.

16. He H, Fu G, Wang Y, Chai Z, Jiang Y, Chen Z. Imprinting of protein over silica nanoparticles via surface graft copolymerization using low monomer concentration. Biosens Bioelectron. 2010 Oct 15;26(2):760–5.

17. Fu G, He H, Chai Z, Chen H, Kong J, Wang Y, et al. Enhanced lysozyme imprinting over nanoparticles functionalized with carboxyl groups for noncovalent template sorption. Anal Chem. 2011 Feb 15;83(4):1431–6.

18. Hussain M, Northoff H, Gehring FK. Detection of HIT antibody dependent platelet aggregation using novel surface imprinting approach. Talanta. 2016 Jan 15;147:1–7.

19. Zhang W, He X-W, Li W-Y, Zhang Y-K. Thermo-sensitive imprinted polymer coating CdTe quantum dots for target protein specific recognition. Chem Commun. 2012 Jan 12;48(12):1757–9.

20. Liu R, Sha M, Jiang S, Luo J, Liu X. A facile approach for imprinting protein on the surface of multi-walled carbon nanotubes. Talanta. 2014 Mar;120:76–83.

21. Zhang Z, Yang X, Chen X, Zhang M, Luo L, Peng M, et al. Novel magnetic bovine serum albumin imprinted polymers with a matrix of carbon nanotubes, and their application to protein separation. Anal Bioanal Chem. 2011 Nov 1;401(9):2855.

22. Pérez-Moral N, Mayes AG. Comparative study of imprinted polymer particles prepared by different polymerisation methods. Anal Chim Acta. 2004 Feb 16;504(1):15–21.

23. Nicholson J W. The Chemistry of Polymers. Cambridge: RSC Publishing; 2012.

24. Vasapollo G, Sole RD, Mergola L, Lazzoi MR, Scardino A, Scorrano S, et al. Molecularly Imprinted Polymers: Present and Future Prospective. Int J Mol Sci. 2011 Sep 14;12(9):5908–45.

25. Zhang H. Controlled/"living" radical precipitation polymerization: A versatile polymerization technique for advanced functional polymers. Eur Polym J. 2013 Mar;49(3):579–600.

26. Salian VD, Byrne ME. Living Radical Polymerization and Molecular Imprinting: Improving Polymer Morphology in Imprinted Polymers. Macromol Mater Eng. 2013 Apr 1;298(4):379–90.

27. Otsu T, Kuriyama A. Polymer Design by Iniferter Technique in Radical Polymerization: Synthesis of AB and ABA Block Copolymers Containing Random and Alternating Copolymer Sequences. Polym J. 1985 Jan;17(1):97–104.

28. Stenzel MH, Barner-Kowollik C. The living dead – common misconceptions about reversible deactivation radical polymerization. Mater Horiz. 2016 Oct 24;3(6):471–7.

29. Grubbs RB, Grubbs RH. 50th Anniversary Perspective: Living Polymerization—Emphasizing the Molecule in Macromolecules. Macromolecules. 2017 Sep 26;50(18):6979–97.

30. Kryscio DR, Peppas NA. Critical review and perspective of macromolecularly imprinted polymers. Acta Biomater. 2012 Feb;8(2):461–73.

31. Szwarc M. 'Living' Polymers. Nature. 1956 Nov;178(4543):1168–9.

32. Perrier S. 50th Anniversary Perspective: RAFT Polymerization—A User Guide. Macromolecules. 2017 Oct 10;50(19):7433–47.

33. Convertine AJ, Lokitz BS, Lowe AB, Scales CW, Myrick LJ, McCormick CL. Aqueous RAFT Polymerization of Acrylamide and N,N-Dimethylacrylamide at Room Temperature. Macromol Rapid Commun. 2005 May 19;26(10):791–5.

34. Otsu T, Yoshida M. Role of initiator-transfer agent-terminator (iniferter) in radical polymerizations: Polymer design by organic disulfides as iniferters. Makromol Chem Rapid Commun. 1982;3(2):127–132.

35. Otsu T. Iniferter concept and living radical polymerization. J Polym Sci Part Polym Chem. 2000 Jun 15;38(12):2121–36.

36. Li J, Zu B, Zhang Y, Guo X, Zhang H. One-pot synthesis of surface-functionalized molecularly imprinted polymer microspheres by iniferter-induced “living” radical precipitation polymerization. J Polym Sci Part Polym Chem. 2010 Aug 1;48(15):3217–28.

37. Chen R-R, Qin L, Jia M, He X-W, Li W-Y. Novel surface-modified molecularly imprinted membrane prepared with iniferter for permselective separation of lysozyme. J Membr Sci. 2010 Nov 1;363(1–2):212–20.

38. Sellergren B, Rückert B, Hall A j. Layer-by-Layer Grafting of Molecularly Imprinted Polymers via Iniferter Modified Supports. Adv Mater. 2002 Sep 3;14(17):1204–8.

39. Lee H-Y, S. Kim B. Grafting of molecularly imprinted polymers on iniferter-modified carbon nanotube. Biosens Bioelectron. 2009 Nov 15;25(3):587–91.

40. Qin L, He X-W, Zhang W, Li W-Y, Zhang Y-K. Surface-modified polystyrene beads as photografting imprinted polymer matrix for chromatographic separation of proteins. J Chromatogr A. 2009 Jan 30;1216(5):807–14.

41. Garcia-Soto MJ, Haupt K, Gonzato C. Synthesis of molecularly imprinted polymers by photo-iniferter polymerization under visible light. Polym Chem. 2017 Aug 22;8(33):4830–4.

42. Ward JH, Bashir R, Peppas NA. Micropatterning of biomedical polymer surfaces by novel UV polymerization techniques. J Biomed Mater Res. 2001 Sep 5;56(3):351–60.

43. Kolb HC, Finn MG, Sharpless KB. Click Chemistry: Diverse Chemical Function from a Few Good Reactions. Angew Chem Int Ed Engl. 2001 Jun 1;40(11):2004–21.

44. Bowen JL. Detection of Lipolysaccharide Pyrogens by Molecularly Imprinted Polymers. Cardiff University; 2011.

45. Kelly MA. MIPs as Prion biosensors. Cardiff University; 2011.

46. Clayden J, Greeves N, Warren S, Wothers P. Organic Chemistry. Oxford ; New York: OUP Oxford; 2001. 1512 p.

47. Bräse S, Gil C, Knepper K, Zimmermann V. Organic azides: an exploding diversity of a unique class of compounds. Angew Chem Int Ed Engl. 2005 Aug 19;44(33):5188–240.

48. Slimi R, Ben Othman R, Sleimi N, Ouerghui A, Girard C. Synthesis and Characterization of Polystyrene-Supported Piperazine-Substituted Triazoles by CuAAC and First Evaluation for Metal Ion Extraction. Polymers. 2016 May 10;8(5):187.

49. Ouerghui A, Elamari H, Ghammouri S, Slimi R, Meganem F, Girard C. Polystyrene-supported triazoles for metal ions extraction: Synthesis and evaluation. React Funct Polym. 2014 Jan;74:37–45.

50. Albuszis M, Roth PJ, Pauer W, Moritz H-U. Two in one: use of azide functionality for controlled photo-crosslinking and click-modification of polymer microspheres. Polym Chem. 2016 Aug 23;7(34):5414–25.

51. Tornøe CW, Christensen C, Meldal M. Peptidotriazoles on solid phase: [1,2,3]-triazoles by regiospecific copper(i)-catalyzed 1,3-dipolar cycloadditions of terminal alkynes to azides. J Org Chem. 2002 May 3;67(9):3057–64.

52. Hancock WS, Prescott DJ, Vagelos PR, Marshall GR. Solvation of the polymer matrix. Source of truncated and failure sequences in solid phase synthesis. J Org Chem. 1973 Feb 1;38(4):774–81.

53. Westall FC, Robinson AB. Solvent modification in Merrifield solid-phase peptide synthesis. J Org Chem. 1970 Aug 1;35(8):2842–4.

54. Santini R, Griffith MC, Qi M. A measure of solvent effects on swelling of resins for solid phase organic synthesis. Tetrahedron Lett. 1998 Dec 3;39(49):8951–4.

55. Vaino AR, Janda KD. Solid-Phase Organic Synthesis: A Critical Understanding of the Resin. J Comb Chem. 2000 Nov 1;2(6):579–96.

56. Rodionov IL, Peshenko IA, Baidakova LK, Ivanov VT. Swellographic Study of Peptide Resin Swelling Behavior during Solid Phase Peptide Synthesis. Int J Pept Res Ther. 2007 Jun 1;13(1–2):161–71.

57. Mendel CM, Mendel DB. 'Non-specific' binding. The problem, and a solution. Biochem J. 1985 May 15;228(1):269–72.

58. McInerney MP, Roberts KD, Thompson PE, Li J, Nation RL, Velkov T, et al. Quantitation of Polymyxin-Lipopolysaccharide Interactions Using an Image-Based Fluorescent Probe. J Pharm Sci. 2016 Feb;105(2):1006–10.

59. Soon RL, Velkov T, Chiu F, Thompson PE, Kancharla R, Roberts K, et al. Design, synthesis, and evaluation of a new fluorescent probe for measuring polymyxin-lipopolysaccharide binding interactions. Anal Biochem. 2011 Feb 15;409(2):273–83.

60. David SA, Balasubramanian KA, Mathan VI, Balaram P. Analysis of the binding of polymyxin B to endotoxic lipid A and core glycolipid using a fluorescent displacement probe. Biochim Biophys Acta BBA - Lipids Lipid Metab. 1992 Dec 2;1165(2):147–52.

61. Srimal S, Surolia N, Balasubramanian S, Surolia A. Titration calorimetric studies to elucidate the specificity of the interactions of polymyxin B with lipopolysaccharides and lipid A. Biochem J. 1996 Apr 15;315(Pt 2):679–86.

62. Brandenburg K, Andrä J, Müller M, Koch MHJ, Garidel P. Physicochemical properties of bacterial glycopolymers in relation to bioactivity. Carbohydr Res. 2003 Nov 14;338(23):2477–89.

63. Santos Nuno C., Silva Ana C., Castanho Miguel A. R. B., Martins-Silva J., Saldanha Carlota. Evaluation of Lipopolysaccharide Aggregation by Light Scattering Spectroscopy. ChemBioChem. 2003 Jan 3;4(1):96–100.

64. Marchyk N, Maximilien J, Beyazit S, Haupt K, Tse Sum Bui B. One-pot synthesis of iniferter-bound polystyrene core nanoparticles for the controlled grafting of multilayer shells. Nanoscale. 2014 Mar 7;6(5):2872–8.

65. Patel A, Mequanint K. Syntheses and characterization of physically crosslinked hydrogels from dithiocarbamate-derived polyurethane macroiniferter. J Polym Sci Part Polym Chem. 2008 Sep 15;46(18):6272–84.

66. Turner NW, Jeans CW, Brain KR, Allender CJ, Hlady V, Britt DW. From 3D to 2D: a review of the molecular imprinting of proteins. Biotechnol Prog. 2006 Dec;22(6):1474–89.

67. Ge Y, Turner APF. Too large to fit? Recent developments in macromolecular imprinting. Trends Biotechnol. 2008 Apr;26(4):218–24.

68. Verheyen E, Schillemans JP, van Wijk M, Demeniex M-A, Hennink WE, van Nostrum CF. Challenges for the effective molecular imprinting of proteins. Biomaterials. 2011 Apr;32(11):3008–20.

69. Hilt JZ, Byrne ME. Configurational biomimesis in drug delivery: molecular imprinting of biologically significant molecules. Adv Drug Deliv Rev. 2004 Sep 22;56(11):1599–620.

Chapter 3. Polymerisable Polymyxin Experiments

3.1 Introduction

3.1.1 Chapter outline

This second experimental chapter outlines work with the peptide antibiotic polymyxin B (PMB) to facilitate molecular imprinting without the need of a solid support (Merrifield resin). This chapter describes methods of PMB structure manipulation to render it polymerisable (p-PMB) with subsequent synthesis of a polymyxin B polymer. Polymyxin is introduced in section 3.1.2 with subsequent explanation of the important PMB/LPS interaction.

3.1.2 Polymyxin's structure

The Polymyxins are a group of naturally occurring peptide antimicrobials, the most studied being polymyxin B (PMB) and colistin (Polymyxin E). PMB is isolated from *Bacillus Polymyxa,* a strain of the *bacillus* genus and was originally named 'Aerosporin' by Ainsworth *et al.* in 1947 (1,2), the potent anti Gram-negative activity of Polymyxin was clear at this early stage (1).

Shown in figure 3.1 is the structure of PMB, comprising a positively charged cyclic peptide ring and a fatty acid tail. The peptide ring contains seven amino acid residues, with a further two 2,4- diaminobutyric acid (Dab) and one Threonine (Thr) within the fatty acid tail.

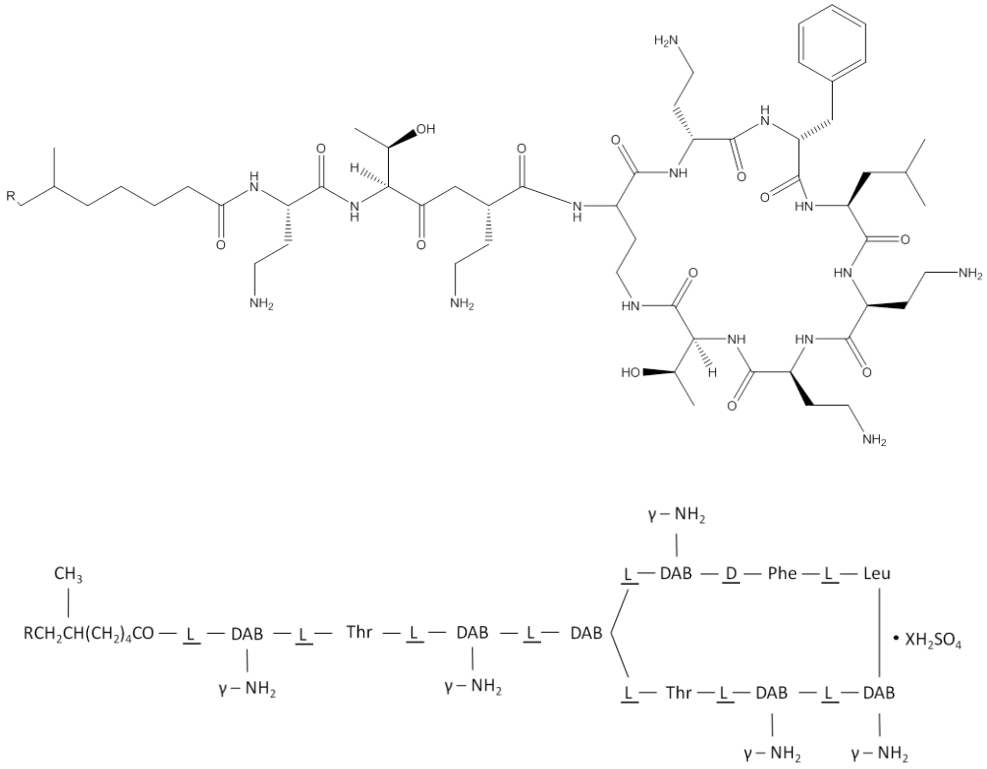

Figure 3.1: PMB structure. In polymyxin B1 R= CH_3 and in polymyxin B2, R= H.DAB: γ- diaminobutric acid; Thr: threonine ($C_4H_9N_{O3}$); Phe: phenylalanine ($C_9H_{11}NO_2$); Leu: leucine ($C_6H_{13}NO_3$). Positively charged cyclic ring confers overall charge of +5. The fatty acid tail provides hydrophobicity.

3.1.3 Polymyxin/LPS interaction

The interaction between PMB and LPS has been investigated since the 1950s and an extensive review published in 1956 by Newton focused heavily on the interaction of polymyxin with the cell wall of Gram-negative bacteria (3). Newton's work also provided the first evidence of interaction between polymyxin and a 'membrane underlying the bacterial cell wall' (3). Since the 1950s, many investigative techniques have since been used to explore PMB/LPS interaction and recent examples of work in this area include use of computational modelling (4), NMR analysis (5), SPR analysis (6,7), dynamic light scattering (8) and the use of zeta potentials (8). Understanding this interaction may help address problems like polymyxin

toxicity, bacterial polymyxin resistance or the development of future peptide antibiotics. Furthermore, there are distinguishing features between the interaction of polymyxin with free LPS and interaction at LPS attached to Gram-negative bacteria cell walls.

3.1.3.1 Free LPS

NMR studies have provided a vast amount of information relating to the interaction of PMB and LPS and elucidated important structural considerations. Studying conformational changes of free PMB compared to PMB-LPS complexes using solution-state NMR allowed Pristorsek *et al.* to construct a molecular model for PMB/LPS interaction that showed both electrostatic and hydrophobic interactions serve to stabilise the PMB-LPS complex (9,10). Furthermore, modelling studies have shown a distinct conformational change of LPS upon interaction with PMB that results in increased separation of LPS polar and hydrophobic areas (9,10). This accentuates the amphiphilic nature of the LPS; a characteristic that is widely regarded of utmost importance in the interaction with PMB (11).

As a result of interaction with free LPS, polymyxin B has been shown to promote LPS aggregation, disrupting LPS/TLR-4 binding and reducing the subsequent cascade of LPS triggered cytokine release from macrophages (8). Furthermore, it is proposed that in an aggregated cluster LPS is amenable to phagocytosis by macrophages; effectively sequestering LPS from the circulation (8,12). In their 2012 paper, Domingues *et al.* used biomembrane modelling and dynamic light scattering techniques to study PMB/LPS interaction. They showed that at relatively high LPS concentrations (0.3 - 3 mg ml^{-1}), PMB causes the aggregation of LPS, forming clusters of the magnitude of 60 -100 nm width (8). This interaction as described by Domingues *et al*. is shown in figure 3.2.

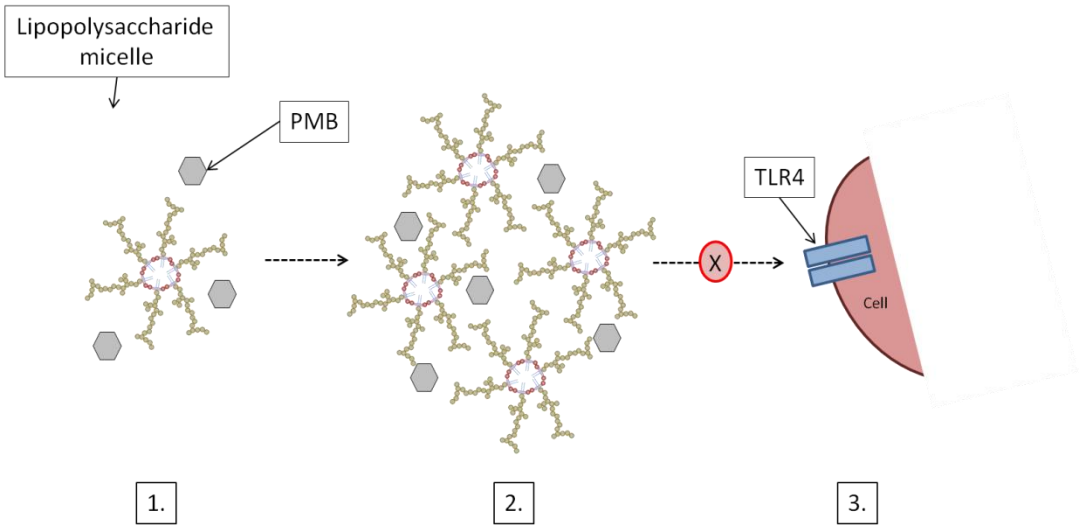

Figure 3.2: Demonstration of PMB interaction with LPS aggregates as proposed by work from Domingues and colleagues. **1.)** PMB introduced to circulation; **2.)** Interaction of PMB and aggregates of LPS (LPS micelles) causes further aggregation forming 'clumps' of LPS and finally **3.)** These aggregates fail to elicit a response from the cell via TLR4 therefore reducing the release of sepsis mediators. Adapted from (8).

Using X-ray diffraction techniques, Howe *et al.* tracked diffraction pattern changes in the aggregate structures of two LPS subtypes (LPS-R45 and LPS-R595 from *Proteus mirabilis* and *Salmonella minnesota*, respectively) with and without PMB present (13). Aggregate pattern changes associated with a change from unilaminar to multilaminar structures were observed on the addition of PMB (13), demonstrating a PMB induced conformational change in LPS aggregates. However, the concentrations of LPS used by both Domingues and Howe were many magnitudes greater than found in the circulation of patients with sepsis (milligrams compared to picograms per ml (14)).

3.1.3.2 Cell wall interaction

The combination of electrostatic and hydrophobic interactions forms a widely accepted model for the interaction of PMB and Gram-negative

bacteria cells (11,15). Initially, the positive overall charge of PMB reliably allows the drug's accumulation at the anionic bacterial membrane. Thereafter, further electrostatic interaction between the positively charged Dab residues of PMB and the negatively charged lipid A portion of LPS disrupts stabilising bridges of divalent cations that would normally serve to stabilise the outer cell membrane (11,15–17). This disruption is the catalyst for cell death as the increased permeability allows leakage of bacterial cell contents whist also allowing the influx of host serum complement (11,18,19). Furthermore, this action brings the PMB fatty acid tail into close contact with the outer membrane and this inserts itself into the cell, expanding (and further disrupting) the cell wall (11,20,21). NMR studies have shown the N-terminal fatty acid chain of PMB moves independently of the PMB peptide core, providing a flexibility that aids cell insertion (11,22,23). In their 2015 computational biology paper, Berglund *et al.* mapped the interaction of PMB1 with both the outer and the inner cell membrane of *Escherichia coli*. In agreement with previous work (11,24,25), they observed the importance of Dab residues to the interaction with the bacterial outer cell membrane and describe how PMB 'anchors' itself to the membrane via this electrostatic Dab interaction with LPS lipid head groups (4). Interestingly, this group also showed that within 16 milliseconds of PMB1/LPS interaction, PMB1 aggregates in the LPS headgroup region of the *Escherichia coli* outer membrane; forming a micelle-like structure (4). The cell wall defects forged by polymyxin facilitate further drug uptake hence the widely used term 'self promoted uptake' is used to summarise the mode of action of PMB (20). Figure 3.3 shows these PMB/LPS cell wall interaction events.

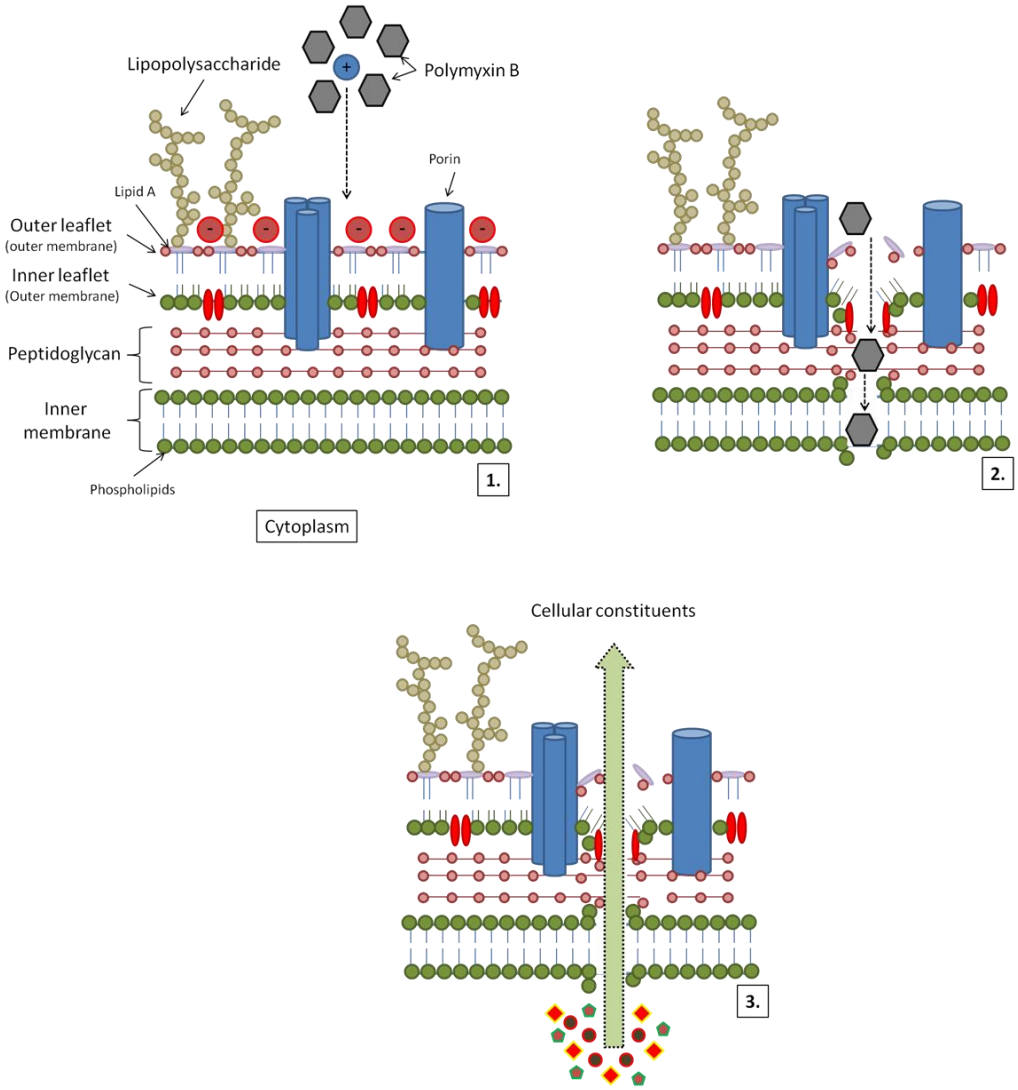

Figure 3.3: Simplified schema of the interaction of PMB at the cell wall of *Escherichia coli*. **1.)** PMB in close proximity to the bacterial outer cell wall, the positive charge of PMB and the negative charge of the cell wall are shown. **2.)** Cell wall disruption caused by an initial electrostatic interaction between the positively charged Dab residues (PMB) and the negatively charged lipid A portion of LPS. Cell wall disruption follows as the hydrophobic tail of PMB inserts itself into the bacterial cell. **3.)** Having successfully rendered the bacterial outer cell walls and inner membrane unable to maintain an effective barrier, both inward flux of host cell complement and outward flow of bacterial cell contents occur.

In addition to its direct antibacterial action, PMB also exhibits potent anti-endotoxin activity and the release of factors such as TNF- α and interleukin-1 activated by LPS has been shown to be inhibited by PMB and colistin (26). Tsuzuki and colleagues suggest this is secondary to inhibition by PMB of the NF-kB pathway with demonstration of an immediate decrease in NF-kB binding activity when PMB was added to LPS activated human blood mononuclear cells *in vitro* (27). However, in high concentrations PMB has previously been shown to conversely stimulate the NF-kB pathway in monocytes and increase the production of TNFα (28).

3.1.4 Polymyxin B structure manipulation

The initial interaction between PMB and the cell membrane of bacteria is dependent on an overall positive charge of PMB (attributed to positively charged amine groups) and a negatively charge portion of LPS (KDO-Lipid A region) (29). Therefore, in order to maintain this interaction, PMB must carry a positive charge and it has been shown that reducing the available number of amine groups in PMB structure dramatically affects the affinity of LPS binding (11). Furthermore, structural variants of PMB that lack certain Dab residues show decreased levels of insertion into bacterial cell membranes (both LPS and peptidoglycan monolayer) (30). An example is polymyxin B nonapeptide (PMBN) that lacks the fatty acid and the terminal dab residue of PMB (31). This PMB structural manipulation historically demonstrated a decrease in antimicrobial action (32) however, findings in successive years reported potential, indirect PMBN antimicrobial activity. For example, a bacterial 'sensitisation' effect of PMBN was demonstrated by Vaara and Vaara in the 1980s who found the susceptibility of *Escherichia coli* (using a smooth strain resistant to the hydrophobic antibiotics erythromycin, clindamycin, rifampicin and fusidic acid) to certain hydrophobic agents was markedly increased following the addition of PMBN. These findings are credited to the increased permeability of

bacteria cells caused by PMBN, facilitating the influx of other antibiotics (33). Moreover, the addition of PMBN to the same strain of *Escherichia coli* sensitised the bacteria to serum complement (33). Further work confirmed the susceptibility of other strains of Gram-negative bacteria (strains of *Klebsiella pneumonia*, *Salmonella tryhimurium* and *Pseudomonas aeruginosa* amongst others) to erythromycin, fusidic acid and novobiocin when PMBN was introduced (34). Building on a body of investigative work on PMBN, the Vaara group have worked on a library of PMB derivative antibiotics with varied structure manipulations (35–37). Recently, one such derivate compound (denoted by NAB739) that possesses the same cyclic portion of PMB but the linear diaminobutyryl-theronyl-diaminobutyryl residue is substituted by threonyl-D-serinyl (therefore carrying only three positive charges), has been investigated. Findings initially showed comparable results of NAB739 and PMB when looking at the action against 15 *Escherichia coli* strains with similar MIC_{50} obtained (0.5-1 μg ml^{-1} and 0.25-1 μg ml^{-1}, respectively) (38). Furthermore, ongoing work from this group continued to demonstrate NAB739's ability to inhibit the growth of other Gram-negative species, the closest comparable action seen against *K. pneumonia* (MIC_{90} of 2 mg l^{-1} compared to 1 mg l^{-1}) (39). In 2017 the Vaara group also published work about another PMB derivative, NAB815 that has only two positives charges in its cyclic portion (40), this compound demonstrated impressive MICs compared to PMB.

3.1.5 Clinical use of PMB

3.1.5.1 General overview

In the clinical setting, PMB has been shown to moderate adverse clinical conditions in septic shock such as hypotension and acidosis (41,42). Despite this, use of PMB declined following findings from large clinical studies in the 1970s that investigated polymyxin related nephrotoxicity and neurotoxicity. However, the advent of multi-drug resistant Gram-negative

bacteria in some countries has led to the resurgence of polymyxin use (17,43). In their 2006 systematic review, Falagas and Kasiakou reviewed both old and new evidence regarding polymyxin toxicity (44). Incidence of nephrotoxicity taken from older studies was up to 36%, whereas more recent studies found much lower incidence, around 15%. However, studies are still emerging that document the renal cellular damage caused by PMB (45) and the dose dependent nature of PMB renal toxicity (46). Similarly, discrepancy exists between old and new studies looking at neurotoxicity; Falagas and Kasiakou highlight that no episodes of significant neurotoxicity have appeared in the literature for at least the last 15 years.

Interestingly, antimicrobial activity has been demonstrated with PMB immobilised on Agarose beads; demonstrating effective antimicrobial potency with cell membrane disruption alone without the need to directly enter the bacterial cell (10). Incorporation of polymyxin into carrier compounds, such as liposomes, has also shown benefit and effective antimicrobial activity against *Pseudomonas aeruginosa* has been demonstrated using liposomal PMB (47). These findings are relevant to this work as there is theoretical potential for synthesised polymerisable polymyxin to be used in LPS sequestration applications, such as in adapted extracorporeal circuits.

3.1.5.2 Polymyxin in extracorporeal circuits

In 2011, Onaizi & Leong discussed relevant issues in the attachment strategies of antimicrobial peptides to medical device surfaces in their extensive review (48). With focus on antimicrobial peptides, the paper looked at both the advantages of combating infection secondary to biofilm formation on medical devices, and the pitfalls. Importantly, the review highlighted the contribution to antimicrobial resistance that an increased availability of antimicrobial peptide coatings could bring to the population. Antimicrobial resistance is a major global health concern and medical

devices that contribute to this growing problem have no place in modern medicine. However, the burden of sepsis is ever present and considering the wealth of investigative work on extracorporeal strategies, such devices may have a place in the treatment of patients.

Patients with sepsis commonly require the use of extracorporeal systems to undertake the role of failing kidneys (figure 3.4).

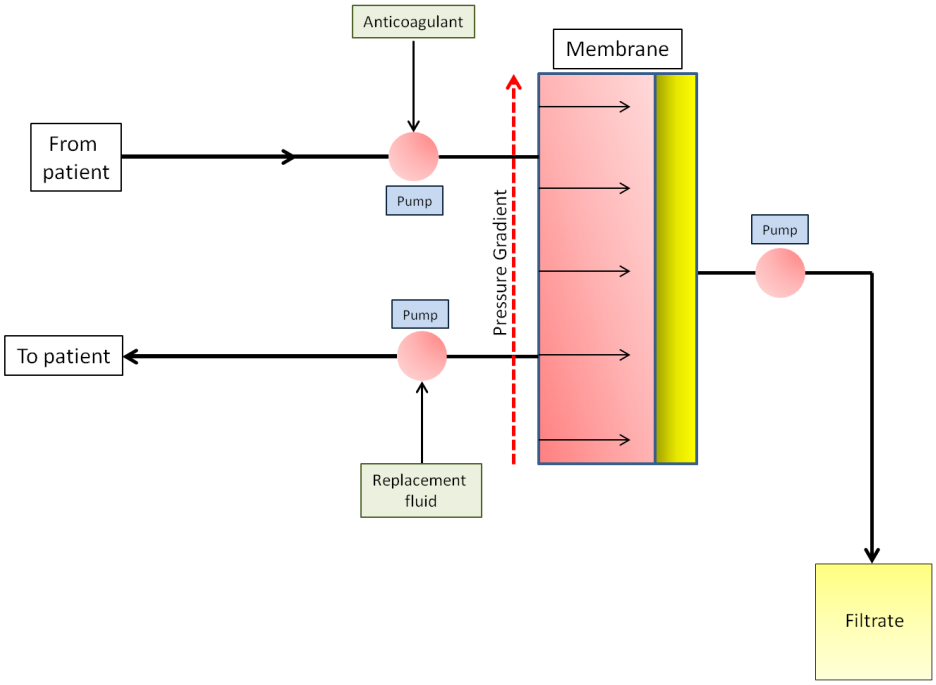

Figure 3.4: Simplified schematic of a CVVH circuit (continuous veno-venous hemofiltration). The patient is attached to the extracorporeal circuit via large cannulae placed into a major vein (internal jugular or femoral veins for example). Blood is then pumped from the patient and is passed over membranous circuit components which serve as surrogate kidneys for the filtration of blood. Following filtration, waste filtrate is discarded and blood is pumped back to the patient. The membrane unit is representative of a possible point on the circuit where specialised components could be utilised. For example, the addition of PMB coated membranes in circuitry allowing the sequestration of LPS.

Also commonplace in some countries is the use of more specialised extracorporeal filter system designs specifically for the removal of endotoxin. In Japan the use of such devices has been part of the critical care approach in sepsis for over 20 years (49). The key part of the specialised design of these systems is polymyxin, and the attachment of PMB to specifically designed extracorporeal endotoxin removal cartridges (Toraymyxin®- Spectral Medical INC) (49,50).

By the early 2000s small trials looking at such extracorporeal devices for the treatment of sepsis were frequently appearing in the literature. Many desirable features were highlighted by these studies including improved cardiovascular parameter profile (51), improved oxygenation of study patients (52,53) and, importantly, the apparent decrease in mortality (15,16) . Larger randomised control trials was a natural next step, ushered in by analysis of these preceding smaller trials (54). Published in 2009, the EUPHAS clinical trial (**E**arly **U**se of **P**olymyxin B **H**emoperfusion **A**bdominal Septic shock) (55) was a multicentre randomised controlled trial that included 64 patients from ten centres around Italy. This preliminary study showed a decrease in 28 day mortality rate in patients randomised to receive PMB hemoperfusion therapy (34% vs 53%). Commencing in 2014, the EUPHRATES trial (**E**valuating the **U**se of Polymyxin B **H**emoperfusion in a **R**andomised controlled trial of **A**dults **T**reated for **E**ndotoxemia and **S**eptic shock) was designed to further investigate the use of this specialised therapy for patients with sepsis (56). Interim analysis following randomisation of 184 patients lead to key recommendations including the increase in power to 650 patients (from 360) leading to the expansion to 60 centres, also the exclusion criteria of a MODS (multiple organ dysfunction score) greater than or equal to nine being added, essentially excluding all but the sickest of patients. Unfortunately, results published in 2018 showed no difference in 28 day mortality between patients in the treatment group to those in the control group (57). However, an

interesting paper reporting on an exploratory *post hoc* analysis of the EUPHRATES data showed a statistically significant increase in mortality in the treatment group when analysis was focussed on the sickest patients (high MODS sores) with moderate endotoxin activity assay (EAA) levels (58). Extracorporeal PMB systems also reduce other circulating bio-molecules in addition to LPS that may be beneficial in the treatment of sepsis. For example, PMB sequestration cartridges can also reduce serum levels of the chemokine IL-8 (52), IL-6 (59), IL-18 (60) and anandamide (61).

The stratification of patients with sepsis to treatment arms tailored to their own therapeutic responses may, in the future, include use of extracorporeal PMB devices to sequester LPS. Indeed, this is already employed in parts of the world.

3.2 Aims and Objectives

The main aim of this chapter was to investigate the feasibility of the manufacture of a polymer, using a polymerisable PMB, capable of binding to LPS.

Key objectives of this chapter were as follows:

1. Successful synthesis of a modified PMB with methacrylate groups attached to structure.
2. Subsequent successful integration of this synthesised modified PMB (denoted p-PMB (polymerisable PMB)) into a bulk polymer.
3. Demonstrate efficient binding capability of this synthesised p-PMB polymer to LPS.

3.3 Materials and Methods

3.3.1 Materials

The polymyxin B used in all experiments was from Enzo (Exeter, UK). All LPS used was FITC- labelled *Escherichia coli* 0111:B4 LPS (Sigma-Aldrich). All other chemicals purchased from Sigma-Aldrich (Poole, UK). All organic solvents were of HPLC grade and were obtained from Fisher Scientific, (Loughborough, UK).

3.3.2 Analysis

3.3.2.1 Mass spectrometry

Mass spectrometry analysis used Quattro Ultima Mass Spectrometer (Waters Micromass, Elstree, Herts, UK).

3.3.2.2 Nuclear Magnetic Resonance

Nuclear magnetic resonance performed using Bruker Avance 500Mhz multi-nuclear gradient NMR (Bruker, Coventry, UK). All predictive NMR data generated from ChemDraw Professional® software.

3.3.2.3 Fluorescence

Fluorescence analysis was undertaken using a FLUOstar OPTIMA platereader (BMG Labtech GmbH, Ortenburg, Germany). The florescence properties of the FITC labelled *Escherichia coli* 0111: B4 LPS used in all binding experiments was as follows: excitation wavelength of 485 nm and emission wavelength 520 nm (λ_{ex} 485 nm/ λ_{em} 520 nm). Analysis of binding performance data obtained from fluorescence analysis was carried out with GraphPad Prism® V8 software (B_{max} and K_d values from single-site specific binding curve fitting algorithm).

3.3.2.4 HPLC

Thermo Scientific Products (Paisley, UK) automated HPLC system was used. Column: C18, 4.6 x 250 mm, 5µm. Two mobile phases were used - A: 99% ACN; 0.1% TFA and B: 99% DI water; 0.1% TFA – and a gradient elution employed (98% A: 2% B at time zero to 2% A: 98% B at 30 minutes). Flow rate: 1.8 ml min^{-1}; injection volume: 200 µl; UV detection: 215 nm.

3.3.3 General method overview

The aim was to synthesise a PMB analogue that could polymerise. This was achieved with the substitution (to a varying degree) of PMB amine groups for methacrylate groups. Structure modification of PMB produce polymerisable PMB (p-PMB) via two routes is described. Section 3.3.5 describes the reaction of PMB and methacryloyl chloride and section 3.3.6 describes the reaction of PMB and glycidyl methacrylate. The different modification routes (figure 3.5) leave the resultant p-PMB with different molecular structures, which is important when analysing the mass spectrometry data.

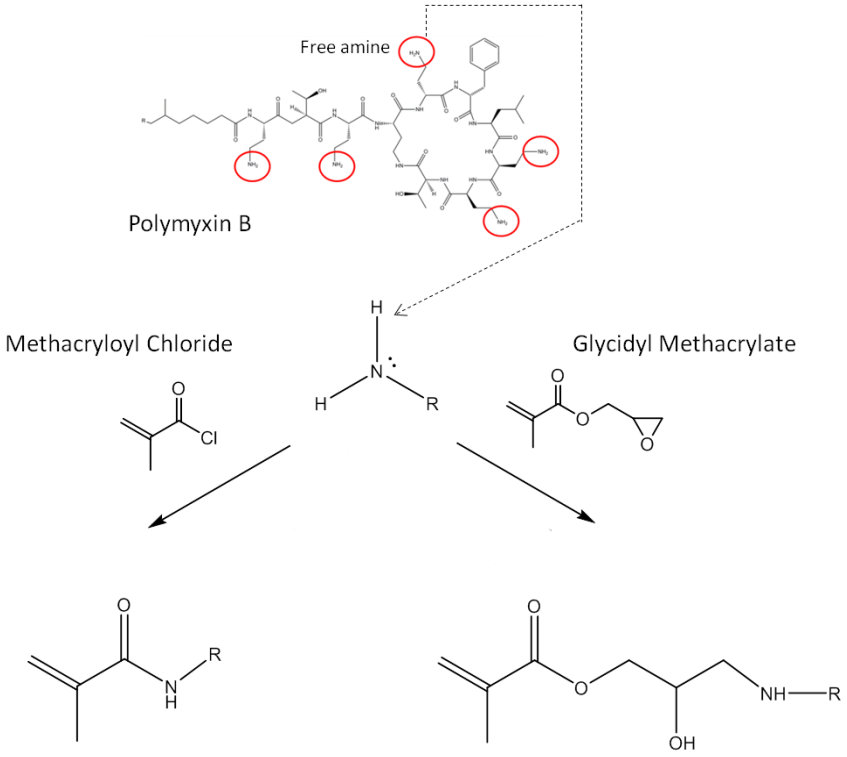

Figure 3.5: Reaction schematic of two possible routes to the structural manipulation of PMB to substitute free amine groups for methacrylate groups. The left arm of the schematic shows the reaction of PMB with methacryloyl chloride. Shown on the right arm of the schematic is a second process using glycidyl methacrylate.

3.3.4 Plain PMB analysis

Plain PMB (as purchased from Enzo®) was analysed by mass spectrometry and NMR. These results were then used to compare synthesised PMB products from methacryloyl chloride and glycidyl methacrylate experiments.

3.3.5 Methacryloyl chloride experiments

3.3.5.1 Synthesis of polymerisable polymyxin (p-PMB$_{MC}$)

Into a small, two-necked, round bottomed flask, 5 ml of deionised water was added to 300 mg of PMB (0.25 mmol) and sonicated until a clear

solution obtained. The mixture was then cooled on ice. Whilst still on ice the following were added simultaneously in a dropwise fashion: 2 ml 1% sodium hydroxide, 2 ml dichloromethane containing 24.4 µl (0.25 mmol) methacryloyl chloride. This remained on ice and was stirred gently for 90 minutes.

Following 90 minutes stirring on ice the organic phase was extracted from the aqueous with deionised water and dichloromethane. Both aqueous and organic phases were sampled for analysis by thin layer chromatography, mass spectrometry and NMR. Aqueous phase (containing product) was freeze dried to fine white powder, this was stored at 4 °C.

Furthermore, 10 mg of aqueous phase freeze dried powder (post extraction and post lyophilisation) was dissolved in 2 ml DI water/1 ml MeOH (sonicated) and analysed with HPLC. Timings of major peaks were noted and samples were taken from the HPLC run and were then analysed by mass spectrometry.

Methacryloyl chloride experiments were not taken any further; thereafter, glycidyl methacrylate methods to synthesise polymerisable polymyxin and associated control polymers were the focus. The experimental section 3.4.3 details findings from methacryloyl chloride experiments and therefore dictated the decision to continue only with the alternative experimental arm (glycidyl methacrylate experiments). Results in section 3.4.3 will show an inefficient process of synthesising single or double methacrylate substituted PMB in comparison to the results from glycidyl methacrylate experiments detailed in section 3.4.4.

3.3.6 Glycidyl methacrylate experiments

3.3.6.1 Synthesis of polymerisable polymyxin (p-PMB_{GMA})

Polymyxin B 300mg (0.25 mmol) was added to 20 ml of methanol. Glycidyl methacrylate 35.5 mg (0.25 mmol) was then added to give a 1:1 molar ratio of PMB: glycidyl methacrylate. Sealed in a freeze-drying vial, the reaction was stirred gently at 40°C in a water bath overnight. This was repeated using a 1:2 molar ratio of PMB: glycidyl methacrylate (300mg PMB (0.25 mmol); 71 mg (0.5 mmol) glycidyl methacrylate). The reaction was rotavap dried and resultant white powder was analysed with NMR and MS.

3.3.6.2 Polymer production

a. p-PMB_{GMA} composite polymers

Two polymers containing p-PMB_{GMA} were synthesised (denoted p-PMB_{GMA} Polymer A and p-PMB_{GMA} Polymer B). Polymer A: p-PMB_{GMA} 100 mg; AAm 216 mg (3.04 mmol); MBAam 56 mg (0.36 mmol); azo initiator (2'2' Azo (2-methyl-propionamide) dihydrochloride/AAPH) 3.6 mg in DI water 800 µl. Polymer B: p-PMB_{GMA} 100 mg; AAm 144 mg (2.03 mmol); MBAam 84 mg (0.55 mmol); AAPH 3.6 mg in DI water 800 µl. Each sample was sparged with nitrogen for 7 minutes and samples were then stirred gently under UV light of 100mw/cm^2/325 nm at a distance of 20 cm for one hour. Following irradiation all samples were washed and filtered in the following sequence: MeOH 15 ml (x2); 50/50 DI water/MeOH 15 mls (x2); MeOH 15 mls. Samples were dried overnight under vacuum at 40°C.

b. Matched (control) polymers

Two matched polymers were synthesised that did not contain p-PMB_{GMA} . Matched polymer A: AAm 1.2 g (16.90 mmol); MBAam 0.3 g (1.95 mmol); AAPH 3.6 mg in DI water 800 µl. Matched polymer B: AAm 0.918 g (12.91

mmol); MBAam 0.54 g (3.51 mmol); azo initiator 3.6 mg in DI water 800 µl. Each sample was sparged with nitrogen for 7 minutes. Samples were then stirred gently under UV light of 100mw/cm^2/ 325 nm at a distance of 20cm for one hour. Following irradiation all samples were washed and filtered in the following sequence: MeOH 15 ml (x2); 50/50 DI water/MeOH 15 ml (x2); and MeOH 15 ml. Samples were dried overnight under vacuum at 40°C.

Table 3.1 shows the composition of polymers described in this method section.

Table 3.1: Composition of polymers used in glycidyl methacrylate experiments. (Polymer (m) denoting the matched polymer to that particular p-PMB$_{GMA}$ polymer).

	p-PMB$_{GMA}$ mg (mmol)	**AAm mg (mmol)**	**MBAam mg (mmol)**
Polymer A	100 (0.74)	216 (3)	56 (0.3)
Polymer A (m)	Nil	1200 (16)	300 (2)
Polymer B	100 (0.74)	144 (2)	84 (0.5)
Polymer B (m)	Nil	918 (13)	540 (3.5)

3.3.6.3 Polymer/LPS binding Studies

Both p-PMB$_{GMA}$ polymers and matched (non p-PMB$_{GMA}$) were tested for FITC-LPS binding capability. Dried polymer (10 mg) was incubated with known concentrations of LPS in a glass vial. Concentrations of LPS were as follows (volume 1ml water for injection): blank (water for injection only); 0.1 µ ml^{-1}; 1 µ ml^{-1}; 2 µ ml^{-1}; 4 µ ml^{-1}; 6 µ ml^{-1}; 8 µ ml^{-1} and 10 µ ml^{-1}. Three repeats of all concentrations were prepared. Samples were sealed and shaken gently overnight. Following overnight incubation all samples were filtered via a mixed cellulose filter and filtrate was analysed with fluorescence spectroscopy using a 96 well plate. The florescence properties

of the FITC labelled *Escherichia coli* 0111: B4 LPS used in all binding experiments was as follows: excitation wavelength of 485 nm and emission wavelength 520 nm (λ_{ex} 485 nm/ λ_{em} 520 nm).

3.4 Results and Discussion

3.4.1 Plain PMB analysis

The Polymyxins are a naturally derived group of peptides; therefore, multiple closely related structural species occur. In 1981, Elverdam and Lund published chromatography separation work that isolated 13 components from PMB and colistin (62). Furthermore, in 2001 Orwa *et al*. looked solely at PMB and isolated seven components using a poly (styrene-divinyal benzene) semi-preparative column (63).

PMB from Enzo® is composed of three forms of PMB (PMB1, B2 and B3). The minor structural differences derive from the fatty acid component. As shown in figure 3.6, the fatty acid component for B1 is 6-methyloctanoic acid, for B2 it is 6- methylheptanocic acid and for B3 the fatty acid component is octanoic acid (17).

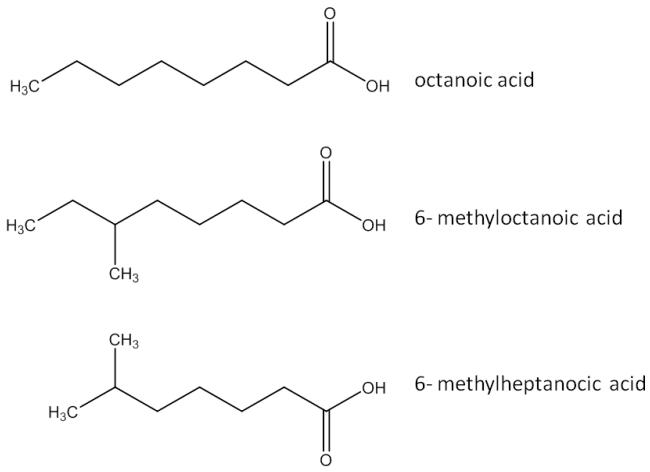

Figure 3.6: Schematic representation of the variable fatty acid portion of different varieties of PMB. PMB1 contains the fatty acid 6-methyaloctanoic; PMB2 contains 6-methyalhepanocic and B3 contains the fatty acid portion octanoic acid.

Purchased PMB was analysed by mass spectrometry (figure 3.7) and NMR (figure 3.9). Despite the purchased PMB being a mixture of polymyxin B1, B2 and B3 (MW 1203.5, 1287.53 and 1287.55 $gmol^{-1}$ respectively), the abundance of PMB1 is evident from the mass spectrometry analysis (peak at 1203.7, figure 3.7).

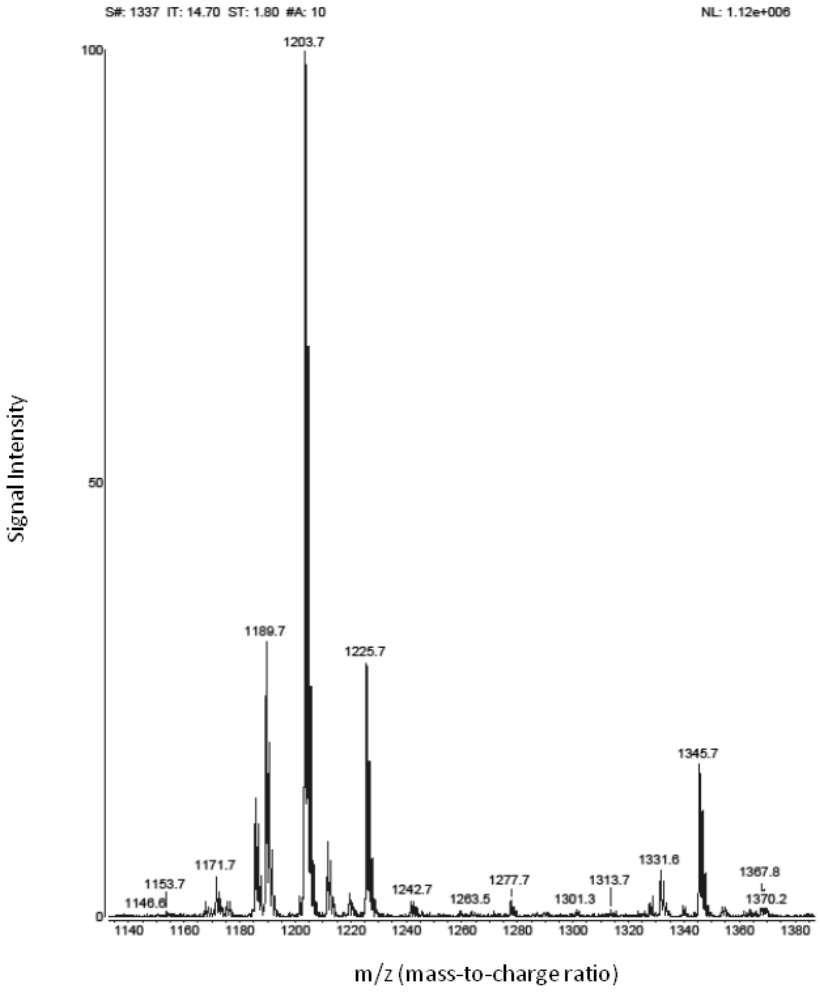

Figure 3.7: Mass spectra for polymyxin B sulphate as purchased from Enzo®. M/Z 1203.7 represents PMB1.

NMR data from purchased PMB analysis is shown in figure 3.9 and is similar to that obtained from a digital prediction model (figure 3.8).

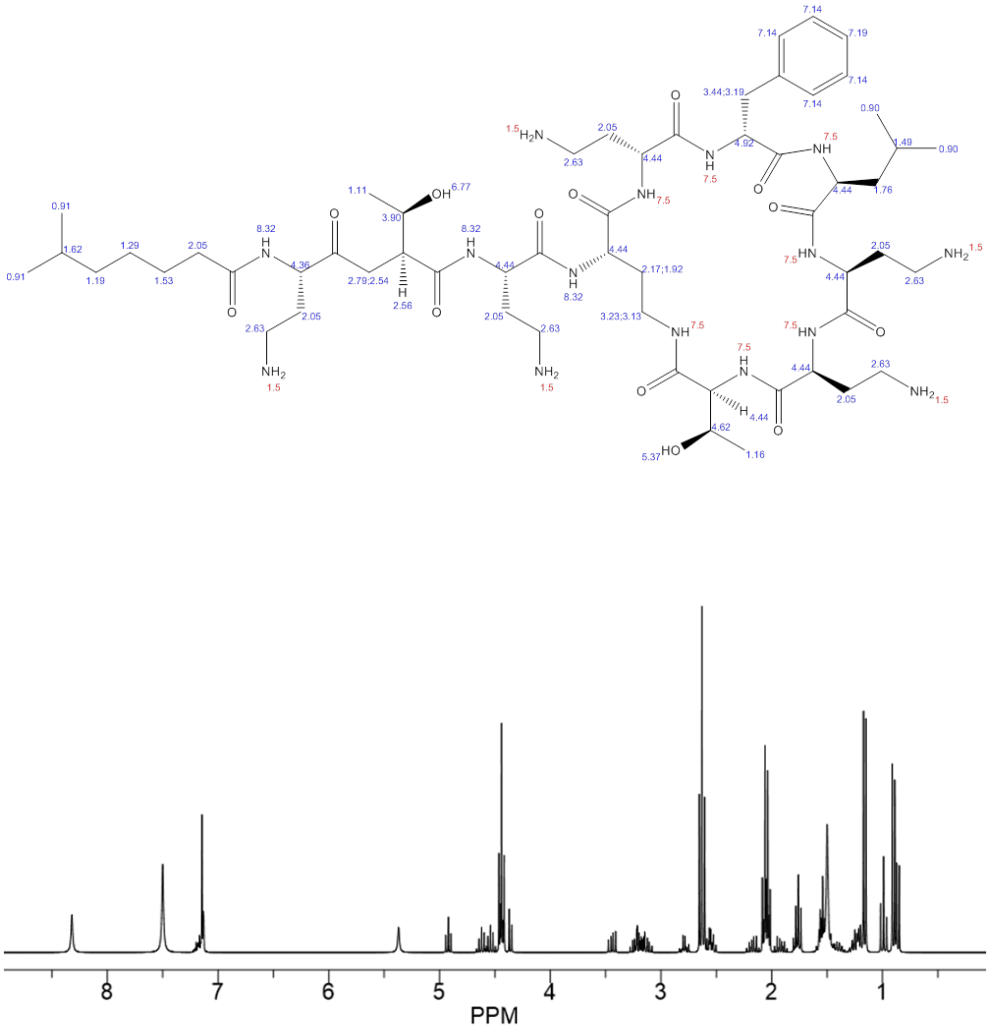

Figure 3.8: Predicted ^{1}H NMR for PMB1 as generated by ChemDraw®.

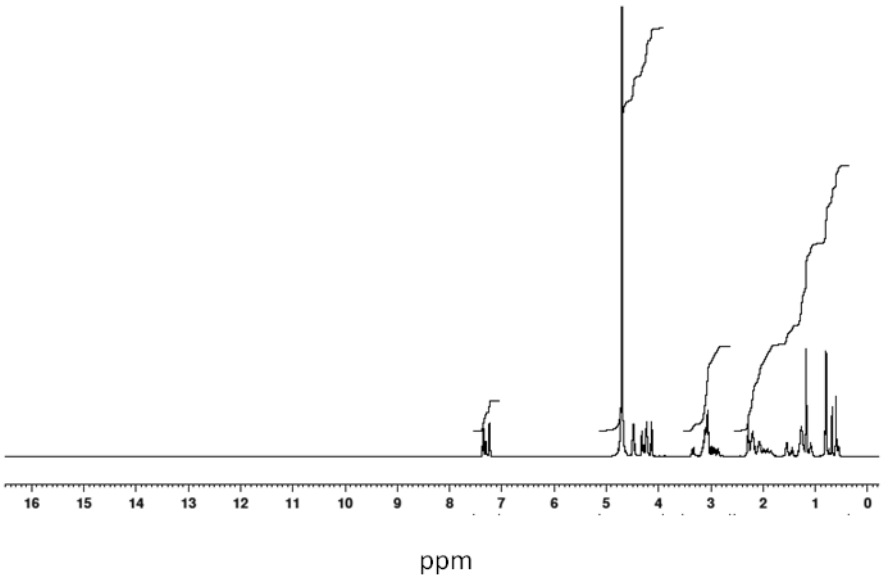

Figure 3.9: 1H NMR (500MHz,D_2O) of PMB sulphate. δ=0.605 ppm (d,1H); δ=0.681(d, 1H); δ=0.794 ppm (m,2H); δ=1.104 ppm (m, 1H); δ=1.178 ppm (d, 2H); δ= 1.27 ppm (m, 2H); δ= 1.494 ppm (m, 1H); δ= 1.93 (m, 1H); δ= 2.07 ppm (m, 1H); δ= 2.206 ppm (m, 1H); δ= 2.293 ppm (m, 2H); δ= 2.942 ppm (m, 1H); δ= 3.093 ppm (m, 4H); δ= 4.142 ppm (m, 1H); δ= 4.236 ppm (m, 2H); δ= 4.305 ppm (m, 1H); δ= 4.482 ppm (m, 2H); δ= 7.233 ppm (d, 2H); δ= 7.332 ppm (m, 3H).

3.4.2 Theoretical resultant polymerisable PMB structure

3.4.2.1 Structure schematic

The theoretical resultant structures of p-PMB_{MC} and p-PMB_{GMA} are shown in figure 3.10.

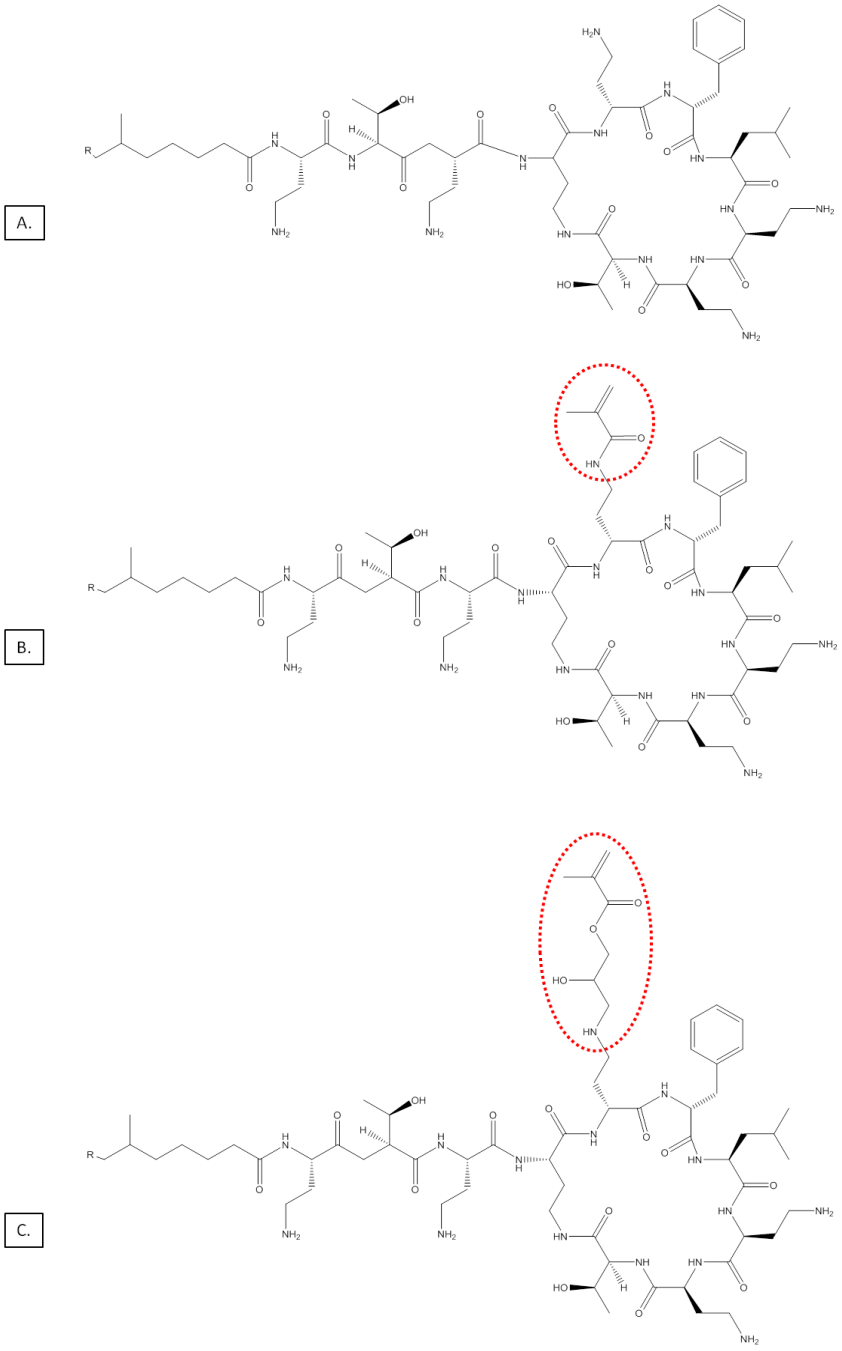

Figure 3.10: Schematic representation of structure modification of PMB. **A.)** Structure of plain PMB; **B.)** PMB following reaction with methacryloyl chloride; **C.)** PMB following reaction with glycidyl methacrylate. Modification circled in red.

3.4.2.2 Molecular weights

The successful conversion of PMB to a polymerisable PMB via the substitution of one or two of the free amine groups to methacrylate groups was the desired outcome. The small difference in attachment of methacrylate group between the structures shown in figure 3.10B and 3.10C is reflected in a molecular weight difference. These structures could therefore be compared with mass spectrometry analysis of the resultant polymerisable PMB.

Drawing B in figure 3.10 shows the theoretical structure of a resultant p-PMB following reaction of PMB and methacryloyl chloride, a weight of 68 g mol^{-1} is added to the molecular weight of PMB of 1203.7 g mol^{-1} giving a p-PMB_{MC} weight of 1271.7 g mol^{-1}. Drawing C in figure 3.10 shows the theoretical structure of a resultant p-PMB following reaction of PMB and glycidyl methacrylate and results in an additional weight of 142 g mol^{-1} giving a p-PMB_{GMA} weight of 1345.7 g mol^{-1}.

3.4.2.3 Relative free amine reactivity

In figure 3.11, PMB Dab residue positions are highlighted with their associated identifying number.

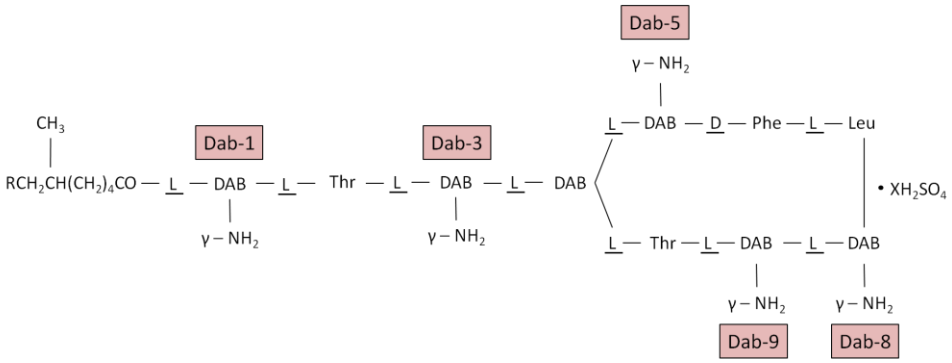

Figure 3.11: PMB structure. In polymyxin B1 R= CH_3 and in polymyxin B2, R= H. Dab residue position identifiers are shown.

Therefore, the theoretical PMB derivative structures shown in figure 3.10 demonstrate modifications to the Dab-5 residue. In their 1998 paper, Weinstein and colleagues investigated selective modifications of PMB to give tetra-boc derivatives, with antimicrobial activity of the derivatives also investigated (64). As part of this work, Weinstein *et al.* protected the most reactive amine group via protonation with a strong acid, whilst other free amine groups were BOC protected. Of the tetra-boc derivatives they synthesised, the structure with the protonated amine group at position Dab-5 (most reactive) was abundant (64). Furthermore, recent extensive investigative work by Gallargo-Godoy *et al.* concerning the antimicrobial action of PMB analogues alluded to relative importance of Dab residue position for the maintenance of antimicrobial function (65). They demonstrated Dab-5 and Dab-9 alteration had the greatest effect on PMB potency (Dab-5 more so), whereas Dab-8 and Dab-3 alterations had minimal effect (65).

3.4.3 Methacryloyl Chloride Experiments

3.4.3.1 Synthesis of polymerisable polymyxin (p-PMB_{MC})

a. General overview

Carl Schotten was a German chemist who, along with Eugen Baumann, described the Schotten–Baumann reaction in 1884 (66). It was described as a method to circumvent the formation of carboxylic acids formed via OH^- attack on acyl chlorides during the formation of amides from acyl chlorides and amines in the presence of base (base added to neutralise the HCl formed) (67). The method necessitates the use of a two-phase system of water and DCM. Figure 3.12 shows a simplified schematic of a Schotten-Baumann reaction.

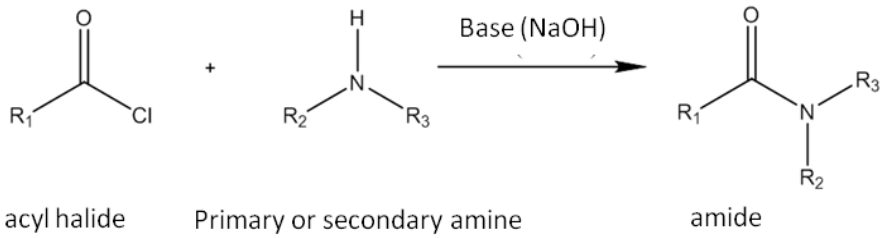

Figure 3.12*:* Simplified schema of a Schotten-Baumann reaction.

Schotten-Baumann conditions are regularly used by polymer chemistry groups as a reliable way of synthesising specialist monomers (68,69). For example, in their 2004 paper Emilitri and colleagues used Schotten-Baumann conditions to synthesise two bisarylamide monomers (for subsequent polymerisation into polymers containing disulphide linkages on their backbone) (68), demonstrating successful monomer synthesis, and subsequent polymer assembly, from a cystamine dihydrochloride and acryloyl chloride reaction. Moreover, in 2010 Boehner *et al.* achieved high yields of acrylamide from the coupling of an amine and acryloyl chloride under Schotten-Baumann conditions as part of a complex process to graft gel spots of a tetrafluorophenol polymer onto glass (69).

Similarly, the method used to synthesise p-PMB_{MC} via reaction of PMB and methacryloyl chloride (section 3.3.5.1) uses Schotten-Baumann conditions to attach methacrylate groups to free PMB amine groups. With the addition of base (1% NaOH), hydrogen chloride (reaction by-product) is neutralised during the reaction. Figure 3.13 shows the mechanism for the methacryloyl chloride and PMB reaction.

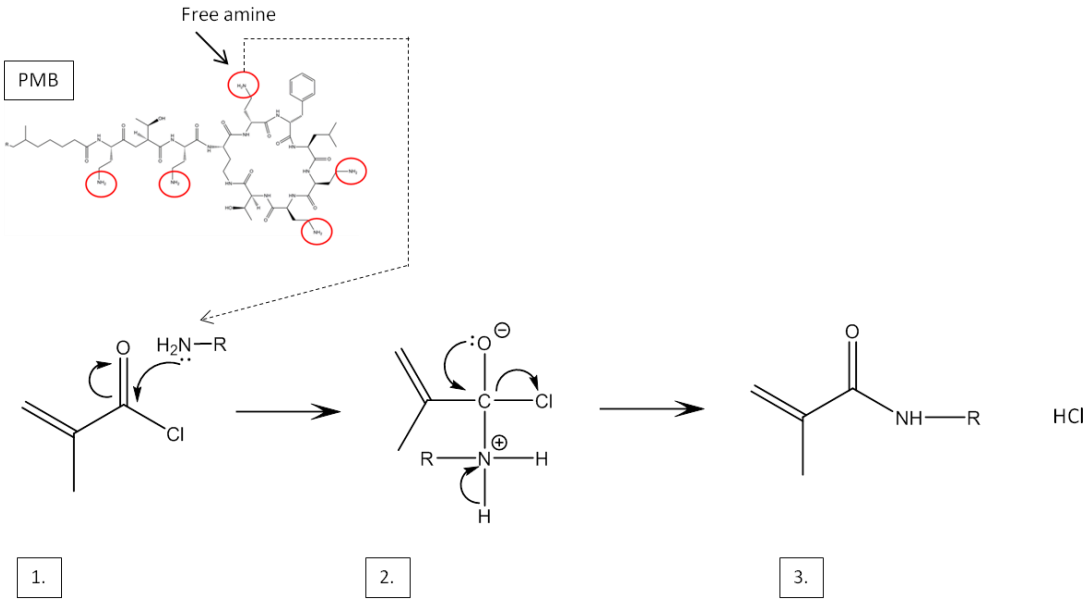

Figure 3.13: Methacryloyl chloride/PMB reaction. **1.)** Nucleophilic attack on carbon by lone pair on nitrogen atom from free PMB amine group (Dab-5 position); **2.)** Reformation of oxygen double bond and loss of chloride, removal of one hydrogen from the nitrogen is seen (removed by chloride ion); **3.)** Formation of product.

b. Mass spectrometry results

The reaction to synthesise polymerisable PMB from methacryloyl chloride and PMB involved extraction steps using DI water and DCM. MS analysis of both extraction phases is shown in figures 3.14 (DI water) and 3.15 (DCM). Results were compared to those obtained for plain PMB (shown in figures 3.7 and 3.9).

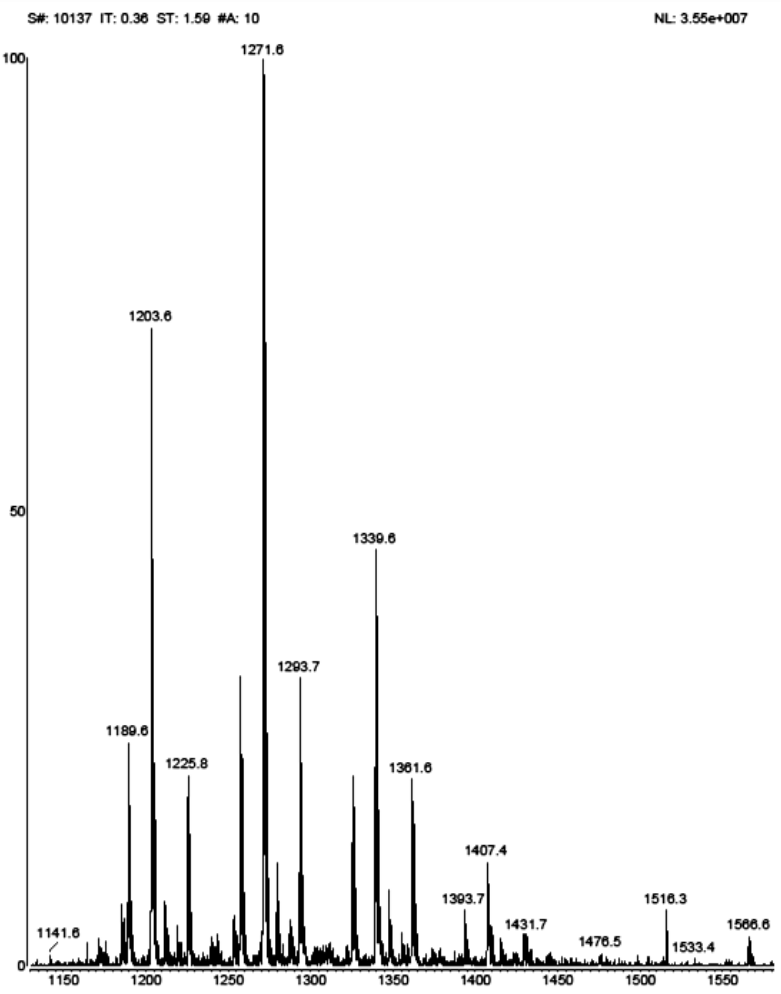

Figure 3.14: Mass spectrometry of aqueous phase of extraction stage of methacryloyl chloride experiments. M/z 1271.6: single substituted PMB; m/z 1203.6: plain PMB with no substitution; m/z 1339.6: double substituted PMB; m/z 1407.4: triple substituted PMB.

Figure 3.14 shows a base peak at m/z of 1271.6 that represented single substituted PMB (1203.6 plus molecular weight of methacrylate group 68). Thereafter, m/z 1203.6 represented plain PMB with no substitution; m/z 1339.6 represented double substituted PMB (1203.6 plus 136); and m/z 1407.4 represented triple substituted PMB (1203.6 plus 204). These results were encouraging as the desired outcome was a dominance of single, double or triple substituted PMB.

MS analysis of DCM extraction phase is shown in figure 3.15.

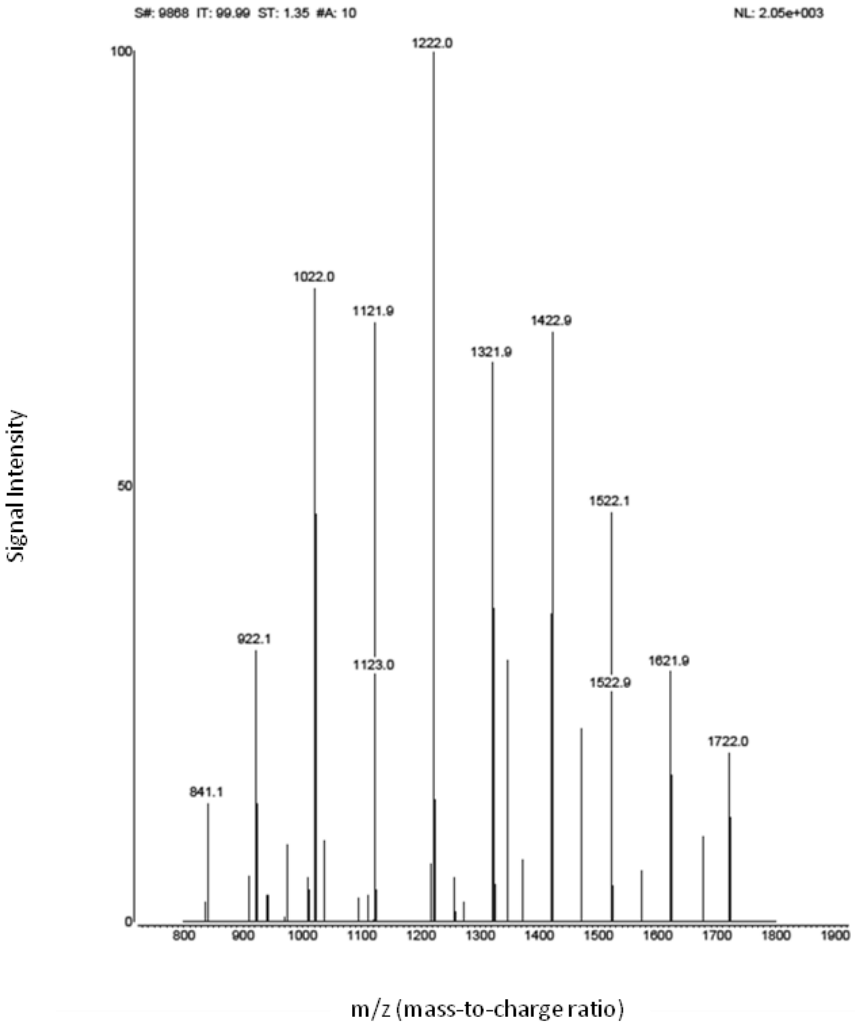

Figure 3.15: Mass spectrometry results from a sample taken from the organic phase of the extraction step (methacryloyl chloride experiments).

There is no evidence of the presence of plain (un-reacted PMB) or PMB with any degree of modification from the MS result shown in figure 3.15. However, of note in this spectrum is the repeating mass increase of m/z 100, from 922.1 to 1722. This distinctive pattern could reflect repeating units of the same molecular weight that occurs with polymer formation. With a molar mass of 100.12 $gmol^{-1}$, a poosibility is the presence of methyl methacrylate in the organic phase.

Mass spectrometry results shown in figures 3.14 and 3.15 suggested p-PMB_{GMA} product was present in the post-extraction aqueous phase. The aqueous phase was then freeze dried overnight giving a fine white powder and the organic phase was discarded. However, further sample purification was indicated to improve outcome from any further experiments in which this modified PMB was used to make a polymer.

c. HPLC analysis

In an attempt to further purify the aqueous phase of this experiment, and obtain product with a greater percentage of di or tri substituted PMB, freeze-dried aqueous extract (10 mg) was dissolved in 2 ml DI water/1 ml MeOH (sonicated) and analysed with HPLC (figure 3.16). Timings of major peaks were noted and fractions were collected from the HPLC run at these times. These fractions were analysed by mass spectrometry and resultant spectra are shown in figures 3.17, 3.18 and 3.19.

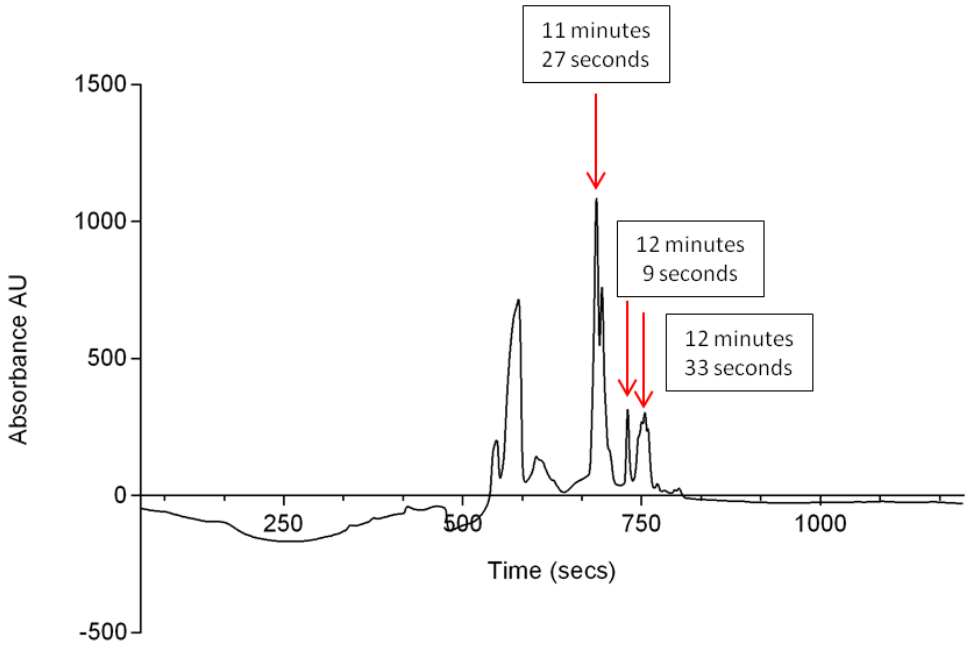

Figure 3.16: HPLC chromatogram for p-PMB_{MC} aqueous phase. Fractions were then siphoned corresponding with the timings of major peaks and analysed by mass spectrometry.

Shown in figure 3.17 is the mass spectrometry data from analysis of a fraction siphoned from the HPLC analysis run at 11 minutes and 27 seconds.

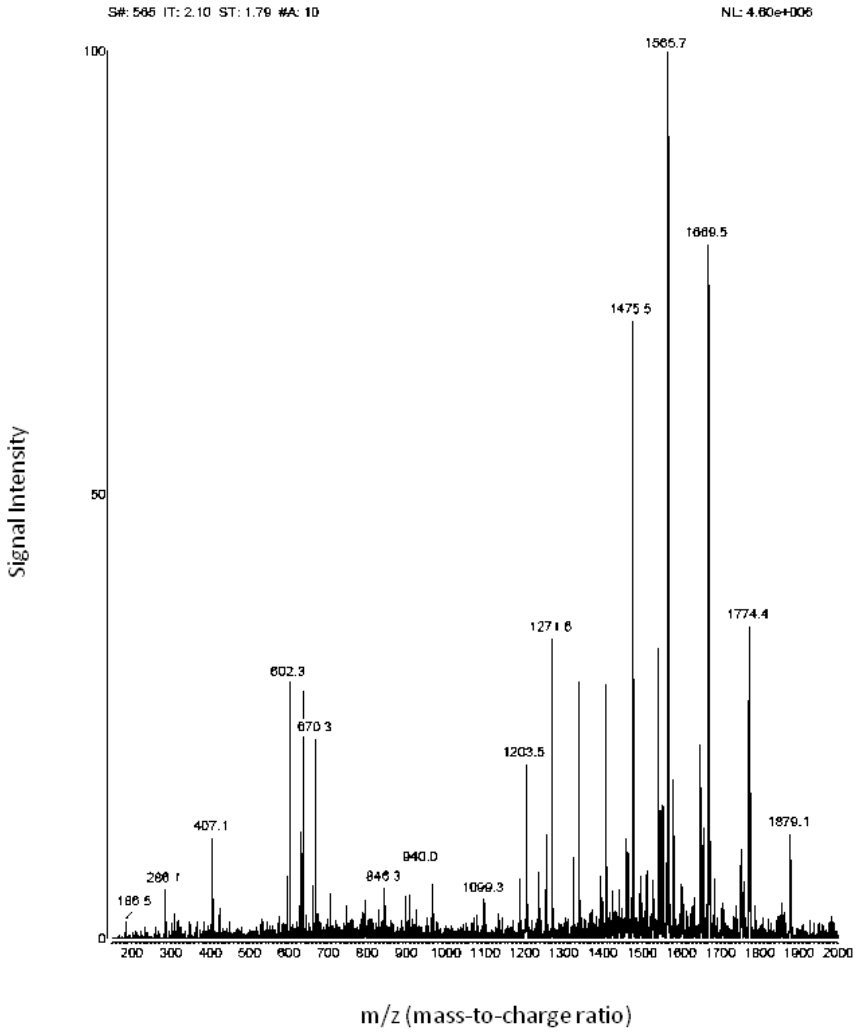

Figure 3.17: Mass spectrometry analysis of product retrieved at 11 minutes, 27 seconds from start of HPLC run.

Major peaks are seen at m/z 1565.7; m/z 1669.5; m/z 1475.5; m/z 1271.8 and m/z 1774.4. Unfortunately mass calculations for PMB methacrylate products from methacryloyl chloride/PMB experiments do not correspond with any of these m/z values. However, minor peaks are seen in the

spectra at m/z 1203.5 and 1271.5, representing un-reacted (plain) PMB and single substituted PMB respectively.

Figure 3.18 shows the mass spectrometry data from analysis of a fraction siphoned from the HPLC analysis run at 12 minutes and 9 seconds.

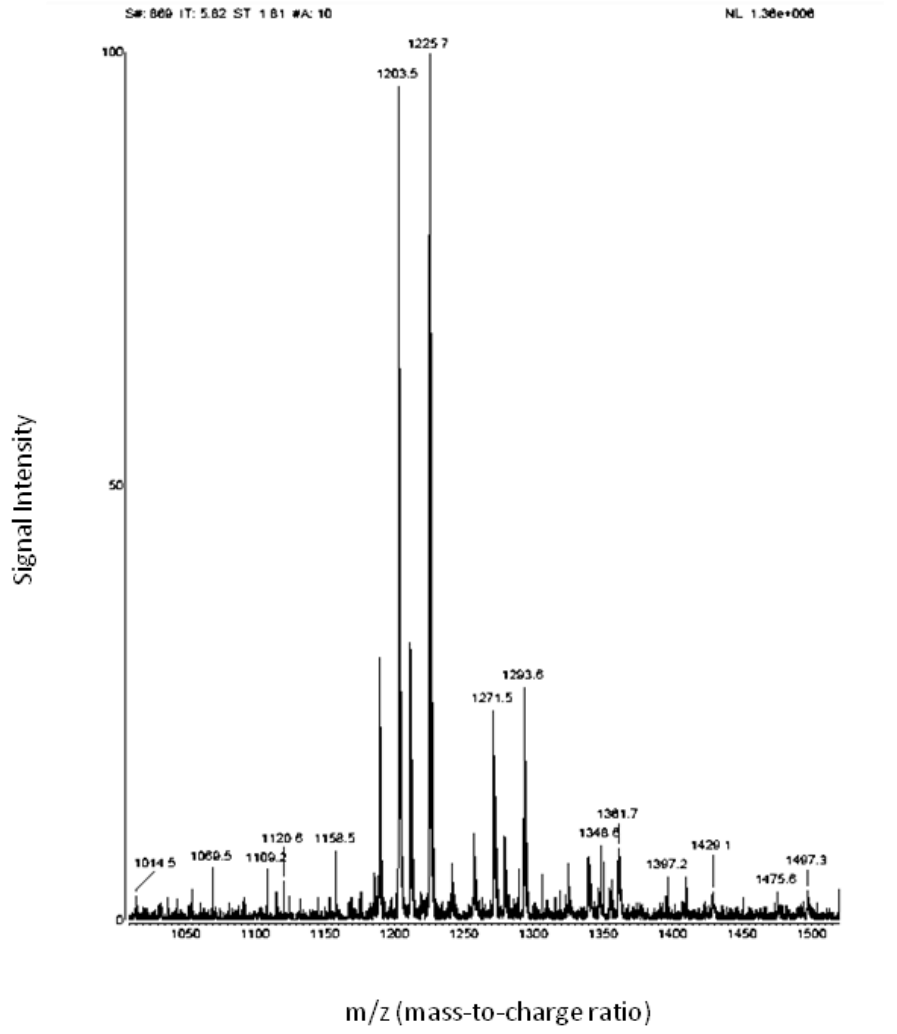

Figure 3.18: Mass spectrometry analysis of product retrieved at 12 minutes, 9 seconds from start of HPLC run.

The base peak at m/z 1225.7 represents unmodified PMB plus sodium and m/z 1203.5 represents unmodified PMB. This particular fraction therefore

contained plain, unmodified PMB (no free amine groups substituted for methacrylate groups).

Shown in figure 3.19 is the mass spectrometry data from analysis of a fraction siphoned from the HPLC analysis run at 12 minutes and 33 seconds.

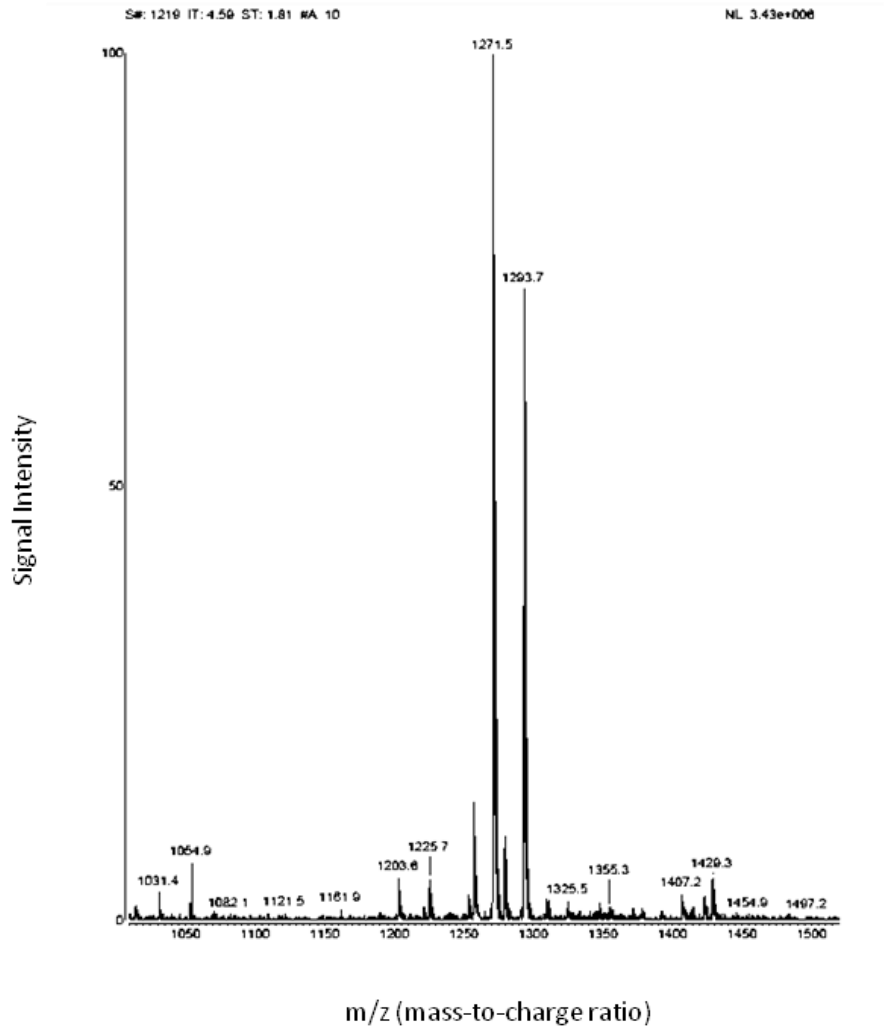

Figure 3.19: Mass spectrometry analysis of product retrieved at 12 minutes 30 seconds from start of HPLC run.

A major peak at m/z 1271.5 is single substituted PMB and m/z 1293 is single substituted PMB plus sodium. Therefore, this fraction contained predominately single substituted PMB.

A significant change in the absorption of UV at 215 nm dependent on the modifications to PMB carried out in these experiments is unlikely. Therefore the peak at 12 minutes 33 seconds on the HPLC spectra shown in figure 3.16 likely corresponds, as the size of the peak suggests, to the least abundant product in the sample tested. The mass spectrometry analysis results shown in figures 3.16, 3.17 and 3.19 demonstrated spectra pertaining to the peak at 12 minutes 33 seconds was the only fraction that showed desired product in significant abundance. Therefore, the majority of the sample analysed by HPLC contained undesired products.

In conclusion, although it would seem product was in the aqueous phase and that further purification may be possible, results did not show the abundance of single or double substituted PMB that would be desirable to take forward to the bulk polymer stage. Therefore, an alternative strategy to the synthesis of a modified p-PMB was investigated and reactions with glycidyl methacrylate were undertaken and p-PMB_{MC} was not taken forward to the polymerisation stage.

3.4.4 Glycidyl methacrylate experiments

3.4.4.1 Polymerisable polymyxin B synthesis

a. General overview

Glycidyl methacrylate is an epoxide. Epoxides are three-membered cyclic ethers and exhibit a high degree of ring strain and therefore react readily with nucleophiles in ring-opening reactions that give rise to more stable bond angles (67,70,71). Examples of epoxides and their reactions with nucleophiles are shown in figure 3.20.

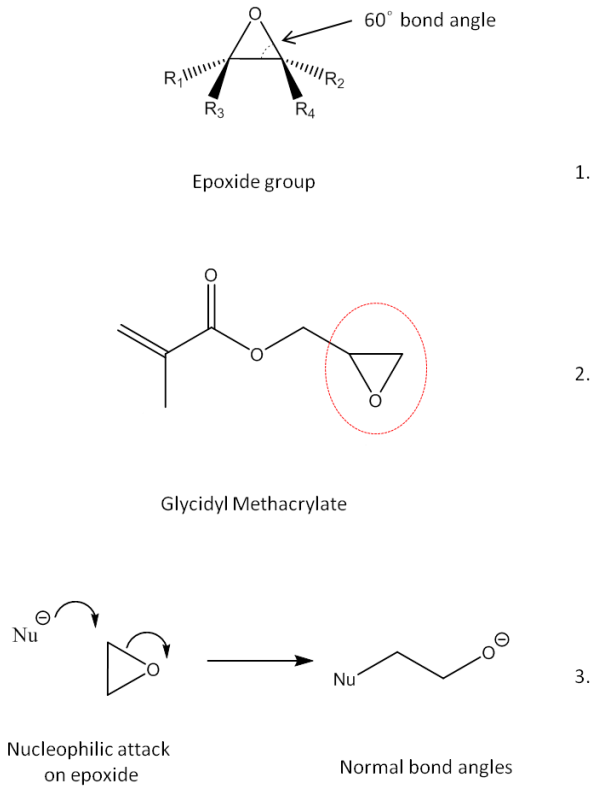

Figure 3.20: Epoxides and their reaction with nucleophiles. **1.)** Example of an epoxide showing 60° bond angles. This bond arrangement is different from the 109° bond angle seen in an ideal tetrahedron, therefore a high degree of ring strain is present (67). **2.)** Structure of glycidyl methacrylate, the epoxide ring is circled. **3.)** The reaction between an epoxy and a nucleophile containing a hydroxyl, carboxyl or amine group (epoxide ring opening reactions). Normal bond angles are restored during this reaction. (Diagram 3 adapted from (67), page 435).

The reactivity of epoxides is exploited by polymer chemists to functionalise polymers and several extensive reviews on the post-polymerisation functionalisation of polymers indicate the usefulness of epoxides for production of diverse polymer end-products (72–74). For example, In their 2013 paper, McEwen and colleagues synthesised a range of functionalised poly (glycidyl methacrylate) polymers via epoxide ring opening reactions using primary and secondary amines (71). A further example is the work of

Potén *et al.*, who described the fluorophore functionalisation of glycidyl methacrylate based monoliths for the detection of hydrogen peroxide in their 1996 paper (75). More recently, Kimmins *et al.* successfully immobilised the analytical enzyme proteinase K via a ring-opening reaction following amine functionalisation of glycidyl methacrylate emulsion-templated porous polymers (76).

In this experimental section the ring opening of glycidyl methacrylate epoxy group via nucleophilic attack by an amine was used to successfully substitute methacrylate groups into the PMB structure (figure 3.21).

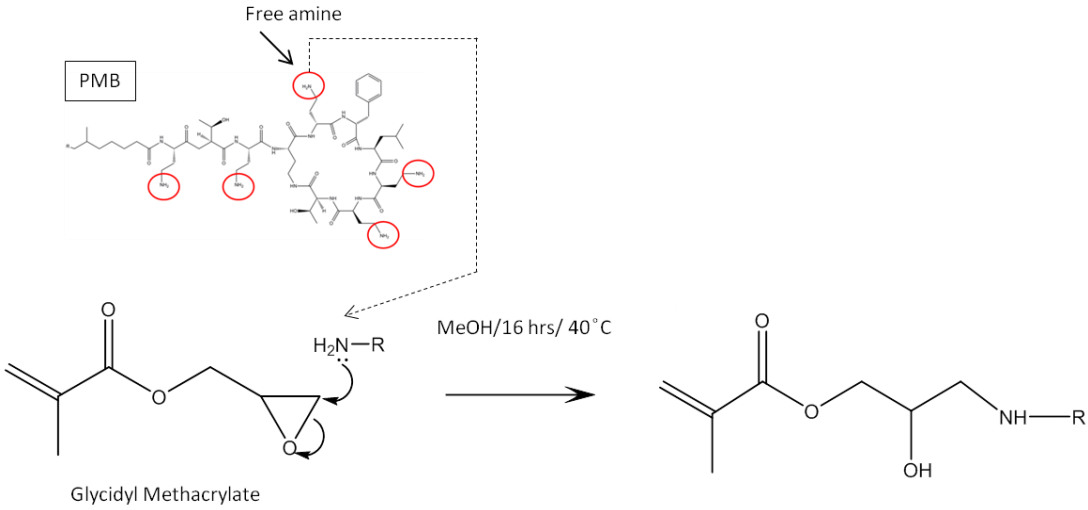

Figure 3.21: Schematic of the reaction to synthesised polymerisable polymyxin B using glycidyl methacrylate. Epoxide ring comes under nucleophilic attack by free amine group of PMB (Dab-5 position) leading to opening of ring and adoption of a more stable bond angle configuration.

b. Mass spectrometry results

Shown in figures 3.22 and 3.23 are the MS spectra from analysis of the resultant product from glycidyl methacrylate /PMB experiments. Figure 3.22 shows initial analysis of a 1:1 molar ratio reaction of PMB/glycidyl methacrylate.

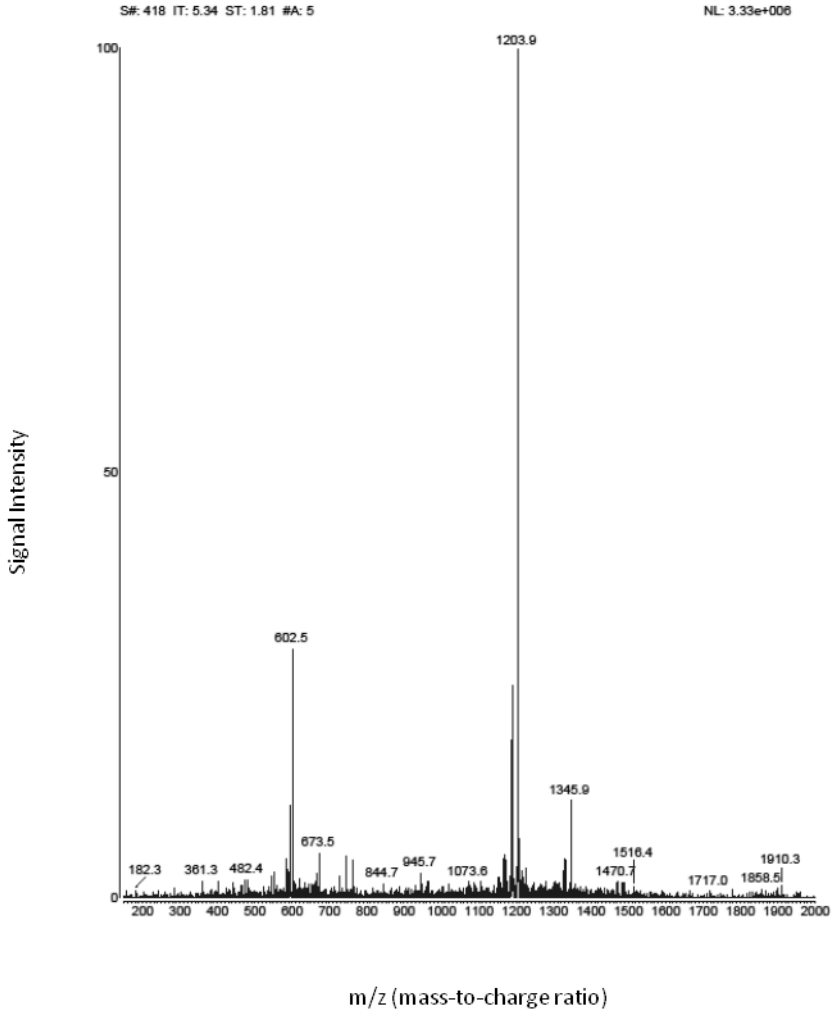

Figure 3.22: Mass spectrometry of plain polymyxin B sulphate reacted with glycidyl methacrylate to give a polymerisable PMB (using a 1:1 molar ratio GMA:PMB). M/z 1203.9 base peak: plain PMB (no methacrylate group attached); m/z 1345.9: single substituted PMB (substitution of one amine group to methacrylate group).

Results demonstrated in figure 3.22 were disappointing. The abundant peak at m/z of 1203.9 was associated with as-purchased PMB, suggesting no reaction of free amine groups with glycidyl methacrylate. A smaller peak relative to this base peak at m/z 1345.9 corresponded to the expected molecular weight of PMB plus one methacrylate group. The experiment to produce a p-PMB using reaction with glycidyl methacrylate was therefore

repeated using an increased concentration of glycidyl methacrylate to give the molar ratio of PMB : GMA of 1:2. Figure 3.23 shows analysis of a 1:2 molar ratio reaction of PMB/glycidyl methacrylate.

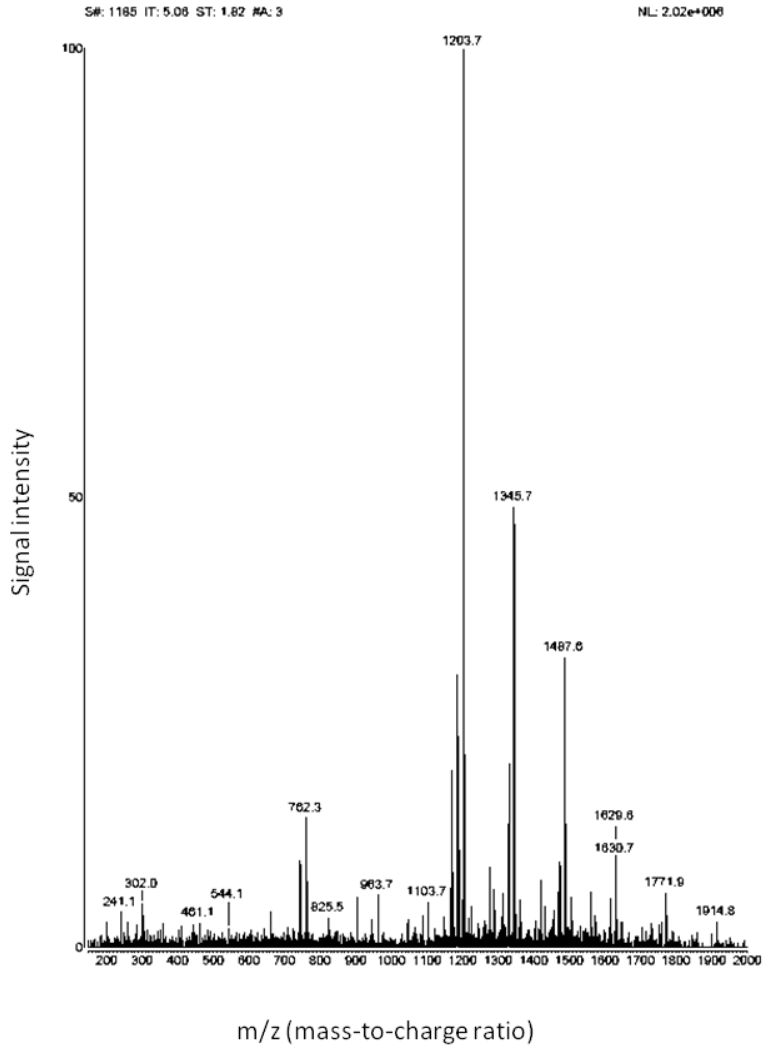

Figure 3.23: Mass spectrometry of plain polymyxin B sulphate reacted with glycidyl methacrylate to give a polymerisable PMB (using a 1:2 (PMB: GMA) molar ratio). M/z 1203.7: non-substituted PMB; m/z 1345.7: single substituted PMB; m/z 1487.6: double substituted PMB.

Results shown in figure 3.23 were more encouraging than those shown in figure 3.22. The base peak remained representative of plain as-purchased PMB (m/z 1203.7); however, the species in secondary abundance (m/z 1345.7) represented a double substituted PMB (two amine groups modified with methacrylate functionality). The risk with this approach is the conversion of too many free amine groups; as discussed previously, the preservation of at least 3 amino groups is vital to ensure PMB retains LPS binding ability (11). The spectrum in figure 3.23 demonstrated the presence of PMB with more than the desired number of amine groups substituted: m/z 1629.5 represented a triple substituted species and m/z 1771.9 represented a quadruple substituted species. However, these are less abundant in comparison to the double substituted species.

c. NMR results

Glycidyl methacrylate structure and predicted ^{1}H NMR spectra are shown in figure 3.24. Thereafter; ^{1}H NMR results are shown for plain as-purchased glycidyl methacrylate (figure 3.25).

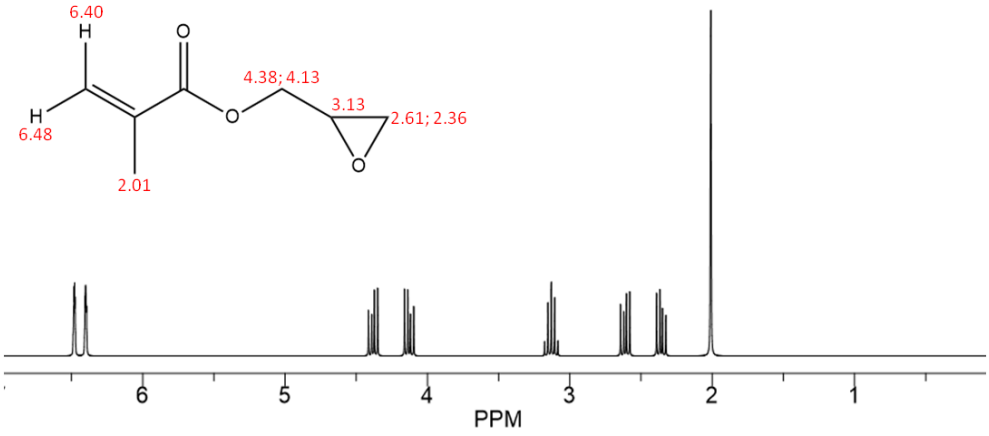

Figure 3.24: Predicted ^{1}H NMR for glycidyl methacrylate as generated by ChemDraw®

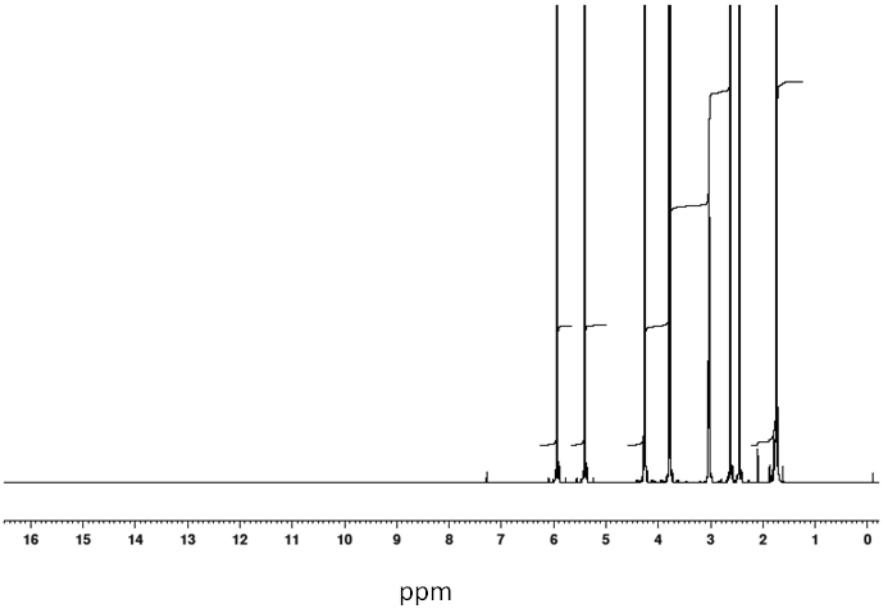

Figure 3.25: ^{1}H NMR (500MHz, D_2O) for glycidyl methacrylate. δ = 1.7474 (t, 3H); δ =2.45 (q, 1H); δ =2.62 (t, 1H); δ = 3.03 (m, 1H); δ = 3.787 (q, 1H); δ = 4.264 (d,d, 1H); δ = 5.407 (s, 1H); δ = 5.938 (s, 1H).

Shown in figure 3.26 is the ^{1}H NMR analysis of product from PMB/glycidyl methacrylate reaction to synthesise a polymerisable polymyxin B (p-PMB_{GMA}).

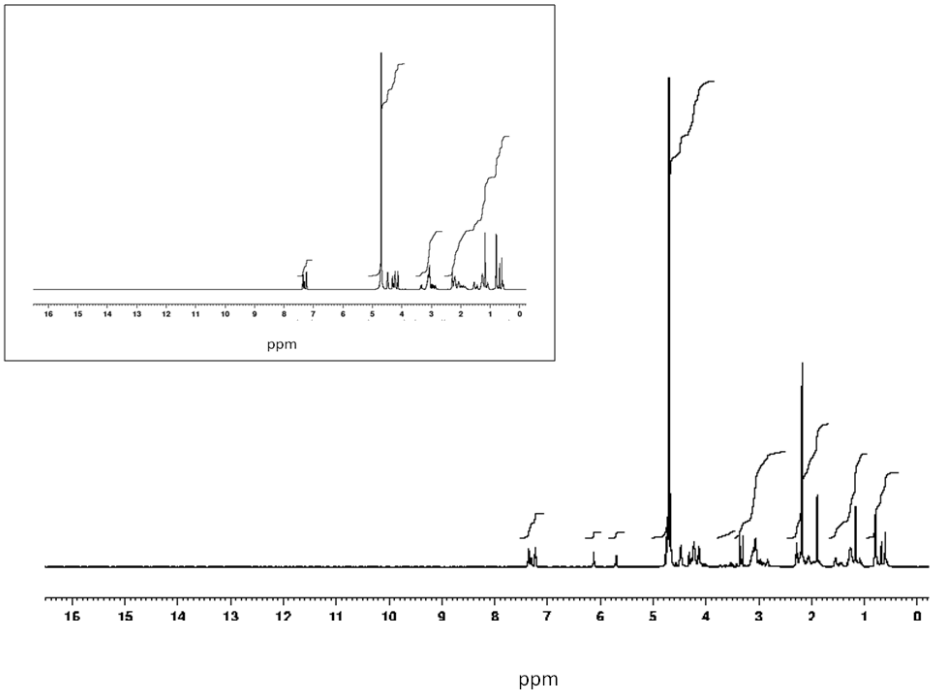

Figure 3.26: ^{1}H NMR (500 MHz, D_2O) spectra of p-PMB_{GMA} (from PMB /GMA reaction 1:2 molar ratio) for comparison, the inlay shows NMR spectra for plain PMB. δ= 0.893ppm (m,4H); δ= 1.31 ppm (m, 15H); δ= 1.967 ppm (s, 30H); δ= 2.691 ppm (q, 5H); δ= 2.855 ppm (t, 5H); δ= 3.39 ppm (s, 8H); δ= 3.474 ppm (d,d, 5H); δ= 3.606 ppm (m, 3H); δ= 3.99 ppm (q,3H); δ= 4.155 ppm (m, 5H); δ= 4.23 ppm (m, 5H); δ= 4.495 ppm (d, 3H); δ= 4.52 ppm (d, 3H); δ= 5.671 ppm (d, 4H); δ= 6.157 ppm (s, 4H); δ= 7.299 ppm (m, 5H).

Shown in figure 3.26 are additional signals at ~ 5.7 and 6.2 ppm in the ^{1}H NMR spectra from p-PMB_{GMA} compared to that of the plain, as purchased PMB. These signals represent a methacrylate group. These signals are also absent from the predictive ^{1}H NMR spectra for plain PMB1 shown in figure 3.8. The remaining NMR spectra from the p-PMB_{GMA} shown in figure 3.26 is comparable to that of the plain PMB.

Overall, NMR analysis supported mass spectrometry analysis findings and showed modification of PMB structure by the addition of methacrylate groups had been achieved. With encouraging mass spectrometry and NMR

data this synthesised p-PMB_{GMA} was taken forward and integrated into a polymer.

3.4.4.2 p-PMB_{GMA} composite Polymer synthesis and LPS binding Studies

Having established the attachment of one or more methacrylate groups to PMB via the glycidyl methacrylate reaction, p-PMB_{GMA} was used as a monomer to synthesise a p-PMB_{GMA} polymer. Two p-PMB_{GMA} polymers were synthesised, denoted polymer A and B. Furthermore, matched polymers to A and B were synthesised that did not contain p-PMB_{GMA}. The composition of these polymers is shown in table 3.2.

Table 3.2: Composition of polymers used in glycidyl methacrylate experiments. (Polymer (m) denoting the matched polymer to that particular p-PMB_{GMA} polymer).

	p-PMB_{GMA} mg (mmol)	**AAm mg (mmol)**	**MBAam mg (mmol)**
Polymer A	100 (0.74)	216 (3)	56 (0.3)
Matched polymer A	Nil	1200 (16)	300 (2)
Polymer B	100 (0.74)	144 (2)	84 (0.5)
Matched Polymer B	Nil	918 (13)	540 (3.5)

Thereafter, a series of binding experiments to test polymer LPS binding capability were carried out. Binding isotherms were obtained from filtrate analysis of samples incubated with the p-PMB_{GMA} polymers (A and B) and their corresponding matched polymers. All polymers (10 mg) were tested over a FTIC-LPS concentration range of 0.1 to 10 mcg ml^{-1}. Shown in figure 3.27 is a typical calibration curve (post-filtering) obtained for analysis of purchased FITC-LPS.

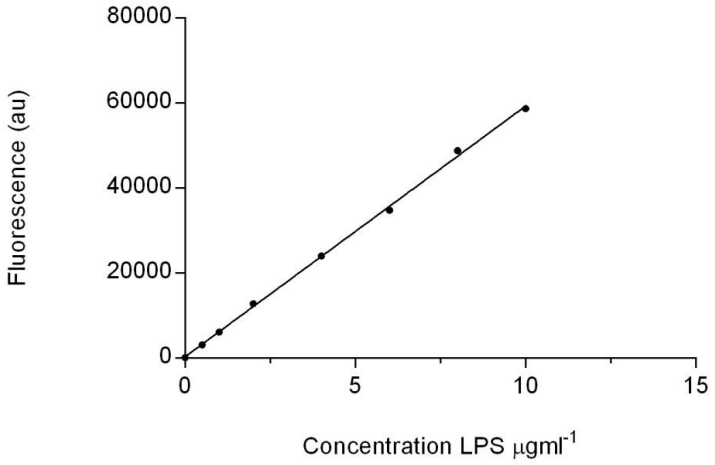

Figure 3.27: FITC-LPS calibration curve used for p-PMB_{GMA} and plain (matched) polymer binding studies. y=58992.9x + 375; R2= 0.999.

Figure 3.28 shows the binding isotherms from analysing filtrate following incubation of p-PMB_{GMA} polymer A compared to matched polymer A.

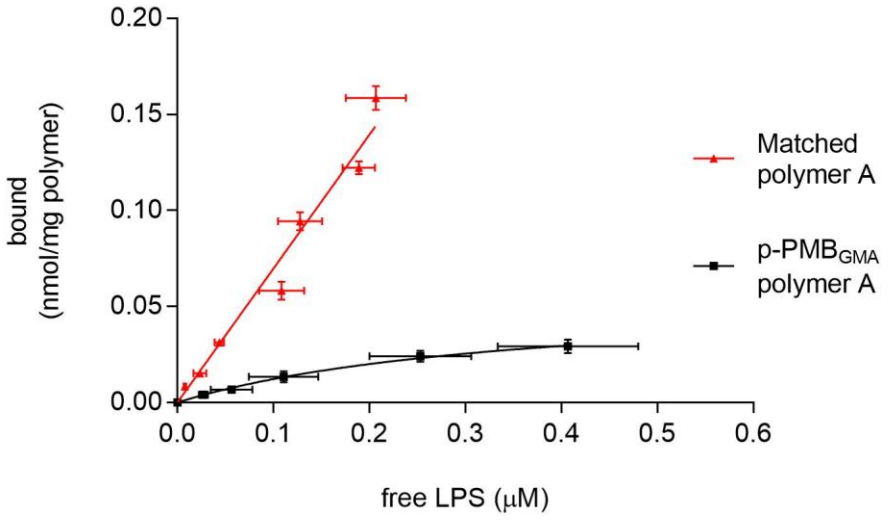

Figure 3.28: Binding isotherms showing amount of FITC labelled Escherichia coli 0111:B4 LPS bound to 1 mg of polymer at differing concentrations of LPS for p-PMB_{GMA} Polymer A and matched polymer A.

Note the straight isotherm seen for the matched Polymer A suggesting tendency toward non–specific binding (B_{max} and K_d ambiguous). However, a curve is seen in the isotherm depicting binding in the p-PMB polymer system with a B_{max} value of 0.055 nmol/mg polymer and K_d of 0.354 µM.

The curve obtained for Polymer A, albeit slight, was encouraging in comparison to the straight line seen for the control polymer (matched polymer A) suggesting a degree of specific binding of LPS to the PMB polymer. Considering the main composite difference between these two polymers is the presence of p-PMB_{GMA} , results initially indicate a polymer had been synthesised capable of binding to LPS. However, the binding performance figures are lower than expected for an efficient p-PMB polymer system considering the affinity of PMB for LPS and suggest a re-design of the polymer was necessary or the initial synthesis of p-PMB_{GMA} was the issue.

Figure 3.29 shows the binding isotherms from analysing filtrate following incubation of p-PMB$_{GMA}$ polymer B compared to matched polymer B.

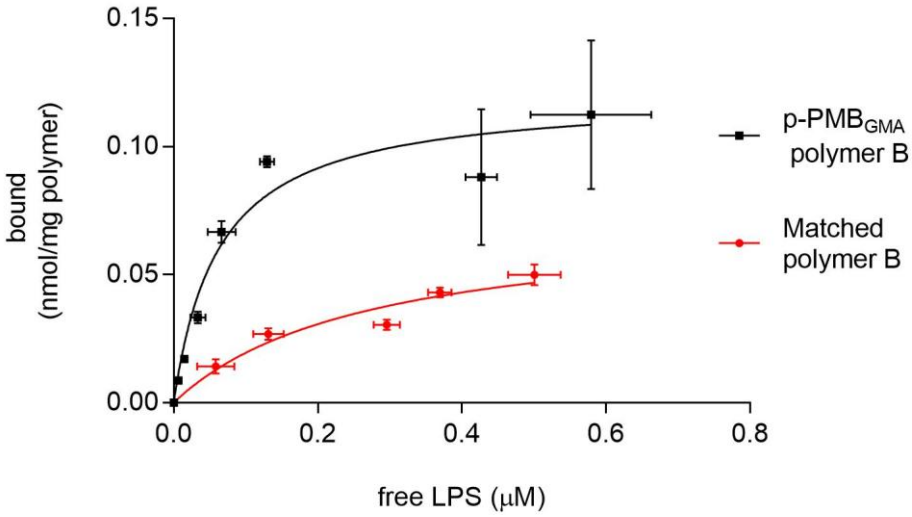

Figure 3.29: Binding isotherms showing amount of FITC labelled *Escherichia coli* 0111:B4 LPS bound to 1 mg of polymer at differing concentrations of LPS for p-PMB$_{GMA}$ Polymer B and matched polymer B.

The binding data shown in figure 3.29 was more promising than that for Polymer A. For p-PMB polymer B a curved binding isotherm was demonstrated with a derived apparent B_{max} value of 0.133 nmol/mg polymer and apparent K_d of 0.074 μM. Figure 3.30 shows a comparison of the binding isotherms for both p-PMB$_{GMA}$ polymers.

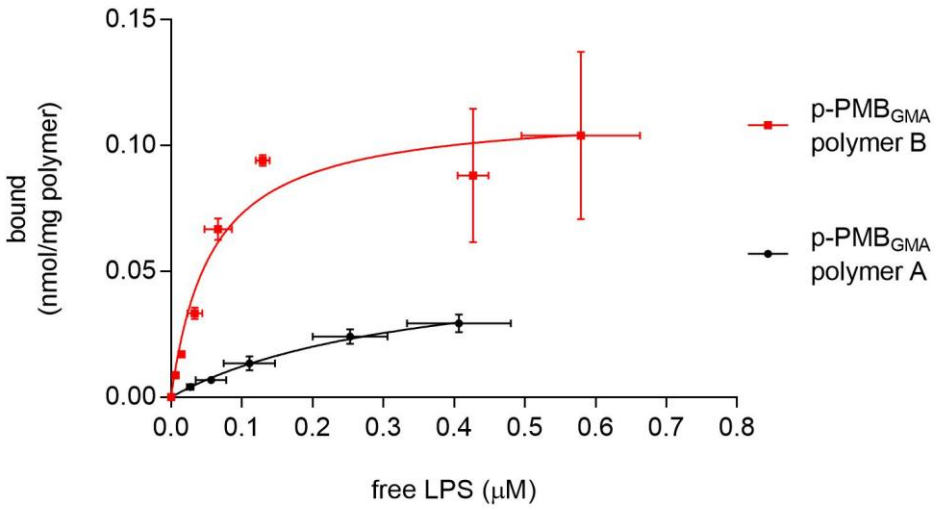

Figure 3.30: Comparison of LPS binding of both tested p-PMB$_{GMA}$ polymers. Both p-PMB$_{GMA}$ containing polymers demonstrate curved binding isotherms.

There is a marked difference in the binding performance between the polymers containing p-PMB$_{GMA}$. The B_{max} values for p-PMB$_{GMA}$ Polymers A and B (0.069 and 0.133 nmol per mg polymer, respectively) show a significant difference in the binding site density between the two polymers. The K_d values are also different, showing that p-PMB$_{GMA}$ Polymer B, with a lower K_d of 0.074 µM, has higher affinity for LPS than p-PMB$_{GMA}$ Polymer A with a K_d 0.327 µM.

This is interesting considering the mass of p-PMB$_{GMA}$ used in the synthesis of both Polymer A and Polymer B was the same. However, both polymers were designed with different degrees of crosslinking, and this variable may explain the observed difference in polymer binding performance. The greater degree of crosslinking seen in Polymer B (AAm: MBAam 4:1) compared to Polymer A (10:1) ensured the successful integration of p-PMB$_{GMA}$ into the polymer matrix and therefore more reliable availability of PMB/LPS binding sites. Furthermore, increased crosslinking may have decreased steric hindrance, allowing the large LPS molecules greater access to PMB binding sites. Given that the initial interaction of LPS and PMB is

electrostatic, the relative surface charge of the two polymers was a determinant in this binding performance difference. However, AAm and MBAam are non-ionic monomers and polyacrylamide matrix is un-charged; if desired charge is often introduced to polyacrylamide with secondary monomers, acrylic acid for example confers a negative charge (77). Conversely, introducing p-PMB_{GMA} as a co-monomer introduced a positive charge (with valence dependent on the degree of methacrylate substitution of the p-PMB_{GMA}). During polymerisation it was hypothesised that p-PMB_{GMA} with the greater number of substituted methacrylate groups would be integrated into the crosslinked polymer matrix before those with a lower number of methacrylate groups. Therefore, p-PMB_{GMA} with less methacrylate substitution (and hence more available amide groups, and a greater positive charge) would be available for LPS binding. A reduction in crosslinking would therefore increase the chance of a polymer with only p-PMB_{GMA} with lower LPS binding ability integrated as a co-monomer.

The performance of the matched (control) Polymers A and B is also different. Matched polymer A demonstrated a straight binding isotherm compared to the curved isotherm generated by matched polymer B. Similar to its p-PMB_{GMA} counterpart, matched Polymer B has a higher degree of crosslinking when compared to matched polymer A (acrylamide to MBA ratios of 3:1 compared to 8:1) suggesting that despite the lack of integrated p-PMB_{GMA} the polymer still demonstrated LPS binding ability dependent on degree of crosslinking.

3.5 Chapter conclusions

3.5.1 General conclusions

The overarching aim was to produce a polymer from a custom-made monomer of modified PMB. The staged approach included the optimisation of two key processes, firstly the successful modification of PMB structure to attach methacrylate groups and secondly, the integration of modified PMB into a polymer.

The experiments to synthesise p-PMB via the methacryloyl chloride route yielded product with predominance of PMB with high degrees of methacrylate substitution and were therefore not taken onto the polymerisation stage. Experiments to synthesise p-PMB focused on controlled substitution of methacrylate for amine groups as interaction of PMB and LPS depends on the presence of at least two PMB amine groups (11,30,31). Therefore, the polymerisable polymyxin from the glycidyl methacrylate experiments was further utilised in p-PMB_{GMA} polymer synthesis.

These polymers were tested to assess binding capability to LPS and binding studies showed the potential specific binding of LPS to this bulk polymer due to integration of p-PMB_{GMA} into the polymer structure. The p-PMB_{GMA} polymer with the best performance in these studies demonstrated a B_{max} of 0.133 nmol/mg polymer and a K_d of 0.074 µM.

3.5.2 Rationale for next chapter

Moving forward, the aim was to produce an imprinted p-PMB polymer bead that would potentially act as a MIP for LPS detection. However, it has been demonstrated that LPS is not a suitable template for conventional molecular imprinting strategies, therefore techniques that circumvent problems associated with the imprinting of biological macromolecules

were needed. One such approach was to localise the template at a surface via chemical immobilisation at a solid-solvent interface (surface imprinting on a solid support) and this was explored in chapter two. Another approach was molecular imprinting via self-assembly at a solvent-solvent interface. Therefore, a solvent-solvent interface system designed to facilitate both the self assembly stage of molecular imprinting and the polymerisation stage was needed. This work involved the integration of a microfluidic system (providing the solvent-solvent interface) into a microwave delivery system (providing the polymerisation stage).

Microfluidic system development is described in chapter four and the microwave delivery system is described in the final experimental chapter, chapter five.

3.6 References

1. Ainsworth GC, Brown AM, Brownlee G. 'Aerosporin', an Antibiotic Produced by Bacillus aerosporus Greer. Nature. 1947 Aug 23;160(4060):263–263.

2. Langlykke RGBF. Antibiotic activity of Bacillus polymyxa. J Bacteriol. 1947 Jul 1;54(1):24.

3. Newton BA. THE PROPERTIES AND MODE OF ACTION OF THE POLYMYXINS. Bacteriol Rev. 1956 Mar;20(1):14–27.

4. Berglund NA, Piggot TJ, Jefferies D, Sessions RB, Bond PJ, Khalid S. Interaction of the Antimicrobial Peptide Polymyxin B1 with Both Membranes of E . coli : A Molecular Dynamics Study. PLOS Comput Biol. 2015 Apr 17;11(4):e1004180.

5. Mares J, Kumaran S, Gobbo M, Zerbe O. Interactions of Lipopolysaccharide and Polymyxin Studied by NMR Spectroscopy. J Biol Chem. 2009 Apr 24;284(17):11498–506.

6. Thomas CJ, Surolia A. Kinetics of the interaction of endotoxin with polymyxin B and its analogs: a surface plasmon resonance analysis. FEBS Lett. 1999 Feb 26;445(2–3):420–4.

7. Thomas CJ, Surolia N, Surolia A. Surface plasmon resonance studies resolve the enigmatic endotoxin neutralizing activity of polymyxin B. J Biol Chem. 1999 Oct 15;274(42):29624–7.

8. Domingues MM, Inácio RG, Raimundo JM, Martins M, Castanho MARB, Santos NC. Biophysical characterization of polymyxin B interaction with LPS aggregates and membrane model systems. Biopolymers. 2012;98(4):338–44.

9. Pristovsek P, Kidric J. Solution structure of polymyxins B and E and effect of binding to lipopolysaccharide: an NMR and molecular modeling study. J Med Chem. 1999 Nov 4;42(22):4604–13.

10. Pristovsek P, Kidric J. The search for molecular determinants of LPS inhibition by proteins and peptides. Curr Top Med Chem. 2004;4(11):1185–201.

11. Velkov T, Thompson PE, Nation RL, Li J. Structure—Activity Relationships of Polymyxin Antibiotics. J Med Chem. 2010 Mar 11;53(5):1898–916.

12. Domingues MM, Castanho MARB, Santos NC. rBPI 21 Promotes Lipopolysaccharide Aggregation and Exerts Its Antimicrobial Effects by (Hemi)fusion of PG-Containing Membranes. PLOS ONE. 2009 Dec 22;4(12):e8385.

13. Howe J, Andrä J, Conde R, Iriarte M, Garidel P, Koch MHJ, et al. Thermodynamic Analysis of the Lipopolysaccharide-Dependent Resistance of Gram-Negative Bacteria against Polymyxin B. Biophys J. 2007 Apr 15;92(8):2796–805.

14. Opal SM, Scannon PJ, Vincent JL, White M, Carroll SF, Palardy JE, et al. Relationship between plasma levels of lipopolysaccharide (LPS) and LPS-binding protein in patients with severe sepsis and septic shock. J Infect Dis. 1999 Nov;180(5):1584–9.

15. Powers J-PS, Hancock REW. The relationship between peptide structure and antibacterial activity. Peptides. 2003 Nov;24(11):1681–91.

16. Falagas ME, Rafailidis PI, Matthaiou DK. Resistance to polymyxins: Mechanisms, frequency and treatment options. Drug Resist Updat. 2010 Aug;13(4–5):132–8.

17. Zavascki AP, Goldani LZ, Li J, Nation RL. Polymyxin B for the treatment of multidrug-resistant pathogens: a critical review. J Antimicrob Chemother. 2007 Dec 1;60(6):1206–15.

18. Teuber M, Bader J. Action of polymyxin B on bacterial membranes. Arch Microbiol. 1976 Aug 1;109(1–2):51–8.

19. Rosenthal KS, Storm DR. Disruption of the Escherichia coli outer membrane permeability barrier by immobilized polymyxin B. J Antibiot (Tokyo). 1977 Dec;30(12):1087–92.

20. Hancock RE. Peptide antibiotics. The Lancet. 1997 Feb 8;349(9049):418–22.

21. Clausell A, Garcia-Subirats M, Pujol M, Busquets MA, Rabanal F, Cajal Y. Gram-negative outer and inner membrane models: insertion of cyclic cationic lipopeptides. J Phys Chem B. 2007 Jan 25;111(3):551–63.

22. Meredith JJ, Dufour A, Bruch MD. Comparison of the structure and dynamics of the antibiotic peptide polymyxin B and the inactive nonapeptide in aqueous trifluoroethanol by NMR spectroscopy. J Phys Chem B. 2009 Jan 15;113(2):544–51.

23. Bruch MD, Cajal Y, Koh JT, Jain MK. Higher-Order Structure of Polymyxin B: The Functional Significance of Topological Flexibility. J Am Chem Soc. 1999 Dec 1;121(51):11993–2004.

24. Morrison DC, Jacobs DM. Binding of polymyxin B to the lipid A portion of bacterial lipopolysaccharides. Immunochemistry. 1976 Oct;13(10):813–8.

25. Kanazawa K, Sato Y, Ohki K, Okimura K, Uchida Y, Shindo M, et al. Contribution of each amino acid residue in polymyxin B(3) to antimicrobial and lipopolysaccharide binding activity. Chem Pharm Bull (Tokyo). 2009 Mar;57(3):240–4.

26. Evans ME, Feola DJ, Rapp RP. Polymyxin B Sulfate and Colistin: Old Antibiotics for Emerging Multiresistant Gram-Negative Bacteria. Ann Pharmacother. 1999 Sep 1;33(9):960–7.

27. Tsuzuki H, Tani T, Ueyama H, Kodama M. Lipopolysaccharide: neutralization by polymyxin B shuts down the signaling pathway of nuclear factor kappaB in peripheral blood mononuclear cells, even during activation. J Surg Res. 2001 Sep;100(1):127–34.

28. Bl J, S S, M CN, Aj K, Bj P. Polymyxin-B stimulates tumor necrosis factor-alpha production by human peripheral blood mononuclear cells. Int J Artif Organs. 1998 May;21(5):269–73.

29. Rifkind D. Studies on the interaction between endotoxin and polymyxin B. J Infect Dis. 1967 Dec;117(5):433–8.

30. Clausell A, Pujol M, Alsina MA, Cajal Y. Influence of polymyxins on the structural dynamics of Escherichia coli lipid membranes. Talanta. 2003 Jun 13;60(2–3):225–34.

31. Vaara M. Polymyxin B nonapeptide complexes with lipopolysaccharide. FEMS Microbiol Lett. 1983 Apr;18(1–2):117–21.

32. Storm DR, Rosenthal KS, Swanson PE. Polymyxin and related peptide antibiotics. Annu Rev Biochem. 1977;46:723–63.

33. Vaara M, Vaara T. Sensitization of Gram-negative bacteria to antibiotics and complement by a nontoxic oligopeptide. Nature. 1983 Jun 9;303(5917):526–8.

34. Viljanen P, Vaara M. Susceptibility of gram-negative bacteria to polymyxin B nonapeptide. Antimicrob Agents Chemother. 1984 Jun;25(6):701–5.

35. Vaara M, Siikanen O, Apajalahti J, Fox J, Frimodt-Møller N, He H, et al. A Novel Polymyxin Derivative That Lacks the Fatty Acid Tail and Carries Only Three Positive Charges Has Strong Synergism with Agents Excluded by the Intact Outer Membrane. Antimicrob Agents Chemother. 2010 Aug;54(8):3341–6.

36. Vaara M. Polymyxins and their novel derivatives. Curr Opin Microbiol. 2010 Oct;13(5):574–81.

37. Vaara M. Novel derivatives of polymyxins. J Antimicrob Chemother. 2013 Jun;68(6):1213–9.

38. Vaara M, Fox J, Loidl G, Siikanen O, Apajalahti J, Hansen F, et al. Novel polymyxin derivatives carrying only three positive charges are effective antibacterial agents. Antimicrob Agents Chemother. 2008 Sep;52(9):3229–36.

39. Vaara M, Sader HS, Rhomberg PR, Jones RN, Vaara T. Antimicrobial activity of the novel polymyxin derivative NAB739 tested against Gram-negative pathogens. J Antimicrob Chemother. 2013 Mar;68(3):636–9.

40. Vaara M, Vaara T, Tyrrell JM. Structure–activity studies on polymyxin derivatives carrying three positive charges only reveal a new class of compounds with strong antibacterial activity. Peptides. 2017 May;91:8–12.

41. Flynn PM, Shenep JL, Stokes DC, Fairclough D, Hildner WK. Polymyxin B moderates acidosis and hypotension in established, experimental gram-negative septicemia. J Infect Dis. 1987 Nov;156(5):706–12.

42. Baldwin G, Alpert G, Caputo GL, Baskin M, Parsonnet J, Gillis ZA, et al. Effect of polymyxin B on experimental shock from meningococcal and Escherichia coli endotoxins. J Infect Dis. 1991 Sep;164(3):542–9.

43. Velkov T, Roberts KD, Nation RL, Thompson PE, Li J. Pharmacology of polymyxins: new insights into an “old” class of antibiotics. Future Microbiol. 2013 Jun;8(6):711–24.

44. Falagas ME, Kasiakou SK. Toxicity of polymyxins: a systematic review of the evidence from old and recent studies. Crit Care Lond Engl. 2006 Feb;10(1):R27.

45. Vattimo M de FF, Watanabe M, Fonseca CD da, Neiva LB de M, Pessoa EA, Borges FT. Polymyxin B Nephrotoxicity: From Organ to Cell Damage. PLOS ONE. 2016 Aug 17;11(8):e0161057.

46. Elias LS, Konzen D, Krebs JM, Zavascki AP. The impact of polymyxin B dosage on in-hospital mortality of patients treated with this antibiotic. J Antimicrob Chemother. 2010 Oct 1;65(10):2231–7.

47. Alipour M, Halwani M, Omri A, Suntres ZE. Antimicrobial effectiveness of liposomal polymyxin B against resistant Gram-negative bacterial strains. Int J Pharm. 2008 May 1;355(1–2):293–8.

48. Onaizi SA, Leong SSJ. Tethering antimicrobial peptides: current status and potential challenges. Biotechnol Adv. 2011 Feb;29(1):67–74.

49. Tani T, Shoji H, Guadagni G, Perego A. Extracorporeal removal of endotoxin: the polymyxin B-immobilized fiber cartridge. Contrib Nephrol. 2010;167:35–44.

50. Shoji H. Extracorporeal endotoxin removal for the treatment of sepsis: endotoxin adsorption cartridge (Toraymyxin). Ther Apher Dial Off Peer-Rev J Int Soc Apher Jpn Soc Apher Jpn Soc Dial Ther. 2003 Feb;7(1):108–14.

51. Uriu K, Osajima A, Hiroshige K, Watanabe H, Aibara K, Inada Y, et al. Endotoxin removal by direct hemoperfusion with an adsorbent column using polymyxin B-immobilized fiber ameliorates systemic circulatory disturbance in patients with septic shock. Am J Kidney Dis Off J Natl Kidney Found. 2002 May;39(5):937–47.

52. Kushi H, Miki T, Okamaoto K, Nakahara J, Saito T, Tanjoh K. Early hemoperfusion with an immobilized polymyxin B fiber column eliminates humoral mediators and improves pulmonary oxygenation. Crit Care. 2005;9(6):R653–61.

53. Tsushima K, Kubo K, Koizumi T, Yamamoto H, Fujimoto K, Hora K, et al. Direct hemoperfusion using a polymyxin B immobilized column improves acute respiratory distress syndrome. J Clin Apheresis. 2002;17(2):97–102.

54. Cruz DN, Perazella MA, Bellomo R, de Cal M, Polanco N, Corradi V, et al. Effectiveness of polymyxin B-immobilized fiber column in sepsis: a systematic review. Crit Care Lond Engl. 2007;11(2):R47.

55. Cruz DN, Antonelli M, Fumagalli R, Foltran F, Brienza N, Donati A, et al. Early use of polymyxin B hemoperfusion in abdominal septic shock: the EUPHAS randomized controlled trial. JAMA. 2009 Jun 17;301(23):2445–52.

56. Klein DJ, Foster D, Schorr CA, Kazempour K, Walker PM, Dellinger RP. The EUPHRATES trial (Evaluating the Use of Polymyxin B Hemoperfusion in a Randomized controlled trial of Adults Treated for Endotoxemia and Septic shock): study protocol for a randomized controlled trial. Trials. 2014;15:218.

57. Dellinger RP, Bagshaw SM, Antonelli M, Foster DM, Klein DJ, Marshall JC, et al. Effect of Targeted Polymyxin B Hemoperfusion on 28-Day Mortality in Patients With Septic Shock and Elevated Endotoxin Level: The EUPHRATES Randomized Clinical Trial. JAMA. 2018 Oct 9;320(14):1455–63.

58. Klein DJ, Foster D, Walker PM, Bagshaw SM, Mekonnen H, Antonelli M. Polymyxin B hemoperfusion in endotoxemic septic shock patients without extreme endotoxemia: a post hoc analysis of the EUPHRATES trial. Intensive Care Med. 2018 Dec 1;44(12):2205–12.

59. Nakamura M, Oda S, Sadahiro T, Hirayama Y, Watanabe E, Tateishi Y, et al. Treatment of severe sepsis and septic shock by CHDF using a PMMA membrane hemofilter as a cytokine modulator. Contrib Nephrol. 2010;166:73–82.

60. Nakamura T, Kawagoe Y, Suzuki T, Shoji H, Ueda Y, Kobayashi N, et al. Changes in plasma interleukin-18 by direct hemoperfusion with polymyxin B-immobilized fiber in patients with septic shock. Blood Purif. 2005;23(6):417–20.

61. Kohro S, Imaizumi H, Yamakage M, Masuda Y, Namiki A, Asai Y, et al. Anandamide absorption by direct hemoperfusion with polymixin B-immobilized fiber improves the prognosis and organ failure assessment score in patients with sepsis. J Anesth. 2006;20(1):11–6.

62. Elverdam I, Larsen P, Lund E. Isolation and characterization of three new polymyxins in polymyxins B and E by high-performance liquid chromatography. J Chromatogr. 1981 Nov 20;218:653–61.

63. Orwa JA, Govaerts C, Busson R, Roets E, Van Schepdael A, Hoogmartens J. Isolation and structural characterization of polymyxin B components. J Chromatogr A. 2001 Apr 6;912(2):369–73.

64. Weinstein J, Afonso A, Moss E, Miller GH. Selective chemical modifications of polymyxin B. Bioorg Med Chem Lett. 1998 Dec 1;8(23):3391–6.

65. Gallardo-Godoy A, Muldoon C, Becker B, Elliott AG, Lash LH, Huang JX, et al. Activity and Predicted Nephrotoxicity of Synthetic Antibiotics Based on Polymyxin B. J Med Chem. 2016 Feb 11;59(3):1068–77.

66. Schotten C. Ueber die Oxydation des Piperidins. Berichte Dtsch Chem Ges. 1884 Jul 1;17(2):2544–7.

67. Clayden J, Greeves N, Warren S, Wothers P. Organic Chemistry. Oxford ; New York: OUP Oxford; 2001. 1512 p.

68. Emilitri E, Ranucci E, Ferruti P. New poly(amidoamine)s containing disulfide linkages in their main chain. J Polym Sci Part Polym Chem. 2005 Apr 1;43(7):1404–16.

69. Boehner CM, Marsden DM, Sore HF, Norton D, Spring DR. High throughput 'catch-and-release' synthesis within spatially discrete gel arrays. Tetrahedron Lett. 2010 Nov 10;51(45):5930–2.

70. Kolb HC, Finn MG, Sharpless KB. Click Chemistry: Diverse Chemical Function from a Few Good Reactions. Angew Chem Int Ed Engl. 2001 Jun 1;40(11):2004–21.

71. McEwan KA, Slavin S, Tunnah E, Haddleton DM. Dual-functional materials via CCTP and selective orthogonal thiol-Michael addition/epoxide ring opening reactions. Polym Chem. 2013 Mar 19;4(8):2608–14.

72. Matyjaszewski K, Tsarevsky NV. Nanostructured functional materials prepared by atom transfer radical polymerization. Nat Chem. 2009 Jul;1(4):276–88.

73. Peters EC, Svec F, Fréchet JMJ. Rigid Macroporous Polymer Monoliths. Adv Mater. 1999 Oct 1;11(14):1169–81.

74. Gauthier MA, Gibson MI, Klok H-A. Synthesis of Functional Polymers by Post-Polymerization Modification. Angew Chem Int Ed. 2009 Jan 1;48(1):48–58.

75. Pontén E, Viklund C, Irgum K, Bogen ST, Lindgren ÅN. Solid Phase Chemiluminescence Detection Reactors Based on in Situ Polymerized Methacrylate Materials. Anal Chem. 1996 Jan 1;68(24):4389–96.

76. Kimmins SD, Cameron NR. Functional Porous Polymers by Emulsion Templating: Recent Advances. Adv Funct Mater. 2011;21(2):211–225.

77. Verheyen E, Schillemans JP, van Wijk M, Demeniex M-A, Hennink WE, van Nostrum CF. Challenges for the effective molecular imprinting of proteins. Biomaterials. 2011 Apr;32(11):3008–20.

Chapter 4. Towards molecular imprinting without a solid support: Microfluidic system development

4.1 Introduction

4.1.1 Chapter outline

This experimental chapter introduces a strategy for molecular imprinting at a liquid/liquid interface. It describes the initial stages of a microfluidic system development to establish an organic/aqueous interface within a generated segmented flow.

4.1.2 General principles of microfluidics

4.1.2.1 Overview

Microfluidics (MF) describes the strategic flow manipulation of small volumes of fluid (10^{-8} to 10^{-11}L) (1). MF systems therefore comprise of multiple components all designed for the throughput of fluids on a small scale. Owing to the desirable handling of small volumes of fluid, MF technology has multiple applications in a diverse range of scientific fields. For example, MF systems are used for the handling of single cells for analysis in cell biology (2,3), the separation of DNA for analysis (4), the encapsulation of biological material (5,6), complex immunoassays (7,8), and for drug development (9,10).

The foundation of modern microfluidics is work from the late 1970s when, in 1979, the concept of a 'lab-on-a-chip' was realised with the manufacture of a miniature gas chromatography device chemically etched into silicon (11). Lab-on-a-chip refers to technology capable of laboratory grade analysis undertaken by a device on a miniscule scale (12) and it is an important facet of MEMS (micro-electro-mechanical systems). Lab-on-a-chip is also interchanged with the term micro Total Analysis Systems (μTAS); all of which labour the important point of miniaturisation.

Sophisticated MF systems now exist demonstrating countless combinations of channel geometry to allow processing of small fluid volumes (13). Furthermore, systems often integrate components such as separators,

filters and pumps. Components can also be added for specific analytical purpose and in this project a microwave resonator cavity as a specialised method of polymerisation was eventually included. In their 2017 comprehensive review of microfluidics for the chemical and biological sciences, Chiu *et al.* outlined their perceived future for microfluidic technology. They provided vast evidence for the field of microfluidics fulfilling expectations seeded in the 1990s (improved analytical performance, functionality and economics) and predicted that greater and greater numbers of 'microfluidic-embedded' instruments would be available in the future (14).

A key consideration in the application of MF systems is the difference in fluid behaviour on the micro when compared to the macro scale. The interplay of forces (section 4.1.2.2) and dimensionless parameters (section 4.1.2.3) that dictate fluid flow through small channels are important in the understanding of flow manipulation.

4.1.2.2 Forces

When immiscible fluids like water and chloroform meet in a macrofluidic setting, the fluids will separate dictated by their respective densities. Forces such as gravity and inertial force are therefore important in the observation of fluid behaviour. This is a more tangible situation; the notion of gravity being responsible for observations is familiar. However, on the microscale forces dependent on volume (gravity, inertia) are insignificant in comparison to surface forces (surface tension, shear stresses). This is because forces dependent on characteristic length scale (which signifies magnitude) change in their relative contribution to fluid behaviour as the magnitude of the system decreases (as in microfluidics) (15).

This shift can be explained by microfluidics scaling laws that express the variation in physical phenomena as the characteristic length scale of a system (denoted *l*) changes (equation 4.1) (15).

$$surface\ area\ \propto l^2 \qquad (4.1a)$$

$$volume\ \propto\ l^3 \qquad (4.1b)$$

$$\frac{surface\ forces}{volume\ forces}\ \propto \frac{l^2}{l^3} = \frac{1}{l} \qquad (4.1c)$$

Scaling laws shown in equations 4.1a, b and c demonstrate that forces dependent on volume (proportional to l^3) decrease to a greater degree than surface forces (proportional to l^2) when length scale is reduced.

4.1.2.3 Dimensionless parameters

Fluid flow in microfluidic systems is governed by physical phenomena that are described by a group of dimensionless parameters (15). These parameters can also be expressed as ratios between forces, length scales or other quantities of the relevant physical properties (15). Perhaps the two most important of these dimensionless parameters is the Reynold's Number and the capillary number.

a. Reynold's number:

The Reynold's number describes the relative contribution of inertial forces and viscous forces and is a key parameter in the characterisation of viscous flow.

$$Re = \frac{\rho v l}{\eta} \qquad (4.2)$$

In equation 4.2 ρ: fluid density (kg m^{-3}); v: characteristic velocity (m s^{-1}); *l*: characteristic length scale (m); η: dynamic viscosity (Pa. s).

On the macroscale, when Reynold's number is low, viscous forces dominate over inertial forces and flow is laminar as opposed to turbulent.

Conversely, flow of two *miscible* fluids in microfluidic systems occurs in parallel, with the fluids demonstrating low Reynold's numbers (indicating the relative unimportance of inertial forces and predominance of laminar flow (16,17)). However, *immiscible* fluids bring another force into consideration as surface tension also contributes to fluid behaviour. The capillary number highlights the importance of surface tension.

b. Capillary number:

The capillary number describes the relationship between viscous force and surface tension.

$$Ca = \frac{\eta v}{\gamma} \qquad (4.3)$$

In equation 4.4 η: dynamic viscosity (Pa. s); v: velocity (m s^{-1}); γ: surface tension (interfacial tension) (N m^{-1}). Practically speaking, microfluidic systems tend to demonstrate capillary numbers between 10^{-4} and 10^{-1} (18) and these low Ca values indicate that interfacial tension dominates viscous stresses in MF systems (19). Furthermore, spheres are more likely to form under these conditions as drops attempt to minimise surface area (18,20). The capillary number therefore defines flow characteristics for multiphase flow, where the constraints forced upon two mixing phases by surface force combined with viscous forces give rise to droplet formation (21).

4.1.3 Droplet formation in microfluidic systems

4.1.3.1 General overview

The formation of droplets is often the primary aim in MF system design and is a discipline in of itself with many extensive reviews dedicated solely to this aspect of MF technology (22–26). Control of both morphology and polydispersity of droplets are often the focus of droplet microfluidics studies. Factors such as liquid flow speeds (27–30), channel geometries (25,31,32) and external physical factors (exposure to electricity (33) and

temperature manipulation (30) for example) have all been investigated when exploring droplet formation.

4.1.3.2 Geometries and droplet formation

The formation of droplets of a desired geometry hinges on the way in which two (or more) streams of liquids are introduced within the MF system. This is commonly the most complex element of any MF system from a design perspective and groups routinely design ever more elaborate MF systems to fit their purpose (34,35). For example, microfluidic Large Scale Integration (mLSI) describes the development of MF systems with hundreds or thousands of integrated micromechanical valves (36), allowing the multiplexing of biological assays.

Shown in figure 4.1 are the three geometric configurations that dominate droplet formation dynamics: t-junction, flow focusing and co-flow.

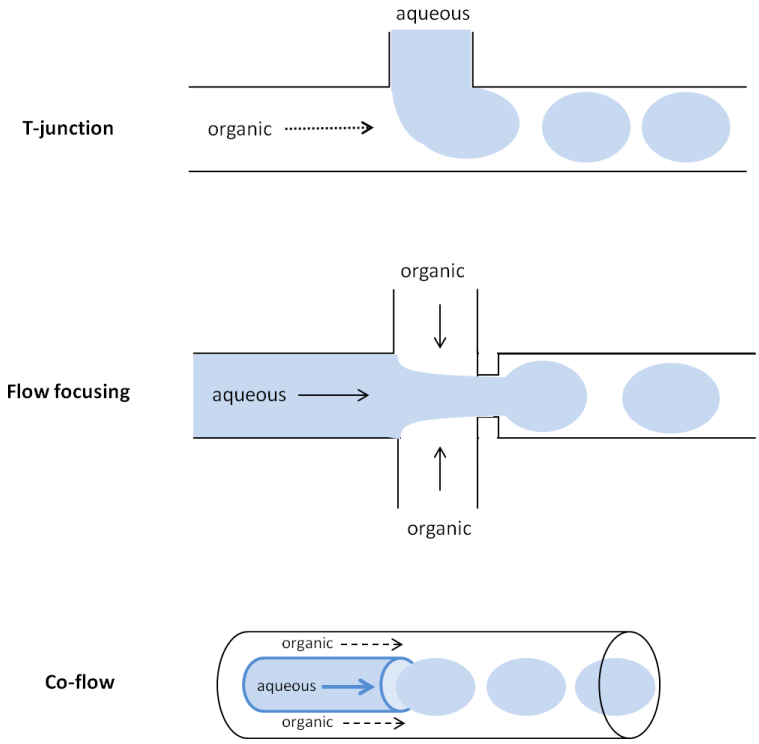

Figure 4.1: Schematic representation of the three main microfluidic configurations for droplet forming junctions. The t-junction represented by the top diagram is the configuration used in this study. Diagram adapted from (37).

In this study a t-junction was used to generate segmented flow, therefore further discussion focuses on this geometry.

4.1.3.3 The t-junction

The two main advantages of t-junctions are the ease in which they can be fabricated (allowing the relatively straightforward process of on-bench design and manufacture) and predictable droplet formation owing to pre-determined channel geometries (32,38). The main determinant of the size

of droplets formed within a microchannel system is the geometry of the t-junction (9).

Shown in figure 4.2 are the two principle flow configurations seen at a t-junction. The t-junction design in this study channelled the continuous flow via the horizontal channel and the dispersed phase via the perpendicular channel. This *cross-flow* arrangement distinguishes it from a *perpendicular flow* system where continuous phase flows via the perpendicular channel and the dispersed phase via the horizontal channel.

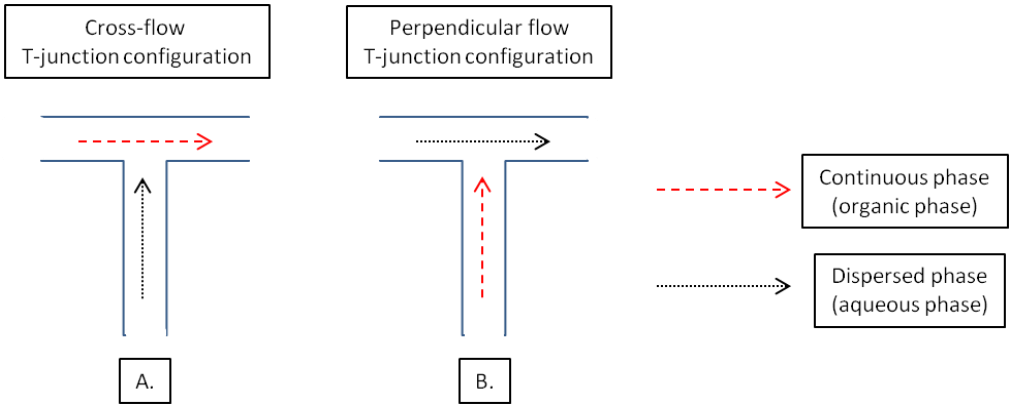

Figure 4.2: Schematic representation of cross-flow and perpendicular flow t-piece designs. **A.)** Cross-flow design; the dispersed phase is introduced to the continuous steam. **B.)** Perpendicular flow; in this design the continuous phase is introduced to the dispersed phase.

There are also two main distinct flow regimes observed in the formation of droplets at a t-junction: squeezing and dripping (figure 4.3). Squeezing occurs when the droplet occupies the entirety of the main channel and dripping occurs when the droplet only occupies a proportion of this channel width (39). Furthermore, the regimes can be classified according to calculated capillary number of the continuous phase (C_a <0.002 for squeezing and C_a 0.01- 0.3 for dripping (40)).

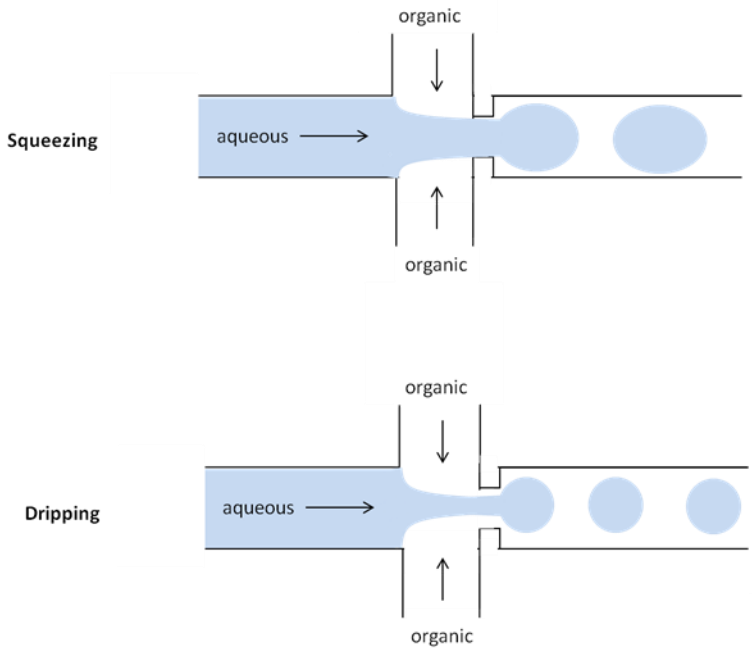

Figure 4.3: Demonstration of squeezing and dripping flow regimes through a microfluidic co-flow t-junction. Adapted from (37).

In 2001, Thorsen *et al.* neatly described, via mathematical models, the formation of a droplet at a t-junction (29). Thorsen *et al.* looked at the size of droplets obtained from a variety of flow speeds and concluded that droplet break off was dictated by a balance of the shear stress exerted on the droplet by the continuous phase and the interfacial tension between the two phases (29). A scaling model for the prediction of droplet size is also proposed in this paper, referring to the space between the droplet and the channel wall, therefore indicating the applicability of this model to the dripping regime of droplet formation. However, when alternative flow regimes occur, (squeezing) the model proposed by Thorsen *et al.* becomes inaccurate. In a squeezing scenario modelling papers from Garstecki (23) and Menech (24), for example, are more relatable. These authors both stress the importance of relative hydrostatic pressures of the continuous phase and dispersed phase in droplet break off. Furthermore, both

highlight the importance of the capillary number for the continuous phase when establishing the mechanism of droplet formation.

4.1.3.4 Droplets to beads

A logical step from the production of droplets is the eventual production of solid beads and microfluidic systems are well placed to efficiently produce beads of a pre-determined size (41). The use of microfluidics to prepare polymer particles in particular is the subject of many review articles (41–44). In their comprehensive 2008 review of microfluidic assisted synthesis of polymer particles, Chang & Serra highlighted how microfluidics is the *only* way to prepare certain polymer particles (varying morphologies, novel multi-component polymer particles, Janus particles) (41). Despite this, in his 2006 overview of microfluidics, George Whitesides commented that chemical synthesis has perhaps not exploited MF technology to its full potential in comparison with other disciplines (45). Aside from use in the production of polymer beads, MF technology has been used to successfully synthesise beads of varied materials including alginate (46), hydrogel (47) silica (48) and gold (49).

4.1.4 Microfluidic applications

4.1.4.1 Imprinting at a liquid/liquid interface

As introduced in chapters one and two, traditional molecular imprinting methods often use a bulk imprinting approach in which a target molecule (template) is 'imprinted' into a polymer matrix (50). However, this results in a polymer in 'bulk' form and milling is required to give fine, often heterogeneous, particles (51). Therefore, molecular imprinting technology (MIT) has developed alternative polymerisation methods to facilitate the manufacture of stable, uniform polymer beads and successful imprinting strategies have been demonstrated using emulsion polymerisation (52–55).

An emulsion is the stable dispersion of one fluid in another immiscible fluid (56), therefore emulsion polymerisation describes the suspension of organic monomers in an aqueous phase (oil-in-water), or vice-versa in reverse-phase emulsion polymerisation (57). It is used in industry to make large batches of latex for example (used for multiple coating and covering applications) (58). Furthermore, emulsion polymerisation techniques have been used by molecular imprinters to facilitate the imprinting of template molecules at the interface of dispersed phase (the bead) and continuous phase (51,59,60). For example, recently Liang *et al.* described the generation of molecularly imprinted polymer microspheres for the detection of malachite green (a carcinogenic dye also used in aquaculture as an antimicrobial) (51) using emulsion polymerisation with the template in the oil phase.

Using MF technology to generate emulsions offers several advantages to traditional techniques. For example, in most conventional emulsion techniques a degree of agitation is needed to promote the formation of an emulsion; if this is not uniform across large mixtures, polydisperse emulsions result (61). Smaller scale microfluidic techniques can offer a more controlled agitation environment, furthermore they provide the advantage of carefully crafting one bead at a time, further reducing polydispersity (56,62). It follows therefore that multiphase microfluidics as a discipline is well placed to facilitate molecular imprinting at an oil/water interface (63,64).

4.1.4.2 Microfluidics and molecular imprinting

Integrating molecular imprinting and microfluidics can be broadly categorised as either direct manufacture of molecularly imprinted beads or a MIP integrated into an MF system for analytical purpose. The former

category reflects the molecular imprinting process taking place at a liquid/liquid interface, a strategy employed in this study.

Work from Takimoto *et al.* in 2015 is an example of imprinting at a liquid/liquid interface. Their paper described the synthesis of imprinted submillimeter microgels capable of human serum albumin detection using a water-in-oil arrangement via fabricated microfluidic channels. Interestingly, in contrast to this study, where the MF system was designed for *in-situ* polymerisation of beads, Takimoto's work describes polymerisation of droplets *outside* of an MF system via photopolymerisation over 24 hours (63). In contrast, and exemplifying the latter category of MIP integrated into MF systems, Huang *et al.* described a microfluidic system designed with a MIP film integrated for use in an SPR (Surface Plasmon Resonance) detection system for progesterone (65). Furthermore, Birnbaumer *et al.*, in their 2009 paper, integrated a virus detection system into an MF channel using a MIP capable of detecting viral binding events (66). Integrated MIP/MF systems have also previously been developed for drug detection. For example, systems for the detection of morphine (an opioid analgesic) (67) and propofol (an intravenous general anaesthetic agent) (68) have both been developed.

4.1.4.3 Microfluidics and biotechnology

a. General overview

The scale of analytes associated with biomedical technology such as individual cells or pathogens makes microfluidics a useful tool owing to its relative size. In Yeo's comprehensive 2010 review paper, microfluidics in biotechnology is explored under a wide range of subheadings from pathogen detection to protein manipulation, demonstrating the comprehensive array of biomedical uses for microfluidic technology (69). A wide range of biomedical devices therefore utilised MF technology (for

example, the ubiquitous analysis strips used for blood glucose testing) and microfluidic bioanalysis as a thriving discipline (70). An interesting application of MF in bioanalysis is in point-of-care diagnostics and the use of point-of-care testing for the diagnosis of infection is a particular area of growth in this field (71).

b. Microfluidics and point-of-care diagnostics

The ability for both healthcare professionals to achieve laboratory based diagnostics using a portable device is the aim of point of care diagnostics. Furthermore, the end user (patient) can also use such devices to carry out testing at home for a variety of chronic and acute conditions, facilitating patient-centred healthcare (71). In a recent comprehensive review of MF technology in point-of-care testing, Pandey *et al.* also highlighted the potential of MF technology to facilitate diagnostics for non-invasive biosensors using bodily fluids such as sweat or saliva (72). Devices utilising this non-invasive approach have several advantages over those requiring blood (ease of patient use and decreased discomfort of testing for example (72)) and are therefore an interesting sub-field of MF driven point-of-care diagnostics.

Micro and nano fluidics are therefore popular techniques employed by many scientific groups for a diverse range of disciplines. Moreover, small scale fluidics can be integrated into complex systems for biomedical and sensing applications and provides the key phenomena underpinning 'lab-on-a-chip' technology. Therefore, the scope for integration of MF systems into detection devices for biomarkers is wide.

4.2 Chapter aims and objectives

The overarching chapter aim was to manufacture a microfluidic system to manipulate the interaction of two immiscible fluids in order to promote a stable imprinting environment with the end result of polymer bead production.

Key objectives in this chapter were as follows:

1. To establish the optimal t-junction design integral to the microfluidic system to promote segmented flow.
2. To establish optimal respective flow rates for aqueous and organic fluids, constituting the dispersed and continuous phases respectively.
3. To use the designed microfluidic system as a platform for the investigation of MF system polymerisation capability.

4.3 Materials and Methods

4.3.1 Materials

All organic solvents were of HPLC grade and were obtained from Fisher Scientific, (Loughborough, UK) unless otherwise stated. All polytetrafluroroethylene (PTFE) and PET tubing was from Fisher Scientific; prefabricated T-junction fitting (PTFE), zero volume connectors (PTFE) and standard connector fittings and ferrules all Upchurch Scientific (Silsden, UK). Glass syringes: SGC Analytical Science (Trajan Scientific, Milton Keynes, UK); Syringe drivers: kd Scientific (MA, USA);

4.3.2 Analysis

Multizoom upright microscope: Nikon AZ 100; high speed camera: AOS Technologies AG (Baden, Switzerland).

4.3.3 General method overview

Described herein are method development stages in the design of a microfluidic system capable of generating segmented flow. The overall aim of immiscible fluid interaction was to produce aqueous 'packets' (water soluble monomer solution containing initiator) travelling in a continuous flow of organic solvent (figure 4.4). Furthermore, the aim was for these 'packets' to adopt the geometrically stable shape of a sphere, creating a stable environment for molecular imprinting at a liquid-liquid interface.

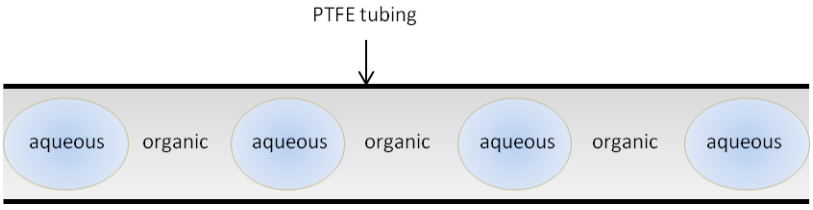

Figure 4.4: Simplified diagram demonstrating desired MF segmented flow pattern.

Microfluidic system development took part in three distinct stages:

1. System A development and testing (prefabricated t-junction testing),
2. System B development and testing (micromilled t-junction testing),
3. Development of MF system B with integration of a polymerisation point.

4.3.4 Microfluidic system development: systems A & B common components

4.3.4.1 Tubing

PTFE tubing with fixed external diameter of 1/16 inch (1.59 mm) was used in the MF system construction. Tubing internal diameter was 100 µm initially and then connected via a zero volume connector to a larger internal diameter of 250 µm. Tubing was connected to t-junction and zero volume connectors (PTFE) and standard connector fittings and ferrules.

4.3.4.2 Syringe drivers

Two syringe drivers were needed for the system, one for the aqueous phase and one for the organic phase. Both were programmable digital syringe drivers for syringe sizes 10 µl to 140 ml.

4.3.4.3 Syringes

Glass SGE Analytical Science syringes, 5 ml or 10 ml were used for all experiments.

4.3.5 Microfluidic system development: System A

4.3.5.1 Pre fabricated t-junction

A purchased prefabricated t-junction was used to establish segmented flow in microfluidic system A. Manufactured in ethylene tetrafluoroethylene

(ETFE), it was made to fit tubing of external diameter 1/16 inch (1.59 mm) and had an internal though-hole diameter of 0.5 mm.

4.3.5.2 Immiscible fluid interaction: system A

Continuous (chloroform) and dispersed phases (monomer solution) were pumped into the microfluidic system with syringe drivers capable of generating a wide range of flow rates. Observations were made systematically to ascertain the optimum dispersed/aqueous (Q_d) and continuous/organic flow rate (Q_c) combination that would result in spherical bead formation. A variety of flow speeds were investigated, however the following combinations resulted in representative bead morphology for different classifications of aqueous packet shape: Q_d: 1.5 ml hr^{-1} with a Q_c: 1.5 ml hr^{-1}; Q_d: 1.5 ml hr^{-1} with a Q_c: 2 ml hr^{-1}, and finally, Q_d: 1.5 ml hr^{-1} with a Q_c: 3 ml hr^{-1}.

4.3.6 Microfluidic system development: System B

4.3.6.1 Micromilled t-junction

To improve the system described in section 4.3.5, a t-junction with rectangular cross sectioned channels was designed on SolidWorks™ CAD software. This design was then milled onto a PTFE disc using a micro milling machine. Offering several advantages over the original t-junction, this milled PTFE chip had pre-determined planar geometry and allowed direct observation of droplet formation at the junction using a high speed camera.

4.3.6.2 Immiscible fluid interaction: system B

Using the micromilled t-junction, observational data was collected pertaining to immiscible fluid interaction at the t-junction. All observations were made via a high speed camera experimental set up which is shown in figure 4.5.

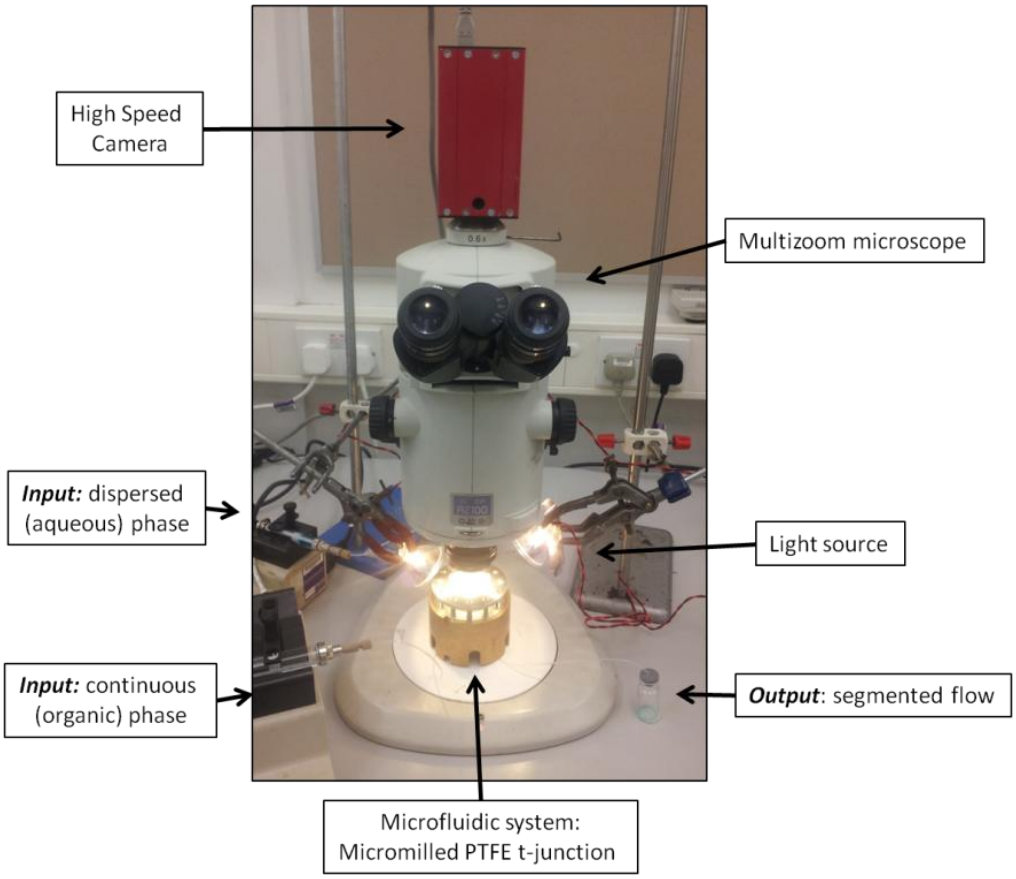

Figure 4.5: Experimental set-up for the filming and photographing of microfluidic flow via a micromilled t-piece.

Data collected included general aqueous packet appearance and inter-packet distance for the organic and aqueous flow speed combinations shown in table 4.1.

Table 4.1: Table showing all combinations of organic and aqueous phase flow speeds used in observational data experiments.

Test number	Q_c (organic) ml hr^{-1}	Q_d (aqueous) ml hr^{-1}	Test number	Q_c (organic) ml hr^{-1}	Q_d (aqueous) ml hr^{-1}
1	1	0.5	**13**	5	2.5
2	1	0.25	**14**	5	1.25
3	1	0.1	**15**	5	0.5
4	2	1	**16**	6	3
5	2	0.5	**17**	6	1.5
6	2	0.2	**18**	6	0.6
7	3	1.5	**19**	10	2.5
8	3	0.75	**20**	20	2.5
9	3	0.3	**21**	20	10
10	4	2	**22**	30	10
11	4	1	**23**	35	10
12	4	0.4	**24**	50	10

4.3.7 Integration of polymerisation point

4.3.7.1 General overview

Final iterations of the designed MF system included a 'polymerisation point'. This involved the design of a portion of the MF system capable of polymerising aqueous beads flowing through the system. Experiments were carried out with direct, volumetric heating by submergence of MF

tubing in a water bath and with an integrated UV light exposure. Finally, the integration of microwave resonator was investigated.

4.3.7.2 Volumetric heating

Initial polymerisation studies used a water bath to directly heat a length of MF system tubing. PTFE tubing, 210 cm (ID 250 µm; volume 47.1 ml), was coiled around a water bath allowing complete submergence under water. This water was heated to 55 ˚C. Segmented flow was established (using system A) with a Q_d: 1.5 ml hr^{-1} and a Q_c: 3 ml hr^{-1} and fluid flowed through the water bath that remained at 55˚C.

4.3.7.3 UV-initiated polymerisation

A UV LED bulb (10 mm size; dominant wavelength 400- 405 nm; intensity 80-120 mcd) was attached to a power source and mounted onto a prefabricated t-junction as to deliver UV light to the perpendicular flow stream. Segmented flow was established (using system A) with a Q_d: 1.5 ml hr^{-1} and a Q_c: 3 ml hr^{-1}.

4.3.7.4 Microwave-initiated polymerisation

This chapter gives an overview of experiments preceding the introduction of microwave-initiated polymerisation. Chapter five (Molecular imprinting without a solid support: microwave-initiated polymerisation) gives a detailed account of experiments using a hybrid MF/microwave polymerisation system.

4.4 Results and discussion

4.4.1 Microfluidic system development: system A

4.4.1.1 Prefabricated t- junction

Shown in figure 4.6 is the pre-fabricated t-junction used for MF system A. Blue dye was added to the aqueous phase allowing observation of droplet formation and downstream segmented flow.

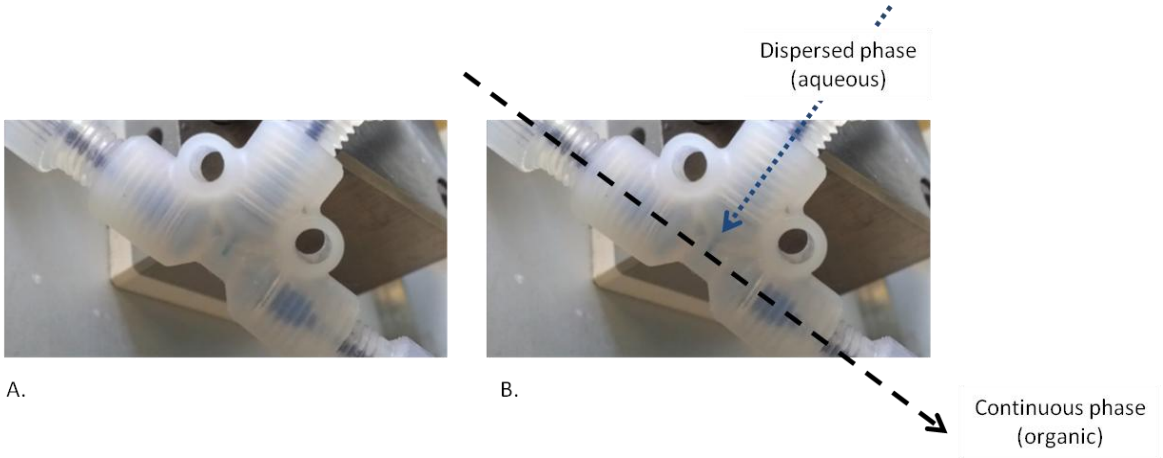

Figure 4.6: **A.)** Photograph of first iteration of t-piece used in MF system A. **B.)** Black dashed line: flow direction continuous phase (organic); blue dashed line: flow direction dispersed phase (aqueous). This is a cross flow t-junction configuration.

4.4.1.2 Immiscible fluid interaction: system A (Pre-fabricated t-junction testing)

Direct observation could be made of bead formation at this t-junction and by using a blue dye in the aqueous phase, subsequent bead shape within downstream MF tubing was observed. Figure 4.7 shows the formation of segmented flow at the pre-fabricated junction.

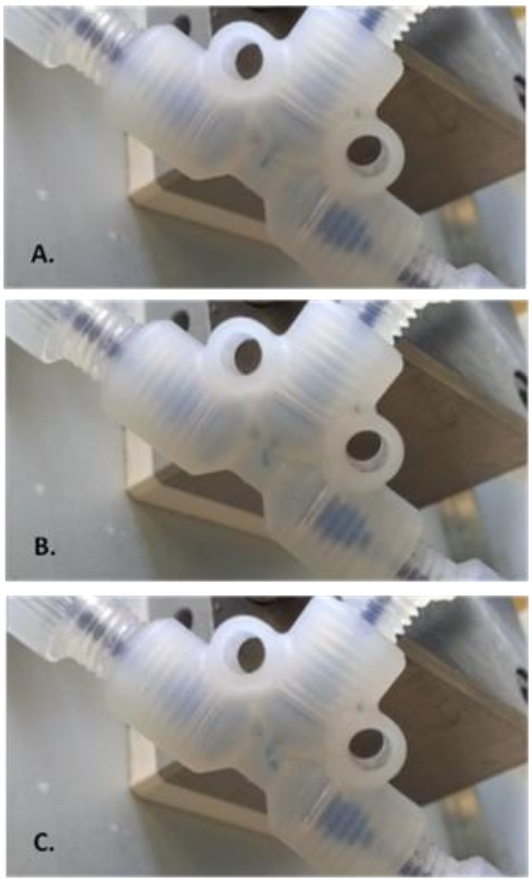

Figure 4.7: Formation of beads at the pre-fabricated t-junction. **A.)** Dispersed phase has approached the t-junction; **B.)** Continuous phase flow has started to drag the emerging dispersed phase along the perpendicular flow path; **C.)** Pinch off is seen, giving a packet of aqueous phase travelling in a continuous organic phase.

Further observations were then made of downstream bead appearance at various flow speeds of the dispersed and continuous phases. Figure 4.8 shows three examples of how differing respective flow speed ratios generated aqueous packets (again shown in blue) of differing shape and with variable inter-packet space.

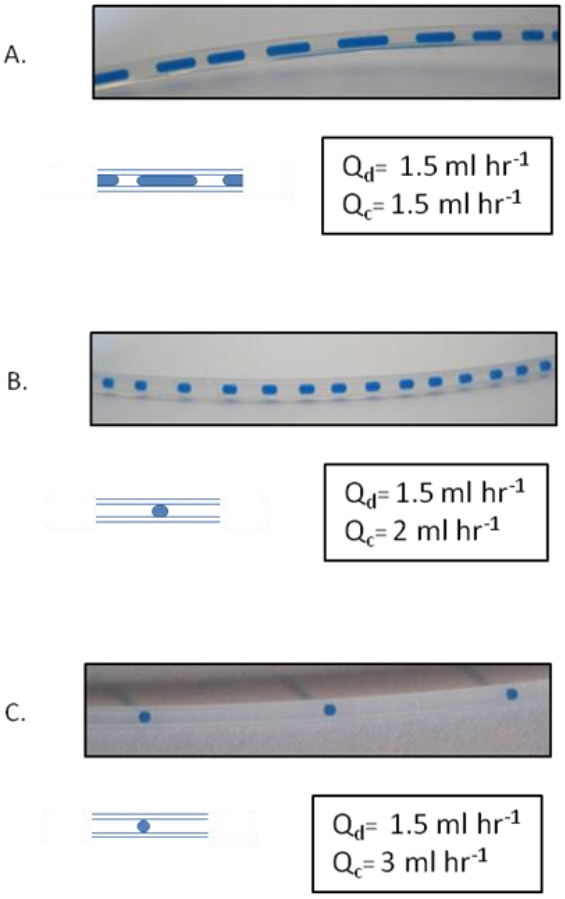

Figure 4.8: Bead appearance depending on relative speeds of aqueous (Q_d) and organic (Q_c) phases. **A.)** phases are flowing at the same rates. **B.)** Organic phase was flowing at 2 ml hr^{-1}, aqueous phase 1.5 ml hr^{-1}. **C.)** Organic phase was flowing at 3 ml hr^{-1}, aqueous phase 1.5 ml hr^{-1}.

When the aqueous and organic phases are flowing at the same rate a slug appearance was seen with small inter-bead distances (figure 4.8 a). However, when the organic phase was set to flow at 2 ml hr^{-1}, a rate approximately 33% greater than the dispersed aqueous phase that was flowing at 1.5 ml hr^{-1}, the packets remained slug-like but decreased in width (figure 4.8b). When the continuous organic phase (3 ml hr^{-1}) was flowing at twice the speed of the dispersed aqueous phase (1.5 ml hr^{-1}). The dispersed aqueous packets adopted a spherical shape.

Despite the documented generation of spherical beads at continuous and dispersed flow rates of 3 and 1.5 ml hr^{-1} respectively, there were limitations of this prefabricated t-junction. Importantly, the findings shown in figure 4.8c were not reliably reproduced. Good runs of spherical beads were often interspersed with more chaotic appearance of slugs and a variable inter-sphere distance. It was possible these findings were secondary to syringe drivers or choice of syringe; however, once these issues were resolved the droplet formation remained erratic. Moreover, any dead space volume at the connection between the t-junction and the MF tubing could potentially disrupt droplet formation. If droplets are given the opportunity to collect at the junction between two MF components (the t-junction and the tubing) this could cause disconnect between the bead morphology formed at the t-junction and what is observed downstream. Therefore, rather than a pre-fabricated, purchased MF component, a t-piece was specifically designed and manufactured (system B).

4.4.2 Microfluidic system development: system B

4.4.2.1 Micromilled t-junction manufacture

An improved t-junction was designed and manufactured by micromilling a CAD drawing design onto a PTFE disc. Figure 4.9 shows CAD drawings from the t-junction design. The diagrams indicate the path taken by the programmed milling (the channel width is dictated by the choice of milling tool).

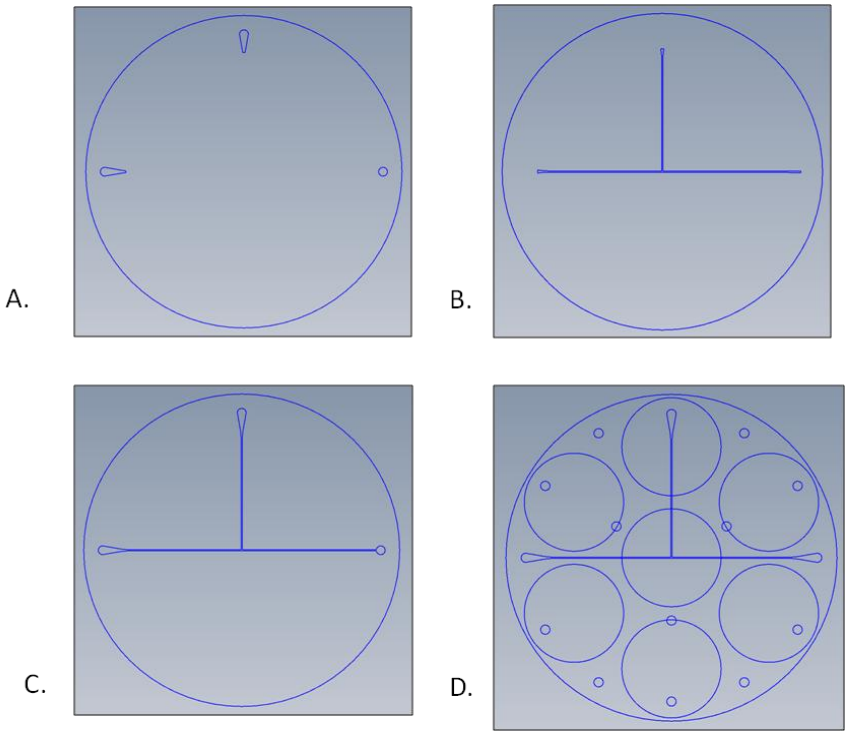

Figure 4.9: 2d, bird's eye view of Solidworks CAD drawing for the design of the micromilled t-junction. **A.)** Design of inlet and outlet holes. **B.)** Design of channels. **C.)** Channels and holes integrated. **D.)** Appearance of complete drawing for micromilled t-junction. The formation of the holes in the brass manifold is shown in picture D, demonstrating ideal placement for the viewing of droplet formation at the t-junction. Channel width: 200 µm; channel depth 200 µm.

Figure 4.10a and 4.10b show the measurements of the pattern milled onto the PTFE disc. Figure 4.10b shows an example of a milled inlet (indicated by the black circle in 4.10a) and the relevant dimensions.

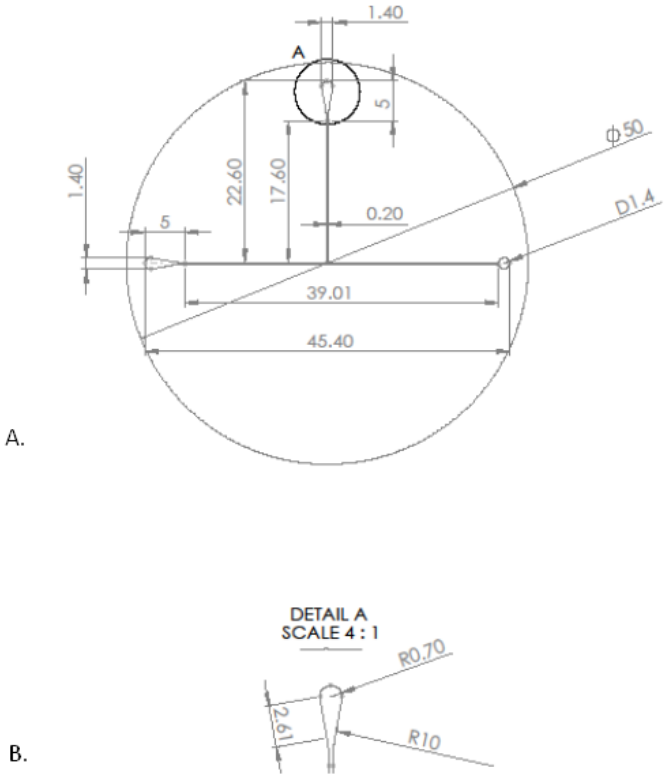

Figure 4.10: Micromilled pattern measurements with all measurements shown in mm. **A.)** Global picture of pattern that was micromilled onto a PTFE disc. **B.)** As indicated by the black circle on A, a close-up of a milled inlet is shown (measurements in mm)

The design shown in figures 4.9 and 4.10 were then milled onto a PTFE disc. This was subsequently held in a brass manifold, specifically designed for the integration of MF tubing. The finished, milled, PTFE disc and the brass manifold with the disc *in situ* are shown in figure 4.11.

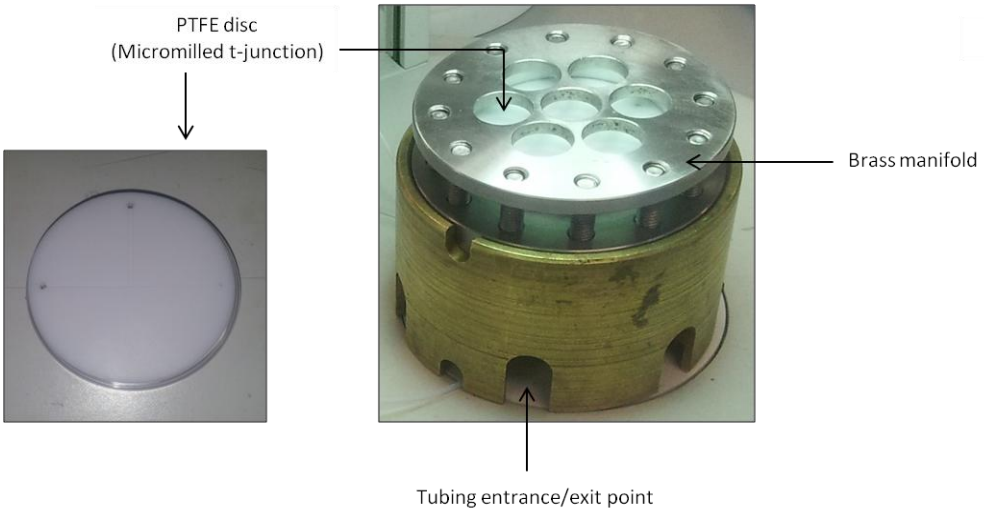

Figure 4.11: Photograph showing micromilled PTFE chip *in situ* held in a brass manifold.

Figure 4.12 is a schematic representation of the manifold cross section showing the layered components that comprised the design. The chip is held in place sandwiched between a hydrophobic perfluoralkoxy alkane (PFA) film layer and the brass manifold. A quartz disc sits between the upper manifold and the PFA film.

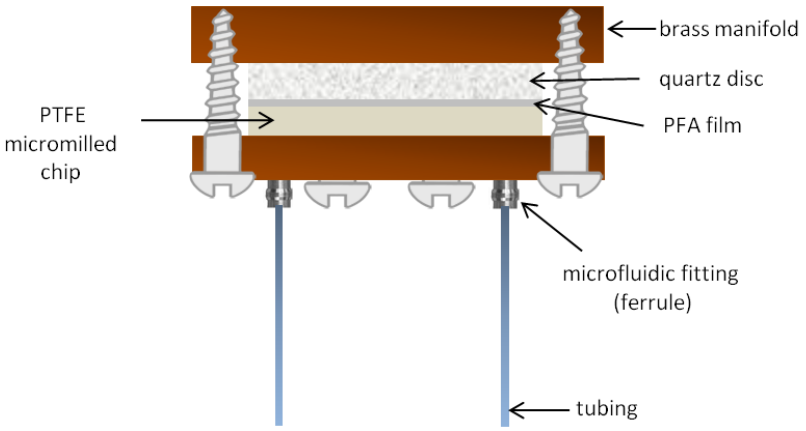

Figure 4.12: Schematic showing a cross section of the brass manifold holding system for the micromilled PTFE chip. PTFE: polytetrafluroethelene; PFA: perfluoralkoxy alkane.

4.4.2.2 Immiscible fluid interaction: system B

a. Observational data

A set of observational data (table 4.2) was collected for a range of aqueous and organic flow rates via the micromilled t-junction. The flow rates of the continuous and dispersed phases were systematically changed and resultant droplet formation was observed.

Table 4.2: Observational data from flow experiments (system B).

Test number	Q_c (organic) ml hr^{-1}	Q_d (aqueous) ml hr^{-1}	Observations
1	1	0.5	Slugs; pronounced inter-slug space. **Figure: 4.14**
2	1	0.25	Slug appearance; pronounced inter-slug space
3	1	0.1	Slow flow, slugs, pronounced inter-slug space
4	2	1	Slug appearance
5	2	0.5	Slug appearance
6	2	0.2	Spheres formed, increased inter-sphere spacing
7	3	1.5	Good spherical formation. **Figure 4.15**
8	3	0.75	Spheres formed
9	3	0.3	Increased spacing
10	4	2	Good sphere formation
11	4	1	Good sphere formation
12	4	0.4	Spheres, increased inter-sphere space
13	5	2.5	Good sphere formation
14	5	1.25	Good sphere formation
15	5	0.5	Spheres, increased inter-sphere space
16	6	3	Good sphere formation
17	6	1.5	Good sphere formation
18	6	0.6	Good sphere formation
19	10	2.5	Good sphere formation
20	20	2.5	Good sphere formation
21	20	10	Spherical shape lost- slug appearance
22	30	10	Spherical shape lost, 'string-of-pearls'
23	35	10	'String-of-pearls'; **Figure 4.16a**
24	50	10	Stratification present; **Figure 4.16b**

Observation of bead morphology, inter-bead separation distance and any resultant break up/coalescence was noted. The appearance of the aqueous phase as it travelled in the continuous phase could be broadly described under four headings: slugs, spheres, 'string-of-pearls' and stratified. 'String-of-pearls' or beads-on-a-string are terms that aptly describe the characteristic flow pattern observed, and are used interchangeably by several groups when describing segmented flow through MF systems when distinct bead separation is lost (73–75). Figure 4.13 demonstrates these four resultant slug appearances in relation to respective aqueous and organic flow speeds.

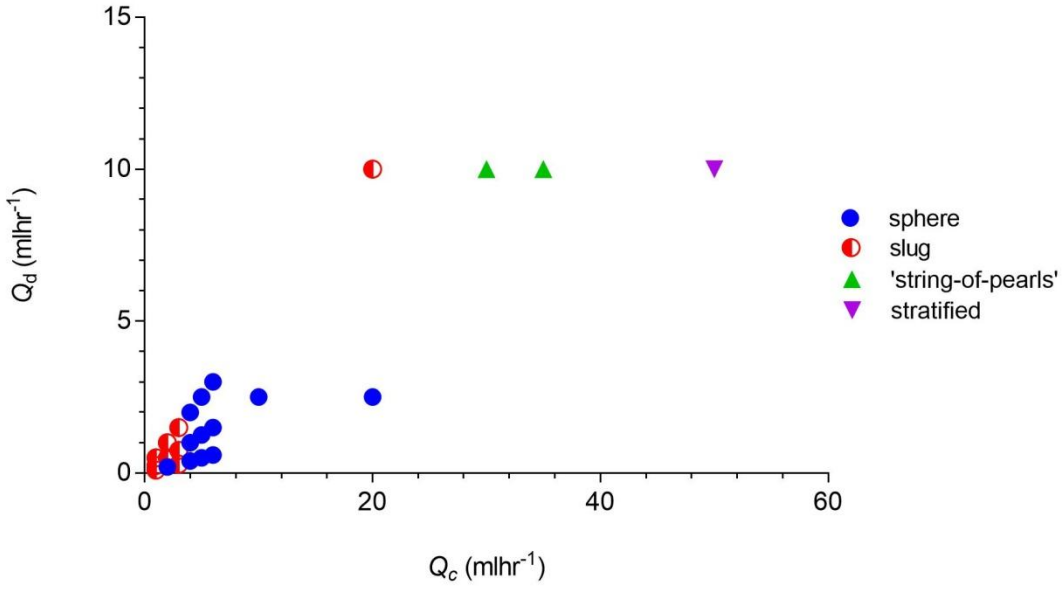

Figure 4.13: Relationship between respective flow rates of aqueous and organic flow rates and appearance of resultant beads.

At low flow rates of both organic and aqueous phases, the aqueous segments travelling in the organic continuous phase had a slug appearance. When the organic flow rate reached 4ml hr^{-1}, aqueous phase appearance began to change and spheres were formed. At higher flow rates distinct

shape aqueous packets were lost and appearance moved towards stratified.

b. Photographic results

The experimental set up for the filming of bead formation by a high speed camera is shown in figure 4.5, this allowed for direct observation of flow rate effects on the morphology of subsequent segmented flow. Images shown in figures 4.14 were taken at continuous flow speed of 1 ml hr^{-1} and a dispersed flow speed of 0.5 ml hr^{-1}.

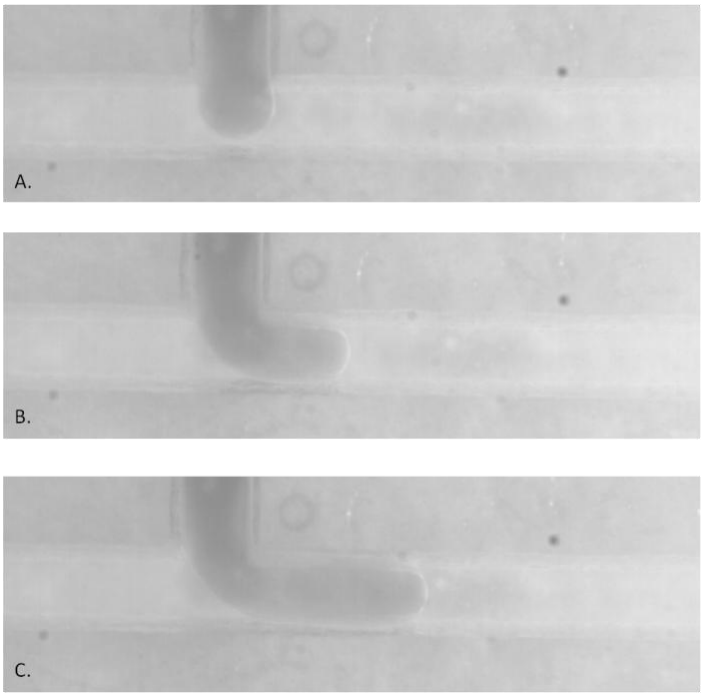

Figure 4.14: High speed camera pictures of flow through micromilled t-junction (shutter speed 1/1000). Pictures taken at continuous flow speed of 1 ml hr^{-1} and a dispersed flow speed of 0.5 ml hr^{-1}. **A.)** Tip of the dispersed phase enters the continuous phase channel; **B.)** The droplets starts to grow; **C.)** Elongation of the droplet continues giving a slug-like appearance.

Captured images in figure 4.14 demonstrate the formation of a slug-like aqueous packet travelling in the organic continuous phase. This was not the desired spherical conformation, therefore investigation continued of dispersed and continuous flow speed ratios. For example, figure 4.15 shows pictures taken at continuous phase flow speed of 3 ml hr^{-1} and a dispersed phase flow speed of 1.5 ml hr^{-1}.

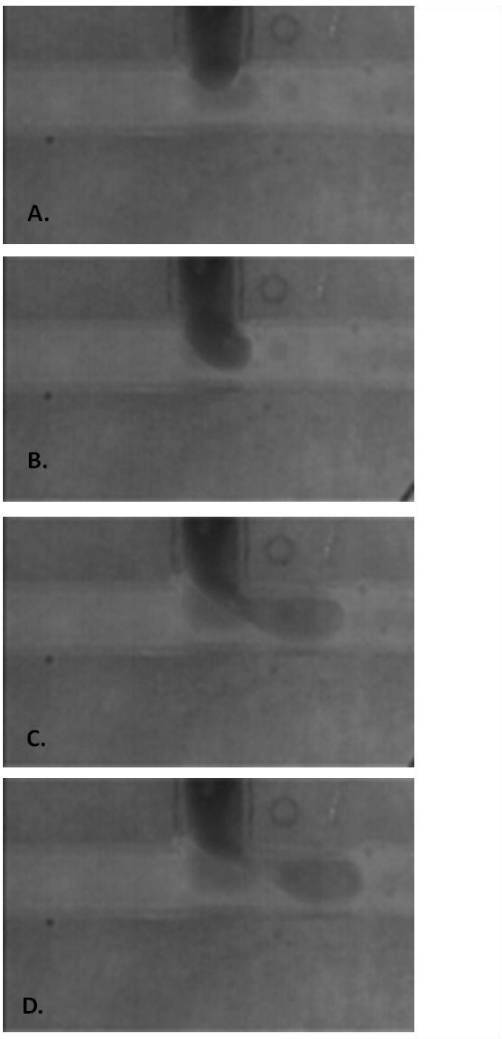

Figure 4.15: High speed camera pictures of flow through micromilled PTFE t-junction (shutter speed 1/1000). Pictures taken at continuous flow speed of 3 ml hr^{-1} and a dispersed flow speed of 1.5 ml hr^{-1}. **A.)** Tip of the dispersed phase enters the continuous phase channel; **B.)** The droplets starts to grow; **C.)** Elongation of the droplet; **D.)** The neck of the droplet breaks. (Contrast darkened post production).

Figure 4.15 shows a representation of droplet formation beginning to form the desired spherical geometry. In figure 4.15a the tip of the dispersed phase can be observed entering the main MF channel, containing continuous phase. Thereafter, in figure 4.15b, the droplet starts to grow and begins to fill the main channel; in 4.15c elongation of the droplet can be observed with associated thinning of the neck connecting it to the stream of dispersed phase liquid. Finally, in 4.15d, the neck of the droplet breaks and it continues downstream as the neck retreats into the feeder channel.

Shown in figure 4.16 are high speed camera images from experiment run using high flow rates.

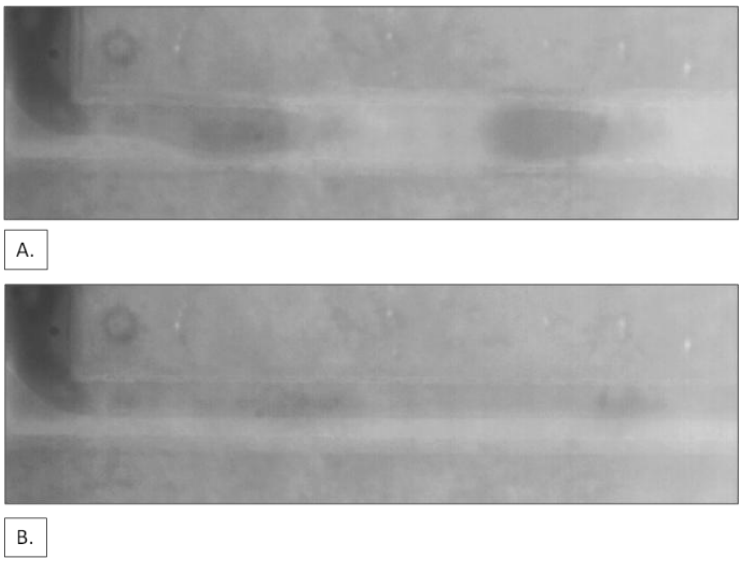

Figure 4.16: High speed camera pictures of segmented flow at higher flow speeds. **A.)** Continuous flow speed: 35 ml hr^{-1}; dispersed flow speed: 10 ml hr^{-1}; **B.)** Continuous flow speed: 50 ml hr^{-1}; dispersed flow speed: 10 ml hr^{-1}.

Figure 4.16a shows an image captured at a continuous phase flow speed of 35 ml hr^{-1} together with a dispersed phase flow speed of 10 ml hr^{-1}. The distorted pinch off can be observed as the dispersed phase meets the continuous, giving a 'string of pearls' appearance. Figure 4.16b shows an

image captured at continuous phase flow speed of 50 ml hr^{-1} and dispersed flow speed of 10 ml hr^{-1}. In this image two streams flowing in parallel (stratified) can be observed, with the dispersed (aqueous) phase occupying the top of the tubing as it appears in the picture.

c. Capillary number calculations

The capillary number is a dimensionless parameter that describes the relationship between viscous forces and surface tension (19). Both viscous force and surface tension become important in multiphase flow on a microscale and at small capillary numbers (dominant interfacial tension) plugs start to take on a spherical shape (20).

Capillary numbers for selected continuous phase flow speeds were calculated and are shown in table 4.3. These continuous phase flow speeds are representative of the flow speeds shown in figures 4.14 to 4.16.

Table 4.3: Table showing continuous phase (Q_c) capillary numbers (Ca) for the flow speeds demonstrated in figures 4.15 to 4.17.

*calculated for flow speed through 200 µm channel; **calculated with denominator of interfacial tension chloroform/water of 32.8 mN m^{-1}.

Q_c ml hr^{-1}	*Velocity ms^{-1}	**C_a
1	0.008	1.3×10^{-4}
3	0.026	4.3×10^{-4}
35	0.309	5.1×10^{-3}
50	0.442	7.2×10^{-3}

d. General discussion

Results from immiscible fluid experiments generally correlate with those from the seminal work from Thorsen, showing a decrease in droplet size as the flow rate of the continuous phase increased (29). This observation has since also been made by several groups investigating droplet dynamics at t-junctions (27,28,30).

In this work the manufactured t-junction encourages the 'squeezing' regime of droplet formation as $W_{in} = W_{out}$ (W_{in} refers to the width of feeder channel and W_{out} to the width of main channel; shown in figure 4.17).

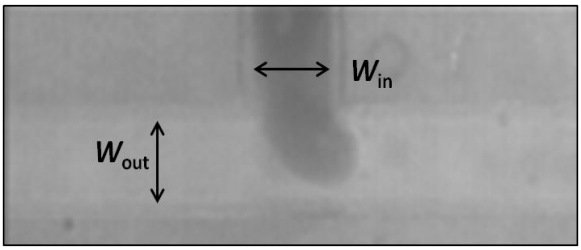

Figure 4.17: Formation of a droplet at the micromilled t-junction. W_{in}: width of feeder channel carrying the dispersed (aqueous) phase; W_{out}: width of main channel carrying the continuous (organic) phase. In the micromilled PTFE chip used in this study, $W_{in} = W_{out}$ (both 200 µm).

Furthermore, as shown in table 4.3, the capillary numbers of the continuous phase are low, also facilitating the 'squeezing' flow dynamic (23,24). In this scenario the droplet fills the main channel as it forms, distinguishing it from the 'dripping' regime when droplets release from the feeder channel before they get big enough to obstruct it (37).

As a droplet formed at the micromilled t-junction in microfluidic system B, the growth of the droplet impeded the flow of organic continuous phase around it. Dynamic pressure then increased downstream of the droplet and eventual pinch off was forced (20). Dynamic pressure (q) is dependent on both density of the fluid and the flow speed, however, from the

equation shown (4.6) flow speed (v) has greater influence than viscosity (ρ):

$$q = \frac{1}{2}\rho v^2 \qquad (4.4)$$

Therefore the greater the speed of continuous phase, the greater the dynamic pressure that builds up and influences neck pinch off of the developing droplet.

When modelling this squeezing regime of droplet formation Guilliot and Colin investigated conditions for parallel flow of two phases in microfluidic channels. However, they demonstrated parallel flow streams when the flow rate of the dispersed phase became greater than the flow speed for the continuous phase (76). Moreover, Guilliot and Colin showed the importance of respective phase viscosities and showed that as the viscosity of the dispersed phase increased, the velocity of the dispersed needed to encourage parallel flow decreased (76). However, results in figure 4.16b show the transition to parallel co-flow at a dispersed flow rate at only 20% of the continuous flow rate (Q_c 50 ml hr^{-1}; Q_d 10 ml hr^{-1}) this is due to the difference in dynamic viscosity between organic and aqueous phases, 0.54 and 0.89 mPa s^{-1} (41) respectively (at 25 °C). In Guilliot and Colin's paper the dynamic viscosity ratio of organic phase: aqueous phase was 1:0.4 (compared to 1:1.65 in this study). Therefore, this work demonstrates that parallel flow appears more readily achievable at lower flow speeds with higher dynamic viscosity ratios. At high viscosity ratios the emerging dispersed phase droplet will experience less shear stress on the interface between itself and the continuous phase than if the viscosities between the two phases were similar. Therefore, this increased stability of the dispersed phase allows the formation of parallel flow at lower flow speeds (78,79).

4.4.3 Integration of polymerisation point

4.4.3.1 Water bath heating

The use of conventional, volumetric heating using a water bath to initiate polymerisation within the MF tubing was unsuccessful. Segmented flow was established through the MF system and this was subsequently passed through a water bath heated to 55° C and polymerisation of the aqueous packets within the MF tubing was absent over repeated attempts.

4.4.3.2 UV-initiated polymerisation

Attempts to initiate polymerisation with UV exposure were unsuccessful. No polymerisation was evident and this was also abandoned (along with conventional heating) as a method for polymerising monomer beads within MF tubing.

UV-initiated polymerisation within microfluidic systems requires optically clear polymer (PDMS (polydimethylsiloxane) for example) or glass channels. PDMS is transparent from 240 to 1100 nm (7,80) making it possible to couple PDMS with UV light sources. Therefore groups working with the UV curing or gelation of polymers and hydrogels in MF systems often use PDMS components (81–83). However, PDMS exhibits unfavourable behaviour when exposed to certain solvents, making the use of PDMS in this study unviable. PDMS swells in non polar solvents such as chloroform (34) whereas PTFE is highly compatible with both chloroform and toluene (both used as organic phases in this study) (84).

4.4.3.3 Microwav- initiated polymerisation

Attempts to reliably polymerise aqueous packets in PTFE tubing using both volumetric heating and UV-initiated polymerisation were unsuccessful. Therefore, an alternative method of achieving *in-situ* polymerisation by dielectric heating was investigated. The use of microwaves for organic

synthesis reactions is a well established (85) and microwave-initiated polymerisation is a notable branch of this discipline (86,87). However, the integration of microfluidics and microwave-initiated in-situ polymerisation is relatively under-represented in the literature. A stepwise approach from the use of an adapted domestic microwave to a cavity resonator was used and the polymerisation of dispersed aqueous beads within PTFE tubing was eventually achieved.

Hybrid MF/microwave system development and polymer bead generation is the subject of chapter five and a detailed look at the field of microwave assisted organic synthesis reactions is given in this chapter.

4.5 Chapter Conclusions

4.5.1 General conculsions

The general aim of this chapter was to create a stable environment for liquid/liquid interface imprinting. Once optimisation of MF system components was undertaken (manufacture of t-junction), systematic testing of micromilled t-junction gave an optimal flow speed ratio of continuous to dispersed flow speeds for the production of spherical aqueous dispersed phase.

Undocumented work in the course of this project looked at the feasibility of emulsion polymerisation methods which also promoted molecular imprinting at a liquid/ liquid interface. However, this largely unsuccessful work provided outward focus on alternative ways to promote liquid/liquid interaction. Therefore, the discipline of microfluidics as a more efficient way to produce polymer beads whilst exploiting advantages of liquid/liquid interface imprinting was investigated. Furthermore, the scale of MF systems developed in this chapter allowed microwave integration; this was not possible with emulsion techniques.

In conclusion, this chapter demonstrates the initial stages of developing a microfluidic/microwave hybrid system for the production of polymer beads.

4.5.2 Rationale for next chapter

Chapter five expands on microwave-initiated polymerisation, taking the microfluidic system described in this chapter to a point where the manufacture of imprinted polymer beads was possible.

4.6 References

1. Sackmann EK, Fulton AL, Beebe DJ. The present and future role of microfluidics in biomedical research. Nature. 2014 Mar 13;507(7491):181–9.

2. Wheeler AR, Throndset WR, Whelan RJ, Leach AM, Zare RN, Liao YH, et al. Microfluidic Device for Single-Cell Analysis. Anal Chem. 2003 Jul 1;75(14):3581–6.

3. Yang C-G, Pan R-Y, Xu Z-R. A single-cell encapsulation method based on a microfluidic multi-step droplet splitting system. Chin Chem Lett. 2015 Dec;26(12):1450–4.

4. Wainright A, Nguyen UT, Bjornson T, Boone TD. Preconcentration and separation of double-stranded DNA fragments by electrophoresis in plastic microfluidic devices. Electrophoresis. 2003 Nov;24(21):3784–92.

5. Tan Y-C, Hettiarachchi K, Siu M, Pan Y-R, Lee AP. Controlled microfluidic encapsulation of cells, proteins, and microbeads in lipid vesicles. J Am Chem Soc. 2006 May 3;128(17):5656–8.

6. Eun Y-J, Utada A, Copeland MF, Takeuchi S, Weibel DB. Encapsulating bacteria in agarose microparticles using microfluidics for high-throughput cell analysis and isolation. ACS Chem Biol. 2011 Mar 18;6(3):260–6.

7. Sia SK, Whitesides GM. Microfluidic devices fabricated in poly(dimethylsiloxane) for biological studies. Electrophoresis. 2003 Nov;24(21):3563–76.

8. Ghodbane M, Stucky EC, Maguire TJ, Schloss RS, Shreiber DI, Zahn JD, et al. Development and validation of a microfluidic immunoassay capable of multiplexing parallel samples in microliter volumes. Lab Chip. 2015 Jul 14;15(15):3211–21.

9. Dittrich PS, Manz A. Lab-on-a-chip: microfluidics in drug discovery. Nat Rev Drug Discov. 2006 Mar;5(3):210–8.

10. Kang L, Chung BG, Langer R, Khademhosseini A. Microfluidics for Drug Discovery and Development: From Target Selection to Product Lifecycle Management. Drug Discov Today. 2008 Jan;13(1–2):1–13.

11. Terry SC, Jerman JH, Angell JB. A gas chromatographic air analyzer fabricated on a silicon wafer. IEEE Trans Electron Devices. 1979 Dec;26(12):1880–6.

12. Ahn CH. Microfluidic Devices and Their Applications to Lab-on-a-Chip. In: Springer Handbook of Nanotechnology. Springer Berlin Heidelberg; 2010.

13. Lee C-Y, Chang C-L, Wang Y-N, Fu L-M. Microfluidic Mixing: A Review. Int J Mol Sci. 2011 May 18;12(5):3263–87.

14. Chiu DT, deMello AJ, Di Carlo D, Doyle PS, Hansen C, Maceiczyk RM, et al. Small but Perfectly Formed? Successes, Challenges, and Opportunities for Microfluidics in the Chemical and Biological Sciences. Chem. 2017 Feb 9;2(2):201–23.

15. Bruus H. Theoretical Microfluidics. Oxford ; New York: Oxford University Press, U.S.A.; 2010. 368 p.

16. Mott DR, Peter B. Howell J, Golden JP, Kaplan CR, Ligler FS, Oran ES. Toolbox for the design of optimized microfluidic components. Lab Chip. 2006 Mar 29;6(4):540–9.

17. Squires TM, Quake SR. Microfluidics: Fluid physics at the nanoliter scale. Rev Mod Phys. 2005 Oct 6;77(3):977–1026.

18. Tabeling P. A brief introduction to slippage, droplets and mixing in microfluidic systems. Lab Chip. 2009 Sep 7;9(17):2428–36.

19. Gu H, Duits MHG, Mugele F. Droplets Formation and Merging in Two-Phase Flow Microfluidics. Int J Mol Sci. 2011 Apr 15;12(4):2572–97.

20. N. Baroud C, Gallaire F, Dangla R. Dynamics of microfluidic droplets. Lab Chip. 2010;10(16):2032–45.

21. Shui L, Eijkel JCT, van den Berg A. Multiphase flow in microfluidic systems – Control and applications of droplets and interfaces. Adv Colloid Interface Sci. 2007 May 31;133(1):35–49.

22. Mashaghi S, Abbaspourrad A, Weitz DA, van Oijen AM. Droplet microfluidics: A tool for biology, chemistry and nanotechnology. TrAC Trends Anal Chem. 2016 Sep;82:118–25.

23. Garstecki P, Fuerstman MJ, Stone HA, Whitesides GM. Formation of droplets and bubbles in a microfluidic T-junction-scaling and mechanism of break-up. Lab Chip. 2006 Mar;6(3):437–46.

24. Menech MD, Garstecki P, Jousse F, Stone HA. Transition from squeezing to dripping in a microfluidic T-shaped junction. J Fluid Mech. 2008 Jan;595:141–61.

25. Tan Y-C, Fisher JS, Lee AI, Cristini V, Lee AP. Design of microfluidic channel geometries for the control of droplet volume, chemical concentration, and sorting. Lab Chip. 2004 Aug;4(4):292–8.

26. Xu S, Nie Z, Seo M, Lewis P, Kumacheva E, Stone HA, et al. Generation of Monodisperse Particles by Using Microfluidics: Control over Size, Shape, and Composition. Angew Chem. 2005;117(5):734–738.

27. Ward T, Faivre M, Abkarian M, Stone HA. Microfluidic flow focusing: drop size and scaling in pressure versus flow-rate-driven pumping. Electrophoresis. 2005 Oct;26(19):3716–24.

28. Collins J, Lee AP. Control of serial microfluidic droplet size gradient by step-wise ramping of flow rates. Microfluid Nanofluidics. 2007 Feb 1;3(1):19–25.

29. Thorsen T, Roberts RW, Arnold FH, Quake SR. Dynamic Pattern Formation in a Vesicle-Generating Microfluidic Device. Phys Rev Lett. 2001 Apr 30;86(18):4163–6.

30. Stan CA, Tang SKY, Whitesides GM. Independent Control of Drop Size and Velocity in Microfluidic Flow-Focusing Generators Using Variable Temperature and Flow Rate. Anal Chem. 2009 Mar 15;81(6):2399–402.

31. Chen JM, Kuo M-C, Liu C-P. Control of Droplet Generation in Flow-Focusing Microfluidic Device with a Converging-Diverging Nozzle-Shaped Section. Jpn J Appl Phys. 2011 Oct 20;50(10R):107301.

32. Link DR, Anna SL, Weitz DA, Stone HA. Geometrically Mediated Breakup of Drops in Microfluidic Devices. Phys Rev Lett. 2004 Feb 6;92(5):054503.

33. Tian L, Gao M, Gui L. A Microfluidic Chip for Liquid Metal Droplet Generation and Sorting. Micromachines. 2017 Jan 27;8(2):39.

34. Szydzik C, Niego B, Dalzell G, Knoerzer M, Ball F, Nesbitt WS, et al. Fabrication of complex PDMS microfluidic structures and embedded functional substrates by one-step injection moulding. RSC Adv. 2016 Sep 14;6(91):87988–94.

35. Kaminski TS, Garstecki P. Controlled droplet microfluidic systems for multistep chemical and biological assays. Chem Soc Rev. 2017 Oct 16;46(20):6210–26.

36. Melin J, Quake SR. Microfluidic large-scale integration: the evolution of design rules for biological automation. Annu Rev Biophys Biomol Struct. 2007;36:213–31.

37. Collins DJ, Neild A, deMello A, Liu A-Q, Ai Y. The Poisson distribution and beyond: methods for microfluidic droplet production and single cell encapsulation. Lab Chip. 2015 Aug 11;15(17):3439–59.

38. Wang K, Lu YC, Xu JH, Luo GS. Determination of Dynamic Interfacial Tension and Its Effect on Droplet Formation in the T-Shaped Microdispersion Process. Langmuir. 2009 Feb 17;25(4):2153–8.

39. Fu T, Ma Y, Funfschilling D, Zhu C, Li HZ. Squeezing-to-dripping transition for bubble formation in a microfluidic T-junction. Chem Eng Sci. 2010 Jun 15;65(12):3739–48.

40. Xu JH, Li SW, Tan J, Luo GS. Correlations of droplet formation in T-junction microfluidic devices: from squeezing to dripping. Microfluid Nanofluidics. 2008 May 30;5(6):711–7.

41. Serra CA, Chang Z. Microfluidic-Assisted Synthesis of Polymer Particles. Chem Eng Technol. 2008;31(8):1099–1115.

42. Bouquey M, Serra C, Berton N, Prat L, Hadziioannou G. Microfluidic synthesis and assembly of reactive polymer beads to form new structured polymer materials. Chem Eng J. 2008 Jan 15;135, Supplement 1:S93–8.

43. Yuan Q, Williams RA. Large scale manufacture of magnetic polymer particles using membranes and microfluidic devices. China Particuology. 2007 Feb;5(1–2):26–42.

44. Jiang K, Sposito A, Liu J, Raghavan SR, DeVoe DL. Microfluidic synthesis of macroporous polymer immunobeads. Polymer. 2012 Nov 9;53(24):5469–75.

45. Whitesides GM. The origins and the future of microfluidics. Nature. 2006 Jul 27;442(7101):368–73.

46. Kim C. Droplet-based microfluidics for making uniform-sized cellular spheroids in alginate beads with the regulation of encapsulated cell number. BioChip J. 2015 Jun 1;9(2):105–13.

47. Hwang DK, Dendukuri D, Doyle PS. Microfluidic-based synthesis of non-spherical magnetic hydrogel microparticles. Lab Chip. 2008 Sep 9;8(10):1640–7.

48. Fang A, Gosse C, Gaillard C, Zhao X, Davy J. Tuning silica particle shape at fluid interfaces. Lab Chip. 2012 Dec 7;12(23):4960–3.

49. Duraiswamy S, Khan SA. Droplet-based microfluidic synthesis of anisotropic metal nanocrystals. Small Weinh Bergstr Ger. 2009 Dec;5(24):2828–34.

50. Vasapollo G, Sole RD, Mergola L, Lazzoi MR, Scardino A, Scorrano S, et al. Molecularly Imprinted Polymers: Present and Future Prospective. Int J Mol Sci. 2011 Sep 14;12(9):5908–45.

51. Liang W, Hu H, Guo P, Ma Y, Li P, Zheng W, et al. Combining Pickering Emulsion Polymerization with Molecular Imprinting to Prepare Polymer Microspheres for Selective Solid-Phase Extraction of Malachite Green. Polymers. 2017 Aug 6;9(8):344.

52. Liang H-D, Noble JA, Wells PNT. Recent advances in biomedical ultrasonic imaging techniques. Interface Focus. 2011 Aug 6;1(4):475–6.

53. Zhou T, Shen X, Chaudhary S, Ye L. Molecularly imprinted polymer beads prepared by pickering emulsion polymerization for steroid recognition. J Appl Polym Sci. 2014 Jan 5;131(1):n/a-n/a.

54. Dvorakova G, Haschick R, Chiad K, Klapper M, Müllen K, Biffis A. Molecularly imprinted nanospheres by nonaqueous emulsion polymerization. Macromol Rapid Commun. 2010 Dec 1;31(23):2035–40.

55. Kujawska M, Zhou T, Trochimczuk AW, Ye L. Synthesis of naproxen-imprinted polymer using Pickering emulsion polymerization. J Mol Recognit. 2018; 31:e2626

56. Engl W, Backov R, Panizza P. Controlled production of emulsions and particles by milli- and microfluidic techniques. Curr Opin Colloid Interface Sci. 2008 Aug;13(4):206–16.

57. Elbert DL. Liquid-liquid two phase systems for the production of porous hydrogels and hydrogel microspheres for biomedical applications: A tutorial review. Acta Biomater. 2011 Jan;7(1):31–56.

58. Thickett SC, Gilbert RG. Emulsion polymerization: State of the art in kinetics and mechanisms. Polymer. 2007 Nov 16;48(24):6965–91.

59. Shen X, Svensson Bonde J, Kamra T, Bülow L, Leo JC, Linke D, et al. Bacterial imprinting at Pickering emulsion interfaces. Angew Chem Int Ed Engl. 2014 Sep 26;53(40):10687–90.

60. Shen X, Ye L. Interfacial Molecular Imprinting in Nanoparticle-Stabilized Emulsions. Macromolecules. 2011 Jul 26;44(14):5631–7.

61. Chern CS. Emulsion polymerization mechanisms and kinetics. Prog Polym Sci. 2006 May 1;31(5):443–86.

62. Shah RK, Shum HC, Rowat AC, Lee D, Agresti JJ, Utada AS, et al. Designer emulsions using microfluidics. Mater Today. 2008 Apr 1;11(4):18–27.

63. Takimoto K, Takano E, Kitayama Y, Takeuchi T. Synthesis of Monodispersed Submillimeter-Sized Molecularly Imprinted Particles Selective for Human Serum Albumin Using Inverse Suspension Polymerization in Water-in-Oil Emulsion Prepared Using Microfluidics. Langmuir. 2015 May 5;31(17):4981–7.

64. Takeuchi T, Hayashi T, Ichikawa S, Kaji A, Masui M, Matsumoto H, et al. Molecularly Imprinted Tailor-Made Functional Polymer Receptors for Highly Sensitive and Selective Separation and Detection of Target Molecules. Chromatography. 2016;37(2):43–64.

65. Huang S-C, Lee G-B, Chien F-C, Chen S-J, Chen W-J, Yang M-C. A microfluidic system with integrated molecular imprinting polymer films for surface plasmon resonance detection. J Micromechanics Microengineering. 2006 Jul 1;16(7):1251.

66. Birnbaumer GM, Lieberzeit PA, Richter L, Schirhagl R, Milnera M, Dickert FL, et al. Detection of viruses with molecularly imprinted polymers integrated on a microfluidic biochip using contact-less dielectric microsensors. Lab Chip. 2009 Dec 21;9(24):3549–56.

67. Weng C-H, Yeh W-M, Ho K-C, Lee G-B. A microfluidic system utilizing molecularly imprinted polymer films for amperometric detection of morphine. Sens Actuators B Chem. 2007 Feb 20;121(2):576–82.

68. Hong C-C, Chang P-H, Lin C-C, Hong C-L. A disposable microfluidic biochip with on-chip molecularly imprinted biosensors for optical detection of anesthetic propofol. Biosens Bioelectron. 2010 May 15;25(9):2058–64.

69. Yeo LY, Chang H-C, Chan PPY, Friend JR. Microfluidic Devices for Bioapplications. Small. 2011 Jan 3;7(1):12–48.

70. Gervais L, de Rooij N, Delamarche E. Microfluidic chips for point-of-care immunodiagnostics. Adv Mater Deerfield Beach Fla. 2011 Jun 24;23(24):H151-176.

71. Gomez FA. The future of microfluidic point-of-care diagnostic devices. Bioanalysis. 2012 Dec 20;5(1):1–3.

72. Pandey Chandra M., Augustine Shine, Kumar Saurabh, Kumar Suveen, Nara Sharda, Srivastava Saurabh, et al. Microfluidics Based Point-of-Care Diagnostics. Biotechnol J. 2017 Nov 27;13(1):1700047.

73. Zhao C-X, Middelberg APJ. Two-phase microfluidic flows. Chem Eng Sci. 2011 Apr 1;66(7):1394–411.

74. Sachdev S, Muralidharan A, Boukany PE. Molecular Processes Leading to "Necking" in Extensional Flow of Polymer Solutions: Using Microfluidics and Single DNA Imaging. Macromolecules. 2016 Dec 27;49(24):9578–85.

75. Boyd DA, Adams AA, Daniele MA, Ligler FS. Microfluidic fabrication of polymeric and biohybrid fibers with predesigned size and shape. J Vis Exp JoVE. 2014 Jan 8;(83):e50958.

76. Guillot P, Colin A. Stability of parallel flows in a microchannel after a T junction. Phys Rev E. 2005 Dec 5;72(6):066301.

77. Lide D R. CRC Handbook of Chemistry and Physics. 84th ed. CRC Press.

78. Gupta A, Kumar R. Effect of geometry on droplet formation in the squeezing regime in a microfluidic T-junction. Microfluid Nanofluidics. 2010 Jun 1;8(6):799–812.

79. Christopher GF, Anna SL. Microfluidic methods for generating continuous droplet streams. J Phys Appl Phys. 2007;40(19):R319.

80. McDonald JC, Whitesides GM. Poly(dimethylsiloxane) as a material for fabricating microfluidic devices. Acc Chem Res. 2002 Jul;35(7):491–9.

81. Lewis CL, Lin Y, Yang C, Manocchi AK, Yuet KP, Doyle PS, et al. Microfluidic Fabrication of Hydrogel Microparticles Containing Functionalized Viral Nanotemplates. Langmuir. 2010 Aug 17;26(16):13436–41.

82. Seiffert S, Romanowsky MB, Weitz DA. Janus Microgels Produced from Functional Precursor Polymers. Langmuir. 2010 Sep 21;26(18):14842–7.

83. Seiffert S, Weitz DA. Controlled fabrication of polymer microgels by polymer-analogous gelation in droplet microfluidics. Soft Matter. 2010 Jul 6;6(14):3184–90.

84. Ren K, Dai W, Zhou J, Su J, Wu H. Whole-Teflon microfluidic chips. Proc Natl Acad Sci. 2011 May 17;108(20):8162–6.

85. Tierney J, Lidström P. Microwave Assisted Organic Synthesis. John Wiley & Sons; 2009. 293 p.

86. Hoogenboom R, Schubert US. Microwave-Assisted Polymer Synthesis: Recent Developments in a Rapidly Expanding Field of Research. Macromol Rapid Commun. 2007 Feb 19;28(4):368–86.

87. Komorowska-Durka M, Dimitrakis G, Bogdał D, Stankiewicz AI, Stefanidis GD. A concise review on microwave-assisted polycondensation reactions and curing of polycondensation polymers with focus on the effect of process conditions. Chem Eng J. 2015 Mar 15;264:633–44.

Chapter 5. Microwave-initiated polymerisation

5.1 Introduction

5.1.1 Chapter outline

This final experimental chapter outlines the integration of microwave delivery into an established microfluidic system in order to polymerise aqueous monomer beads. In addition, microwave sensing technology is used to characterise reactants and to provide insight into the polymerisation process.

5.1.2 Microwaves

Heat application to stimulate chemical reactions remains an integral part of laboratory chemistry. In order to hasten reactions that are slow or impossible at room temperature, the use of microwaves is an efficient way of providing heat (1). Described as the Bunsen burner of the 21st century (2), microwaves are electromagnetic waves with a frequency between 1 and 30 GHz (3) and consist of an electric field (E field) and a magnetic field (H field) (figure 5.1). Microwave ovens (domestic and laboratory) operate at an allocated frequency of 2.45 GHz; therefore avoiding interference with mobile phone and telecommunication frequencies.

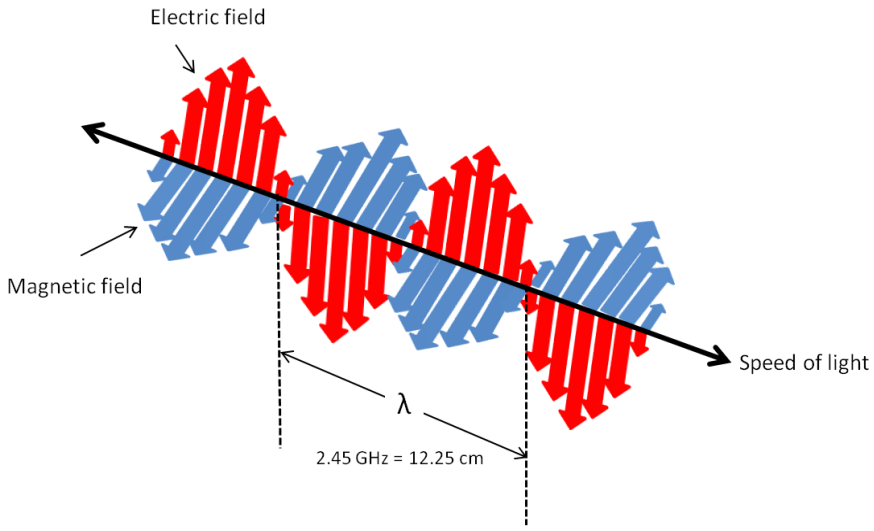

Figure 5.1: Electric (E field) and magnetic (H field) components of microwaves.

Application of microwaves causes a rapid, volumetric heating that is dependent on the materials' ability to convert electromagnetic energy into heat (4). In comparison, conventional heating relies on conduction and describes the transfer of heat at rates dictated by the temperature gradients between two bodies (5). In addition to the regular use of microwaves in the domestic setting, the use of microwave irradiation has gained popularity as a laboratory aid to organic synthesis (2,6,7). The use of microwaves to initiate organic reactions has several advantages over conventional heating methods; for example, shorter reaction times (8,9), noncontact heating (10) and increased yields of purer products (11) have all been demonstrated with microwave use. A summary of advantages of microwave heating in organic synthesis reactions is shown in table 5.1.

Table 5.1: Advantages of microwave heating compared to conventional heating techniques. Adapted from Sosnik (12).

Property	**Conventional conductive heating**	**Microwave heating**
Heating rate	Slow	Fast
Max. Reaction temp	Limited by solvent BP	Not limited by solvent boiling point
Reaction time	Long	Short
Homogeneity of heating	Low	High
Yield	Low	High
Secondary products	High	Low
Solvent-free conditions	Difficult	Easy
Reproducibility	Low	High

5.1.3 Microwave reactors: general introduction

5.1.3.1 Overview

The emergence of microwave-assisted organic synthesis in the 1980s was initially reliant on the use of domestic microwave ovens; however, these devices are often not suitable for laboratory work (13). The main issue with using domestic ovens for organic synthesis reactions is the inherent lack of precise control over their operation (14). For example, accurate temperature control and temperature detection is difficult, leading to uneven heating and inaccurate temperature profiling of reactions. Furthermore, concerns regarding safety of such devices, particularly with the use of organic solvents, has limited their use in the laboratory setting (15). The recognisable domestic microwave has therefore been largely superseded by devices specifically designed for scientific use (11,16). This study, for example, used a domestic microwave for initial polymerisation experiments and graduated to a single mode cavity resonator specifically designed for precise laboratory use.

The increased popularity of custom-made microwave resonators has revolutionised on-bench organic synthesis. Microwave units for laboratory use now range from machines that look much like domestic ovens to bespoke cavity resonators (11,13,16); examples of resonators are shown in figure 5.2.

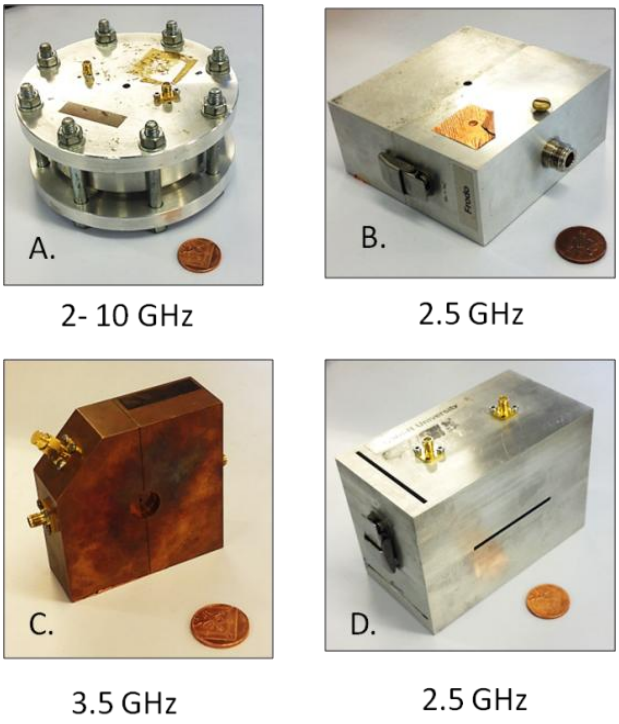

Figure 5.2: Custom made microwave cavity resonators used in the Centre for High Frequency Engineering at Cardiff University's School of Engineering. Each has a resonant frequency shown under each picture.

5.1.4 Microwave reactors: operational overview

5.1.4.1 Introduction

Three major components constitute a microwave processing system: a source for electromagnetic field generation; a transmission line to carry the electromagnetic radiation to an applicator (waveguide); and finally a cavity (i.e. applicator) where microwaves interact with a material (17,18). Cavity design determines the microwave field distribution so therefore cavity resonators used for delivery of microwaves to a loaded sample are designed to facilitate accurate and efficient delivery of microwaves to that particular sample. An important consideration is also the use of a monomodal or mulitimodal microwave processing system.

5.1.4.2 Multimodal vs monomodal

In microwave systems electromagnetic waves propagate in hollow tubes, called waveguides, which transmit energy from the microwave source. Microwaves can travel in waveguides using many different modes, the term 'mode' referring to motion patterns sinusoidal waves (17,18). The cavity is then a resonant length of this waveguide, which is usually rectangular (as in a microwave oven) or cylindrical in cross section.

Domestic microwaves are commonly multimodal; indicating the microwave source in domestic ovens excites multiple resonant modes simultaneously. This 'scattergun' approach of multiple excited modes creates an inefficient heating environment, however, this is desirable for heating food as domestic microwaves are minimally affected by the dielectric properties of materials placed in their cavity (1). However, bespoke resonant cavities for laboratory use are generally single-mode devices (monomodal) (11). Single-mode systems generate microwaves by exciting one resonant mode only and instead of multiple 'hot spots' of electric field found in domestic multi-mode ovens, single-mode cavities have just one E-field spot within the cavity where the microwave field strength is highest (13). This allows the efficient delivery of microwaves- a desirable quality in organic synthesis application. Comparison of mono and multimodal operation is shown in figure 5.3.

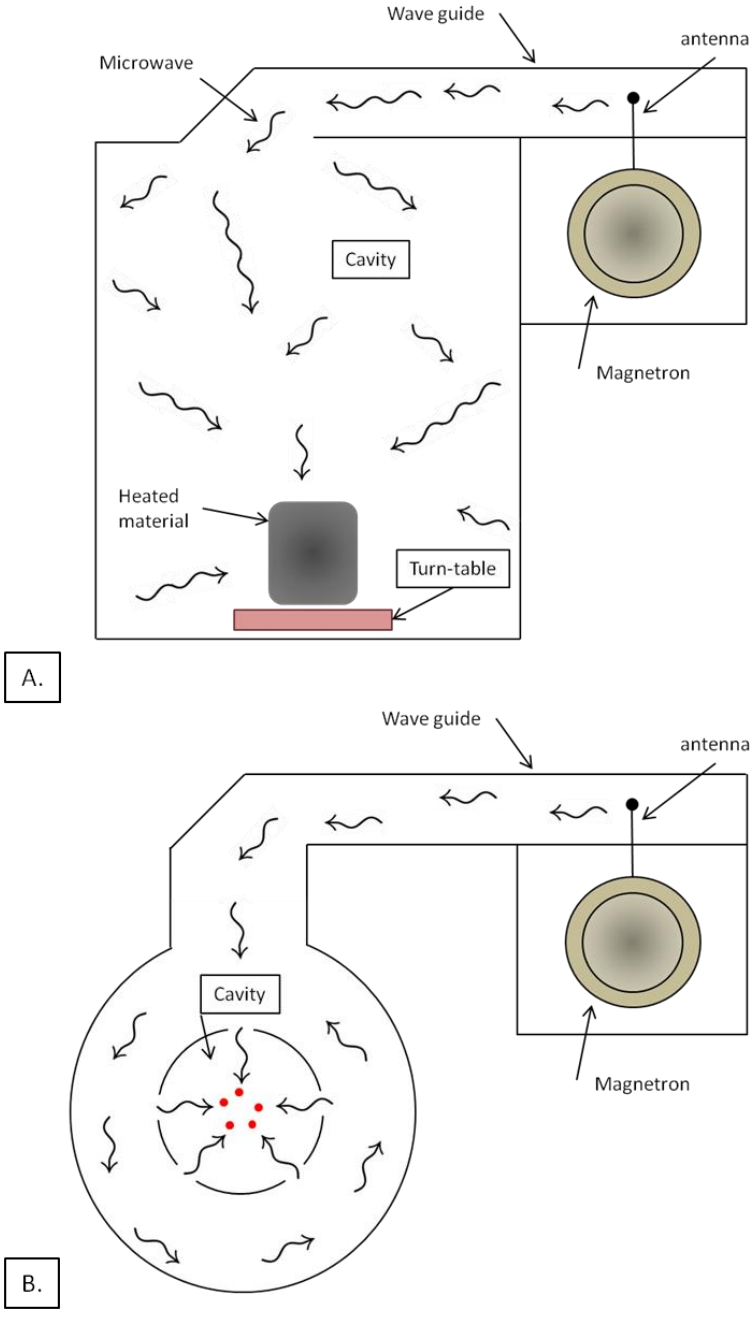

Figure 5.3: Microwave resonators. **A.)** A multimodal microwave processing system representing common domestic microwave operation. The microwave source (magnetron) propagates waves using multiple modes. **B.)** A monomodal microwave processing system representing a system specifically designed for precise laboratory organic synthesis. In monomodal systems the magnetron will propagate waves in one mode only. Adapted from (19).

5.1.4.3 Quality factor

The operation of a microwave cavity is governed by the theory of electromagnetic resonance. A microwave cavity will have a natural oscillating frequency (resonant frequency), this describes the frequency adopted by an object as determined by its physical characteristics (dictated by object size) (1,19). A resonant system will also have a quality factor, referred to as the *Q* factor. The *Q* factor is a dimensionless parameter defined as the ratio between energy stored in the system and the energy losses of the system in one cycle (equation 5.1). A high *Q* factor indicates that a high amount of the energy will be dissipated in the sample, values around 10,000 are considered high for a microwave cavity, operating around 2.45 GHz (18).

$$Q = \frac{f_0}{\Delta f} \tag{5.1}$$

f_0 corresponds to the resonant frequency at maximum peak height and Δf represents the width of the resonance curve at half maximum. In figure 5.4 two resonant peaks of different morphology are shown. The lower amplitude resonance represents a strongly damped system and will have a lower *Q* than the higher amplitude resonance.

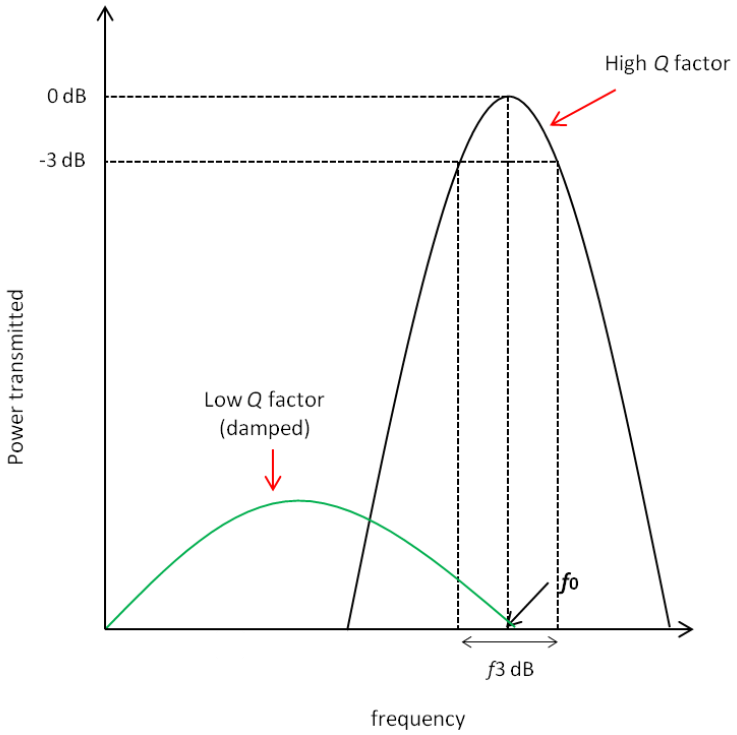

Figure 5.4: Schematic demonstrating differences in Quality (*Q*) factor of two resonant systems.

This *Q* factor can be given as Q_0 (*Q* factor of an empty cavity) and Q_s (*Q* factor when the sample is loaded into cavity). A key element of investigating microwave E-field interaction with a material is dielectric permittivity measurement. In order to use a resonator system for accurate perturbation measurements to determine the permittivity, the *Q* factor of the system needs to be measured with and without the sample in situ, and therefore the resonant frequency shift can be measured (20,21). Permittivity is decribed in more detail in section 5.1.5.1.

5.1.4.4 Cavity resonator used in this chapter

From the cavity resonators shown in figure 5.2, resonator B was used for experiments described in this chapter. Cavity resonator B is a cylindrical cavity with inner height 4 cm and inner radius 4.6 cm, made from aluminium (a high conductivity metal, giving high Q of the empty cavity). The specific mode this cavity operates in is denoted TM_{010}, meaning

Transverse Magnetic mode with a cylindrical mode number given as a suffix. These numbers correspond to the field pattern within cavity. Electromagnetic fields are distributed in one of three ways: transverse electric (TE), transverse magnetic (TM) or transverse electric and magnetic (TEM) (18). Transverse electric indicates electric field is perpendicular to the direction of wave propagation and conversely, transverse magnetic indicates the magnetic field is perpendicular to the direction of wave propagation, in this case the cavity axis (4).

Figure 5.5 shows the field distributions in cavity resonator B.

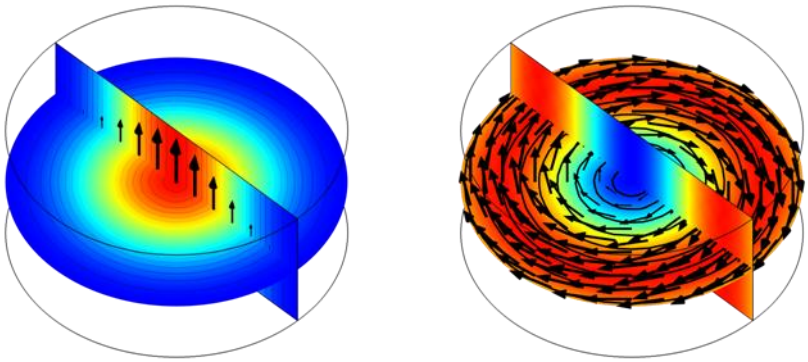

Figure 5.5: Diagram showing E (electric) and H (magnetic) field distributions within the cavity resonator. Colour is representative of field strength, with red being the strongest, yellow medium strength and blue being where the field is weakest within the cavity. Images produced with COMSOL® simulation software by J Cuenca and used with permission.

Figure 5.5 shows the electric field is strongest in the centre of the cavity and the magnetic field conversely is strongest around the perimeter. Samples could therefore be placed in the cavity resonator where the electric field was strongest and accurate heating could be achieved. How the cavity could accommodate different samples is shown in figure 5.6.

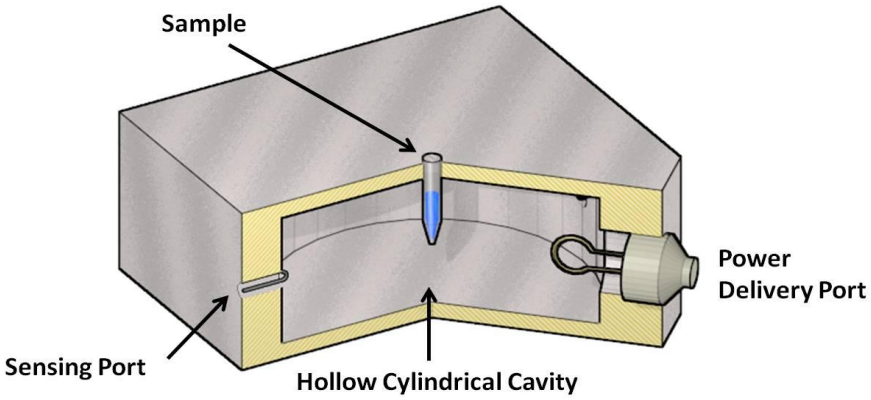

Figure 5.6: Schematic representation of a microwave cavity resonator used in this study, able to accommodate a sample as shown. Diagram courtesy of Dr. J. Cuena, Cardiff School of Engineering.

This arrangement demonstrated in figure 5.6 allowed the investigation of sample interaction with microwaves. Exploring these interactions underpinned experimental work in this chapter.

5.1.5 Microwave/material interactions: general principles

5.1.5.1 Permittivity

When exposed to microwaves, the degree of heating achieved within an exposed material will be ultimately dictated by the inherent properties of said material (1). Therefore, understanding how a reactant will behave when exposed to microwaves helps to guide experiments and allows selection of reactants according to their inherent dielectric properties. A key material property to consider is permittivity.

Permittivity, rather than describing the energy *permitted* through a material, relates to the material's *opposition* to an external electric field. Permittivity is denoted ε and is a fundamental property used to compare dielectric materials. For example, the permittivity constant for a vacuum is

1.0 and that of water (at room temperature) is 80.1 and for Teflon is 2.1 (1).

Once irradiation with electromagnetic fields occurs, an interaction on a molecular level takes place within the exposed material and there are several properties dictating this response. At microwave frequencies the most important mechanism of energy transfer within a material is dipole polarisation (21). An oscillating electric field causes agitation of molecules (figure 5.5); however, this induced rotation of polar molecules is not always as fast as the oscillation of the electric field at a given frequency (electric field oscillates between its maximum and zero values 10^{10} times per second at 2.45 GHz (9)); this disconnect is the phenomenon that underpins dielectric loss, a dimensionless parameter that describes the dissipation of energy (in the form of heat) by a dielectric when subjected to electromagnetic radiation.

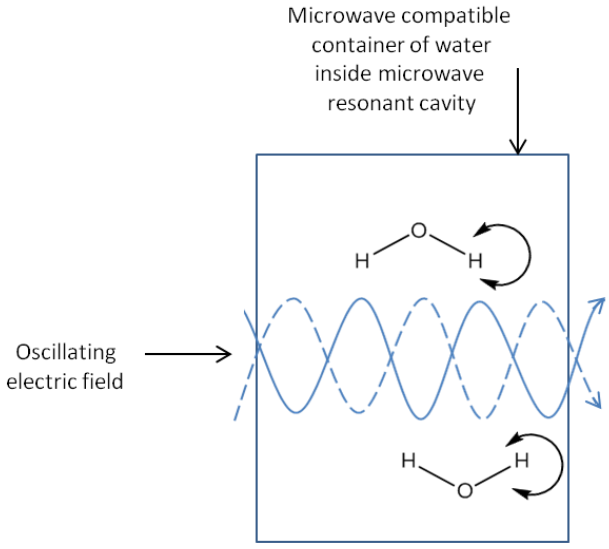

Figure 5.7: Schematic of a container filled with water exposed to microwaves. The oscillating electric (E) field causes orientation changes in the water molecule due to its polarity. The molecules align themselves back and forth with the E field.

Furthermore, microwaves also heat via ionic conduction. This describes the influence of microwaves on charged particles in solution and explains the interaction of ions and microwaves. Ions will oscillate when exposed to a microwave E-field causing collisions with neighbouring molecules and this kinetic energy is released as heat. Ionic conduction heating explains why microwave heating of de-ionised water occurs at a slower rate than the same volume of ordinary tap water (22,23).

5.1.5.2 Complex permittivity

Permittivity (ε) comprises two distinct contributory parameters denoted ε' and ε'', their relationship is expressed by the formula for complex permittivity and is shown by equation 5.2:

$$\varepsilon = \varepsilon' - j\varepsilon'' \quad (5.2)$$

Where ε is the complex dielectric permittivity of a vacuum, ε' is the real part of the complex dielectric permittivity, ε'' is the imaginary part of the complex dielectric permittivity and j is an imaginary constant. ε'' can also be described as the dielectric loss, and ε' as the amount of energy that can be stored within the heated material (21). Another way of looking at these two dimensionless parameters is the real part of the complex permittivity (ε') represents the storage of energy within the dielectric and the imaginary part (ε'') is proportional to the ability of the dielectric material to dissipate microwave energy (1,21).

5.1.5.3 Central Perturbation theory

Perturbation theory describes measurable phenomena that occur when an object is placed inside a cavity resonator and subsequently perturbs the resonant frequency and *Q* (i.e. bandwidth) of the cavity (24,25).

In the 1960s Waldron described the derivation of equations to explain the central perturbation theory of a resonant cavity (26), giving a formula for

the frequency shift seen when a sample is introduced to a resonant cavity; this theory can be simplified to equations 5.3 and 5.4.

$$\varepsilon' \approx -2\frac{\Delta f}{f0}\frac{Ve}{Vs} + 1 \quad (5.3)$$

$$\varepsilon'' \approx \frac{\Delta BW}{f0}\frac{Ve}{Vs} \quad (5.4)$$

In these equations, ε' is the energy stored by the material (real part of permittivity); ε'' is the energy losses (imaginary part of permittivity); Δf is the change in frequency on inserting the sample; V_s is the sample volume; V_e is the effective volume of the resonant cavity (i.e. its physical volume multiplied by a scaling factor, which is 0.269 for the resonant mode used here); ΔBW is the change in bandwidth on inserting the sample and f_0 is the starting (i.e. unperturbed) resonant frequency.

The cavity resonator used in this study was designed such that a sample could be placed in the cavity and changes in resonant frequency of the cavity could be measured. The cavity resonator will have a natural frequency (a frequency of oscillation that is freely adopted when supplied with energy). Therefore, the system resonates when subjected to an oscillating field with a frequency close to its own natural frequency. This resonance can be damped if energy is lost from the system (when a sample is introduced to the cavity for example, as shown in the figure 5.6) and this can be measured. Moreover, the degree to which the resonant frequency of the cavity was damped was dependent on dielectric properties of the material inserted into the cavity (24,26).

Figure 5.8 shows a microwave cavity and a network analyser experimental set-up to measure central perturbation.

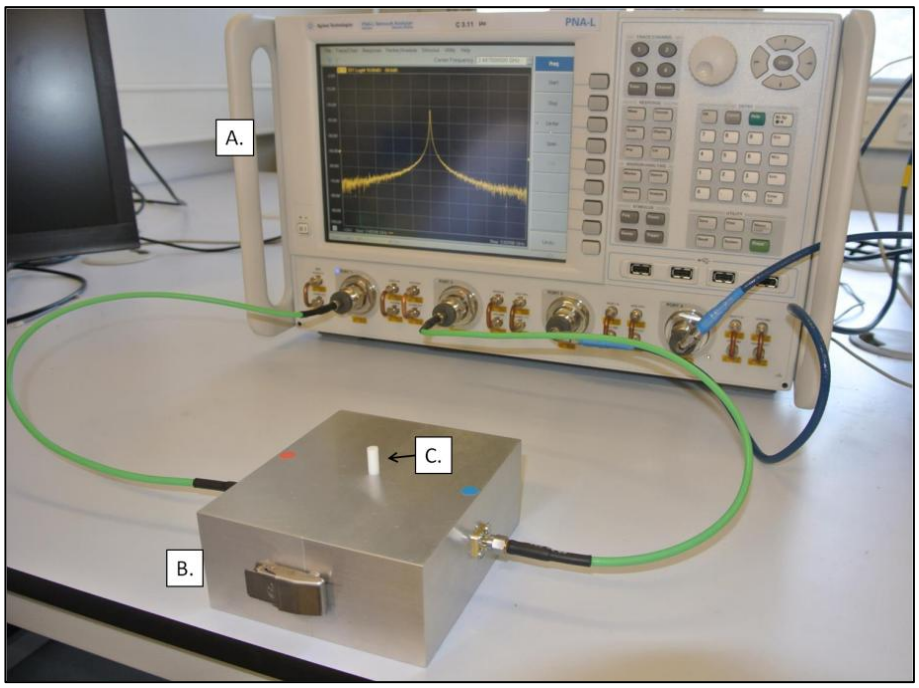

Figure 5.8: Experiment set-up to measure the changes in resonance of a microwave cavity (B) secondary to the introduction of a sample (C) by a network analyser (A).

An exemplar output perturbation measurement by a network analyser is shown in figure 5.9, in which the cavity's transmitted power (in dBm) is plotted against frequency (GHz).

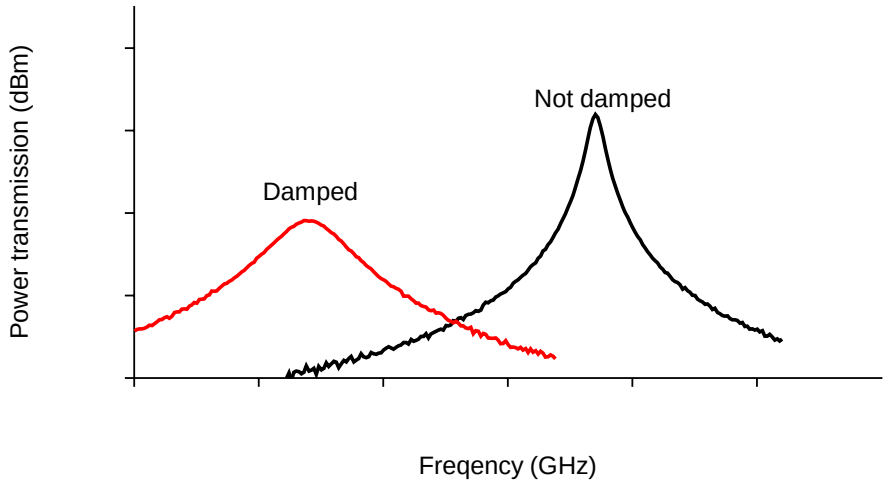

Figure 5.9: Schematic of sample characterisation data that is produced by microwave sensing applications.

Using this sensing capability, studies have used microwave perturbation measurements to characterise a diverse range of materials, including those biological in origin. For example, Blakey *et al.* characterised cells according to lipid content using microwave sensing (27). Furthermore, the dielectric characterisation of pathology samples, including malignant cells, has been demonstrated (28,29). Dielectric characterisation of non-biological material (a strategy used in this work) has previously been investigated including polymers (30–32) and organic solvents (33,34).

5.1.6 Microwave/material interactions: practical applications

5.1.6.1 Microwave-initiated polymerisation

Polymer chemistry has embraced modern microwave delivery methods, using microwave technology to enhance polymer synthesis. Since first appearing in the literature in 1979 (35), microwave assisted polymerisation has been the subject of over 2000 publications with a gradual increase over the last 20 years (figure 5.10).

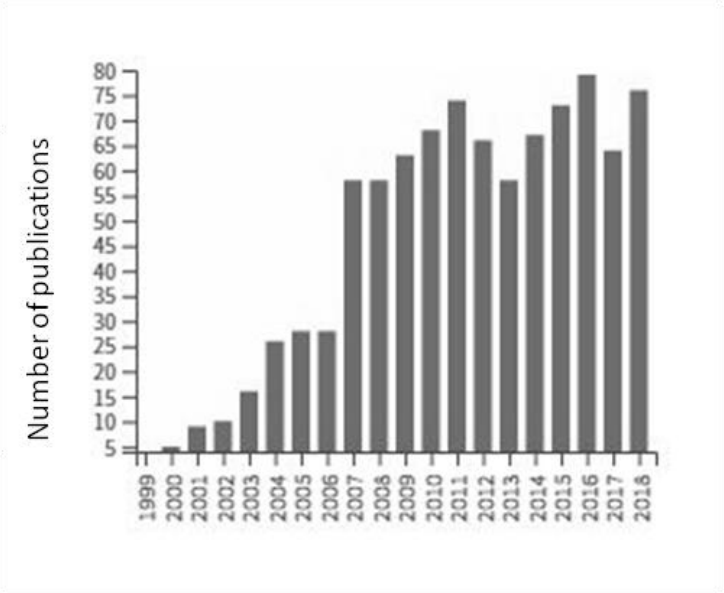

Figure 5.10: Results from a search of 'microwave assisted polymerisation' on Web of Science ™ Core Collection. This is also shown graphically by Schubert *et al.* in their 2004 review (3) and updated in their 2007 review (36).

Polymer synthesis reactions not possible with conventional heating have been reported using microwaves. For example, Singh *et al.* reported the synthesis of polyacrylamide using a reduced initiator concentration (potassium persulfate) under atmospheric conditions in a domestic microwave. Repeating the reaction conditions using conventional heating did not produce a polymer (37). Some authors have also reported microwave synthesised polymers with specific properties not demonstrated in polymers produced using conventional heating. In 2008 Zhao *et al.* produced a poly (*N*-isopropyl acrylamide) hydrogel under microwave conditions that demonstrated increased swelling ability secondary to a higher degree of porosity when compared to the same hydrogel produced with conventional heating (38). Other examples of enhanced polymer synthesis using microwaves include: increased monomer conversion rates (39); increased curing rates for epoxy resins (9); the manufacture of polymers with increased molecular weights (40,41);

improved control of resultant polymer molecular weight (42,43); and improved polydispersity indexes of polymer beads (42,44,45).

5.1.6.2 Molecular imprinting and microwaves

The field of molecular imprinting has also used microwaves to facilitate imprinting for a variety of templates. Using microwave-initiated polymerisation, a significant increase in reaction rates (up 70-fold) compared with conventional heating techniques has been demonstrated by imprinters (46–48). Furthermore, differences in MIP performance dependent on microwave heating have been previously highlighted. For example, using a classical imprinting model of caffeine and theophylline, Turner *et al.* demonstrated reduced MIP binding capacity by microwave heated polymers (using a research scale bench-top microwave reactor) compared to conventionally synthesised polymers (oven heated) (46). This, the authors concluded, was a result of reduced surface area for binding sites found in the microwave MIP.

Schwarz *et al.* also found differences in binding performance between MIPs synthesised with microwaves compared to conventional heating. However, unlike Turner *el al.*, the *overall* binding capacities were similar, the difference was more subtle. Their template was resveratrol, a polyphenol compound, and analysis to determine the distribution of high and low affinity sites in the synthesised MIPs revealed different organisation of these binding sites on MIPs manufactured using microwave assisted polymerisation compared to those manufactured with conventional heating. This resulted in a more selective microwave MIP compared to its thermal counterpart when binding to resveratrol analogues compared to resveratrol was investigated (47).

The microwave application device used in the vast majority of microwave/molecular imprinting studies is primarily used as a heating tool

and the sensing application of microwaves is seldom explored. The opportunity to track the formation of a MIP using resonance data obtained from a sophisticated cavity resonator system (as in this study) is potentially a powerful tool in the investigation of polymer formation.

5.1.6.3 Microfluidics and microwaves

Custom-made microfluidic mini-reactors have been used in combination with microwave heat to facilitate a wide range of organic synthesis reactions (49–51). Effective combination of microfluidic and microwave systems ranging from relatively simple straight microfluidic capillaries travelling through microwave reactors (52,53), to more complex microfluidic systems micromilled onto PTFE chips (54,55) have been shown. Furthermore, the sensing capability of microwaves in an integrated MF system has also been utilised with permittivity measurements being used to characterise non biological (organic solvents (33), polymer composites (56)) and biological materials (bacterial pathogens (57), cancer cells (58), and yeast (59)).

The ability to effectively target microwaves at droplets in microfluidic systems has also been previously explored (60,61). For example, in their 2013 paper, Boybay *et al.* demonstrated a microwave device with sensing and heating capabilities that were dependent on the composition of a particular droplet passing through the device (60). The system could also detect changes in droplet size by measuring resonant frequency shifts initiated by a passing droplet.

The combination of microwave resonators, microfluidics and molecular imprinting using both sensing and heating application was explored in this study and described in this chapter.

5.2 Chapter aim and objectives

The aim of this chapter was to develop a method for preparing molecularly imprinted polymer beads using microwave radiation to initiate polymerisation. The approach was to deliver microwaves as part of an integrated microfluidic /microwave system, in which slugs of aqueous monomer solution were exposed to microwaves as they travelled in an organic continuous phase.

Key objectives of this chapter were as follows:

1. The optimisation of the hybrid microfluidic/microwave system including formation of a reliable protocol for microwave-initiated polymerisation.
2. The use of a microwave cavity resonator as a sensing instrument to track polymerisation.
3. To demonstrate the ability to carry out molecular imprinting at a liquid/liquid interface and produce molecularly imprinted beads capable of surfactant (LPS surrogate) detection.

5.3 Materials and methods

5.3.1 Materials

All organic solvents were of HPLC grade and were obtained from Fisher Scientific, (Loughborough, UK). All PTFE and PET tubing was from Fisher Scientific. The t-junction fitting (PTFE), zero volume connectors (PTFE) and standard connector fittings and ferrules were from Upchurch Scientific, UK.

5.3.2 Analysis

5.3.2.1 Microwave sensing data

Microwave sensing data was collected on Fieldfox N9912A Vector Network Analyser (Agilent Technologies, USA) and exported to LabVEIW (National Instruments, TX, USA).

5.3.2.2 Fluorescence

Fluorescence analysis was undertaken using a FLUOstar OPTIMA platereader (BMG Labtech GmbH, Ortenburg, Germany). Analysis of binding performance data obtained from fluorescence analysis was carried out with GraphPad Prism® V8 software (B_{max} and K_d values from single-site specific binding curve fitting algorithm).

5.3.3 Material characterisation using microwaves

5.3.3.1 Dielectric characterisation

Using a microwave resonant cavity (described in section 5.1.2.3), dielectric properties of the following were measured: DI water, chloroform, hexane, toluene, acrylamide (AAm) (0.15 g ml^{-1} solution), N,N'- methylene-bis-acrylamide (MBAam) (0.03 g ml^{-1} solution); monomer solution A (AAm 0.15 gml^{-1}, MBAam 0.02 g ml^{-1}); monomer solution B (AAm 0.15 g ml^{-1}, MBAam 0.03 g ml^{-1}); monomer solution C (AAm 0.15 g ml^{-1}, MBAam 0.04 g ml^{-1}); and polyacrylamide (PAAm) gel. All samples were placed in a specialised

PTFE vial (designed to sit in the cavity resonator) and were the same volume (200 µl). The following parameters were measured: sample volume; volume of resonant cavity; change in bandwidth and the start frequency.

5.3.3.2 Cavity resonance perturbation

The power transmission between low power ports of the cavity resonator as a function of frequency was measured on placement of the reactants listed in section 5.3.3.1 into the cavity. These resonant frequency measurements allowed investigation of cavity resonance perturbation by each sample.

5.3.4 Method development: system components

5.3.4.1 Microwave delivery

The microfluidic system described in chapter four was further modified to allow microwave-initiated polymerisation capability. Initially, this modification was a domestic microwave. However, the fully optimised MF system utilised a cavity resonator.

5.3.4.2 Tubing

The MF tubing system was modified to accommodate the cavity resonator and several iterations of in-cavity tubing configurations were developed and tested. Tubing was initially taped to the inside of the cavity resonator; thereafter the feasibility of concentrically coiling PTFE tubing onto cardboard inserts was investigated.

5.3.4.3 Temperature detection

Temperature measurements were taken by an infrared camera. The camera was positioned to measure temperature as the tubing emerged from the cavity resonator (figure 5.11).

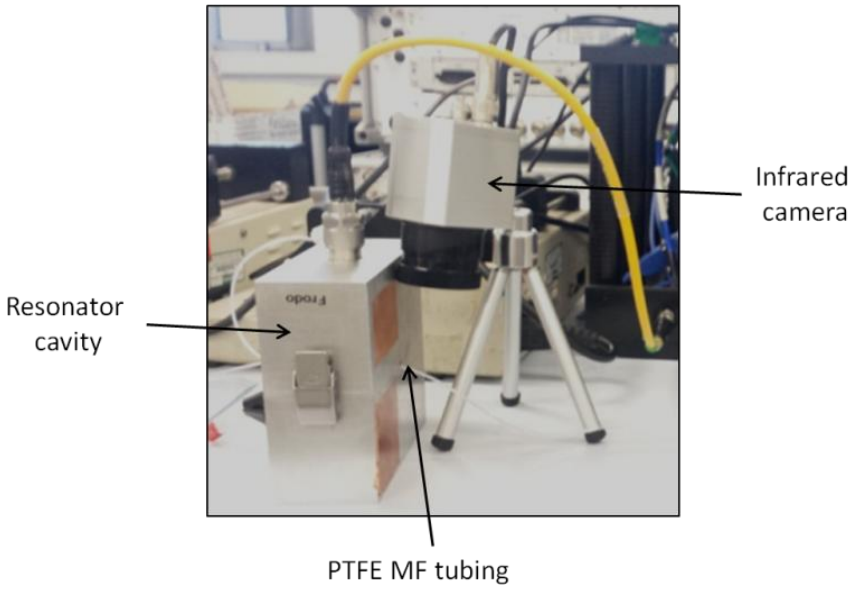

Figure 5.11: Photograph of IR camera placement as part of integrated MF/microwave experimental set-up.

5.3.5 Microwave-initiated polymerisation

5.3.5.1 Polymerisation protocol development

An optimal polymerisation strategy for the preparation for polyacrylamide beads was established through systematic variation of: energy supplied (dBM off maximum); total period of protocol (ms); duty cycle (ratio of the duration of the energy delivered to the total period of a signal); and the addition of a resonance sweep. Serial observational studies using gradual changes in all variables until polymer beads emerged from the system was undertaken. At key junctures manufactured beads were photographed and filmed peri-production.

5.3.6 Dynamic polymerisation sensing

5.3.6.1 Overview

The polymerisation process was tracked using serial central perturbation measurements during the polymerisation of a nominated monomer solution. This dynamic polymerisation sensing was carried out in two ways.

Firstly, polymerisation took place *outside* the resonator and then polymer samples were transferred to the resonator for sensing measurements (ex-resonator polymerisation sensing) and secondly, both polymerisation and sensing took place in the resonator (in-resonator polymerisation sensing). To regulate the temperature of in-resonator sensing, the resonator itself was placed in a bench-top oven.

5.3.6.2 Ex-resonator polymerisation sensing

Resonance peak measurements were taken for the empty cavity and for an empty glass vial. Thereafter, the following solutions were sealed in polymerisation glass vials and degassed for 15 minutes: DI water only (5 ml); polymer 1 (AAm 0.75 g (10.5 mmol) no crosslinker, 5 ml DI water, 1.5 ml MeOH); polymer 2 (AAm 0.75 g (10.5 mmol), MBAam 0.2 g (1.3 mmol), AAPH 6 mg (0.02 mmol), 5 ml DI water, 1.5 ml MeOH); polymer 3 (AAm 0.75 g (10.5 mmol), MBAam 0.3 g (2 mmol), AAPH 6 mg (0.02 mmol), 5ml DI water, 1.5 ml MeOH); polymer 4 (AAm 0.75 g (10.5 mmol), MBAam 0.4 g (2.6 mmol), AAPH 6 mg (0.02 mmol), 5 ml DI water, 1.5 ml MeOH). Following de-gassing, 200 µl of each sample were placed into small, bottom tapered glass vials with care taken to minimise transfer time. If any residual solution was accidentally deposited on the rim or walls of the small glass vials the sample was discarded.

Polymer four was then taken forward for a time-tracked sensing experiment. Following de-gassing, 200 µl of polymer 4 solution was transferred into a small, tapered end glass vial. Polymer four as tested (200 µl) therefore constituted the following: AAm 0.024 g (0.34 mmol); MBAam 0.0124 g (0.08 mmol); AAPH 0.18 mg (0.68 µmol). This vial was placed in a heat sink at 60 $^{\circ}$C and at the following time points perturbation measurements were taken: 0; 5; 10; 15; 20; 25; 30; 35; 40; 45; 50 and 55 minutes. Transport from heat sink to cavity resonator for measurement

was two seconds. The measurements taken were: temperature, bandwidth, resonance peak centre, *Q* factor and dielectric loss.

5.3.6.3 In-resonator polymerisation sensing experiment in oven

The following solution (referred to as polymer 4) was sealed in polymerisation glass vials and degassed for 15 minutes: AAm 0.75 g (10.5 mmol), MBAam 0.4 g (2.6 mmol) 5 ml DI water, 1.5 ml MeOH. Following de-gassing 200 µl of the solution was placed into a small, bottom tapered glass vial with care taken to minimise transfer time. Polymer 4 as tested (200 µl) therefore constituted the following: AAm 0.024 g (0.34 mmol); MBAam 0.0124 g (0.08 mmol); AAPH 0.18 mg (0.68 µmol). This vial was placed into the cavity resonator that in-turn was place in an oven to heat. The following measurements were taken: temperature (fiberoptic temperature monitoring), bandwidth, resonance peak centre, *Q* factor and dielectric loss.

5.3.7 Molecular imprinting experiments

5.3.7.1 Benzethonium chloride analysis (LPS surrogate template)

Benzethonium chloride (BC) was analysed by fluorescence (λ_{ex} 280 nm/ λ_{em} 330 nm) over concentration range of 4.5 µM to 2.2 mM. Fluorescence was recorded using 200 µl of each concentration in a 96 well plate (three repeats of each).

5.3.7.2 Benzethonium polymer bead production

Molecularly imprinted and non-imprinted beads were produced using the microfluidic/microwave system. The following experimental conditions were used:

- Aqueous phase: AAm 0.75 g (10.5 mmol); MBAam 0.3 g (2 mmol), DI water 5 ml; 1.5 ml MeOH; AAPH 6 mg (0.02 mmol)
- Organic Phase: toluene
- Aqueous phase flow speed: 1.5 ml hr^{-1}
- Organic phase flow sped: 3 ml hr^{-1}

Two distinct sets of beads were produced: NIP (plain polyacrylamide beads with no BC added) and MIP (polyacrylamide beads produced with BC added to the organic phase (13 µM BC; 100 µl per run)). Post production all beads were immersed in DI water for 24 hours with regular changing of water (every 8 hours) and filtering via Whatman 1 paper.

5.3.7.3 Benzethonium detection in washings

To eliminate detection of free BC (BC not removed during template removal stage) during binding studies, serial washings were analysed by fluoroscopy during a time frame reflective of the post-production handling of the manufactured beads (beads were washed over 24 hours).

5.3.7.4 Benzethonium bead binding studies

Binding studies were carried out using the beads produced in section 5.3.7.2. Standard solid phase extraction (SPE) cartridges with a filter placed at the distal end were also was cap sealed, 300 mg (wet weight) beads were then packed into SPE cartridges and incubated for 12 hours with incremental concentrations of BC solution. Filtrates were then analysed with fluorescence spectroscopy (λ_{ex} 280 nm/ λ_{em} 310 nm). Three repeats of each NIP and MIP cartridges were prepared. This experimental process is shown in figure 5.12.

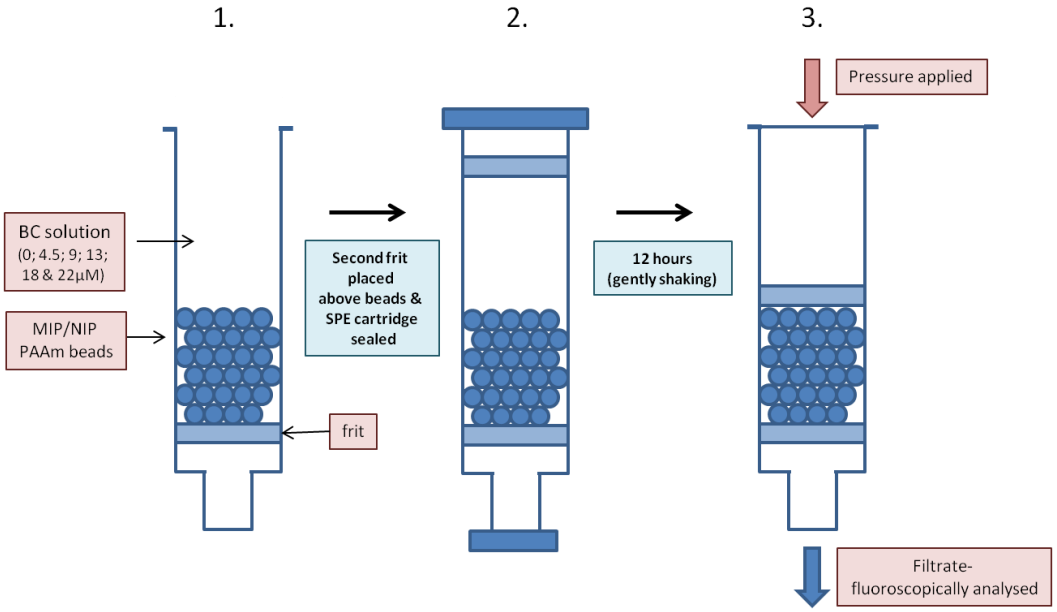

Figure 5.12: Schematic of BC binding experiment. **1.)** Polymer beads (NIP: plain PAAm beads; MIP: beads produced in the presence of BC in organic phase) were packed into SPE cartridge; **2.)** Known concentrations of BC solution were introduced to cartridges; **3.)** Following incubation overnight the filtrate was obtained by applying pressure to the top of the cartridge

The following concentrations of BC solution were used in the binding experiment (three repeats of each): blank (DI water only); 1 µ ml^{-1}; 2 µ ml^{-1}; 4 µ ml^{-1}; 8 µ ml^{-1} and 10 µ ml^{-1}.

5.4 Results and discussion

5.4.1 Material characterisation using microwaves

5.4.1.1 Dielectric characterisation

Results of relative dielectric loss measurements are shown in figure 5.13. Dielectric loss (ε'') was calculated using the equation 5.5 which describes the relationship between the following parameters: V_s: sample volume; V_e: Volume of resonant cavity x scaling factor (0.269); ΔBW: change in bandwidth and f: start frequency.

$$\mathcal{E}'' = \frac{\Delta BW}{f}\frac{Ve}{Vs} \tag{5.5}$$

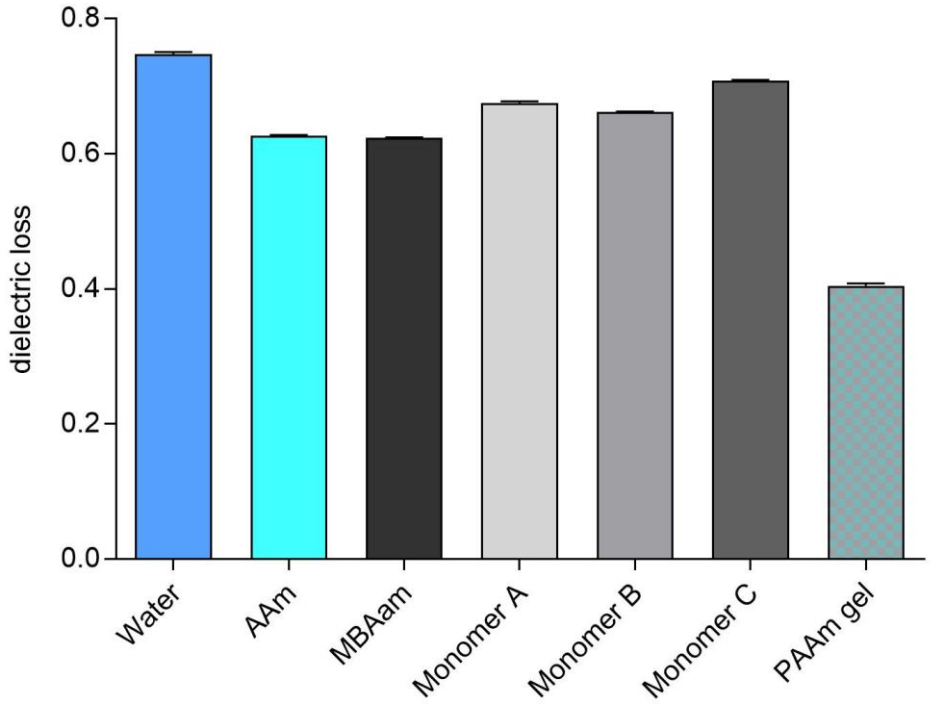

Figure 5.13: Dielectric loss measurements. AAm: 2 M solution AAm; **MBAam**: 2 M solution MBAam; **monomer solution A**: AAm 0.15 g ml^{-1}, MBAam 0.02 g ml^{-1}; **monomer solution B**: AAm 0.15 g ml^{-1}, MBAam 0.03 g ml^{-1}; **monomer solution C**: AAm 0.15 g ml^{-1}, MBAam 0.04 g ml^{-1}; **PAAm**: polyacrylamide gel formed from monomer solution B.

Table 5.2 shows the relative dielectric loss measurement (dimensionless parameter) for tested solvents.

Table 5.2: Relative dielectric loss measurements for four test solvents, shown as mean value, N=3.

Solvent	Relative dielectric loss (SD)
Water	0.7467 (0.0035)
Chloroform	0.1167 (0.0007)
Toluene	0.0056 ($6.05x10^{-5}$)
Hexane	0.0013 (0.0006)

The results from figure 5.13 and table 5.2 show relative dielectric loss measurements for a range of aqueous solutions and organic solvents. A significant result shown in figure 5.13 is the drop in relative dielectric loss seen between a non-polymerised monomer solution and the PAAm gel. As the solution polymerised, the inherent ability to absorb electromagnetic radiation decreased and the material became less efficient at converting microwave energy into heat. This was predicted considering the interaction of materials and microwaves on a molecular level. The heat generated as dielectric heating takes places is reliant on a molecule being able to orientate itself in parallel with an electric field. Once locked within a solid matrix, this ability decreases.

Tested solvents also demonstrated different relative dielectric loss measurements. Furthermore, the results were aligned with the polarity, and therefore electronegativity, of each solvent. Efficient volumetric heating of any given sample by microwaves is dependent on dielectric properties. Such properties will not only dictate the samples ability to be polarised (permittivity, ε') but how efficiently this absorbed electromagnetic radiation is converted to heat (loss factor, ε'') (1,62). Electronegativity is an important consideration when predicting the

behaviour of a dielectric. The Hildebrand Solubility Factor, the Rohrschneider Polarity Scale and calculations of dipole moments can all provide an overview from which prediction of behaviour when exposed to microwaves can be made. Table 5.3 shows electronegativity parameters for the organic solvents used in this study.

Table 5.3: Electronegativity parameters of the solvents used in section. [a] taken from (63,64) [b] taken from (64,65);[c] taken from (66); [d] calculated from (66) as one Debye unit = 3.34×10^{-30} Coulomb-metres.

Solvent	Hildebrand solubility [a]	Rohrschneider polarity scale [b]	Dipole moment ($\mu.10^{-30}$/cm) [c]	Dipole moment (debye units, D) [d]
Water	9.0	23.4	6.2	1.85
Chloroform	4.4	9.3	3.8	1.04
Toluene	2.3	8.9	1.0	0.36
Hexane	0.1	~ 8.0	0.0	0.0

Therefore, predictably from its high electronegativity, water demonstrated the highest dielectric loss when exposed to microwaves in comparison to other solvents in this study. Thereafter, chloroform, toluene and hexane demonstrated dielectric behaviour aligned with their polarity.

5.4.1.2 Cavity resonance perturbation

a. Organic phase studies

Shown in figure 5.14 are the resonance peaks for several organic solvents, showing changes in measured response of the cavity resonator at low power transmissions dependent on the solvent sample within the cavity.

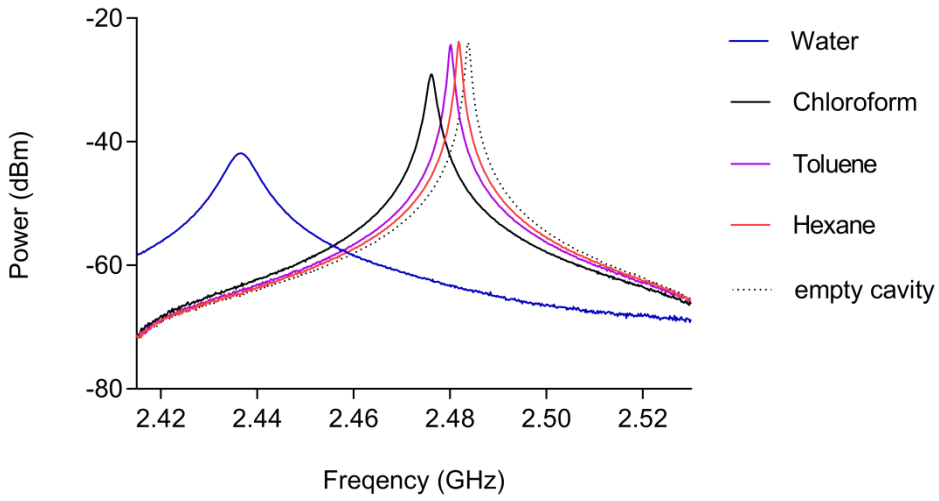

Figure 5.14: Central perturbation resonance peaks for a series of organic solvents prior to choosing the continuous (organic) phase of MF experiments. The dashed line represents the control which was an empty vial sat within the cavity resonator. The peak for water is also shown.

When the cavity was perturbed with solvents, change in resonant frequency was observed to be a function of increasing solvent polarity. This was demonstrated by a change in the measured response of the cavity resonator (at low power transmissions). Similar results have been demonstrated previously by studies using central perturbation capabilities to demonstrate differences in solvents (33,34,54). A rightward shift of the resonance curve (reduction in the peak curve amplitude) and a decrease in peak width can be observed when a series of organic solvents are compared to water.

Prior to experiments using a cavity resonator, on-bench studies integrating MF with a modified domestic microwave formed the bulk of initial studies. During these experiments chloroform was used as the organic phase. However, experiments with a microwave cavity resonator used toluene as the organic phase. Figure 5.15 shows comparison of resonance peaks for chloroform and toluene.

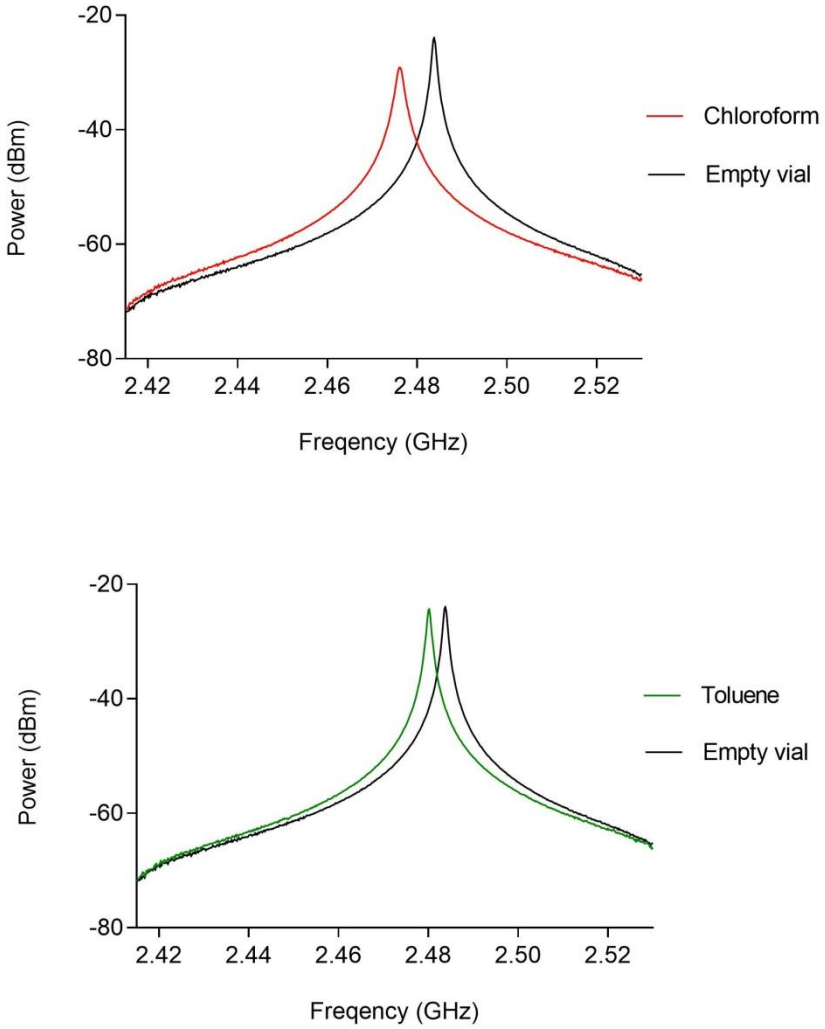

Figure 5.15: Comparison of resonance peaks from central perturbation measurements of an empty vial within the cavity (control) and chloroform (top) and toluene (bottom).

The shift seen between each organic solvent and water is of similar magnitude, therefore toluene was a suitable substitute for chloroform as a continuous phase in the MF/microwave experiments. Furthermore, problems were encountered during chloroform experiments with loss of segmented flow as chloroform approached its boiling point (61.2 °C). Therefore, a change to toluene was made considering its boiling point of

110.6 °C and relative dielectric loss (ε'') of 0.0056 compared to 0.117 for chloroform.

Interestingly, a recognised advantage of using microwave for organic synthesis is the ability to superheat solvents to temperatures beyond their boiling point, effectively negating the concern with solvent boiling points. However, this can only only take place in a sealed vessel (67,68). In 2001 Chemat and Esveld studied this superheating of solvents in detail and highlighted the ability to accelerate reactions due to this solvent superheating alone (69). However, in the system developed for this study, the polymerisation reaction cannot take place in a sealed system as the continuous flow and eventual emergence from the tubing of a polymer bead is the key to bead production. Therefore, boiling points of reactants were an important consideration.

The results shown in figures 5.14 and 5.15 allowed the rational choice of organic phase solvent for ongoing experiments. Overall, the aim was for microwave energy to be delivered with maximal efficiency to the segmented portion of fluid flow within the MF tubing (aqueous component). Therefore, choosing a solvent that had a dielectric loss (ε'') measurement far lower than that of water (is inefficient at converting microwave energy to heat) indicated energy would not be 'taken up' by the solvent and would be available to heat the aqueous phase, initiating polymerisation.

b. Aqueous phase studies

Shown in figure 5.16 are dielectric characterisation results from the aqueous reactants of subsequent MF/microwave polymerisation experiments. The effect on output transmission at low power inputs from the cavity resonator was tested depending on the presence of certain aqueous solutions.

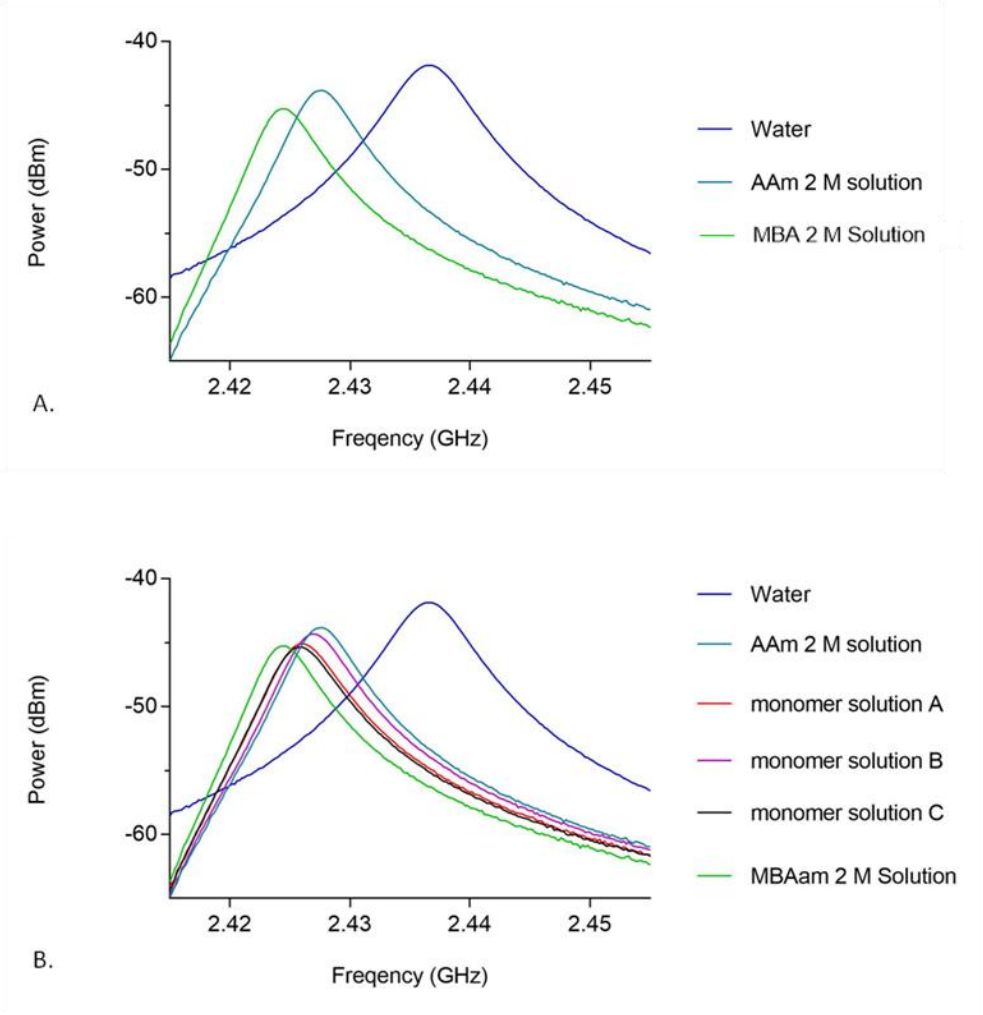

Figure 5.16 : **A.)** resonance graphs for aqueous monomer solutions used in ongoing experiments; **B.)** resonance peaks for three mixed monomer solutions. Monomer solution A: AAm 0.15 gml^{-1}, MBAam 0.02 gml^{-1}; monomer solution B: AAm 0.15 gml^{-1}, MBAam 0.03 gml^{-1}; and monomer solution C: AAm 0.15 gml^{-1}, MBAam 0.04 gml^{-1}.

The presence of both AAm and MBAam in solution caused greater perturbation of resonant frequency than that of water alone; the presence of monomers therefore affects the transmission output from the microwave cavity at a given power input.

As with interpretation of the perturbation results for organic solvents, the electronegativity of aqueous solutions was considered. The dipole moment

is an indicator of bond polarisation and therefore reflects the variation in electronegativity of constituent atoms. Overall molecule conformation and these electronegativity gradients are the key determents of the dipole moment which is measured in Debye units (1 Debye ≡ 3.34 x 10^{-30} coulomb-meters), for example water dipole moment is 1.84 Debye units. In comparison, Marstokk *et al.* measured the dipole moment of acrylamide (70), giving the overall measurement as 3.44 Debye units (planar geometry; carbonyl and vinyl groups in syn-conformation). It was expected, therefore, that the addition of a species with a high dipole moment (in comparison to water) would lead to an increased loss factor being observed and the output resonance of the cavity would demonstrate a decreased peak resonant frequency. This is indeed shown in the resonance peaks shown in figure 5.16.

5.4.2 Method development: system components

5.4.2.1 General overview

Chapter four described the manufacture of a microfluidic system capable of generating segmented flow. The dispersed phase (aqueous) travelled in the continuous phase (organic) following flow manipulation at a t-junction. For ongoing experiments, the system developed in chapter four required the integration of a 'polymerisation point' at which aqueous beads could be polymerised. Shown in figure 5.17 is the final iteration schematic of the integrated system.

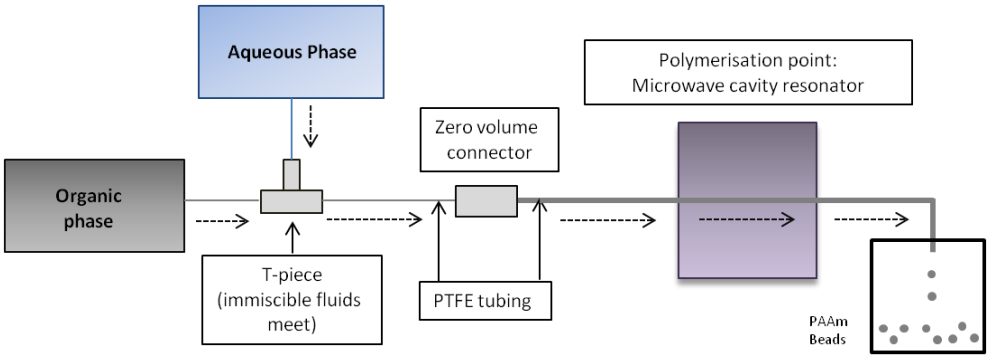

Figure 5.17: Schematic of the integrated MF/microwave system. As packets of aqueous monomer solution travel through the cavity they were subjected to microwaves and polymerisation is initiated. Transit through system is indicated by the dashed line. (PTFE: polytetrafluroethelene; PAAm: polyacrylamide).

5.4.2.2 Microwave delivery

The delivery of microwaves in experiments was with a cavity resonator described in section 5.1.4.4.

5.4.2.3 Tubing

The two key considerations for the tubing in relation to the microwave resonator were the proximity to the energy source and the microwave exposure time. Figure 5.18 shows an initial step in the configuration of tubing within the resonator, followed by the successful tubing arrangement shown in figure 5.19.

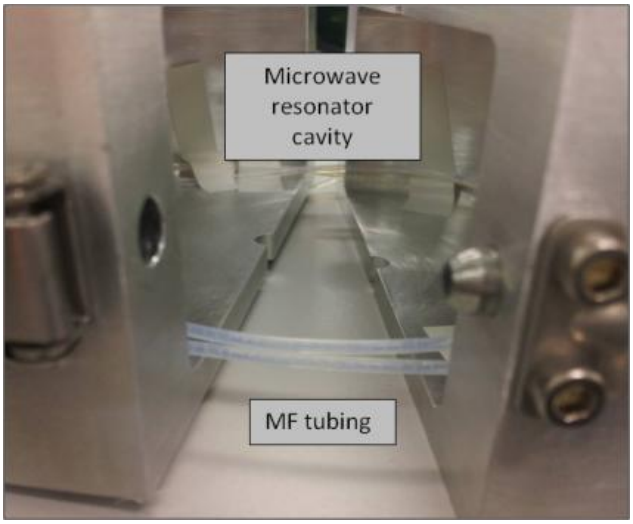

Figure 5.18: Example of initial experiment set-up where MF tubing is taped in concentric circle around the edge of the microwave cavity resonator.

As the microwave-initiated polymerisation protocol and microfluidic flow rates were optimised, the tubing arrangement shown in figure 5.18 was deemed unnecessary. These optimisation steps allowed the reduction of tubing length needed within the cavity to facilitate effective polymerisation of aqueous beads. Traversing of tubing through the 40 mm length of cavity via a central cavity port sufficed for this purpose. This arrangement is shown in figure 5.19.

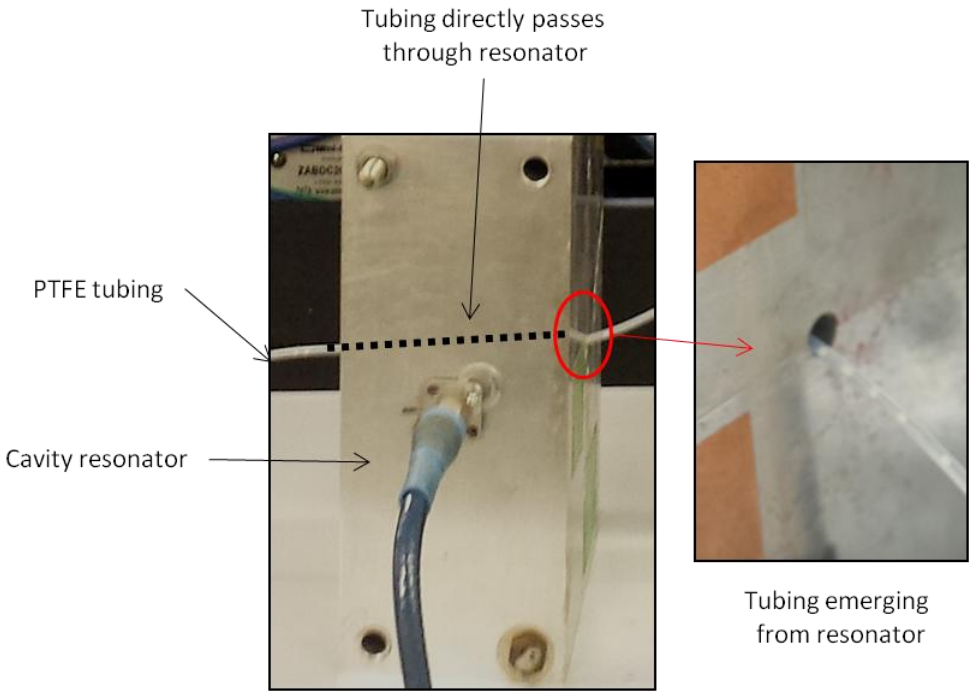

Figure 5.19: Optimised tubing configuration. The polymerisation protocol was optimised with the tubing simply traversing directly through the cavity (40 mm in cavity).

5.4.2.4 Temperature detection

An infrared camera was used to detect temperature of tubing prior to entry into the cavity resonator and for 12 cm following emergence. The temperature profile obtained from the camera is shown in figure 5.20.

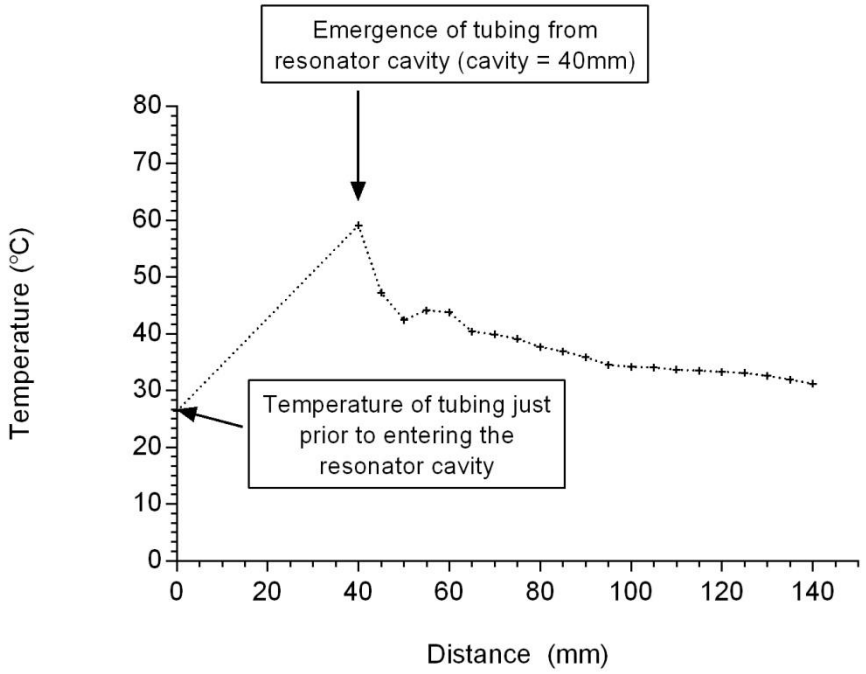

Figure 5.20: Temperature profile of MF PTFE tubing. At time zero the temperature indicated represents the temperature of the tubing just prior to entering the cavity resonator.

The sharp rise in temperature along the 40 mm length from entering the cavity to emerging is shown; the temperature of the tubing rises from 26.4°C to 59.1°C over this distance. Temperature then drops at a rate of approximately 0.28°C per mm along the tubing as readings are taken more distal to the microwave cavity.

However, the use of IR temperature detection in this study should be treated with caution. Previous work by chemist Oliver Kappe highlighted the unreliable nature of IR temperature detection in microwave assisted organic synthesis reactions (11,71,72). Essentially, Kappe firmly dissuaded the use of IR sensing in favour of fibreoptic temperature sensing.

Undoubtedly IR has limitations; however, in this study we are not comparing per se the polymerisation of acrylamide with conventional and microwave heating. The temperature comparison is an added measurement but not the overarching aim of this experimental section.

Therefore, the use of an IR camera as an available and accessible tool in this instance is justified. Furthermore, the creation of a temperature *profile* is an interesting finding rather than just actual figures obtained, allowing visualisation of the rapid heating and then cooling of the MF tubing as it traverses the microwave cavity.

The temperature generated by the cavity resonator was of paramount importance when choosing the solvent for the continuous MF phase (in terms of the proximity to solvent boiling point). Furthermore, the temperature was an important consideration regarding the choice of initiator species. The initiator used in these experiments was 2'2' azo (2-methyl-propionamide) dihydrochloride (AAPH), a free-radical initiator that decomposes on exposure to UV and heat. AAPH can spontaneously decompose at 37-40 °C to give free radical species (73,74), a reaction that is also pH dependent (73). However, polymerisation reactions at temperatures above the decomposition temperature of AAPH have been reported (75–77). Furthermore, an important consideration concerning choice of initiator is $t_{1/2}$ value (time required to reduce the initial initiator content of a solution by 50%, at a given temperature) and AAPH has a 10 hour $t_{1/2}$ temperature of 56 °C in water.

5.4.2.5 Miscellaneous components

The bead generating system is dependent on optimisation of all components, including syringe drivers and choice of syringe. Syringe drivers are an integral part of the MF system and must have quick response time when settings are changed and also have a smooth, 'ratchet' free motion when in action. Segmented flow generation can be markedly disrupted if the driver fails to deliver a smooth forward motion.

In their 2014 paper, Li *et al.* quantified the fluctuations seen in MF flow secondary to the pump motor by looking at ripples at the interface of two

co-flowing liquid streams (78). The liquid/liquid interface in this Li *et al.* experiment was designed to have low interfacial tension therefore this interface was easily disturbed by flow fluctuations (group use polyethylene glycol 17% and tripotassium phosphate with an estimated IF tension of 0.03 mN m^{-1} (79)). Li *et al*. correlated the amplitude of ripples generated to syringe pump motor function, concluding these ripples would be masked in systems with liquid/liquid interfaces of higher IF tension. The IF tension between water and toluene (the liquids used in the experiments described in this chapter) is estimated at 37.3 mN m^{-1} (at 20 °C, averaged over pH 4-9 (80)). Therefore, considering this higher IF tension value, it is plausible that small disturbances in flow due to pump motor function may be undetectable to the naked eye.

The material of syringe for both the aqueous and organic phases was glass, offering smoother flow than polymer syringes. Friction between the plunger and inside walls of glass syringes is lower than that for plastic syringes. For routine use this is inconsequential, but when used to drive small volumes of fluid through microfluidic channels, the smoother flow seen with glass syringes is beneficial.

5.4.3 Microwave-initiated polymerisation

5.4.3.1 Polymerisation protocol development

Whilst directly observing for the emergence of white polymer beads from the cavity resonator within the MF tubing, the following microwave delivery parameters were investigated: duration (ms); power (dBm); pulse period (ms) and high time (ms). *Duration* refers to the total cycle time, *power* refers to the applied microwave power measured in dBm (decibel-milliwatts), *pulse period* refers to the duration in milliseconds of each sub-cycle during overall duration and the *high time* refers to the amount of

time during this that the power is applied (forming the duty cycle, figure 5.21).

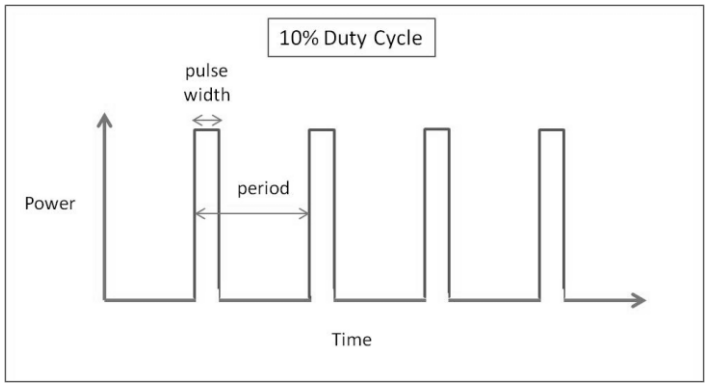

Figure 5.21: Representation of a duty cycle. In the finalised microwave-initiated polymerisation protocol a 10% duty cycle was used (in a 100 ms cycle, power is delivered for 10 ms).

These parameters were systematically tested in various combinations with observation of the corresponding segmented flow appearance within the MF tubing. During initial microwave protocol experiments, runs produced liquid output (no polymerisation) or weak 'beads' that disintegrated within minutes of being expelled from the MF tubing (inadequate polymerisation). Also observed was the production of seemingly intact polymer beads that would amalgamate post production and therefore had a short shelf life, not allowing post production use for binding studies. However, eventually the production of robust polymer beads was observed under the conditions of microwave delivery shown in table 5.4.

Table 5.4: The finalised microwave-initiated polymerisation protocol.

Phase	Duration (ms)	Back off power (dBm)	Pulse period (ms)	High Time (ms)
Resonance sweep	100	0	0	0
Modulation	5000	6	100	10
Resonance sweep	100	0	0	0
Modulation	5000	6	100	10
Resonance sweep	100	0	0	0
Modulation	5000	6	100	10

This finalised protocol was the result of successive systematic experiments to find the optimal settings of the following parameters: energy supplied (dBm off maximum); total period of protocol (ms); duty cycle (ratio of the duration of the energy delivered to the total period of a signal); addition of resonance sweep. Through the course of these experiments it became evident the most influential factor in achieving effective polymerisation was the control of heating by varying the duty cycle of the microwave radiation.

5.4.3.2 Manufactured polymer beads

Once the protocol shown in table 5.4 was found to reliably result in the emergence of polymer beads from the microwave cavity the manufacture of PAM beads could take place. The change in colour from clear to white polymer was obvious to the naked eye and indicated successful polymerisation (figure 5.22).

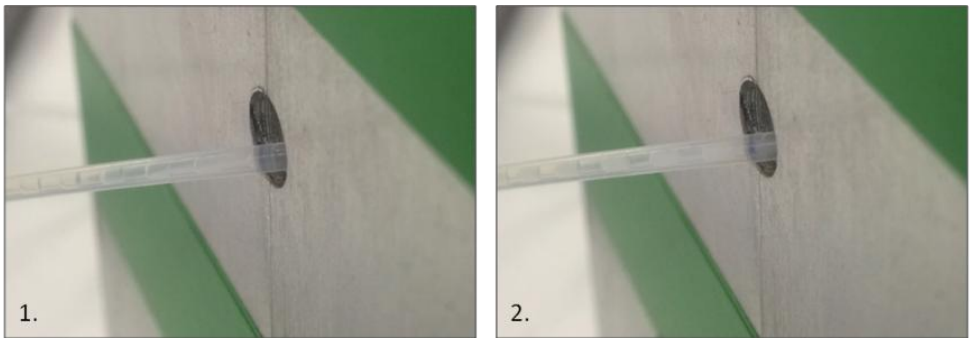

Figure 5.22: Photograph documentation of the microwave polymerisation protocol at work. **1.)** Segmented flow can be seen in the MF tubing as it emerges from a microwave cavity resonator. **2.)** Following commencement of polymerisation protocol these clear 'beads' travelling in the tubing can be observed transforming from clear to white.

As an example of early polymer production, figure 5.23 shows the appearance of successfully polymerised aqueous 'slugs' in the experimental stages during which the MF flow dynamics and microwave-initiated polymerisation protocol were still being optimised.

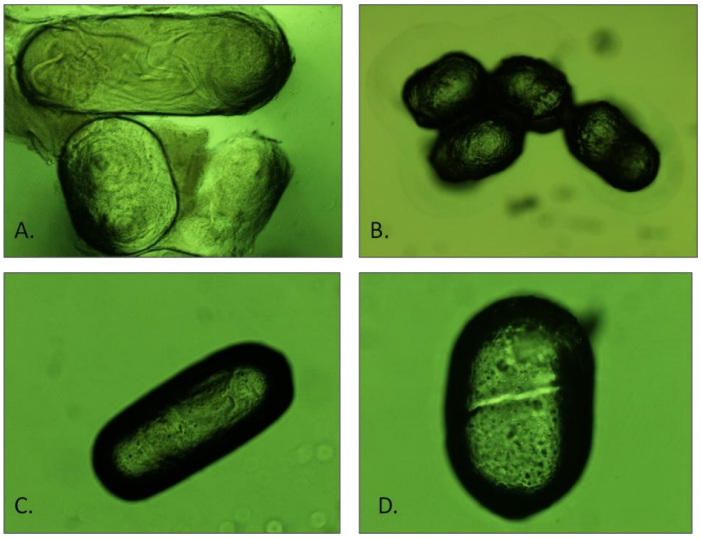

Figure 5.23: Photographs of early 'slugs' produced with the integrated MF/microwave system and using the microwave protocol in early stages of development.

Figure 5.24 shows beads representative of those produced in later experimental stages.

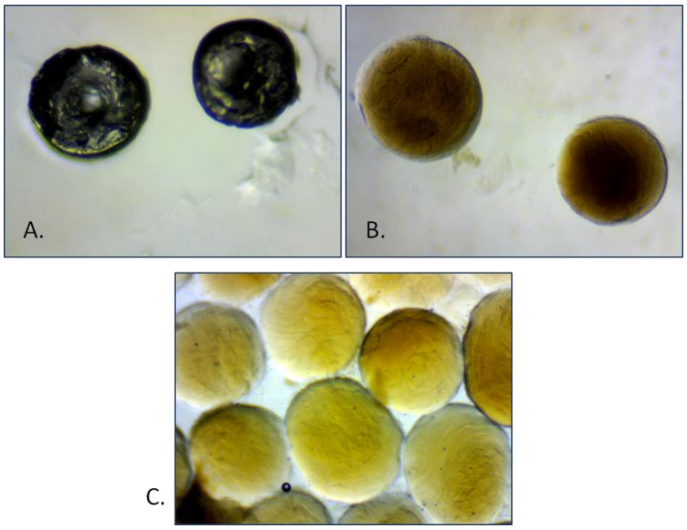

Figure 5.24: Photographs of polymer beads produced in later experimental stages and representative of polymer beads produced in benzethonium chloride experiments.

Comparison of the polymer beads in figures 5.23 and 5.24 demonstrates the progression from polymer slugs to the production of spherical polymer beads as the system was optimised.

5.4.4 Dynamic polymerisation sensing

Previous experimental sections have looked at individual reactants and how their dielectric properties dictate interaction with microwaves. Taking this sensing capability in a different direction, it was hypothesised the formation of the polymer could be monitored using the changing dielectric properties of the material as polymerisation progressed. Furthermore, it was thought it may have been possible to distinguish between levels of crosslinking dependent on the material's dielectric properties.

Shown in figure 5.25 is the comparison of cavity perturbation measurements of polymers with differing degrees of crosslinking (shown by a change in the measured response of the cavity resonator at low power transmissions). These resonance peaks are compared to those of water, an empty glass vial and PTFE tubing.

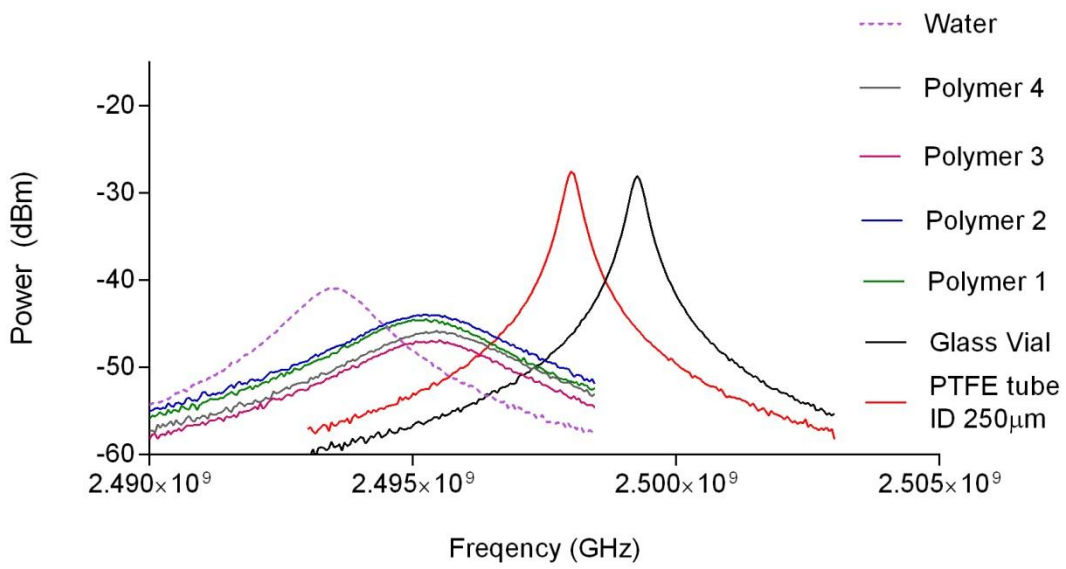

Figure 5.25: Resonance peaks for dynamic polymerisation sensing experiments. **Polymer 1:** 0.75 g AAm, no crosslinker); **polymer 2:** 0.75 g AAm, 0.2 g MBAam; **polymer 3:** 0.75 g AAm, 0.3 g MBAam; **polymer 4**: 0.75 g AAm, 0.4 g MBAam

Figure 5.25 demonstrates a shift downwards in resonance frequency for *all* polymers in comparison to water, reflecting a reduction in peak curve amplitude. Furthermore, resonance peak widths for all polymers are increased in comparison to water. It is interesting to compare these findings with the resonance peaks shown in figure 5.16; in solution monomers demonstrated a decrease in peak curve amplitude compared to water, however, when these monomers polymerise the curve amplitude increases reflecting a reduced ability to damp the resonance of the system. This is explained by polymer matrix formation and increased crosslinking reducing the ability of polar molecules to agitate when exposed to an

oscillating E-field. Permittivity therefore decreases as less energy can be stored in the material and energy is dissipated.

Monomer solutions with differing concentrations of crosslinker (MBAam) were purposefully used in these experiments. However, unfortunately this method of dynamic polymer sensing using low power microwave transmissions was not sensitive enough to detect any changes in perturbation secondary to degree of polymer crosslinking. However, the possibility of being able to track the formation of a polymer using changing dielectric properties was still of interest.

From the tested polymers shown in figure 5.25, polymer four was used for a polymerisation tracking experiment. Polymer 4 as tested (200 µl) constituted the following: AAm 0.024 g (0.34 mmol); MBAam 0.0124 g (0.08 mmol); and AAPH 0.18 mg (0.68 µmol). Shown in figure 5.26 are the resonance peaks measured from the microwave cavity every five minutes for one hour as the solution polymerised. There are clear differences in peak amplitudes between the polymer when at an early aqueous/gel stage (up to 10 minutes) and when a white solid polymer has formed.

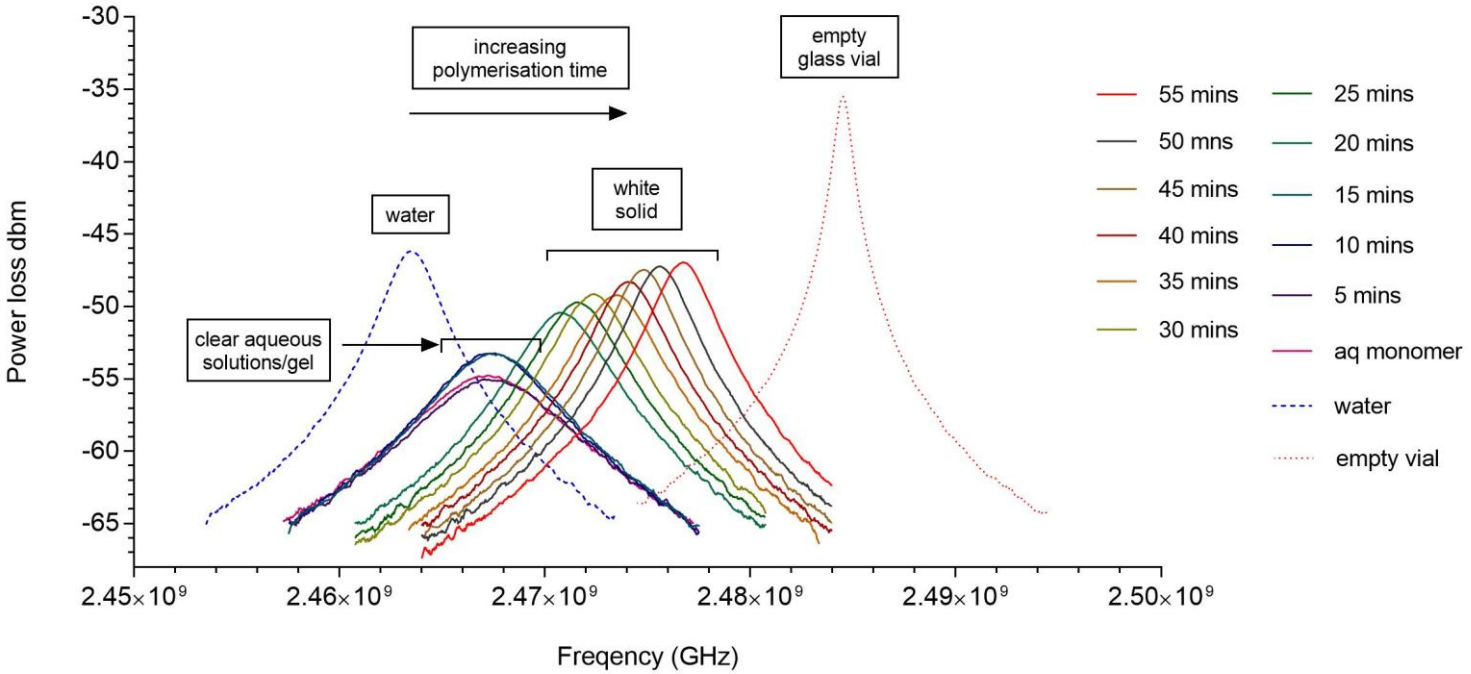

Figure 5.26: Resonance peaks from central perturbation measurements for polymer four (0.75 g AAm, 0.4 g MBAam, 5ml DI water and 1.5 ml MeOH, 200µl). As the polymer cured in a heat sink at 60˚ C the vial was swiftly transferred to the resonant cavity and a resonance peak was measured at the indicated time intervals. A clear distinction between the gel/clear stages and the opaque stages is seen.

Figure 5.27 shows how the *Q* factor of the sample changed from 366 to 940 (mean, n=3) as the polymerisation time increased. This is reflected in the peak morphology shown in preceding figure 5.26 (as *Q* factor increased, the resonance peaks became sharper).

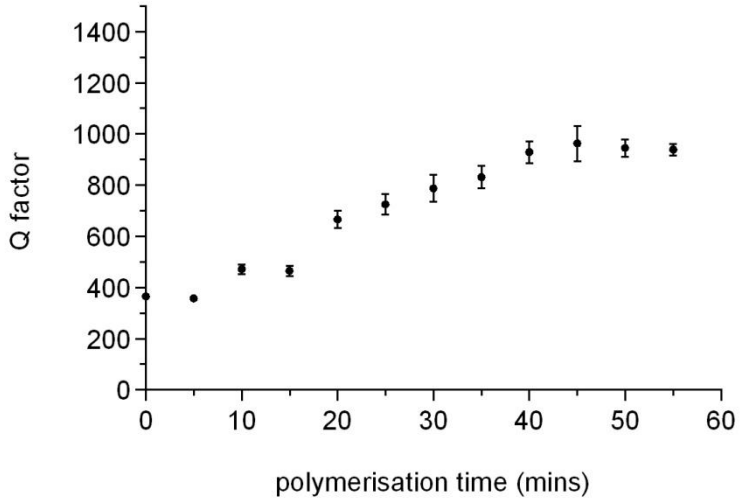

Figure 5.27: Change in *Q* factor of resonant cavity as polymer forms (conventional heating, 60°C heat sink)

As polymerisation proceeded there was a step-wise change in the dielectric properties of the material, evidenced by a change in resonance of the system.

The temperature dependence of the central perturbation measurement is an important consideration. Cavity resonators are carefully designed considering the dependence of the cavity resonant frequency on cavity dimensions (14,18,81). Therefore, dimension change caused by thermal expansion of a metal cavity may contribute to shifts in resonant frequency observed when a sample is introduced; the reason for change is then a temperature affect only, not a change in the dielectric properties of the sample (81). The relationships between temperature of the cavity and changes in the cavity radius (*a*) are shown in equation 5.6a and 5.6b (81).

These equations demonstrate the linear nature of thermal expansion due to temperature increase

$$\Delta a = a(T) - a_0 \tag{5.6a}$$

$$\Delta f = f(T) - f_0 \tag{5.6b}$$

where Δa and Δf represent the change in cavity radius and resonant frequency, respectively; *a(T)* represents the cavity radius at any given temperature; $f(T)$ is the cavity frequency at any given temperature; and the initial cavity dimensions and frequency are represented by a_0 and f_0.

However, the change in resonant frequency of the cavity due to any thermal expansion dimension changes is a negative relationship; cavity resonant frequency decreases with thermal expansion. This is demonstrated in equation 5.7 (82):

$$\frac{\Delta f}{f_0} \approx -\frac{\Delta a}{a_0} \tag{5.7}$$

where f is measured resonant frequency; f_0 is the initial resonant frequency; a_0 is the initial cavity radius; and the cavity radius at any given temperature is a. Therefore, any increase in cavity dimensions due to thermal expansion causes a decrease in cavity resonant frequency (*f*).

The logistics of this experiment involved the transit of the vial containing developing polymer from a heat sink to the resonator with a transit time of approximately two seconds. This may have introduced sample temperature fluctuations as the vial cooled on emergence from the 60 degree heat sink. Despite fluctuations in temperature on exposure to room temperature, cumulatively the temperature of the vial is *increasing* over the time of the experiment. However, once the vial was placed in the cavity following transit from the heat sink, cavity resonance data acquisition time was minimal (of the order of seconds); therefore, the likelihood of a significant thermal expansion (enough to cause dimension changes in the cavity and

affect the resonant frequency) in this time is low. The increase in resonant frequency shown in figure 5.26 is therefore caused by changes in dielectric properties of the sample.

Furthermore, resonant frequency is also dependent on the size of the sample. However, this can be ignored when considering that the size of the cavity is far greater than that of the sample and its relative affect is minimal (82). The temperature generated by polymerisation within the sample vial is also a consideration. The mainstay of dielectric characterisation by central perturbation measurement research is focused on the characterisation of materials having completed any formation reactions, rather than the reaction itself. However, temperature correction with consideration of the enthalpy change of an ensuing reaction within the cavity has previously been employed by researchers (83). The polymerisation of AAm crosslinked with MBAam is an exothermic reaction with an enthalpy of polymerisation of AAm of 17-20 kcal mol^{-1} (84,85). However, considering the reaction ongoing in the glass vial placed in the cavity resonator contained 0.34 mmol of AAm, even at 20 kcal mol^{-1} the enthalpy of polymerisation would have been 6.8 cal (equivalent to 28.5 joules). Much like the contribution of the sample size, this parameter would have negligible effect on any thermal expansion of the microwave cavity resonator and therefore on any observed change in resonant frequency.

In order to reduce any temperature fluctuations caused during sample transit, polymerisation sensing was then carried out with the cavity resonator kept in a temperature-controlled environment (i.e. a finely controlled scientific oven).

5.4.5 Polymerisation sensing experiment in oven

The resonator was placed in a bench top oven allowing accurate temperature sensing and measurement of permittivity (ε') and loss factor (ε''). This experiment used the same monomer solution used to generated results in section 5.4.4 (0.75 g AAm, 0.4 g MBAam, 5 ml DI water and 1.5 ml MeOH (200 µl)) and polymerisation took place in the resonator. Measurements were taken over 18 minutes (time point chosen as white polymer had formed by this time point and the early stages of polymer formation were studied).

A fibreoptic pyrometer recorded temperature of the resonator inside the oven, providing the temperature profile shown in figure 5.28.

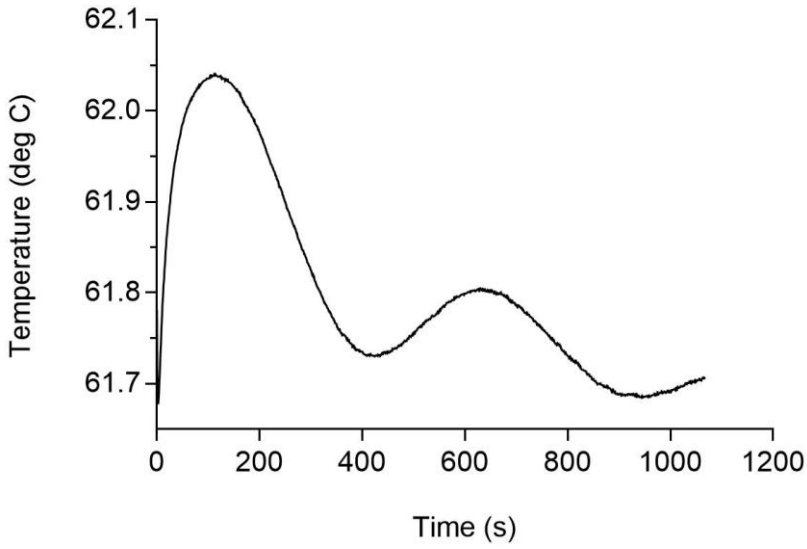

Figure 5.28: Temperature profile from the cavity resonator that was in a bench-top oven.

Fluctuations in the temperature correspond to the oven door opening (sample placed in resonator; temperature briefly falls) and then shut again (temperature rises). Temperature sensing in this experiment followed recommendations from several reviews about the accurate recording of

temperature in microwave-initiated organic reactions (11,67,71,72); the thermometer was fibreoptic, rather than infrared.

Shown in figure 5.29 are the ε' and ε'' values obtained from the sensing of polymerisation within the glass vial in the resonator (that was in-turn in an oven). These dielectric properties were recorded over 1068 seconds.

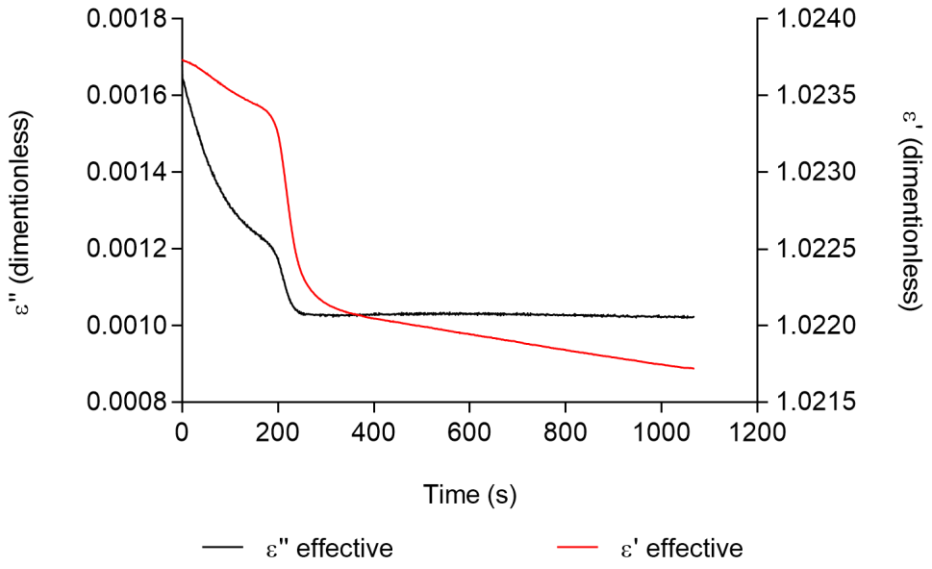

Figure 5.29: Graph showing ε' (real part permittivity) and calculation of ε'' (imaginary part permittivity- dimensionless parameters) of polymer sample as it forms within the cavity resonator.

From 0 to 200 seconds the sample begins to heat and polymerisation begins. Interestingly, a definite step change can then be seen at 200 seconds which could represent a phase change. The rates of change for both parameters dramatically decrease following the step change, ε' continues to fall do a greater degree than the small drop seen in dielectric loss (ε''). Initially as water in the sample is heated, absorption of microwave energy is high due to low opposition to electromagnetic energy (permittivity reflects a material's opposition to electric field). However, as polymerisation takes place and a phase change is potentially seen, the

material begins to establish opposition to electric field which is reflected by a slowing of the drop in permittivity seen in figure 5.27.

The ability to detect small changes in flux generation at early polymerisation is a highly interesting prospect. Brown *et al.* demonstrated a difference between polar and non-polar monomers and their behaviour under microwave irradiation. By comparing polar (methyl acrylate and methyl methacrylate) and non polar (styrene) monomers polymerised by microwaves and conventional heating they observed an increase in polymerisation rate for the polar monomers under microwave irradiation but not for the non-polar monomers (86).

The data shown in figure 5.29 supported the hypothesis that observed shifts in resonant frequency perturbation by the sample were resultant of changes in sample dielectric properties and not simply a reflection of temperature change. This can be further explained by figure 5.30 showing temperature at permittivity plots.

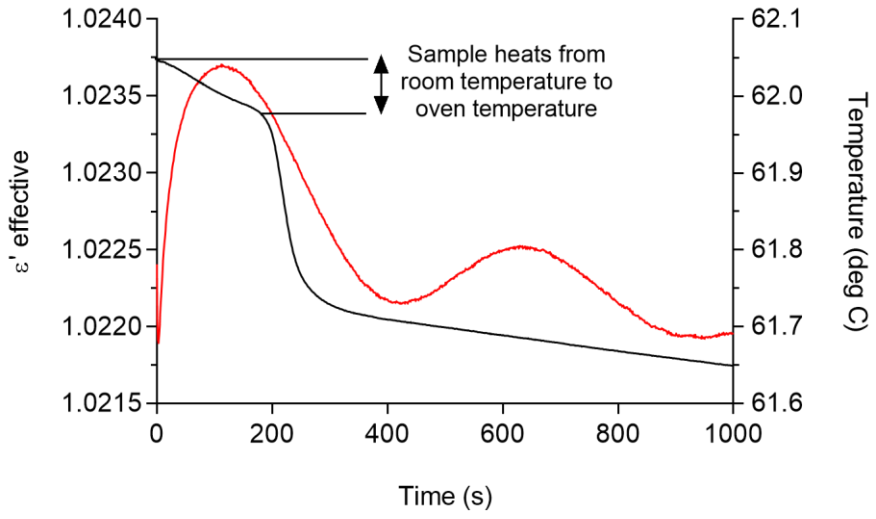

Figure 5.30: Graph showing ε' (real part permittivity) of sample as it polymerises within the cavity resonator (which in-turn is placed in an oven) compared to the temperature fluctuation within the oven

Figure 5.30 shows the change in sample ε′ when placed into the cavity resonator from room temperature. Room temperature in this environment was 19 to 21°C. The sample then increased in temperature reaching approximately 62 °C as it sat within the cavity. Therefore, at the lower room temperature estimate of 19 °C, a temperature increase of 43 °C corresponded to a change in ε' from 1.0237 to 1.0232 at 200 seconds, giving a rate of ε′ change of approximately 0.0000116 per degree rise in temperature. At 1000 seconds ε′ is 1.0217 (-0.002 from time zero) this change in ε′ would therefore have corresponded to a temperature of approximately 172 °C; well above the boiling point of any water still remaining in the sample. Considering there was no boiling or destruction of the sample, the measured decrease in ε′ as temperature rises is due to changes in dielectric properties of the sample and not merely a reflection of increased temperature.

A vast amount of literature concerning microwave-initiated polymerisation makes no reference to the sensing capability of microwaves; they are used as a heating tool only. However, microwave dielectric loss spectroscopy is a tool employed by several groups to characterise a variety of materials including natural rubber/carbon composites (87), titanium dioxide disks (88), magnesium titanate powder (89), and even fruit, meat and grain (for quality control purposes) (90–92). Dielectric sensing using broadband dielectric spectrometers is also used to provide dielectric characterisation, and this method has been used for polymers. However, this method has been employed only once the polymer composite has been formed, rather than during the polymerisation process itself (93–95). Therefore, this work offers an interesting application of microwave sensing to track polymer formation.

5.4.6 Molecular imprinting experiments

5.4.6.1 Benzethonium chloride analysis (LPS surrogate template)

The chemical structure of LPS consists of a hydrophilic polysaccharide and a hydrophobic lipid portion (lipid A); therefore, LPS is amphipathic in nature. This structural arrangement determines conformation and activity of LPS and is a key consideration for the investigation of LPS interaction with antibiotics and host immune cells. Benzethonium chloride (BC), a quaternary ammonium salt, has an amphipathic structure and was used a as a surrogate for LPS as a template in the molecular imprinting process. The structure of BC is shown in figure 5.31.

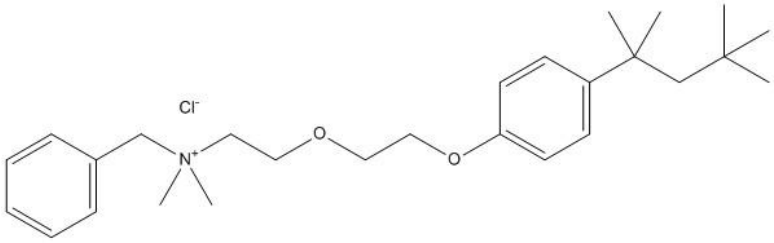

Figure 5.31: Structure of Benzethonium Chloride. (benzyldimethyl [2-[2(p-1,3,3,3-tetramethybutylphenoxy) ethoxy] ethyl]-ammonium chloride).

To ensure accurate detection of BC in the filtrate of binding experiment samples, the limitation of fluorescence detection of BC using available analysis equipment was established. Previous studies concerned with the detection of BC have established a fluorescence profile. For example, Karumbamkandathil *et al.* investigated the shape transformations of BC micelles, using BC purchased from the same supplier (96). Using an excitation wavelength of 270 nm, an emission maxima of 307+/- 1 nm was observed for all BC samples analysed in this study over the concentration range of 0.035 mM to 4.13 mM (96). Therefore, BC was analysed by fluorescence (λ_{ex} 280 nm/ λ_{em} 330 nm) over concentration range of 4.5 µM to 2.2 mM. Figure 5.32 shows a series of calibration curves obtained from

the fluorescence analysis of various concentrations of BC solution, from µM to mM concentrations. All calibration data were fitted with linear regression and coefficient of determination (R^2) values determined.

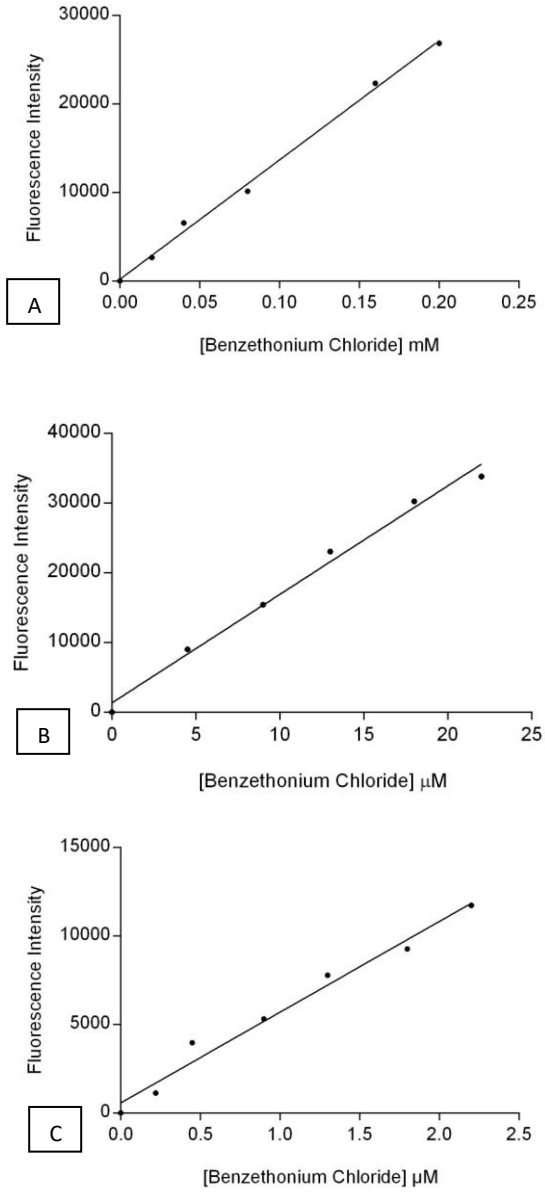

Figure 5.32: Calibration curves of fluorescence intensity (arbitrary units) as a function of BC concentration.
All samples were analysed at λex 280 nm/ λem 330 nm. Equation of the lines and R2 values were as follows **A)** y= 107651x + 158.4; R2: 0.999; **B)** y= 1556.7x + 1336.2; R2: 0.990; and **C)** y= 5127.4x + 567.7; R2: 0.977.

Shown in figure 5.32, the coefficient of determination (R^2) values for calibration graphs demonstrated data fitted well within the graph equation and therefore ongoing accurate determination of values obtained from binding studies was possible.

5.4.6.2 Benzethonium chloride imprinted polymer bead production

The aim of this experimental section was the successful production of molecularly imprinted polymer beads that could subsequently bind to BC. Shown in figure 5.33 is a highly simplified schema of the theoretical interaction of BC at the aqueous/organic interface.

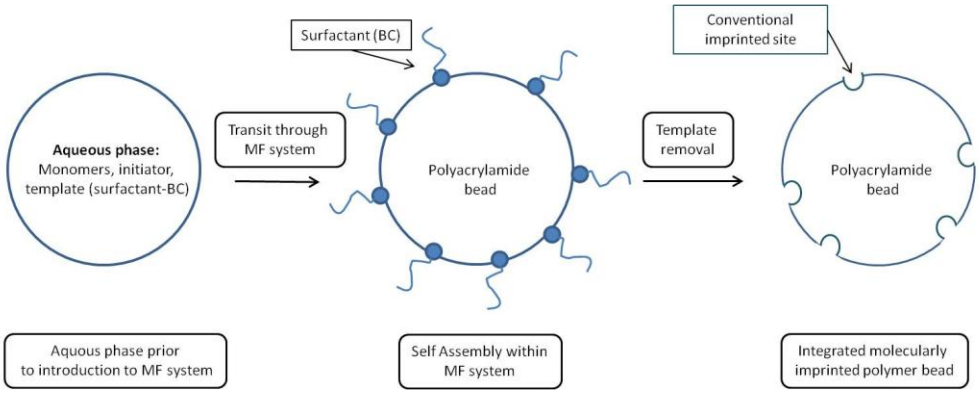

Figure 5.33: Schematic representing method of polymer bead production capable of subsequent BC detection. Microfluidic and microwave integrated system was utilised for this specialised bead production. Highly simplified and theoretical surface interaction shown, representing the self assembly (at a liquid-liquid interface) step of an imprinting process. The amphipathic nature of BC lends itself to the arrangement shown at the interface between the aqueous bead and the organic carrier phase.

The interaction of surfactants and polymers has been extensively reported and several comprehensive reviews on the subject published (97–99), however, studies are typically concerned with surfactant interaction with a formed polymer; not with interactions as the polymer is forming (as in this

study). When discussing polymer/surfactant interaction the critical aggregation concentration (CAC) is an important factor. The CAC is the surfactant concentration at which the polymer becomes saturated with surfactant (100,101). It is widely accepted that CAC is lower than CMC and it is not until this CAC is reached that the optimal polymer/surfactant interaction take place (101). CMCs of cationic surfactants (such as BC) are higher than that of zwitterionic surfactants (102,103), therefore, perhaps promotion of surfactant/ polymer interaction is easier with cationic surfactants considering their relatively higher CMCs.

5.4.6.3 Benzethonium detection in washings

It was important to show in binding studies that any BC detected in the filtrate of study samples was not merely BC leaching from a BC MIP. Shown in figure 5.34 are the absorbance profiles (at λ280 nm) of serial samples analysed during the washing stages post MIP and NIP bead production.

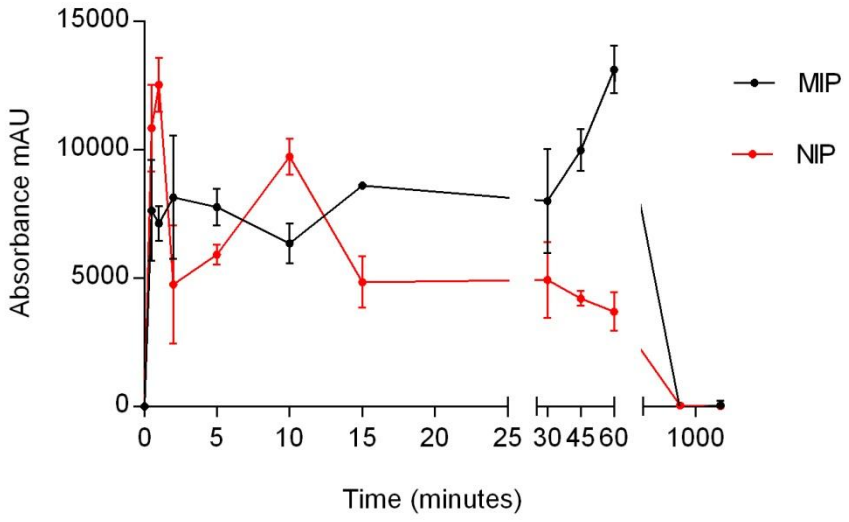

Figure 5.34: Absorbance (arbitrary units) of washing samples at 280 nm (reflecting the presence/or not of BC). Multiple serial samples were taken to track the effectiveness of the template removal washing stage.

Marked variation is seen in sample absorbance at 280 nm for both MIP and NIP in the first 60 minutes. Results in the first 15 minutes are interesting as seemingly washings from NIP polymer beads (beads prepared with no BC present) also showed absorbance levels in keeping with BC detection. This is most likely due to the presence of un-reacted monomers or small particles of polymer that also demonstrated absorption at 280 nm. Results then deviate between 30 and 60 minutes and, as expected, washings from the MIP polymer show increased absorbance at 280 nm compared to those from the NIP washings. Absorbance then decreases to baseline when washings from an extended time period are analysed. Analysis in this way is not quantitative, but shows BC removal using washing protocol used in binding experiments.

5.4.6.4 Benzethonium chloride imprinted bead binding studies

A binding study was carried out to investigate the ability of MIP beads to detect BC using NIP beads as control. Packed into SPE cartridges, both sets of beads were exposed to various concentrations of BC solution and binding capability analysed by fluorescence. Figure 5.35 shows the results of this binding experiment with binding isotherms for both MIP and NIP.

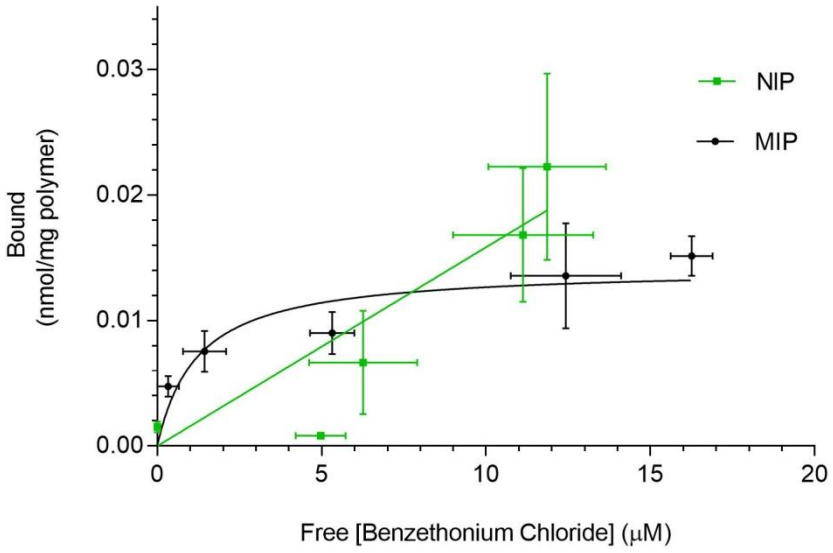

Figure 5.35: Binding isotherms for BC MIP and NIP showing the amount of BC bound to polymer (nmol per mg of polymer) at μM free concentrations of BC.

The two binding isotherms shown in figure 5.35 demonstrated markedly different morphology. The curved isotherm for MIP binding is compared to a straight-line for NIP binding. The derived binding performance data for MIP binding were as follows: B_{max}: 0.014 nmol/mg polymer and K_d: 1.217 μM (analysis of binding performance data was carried out with GraphPad Prism® V8 software from single-site specific binding curve fitting algorithm). The binding results for NIP showed a linear isotherm from which binding performance parameters could not be derived; results for NIP were therefore suggestive of non-specific binding (unsaturatable system) and the result of low affinity binding sites in abundance. This is in comparison to the curved isotherm seen for MIP/BC interaction, which suggests the presence of binding sites within the MIP bead.

However, interpretation of these results are somewhat guarded for two main reasons. Firstly, wide error bars are apparent (for NIP more than MIP) and secondly, investigating results at lower concentrations would be desirable. Nevertheless, results shown in figure 5.35 are encouraging; they

indicate a difference in the binding capability of the two differently manufactured polymers and indicate the ability of a MIP produced in a novel MF/microwave system to bind its original target molecule.

5.5 Chapter conclusions

Presented here are several approaches to circumvent problems encountered in the molecular imprinting of a complex molecule. The molecular imprinting process had moved towards self assembly of template and functional monomers at a liquid/liquid interface, therefore a microfluidic system was developed (chapter four) to promote this process. The main problem to overcome was initiating polymerisation within microfluidic tubing and the development of an integrated MF/microwave cavity resonator system for the manufacture of polymer beads is described in this chapter. Furthermore, the ability to measure dielectric properties whist polymerising samples allowed dynamic dielectric characterisation of the polymerisation process.

This chapter demonstrates the versatility of microwave-initiated polymerisation with the combination of microwave heating and polymerisation with microfluidics, building on previous work of our partner engineering department showing efficient heating of MF systems by microwaves (54). In this work Morgan *et al*. demonstrated efficient heating of microfluidic systems with using a high *Q* cavity resonator, they also utilised the sensing capability of the system obtaining permittivity data on a range of organic solvents.

The use of microwave irradiation to assist polymer synthesis is not new; it is undertaken on a large scale by groups dedicated to this field of organic synthesis chemistry (11,16,104). However, the use of microwave sensing applications is relatively underrepresented in the literature considering the scale of microwave assisted polymerisation. This chapter documents utilisation of microwave resonant cavities to measure polymerisation process dynamics on a small scale, alluding to interesting further scope of microwave sensing.

5.6 References

1. Stuerga D. Microwave–Materials Interactions and Dielectric Properties: From Molecules and Macromolecules to Solids and Colloidal Suspensions. In: Microwaves in Organic Synthesis. Wiley-VCH Verlag GmbH & Co. KGaA; 2012. p. 1–56.

2. Gawande MB, Shelke SN, Zboril R, Varma RS. Microwave-Assisted Chemistry: Synthetic Applications for Rapid Assembly of Nanomaterials and Organics. Acc Chem Res. 2014 Apr 15;47(4):1338–48.

3. Wiesbrock F, Hoogenboom R, Schubert US. Microwave-Assisted Polymer Synthesis: State-of-the-Art and Future Perspectives. Macromol Rapid Commun. 2004;25(20):1739–1764.

4. Thostenson ET, Chou T-W. Microwave processing: fundamentals and applications. Compos Part Appl Sci Manuf. 1999 Sep;30(9):1055–71.

5. Hoz A de la, Díaz-Ortiz Á, Moreno A. Microwaves in organic synthesis. Thermal and non-thermal microwave effects. Chem Soc Rev. 2005 Jan 25;34(2):164–78.

6. Lew A, Krutzik PO, Hart ME, Chamberlin AR. Increasing Rates of Reaction: Microwave-Assisted Organic Synthesis for Combinatorial Chemistry. J Comb Chem. 2002 Mar 1;4(2):95–105.

7. Tierney J, Lidström P. Microwave Assisted Organic Synthesis. John Wiley & Sons; 2009. 293 p.

8. Razzaq T, Kappe CO. On the energy efficiency of microwave-assisted organic reactions. ChemSusChem. 2008;1(1–2):123–32.

9. Johnston K, Pavuluri SK, Leonard MT, Desmulliez MPY, Arrighi V. Microwave and thermal curing of an epoxy resin for microelectronic applications. Thermochim Acta. 2015 Sep 20;616:100–9.

10. Koopmans C, Iannelli M, Kerep P, Klink M, Schmitz S, Sinnwell S, et al. Microwave-assisted polymer chemistry: Heck-reaction, transesterification, Baeyer–Villiger oxidation, oxazoline polymerization, acrylamides, and porous materials. Tetrahedron. 2006 May 8;62(19):4709–14.

11. Kappe CO. Controlled microwave heating in modern organic synthesis. Angew Chem Int Ed Engl. 2004 Nov 26;43(46):6250–84.

12. Sosnik A, Gotelli G, Abraham GA. Microwave-assisted polymer synthesis (MAPS) as a tool in biomaterials science: How new and how powerful. Prog Polym Sci. 2011 Aug;36(8):1050–78.

13. Villemin D, Thibault-Starzyk F. Domestic microwave ovens in the laboratory. J Chem Educ. 1991 Apr 1;68(4):346.

14. Kappe CO, Stadler A. Equipment Review. In: Microwaves in Organic and Medicinal Chemistry. Wiley-VCH Verlag GmbH & Co. KGaA; 2005. p. 29–55.

15. Lidström P, Tierney J, Wathey B, Westman J. Microwave assisted organic synthesis—a review. Tetrahedron. 2001 Nov 5;57(45):9225–83.

16. Raner KD, Strauss CR, Trainor RW, Thorn JS. A New Microwave Reactor for Batchwise Organic Synthesis. J Org Chem. 1995 Apr 1;60(8):2456–60.

17. Kappe CO, Stadler A. Introduction: Microwave Synthesis in Perspective. In: Microwaves in Organic and Medicinal Chemistry. Wiley-VCH Verlag GmbH & Co. KGaA; 2005. p. 1–7.

18. Ondruschka B, Bonrath W, Stuerga D. Devlopment and design of reactors on microwave-assited chemistry. In: Microwaves in Organic Synthesis. Wiley-VCH Verlag GmbH & Co. KGaA; 2012. p. 57–126.

19. Kappe CO, Stadler A. Microwave Theory. In: Microwaves in Organic and Medicinal Chemistry. Wiley-VCH Verlag GmbH & Co. KGaA; 2005. p. 9–28.

20. Subramanian V, Sobhanadri J. New approach of measuring the Q factor of a microwave cavity using the cavity perturbation technique. Rev Sci Instrum. 1994 Feb 1;65(2):453–5.

21. Mishra RR, Sharma AK. Microwave–material interaction phenomena: Heating mechanisms, challenges and opportunities in material processing. Compos Part Appl Sci Manuf. 2016 Feb;81:78–97.

22. Kappe CO, Stadler A. Microwave Theory. In: Microwaves in Organic and Medicinal Chemistry. Wiley-VCH Verlag GmbH & Co. KGaA; 2005. p. 9–28.

23. Gabriel C, Gabriel S, Grant EH, Grant EH, Halstead BSJ, Mingos DMP. Dielectric parameters relevant to microwave dielectric heating. Chem Soc Rev. 1998 Jan 1;27(3):213–24.

24. Carter RG. Accuracy of microwave cavity perturbation measurements. IEEE Trans Microw Theory Tech. 2001;49(5):918–23.

25. Kraszewski AW, Nelson SO. Observations on resonant cavity perturbation by dielectric objects. IEEE Trans Microw Theory Tech. 1992 Jan;40(1):151–5.

26. Waldron RA. Perturbation theory of resonant cavities. Proc IEE Part C Monogr. 1960;107(12):272.

27. Blakey RT, Mason A, Al-Shamma'a A. Dielectric Characterisation of Lipid Droplet Suspensions Using the Small Perturbation Technique. In: Advancement in Sensing Technology. Springer Berlin Heidelberg; 2013. p. 81–91.

28. Huo Y, Bansal R, Zhu Q. Modeling of noninvasive microwave characterization of breast tumors. IEEE Trans Biomed Eng. 2004 Jul;51(7):1089–94.

29. Lazebnik M, Popovic D, McCartney L, Watkins CB, Lindstrom MJ, Josephine Harter, et al. A large-scale study of the ultrawideband microwave dielectric properties of normal, benign and malignant breast tissues obtained from cancer surgeries. Phys Med Biol. 2007;52(20):6093.

30. Castles F, Isakov D, Lui A, Lei Q, Dancer CEJ, Wang Y, et al. Microwave dielectric characterisation of 3D-printed $BaTiO_3$/ABS polymer composites. Sci Rep. 2016 Mar 4;6:srep22714.

31. Massoni E, Silvestri L, Bozzi M, Perregrini L, Alaimo G, Marconi S, et al. Characterization of 3D-printed dielectric substrates with different infill for microwave applications. In: 2016 IEEE MTT-S International Microwave Workshop Series on Advanced Materials and Processes for RF and THz Applications (IMWS-AMP). 2016. p. 1–4.

32. Brosseau C, Quéffélec P, Talbot P. Microwave characterization of filled polymers. J Appl Phys. 2001 Mar 30;89(8):4532–40.

33. Rowe DJ, Porch A, Barrow DA, Allender CJ. Microfluidic device for compositional analysis of solvent systems at microwave frequencies. Sens Actuators B Chem. 2012 Jul 5;169:213–21.

34. Rowe DJ, Porch A, Barrow DA, Allender CJ. Microfluidic Microwave Sensor for Simultaneous Dielectric and Magnetic Characterization. IEEE Trans Microw Theory Tech. 2013 Jan;61(1):234–43.

35. Hoogenboom R, Schubert US. Microwave-Assisted Polymer Synthesis: Recent Developments in a Rapidly Expanding Field of Research. Macromol Rapid Commun. 2007 Feb 19;28(4):368–86.

36. Hoogenboom R, Schubert US. Microwave-Assisted Polymer Synthesis: Recent Developments in a Rapidly Expanding Field of Research. Macromol Rapid Commun. 2007 Feb 19;28(4):368–86.

37. Singh V, Tiwari A, Kumari P, Sharma AK. Microwave accelerated synthesis and characterization of poly(acrylamide). J Appl Polym Sci. 2007 Jun 15;104(6):3702–7.

38. Zhao Z, Li Z, Xia Q, Xi H, Lin Y. Fast synthesis of temperature-sensitive PNIPAAm hydrogels by microwave irradiation. Eur Polym J. 2008 Apr;44(4):1217–24.

39. Stange H, Ishaque M, Niessner N, Pepers M, Greiner A. Microwave-Assisted Free Radical Polymerizations and Copolymerizations of Styrene and Methyl Methacrylate. Macromol Rapid Commun. 2006 Jan 23;27(2):156–61.

40. Holtze C, Antonietti M, Tauer K. Ultrafast Conversion and Molecular Weight Control through Temperature Programming in Microwave-Induced Miniemulsion Polymerization. Macromolecules. 2006 Aug 1;39(17):5720–8.

41. Zhu X, Chen J, Zhou N, Cheng Z, Lu J. Emulsion polymerization of methyl methacrylate under pulsed microwave irradiation. Eur Polym J. 2003 Jun;39(6):1187–93.

42. Gao J, Wu C. Modified Structural Model for Predicting Particle Size in the Microemulsion and Emulsion Polymerization of Styrene under Microwave Irradiation. Langmuir. 2005 Jan 1;21(2):782–5.

43. Sierra J, Palacios J, Vivaldo-Lima E. Effect of Microwave Activation on Polymerization Rate and Molecular Weight Development in Emulsion Polymerization of Methyl Methacrylate. J Macromol Sci Part A. 2006 Mar 1;43(3):589–600.

44. Wu H, Li F, Lin Y, Yang M, Chen W, Cai R. Synthesis of telechelic C60 end-capped polymers under microwave irradiation. J Appl Polym Sci. 2006 Feb 5;99(3):828–34.

45. Assem Y, Greiner A, Agarwal S. Microwave-Assisted Controlled Ring-Closing Cyclopolymerization of Diallyldimethylammonium Chloride Via the RAFT Process. Macromol Rapid Commun. 2007 Sep 18;28(18–19):1923–8.

46. Turner NW, Holdsworth CI, Donne SW, McCluskey A, Bowyer MC. Microwave induced MIP synthesis: comparative analysis of thermal and microwave induced polymerisation of caffeine imprinted polymers. New J Chem. 2010 Apr 1;34(4):686–92.

47. Schwarz LJ, Potdar MK, Danylec B, Boysen RI, Hearn MTW. Microwave-assisted synthesis of resveratrol imprinted polymers with enhanced selectivity. Anal Methods. 2014 Dec 12;7(1):150–4.

48. Hou J, Li H, Wang L, Zhang P, Zhou T, Ding H, et al. Rapid microwave-assisted synthesis of molecularly imprinted polymers on carbon quantum dots for fluorescent sensing of tetracycline in milk. Talanta. 2016 Jan 1;146:34–40.

49. He P, Haswell SJ, Fletcher PDI, Kelly SM, Mansfield A. Scaling up of continuous-flow, microwave-assisted, organic reactions by varying the size of Pd-functionalized catalytic monoliths. Beilstein J Org Chem. 2011 Aug 23;7:1150–7.

50. Jachuck RJJ, Selvaraj DK, Varma RS. Process intensification: oxidation of benzyl alcohol using a continuous isothermal reactor under microwave irradiation. Green Chem. 2006 Dec 23;8(1):29–33.

51. Kunz U, Kirschning A, Wen H-L, Solodenko W, Cecilia R, Kappe CO, et al. Monolithic polymer/carrier materials: Versatile composites for fine chemical synthesis. Catal Today. 2005 Aug 15;105(3–4):318–24.

52. Comer E, Organ MG. A Microcapillary System for Simultaneous, Parallel Microwave-Assisted Synthesis. Chem – Eur J. 2005 Dec 9;11(24):7223–7.

53. Comer E, Organ MG. A Microreactor for Microwave-Assisted Capillary (Continuous Flow) Organic Synthesis. J Am Chem Soc. 2005 Jun 1;127(22):8160–7.

54. Morgan AJL, Naylon J, Gooding S, John C, Squires O, Lees J, et al. Efficient microwave heating of microfluidic systems. Sens Actuators B Chem. 2013 May;181:904–9.

55. Chretiennot T, Dubuc D, Grenier K. A Microwave and Microfluidic Planar Resonator for Efficient and Accurate Complex Permittivity Characterization of Aqueous Solutions. IEEE Trans Microw Theory Tech. 2013 Feb;61(2):972–8.

56. Mani KB, Hossan MR, Dutta P. Thermal analysis of microwave assisted bonding of poly(methyl methacrylate) substrates in microfluidic devices. Int J Heat Mass Transf. 2013 Mar 1;58(1):229–39.

57. Li H, Multari C, Palego C, Ma X, Du X, Ning Y, et al. Differentiation of live and heat-killed E. coli by microwave impedance spectroscopy. Sens Actuators B Chem. 2018 Feb 1;255(Part 2):1614–22.

58. Nerguizian V, Alazzam A, Stiharu I, Burnier M. Characterization of several cancer cell lines at microwave frequencies. Measurement. 2017 Oct 1;109:354–8.

59. Nikolic-Jaric M, Romanuik SF, Ferrier GA, Bridges GE, Butler M, Sunley K, et al. Microwave frequency sensor for detection of biological cells in microfluidic channels. Biomicrofluidics. 2009 Sep 1;3(3):034103.

60. Boybay MS, Jiao A, Glawdel T, Ren CL. Microwave sensing and heating of individual droplets in microfluidic devices. Lab Chip. 2013 Oct 7;13(19):3840–6.

61. Koziej D, Floryan C, Sperling RA, Ehrlicher AJ, Issadore D, Westervelt R, et al. Microwave dielectric heating of non-aqueous droplets in a microfluidic device for nanoparticle synthesis. Nanoscale. 2013 Jun 21;5(12):5468–75.

62. Stuerga D, Pribetich P. Key Ingredients for Mastery of Chemical Microwave Processes. In: Microwaves in Organic Synthesis. Wiley-VCH Verlag GmbH & Co. KGaA; 2012. p. 105–26.

63. Hansen CM. The Universality of the Solubility Parameter. Prod RD. 1969 Mar 1;8(1):2–11.

64. Barwick VJ. Strategies for solvent selection — a literature review. TrAC Trends Anal Chem. 1997 Jun;16(6):293–309.

65. Snyder LR. Classification of the solvent properties of common liquids. J Chromatogr A. 1974 May 22;92(2):223–30.

66. Reichardt C, Welton T. Solvents and Solvent Effects in Organic Chemistry. John Wiley & Sons; 2011. 425 p.

67. Kappe CO. Microwave dielectric heating in synthetic organic chemistry. Chem Soc Rev. 2008 May 22;37(6):1127–39.

68. Van der Eycken E, Appukkuttan P, De Borggraeve W, Dehaen W, Dallinger D, Kappe CO. High-Speed Microwave-Promoted Hetero-Diels−Alder Reactions of 2(1H)-Pyrazinones in Ionic Liquid Doped Solvents. J Org Chem. 2002 Nov 1;67(22):7904–7.

69. Chemat F, Esveld E. Microwave Super-Heated Boiling of Organic Liquids: Origin, Effect and Application. Chem Eng Technol. 2001 Jul 1;24(7):735–44.

70. Marstokk K-M, Møllendal H, Samdal S. Microwave spectrum, conformational equilibrium, 14N quadrupole coupling constants, dipole moment, vibrational frequencies and quantum chemical calculations for acrylamide. J Mol Struct. 2000 Jun 13;524(1–3):69–85.

71. Kappe CO, Pieber B, Dallinger D. Microwave Effects in Organic Synthesis: Myth or Reality? Angew Chem Int Ed. 2013 Jan 21;52(4):1088–94.

72. Herrero MA, Kremsner JM, Kappe CO. Nonthermal Microwave Effects Revisited: On the Importance of Internal Temperature Monitoring and Agitation in Microwave Chemistry. J Org Chem. 2008 Jan 1;73(1):36–47.

73. Werber J, Wang YJ, Milligan M, Li X, Ji JA. Analysis of 2,2'-Azobis (2-Amidinopropane) Dihydrochloride Degradation and Hydrolysis in Aqueous Solutions. J Pharm Sci. 2011 Aug 1;100(8):3307–15.

74. Peyrat-Maillard MN, Cuvelier ME, Berset C. Antioxidant activity of phenolic compounds in 2,2'-azobis (2-amidinopropane) dihydrochloride (AAPH)-induced oxidation: Synergistic and antagonistic effects. J Am Oil Chem Soc. 2003 Oct 1;80(10):1007.

75. Lyoo Won Seok, Kwak Jin Woo, Choi Kyu Ha, Noh Seok Kyun. Preparation of high molecular weight poly(vinyl alcohol) with high yield by emulsion polymerization of vinyl acetate using 2,2'-azobis(2-amidinopropane) dihydrochloride. J Appl Polym Sci. 2004 Oct 22;94(6):2356–62.

76. Dey RE, Zhong X, Youle PJ, Wang QG, Wimpenny I, Downes S, et al. Synthesis and Characterization of Poly(vinylphosphonic acid-co-acrylic acid) Copolymers for Application in Bone Tissue Scaffolds. Macromolecules. 2016 Apr 12;49(7):2656–62.

77. Camli ST, Buyukserin F, Yavuz MS, Budak GG. Fine-tuning of functional poly(methylmethacrylate) nanoparticle size at the sub-100nm scale using surfactant-free emulsion polymerization. Colloids Surf Physicochem Eng Asp. 2010 Aug 20;366(1):141–6.

78. Li Z, Mak SY, Sauret A, Shum HC. Syringe-pump-induced fluctuation in all-aqueous microfluidic system implications for flow rate accuracy. Lab Chip. 2014 Jan 21;14(4):744–9.

79. Shum HC, Sauret A, Fernandez-Nieves A, Stone HA, Weitz DA. Corrugated interfaces in multiphase core-annular flow. Phys Fluids 1994-Present. 2010 Aug 1;22(8):082002.

80. Saien J, Akbari S. Interfacial Tension of Toluene + Water + Sodium Dodecyl Sulfate from (20 to 50) °C and pH between 4 and 9. J Chem Eng Data. 2006 Sep 1;51(5):1832–5.

81. Cuenca JA, Slocombe DR, Porch A. Temperature Correction for Cylindrical Cavity Perturbation Measurements. IEEE Trans Microw Theory Tech. 2017 Jun;65(6):2153–61.

82. Molla J, Ibarra A, Margineda J, Zamarro JM, Hernandez A. Dielectric property measurement system at cryogenic temperature and microwave frequencies. IEEE Trans Instrum Meas. 1993 Aug;42(4):817–21.

83. Eichelbaum M, Stößer R, Karpov A, Dobner C-K, Rosowski F, Trunschke A, et al. The microwave cavity perturbation technique for contact-free and in situ electrical conductivity measurements in catalysis and materials science. Phys Chem Chem Phys. 2011 Dec 14;14(3):1302–12.

84. Abu-Thabit NY. Thermochemistry of Acrylamide Polymerization: An Illustration of Auto-acceleration and Gel Effect. World J Chem Educ World J Chem Educ. 2017 Apr 21;5(3):94–101.

85. Kishore K, Santhanalakshmi KN. Thermal polymerization of acrylamide by differential scanning calorimetry. J Polym Sci Polym Chem Ed. 1981 Oct;19(10):2367–75.

86. Brown SL, Rayner CM, Perrier S. Microwave-Accelerated RAFT Polymerization of Polar Monomers. Macromol Rapid Commun. 2007 Feb 19;28(4):478–83.

87. Lucchese L, Liauw CM, Allen NS, Edge M, Thompson F, Whitehouse RS. Use of microwave dielectric loss for characterisation of natural rubber/carbon black composites. Polym Bull. 2000 Mar 1;44(2):187–94.

88. Templeton A, Wang X, Penn SJ, Webb SJ, Cohen LF, Alford NM. Microwave Dielectric Loss of Titanium Oxide. J Am Ceram Soc. 2000 Jan 1;83(1):95–100.

89. Ferreira VM, Baptista JL, Kamba S, Petzelt J. Dielectric spectroscopy of MgTiO3-based ceramics in the 109–1014Hz region. J Mater Sci. 1993 Jan;28(21):5894–900.

90. Nelson SO, Guo W, Trabelsi S, Kays SJ. Dielectric spectroscopy of watermelons for quality sensing. Meas Sci Technol. 2007;18(7):1887.

91. Castro-Giráldez M, Aristoy M-C, Toldrá F, Fito P. Microwave dielectric spectroscopy for the determination of pork meat quality. Food Res Int. 2010 Dec;43(10):2369–77.

92. Jha SN, Narsaiah K, Basediya AL, Sharma R, Jaiswal P, Kumar R, et al. Measurement techniques and application of electrical properties for nondestructive quality evaluation of foods—a review. J Food Sci Technol. 2011 Feb 18;48(4):387–411.

93. Li H, Liu G, Liu B, Chen W, Chen S. Dielectric properties of polyimide/Al2O3 hybrids synthesized by in-situ polymerization. Mater Lett. 2007 Mar;61(7):1507–11.

94. Xie L, Huang X, Wu C, Jiang P. Core-shell structured poly(methyl methacrylate)/BaTiO3 nanocomposites prepared by in situ atom transfer radical polymerization: a route to high dielectric constant materials with the inherent low loss of the base polymer. J Mater Chem. 2011 Apr 5;21(16):5897–906.

95. Lu J, Moon K-S, Kim B-K, Wong CP. High dielectric constant polyaniline/epoxy composites via in situ polymerization for embedded capacitor applications. Polymer. 2007 Mar 8;48(6):1510–6.

96. Karumbamkandathil A, Ghosh S, Anand U, Saha P, Mukherjee M, Mukherjee S. Micelles of Benzethonium Chloride undergoes spherical to cylindrical shape transformation: An intrinsic fluorescence and calorimetric approach. Chem Phys Lett. 2014 Feb 11;593:115–21.

97. Nedjhioui M, Moulai-Mostefa N, Morsli A, Bensmaili A. Combined effects of polymer/surfactant/oil/alkali on physical chemical properties. Desalination. 2005 Nov;185(1–3):543–50.

98. Dong Y, Sundberg DC. Estimation of polymer/water interfacial tensions: hydrophobic homopolymer/water interfaces. J Colloid Interface Sci. 2003 Feb 1;258(1):97–101.

99. La Mesa C. Polymer–surfactant and protein–surfactant interactions. J Colloid Interface Sci. 2005 Jun;286(1):148–57.

100. Tugay AV, Zakordonskiy VP. Regularities in the association of polymethacrylic acid with benzethonium chloride in aqueous solutions. Russ J Phys Chem. 2006 Jun;80(6):909–14.

101. Khan MY, Samanta A, Ojha K, Mandal A. Interaction between aqueous solutions of polymer and surfactant and its effect on physicochemical properties. Asia-Pac J Chem Eng. 2008 Sep 1;3(5):579–85.

102. Rosen MJ, Kunjappu JT. Surfactants and Interfacial Phenomena. John Wiley & Sons; 2012. 618 p.

103. Lukáč M, Pisárčik M, Lacko I, Devínsky F. Surface-active properties of nitrogen heterocyclic and dialkylamino derivates of hexadecylphosphocholine and cetyltrimethylammonium bromide. J Colloid Interface Sci. 2010 Jul 15;347(2):233–40.

104. Kappe CO, Dallinger D, Murphree SS. Practical Microwave Synthesis for Organic Chemists: Strategies, Instruments, and Protocols. John Wiley & Sons; 2008. 312 p.

Chapter 6. General Discussion and Conclusions

6.1 Background

Mankind has been trying to outsmart microscopic pathogens for millennia. Even prior to any notion of bacteria and viruses, medicine and science has been familiar with the signs and symptoms of severe infection. However, despite the scientific advancements since our ancestors, people still die due to infectious causes. Sepsis, the deregulated host response to infection (1), affects over 30 million people globally per year (2) and poses a significant economic burden for healthcare systems worldwide. Clinicians have biomarkers to help diagnose and monitor therapy for a range of maladies, troponin and Brain Natriuretic Peptide (BNP) in heart disease or Prostate Specific Antigen (PSA) in prostate cancer, for example. However, no such impactful biomarker is available for the diagnosis of sepsis. Therefore, there is an unmet clinical need that warrants investigation of sepsis syndrome biomarkers.

The focus of this work was lipopolysaccharide and its potential as a biomarker for sepsis. Novel ways of facilitating the molecular imprinting of LPS were investigated and lead to extensive work with microwave-initiated polymerisation strategies. However, significant hurdles were met along the way and these are further explored in section 6.3.

Polymyxin is a versatile peptide antibiotic and it features heavily in this work. It is an antibiotic of interest to a few key research groups who have produced vast bodies of work looking at the molecular basis of polymyxin resistance (3), the structural manipulation of PMB to give PMB nonapeptide (4,5) and the investigation of current clinical PMB use (6). Furthermore, the extracorporeal removal of endotoxin in sepsis is an ongoing area of investigation. However, clinical trials of extracorporeal PMB cartridges have not provided a robust case for the widespread use of this therapy in sepsis (7–10). This highlights an ongoing problem with large, multi centred, randomised control trials in sepsis; casting the net too wide

over a whole spectrum of patients with sepsis could be the downfall of effective interventions that would benefit a small subsection of these patients. Endotoxin removal strategies may only be of benefit in the sickest of patients with sepsis and therefore be reserved for this cohort.

Despite the high morbidity and mortality rates caused by Gram positive infection (11), there has been a recent surge in multi drug resistant strains of Gram negative organisms (11). For example, the number of Carbapenem resistant enterobacteriaceae (CRE) infections is rising globally (12,13). In 2002 there were 3 recorded cases of CRE in the UK compared to over 2000 cases in 2015 (14). Incidentally, polymyxin B is considered to be one of the most effective treatments for CRE (15). Furthermore, antimicrobial resistance is a major global concern (16) and it is conceivable we will have no effective antimicrobials in the future with which to fight pathogens. Therefore, maybe a paradigm shift away from antibiotics to alternative approaches such as extracorporeal sequestration of pathogens should be considered for the treatment of sepsis.

6.2 Thesis synopsis

Described herein was the step-wise approach to the molecular imprinting of a complex biomacromolecule via adaptation of conventional imprinting techniques. Experimental chapters described the advance from imprinting on a solid Merrifield resin support, to imprinting at a liquid/liquid interface. This process involved the integration of microfluidic and microwave technologies and the modification of polymyxin B. Referring back to the summary diagram shown in chapter one, Figure 6.1 explains the thesis path from chapter two to chapter five. Novel elements of this work are indicated. Limitations of the work are expanded on in section 6.3.

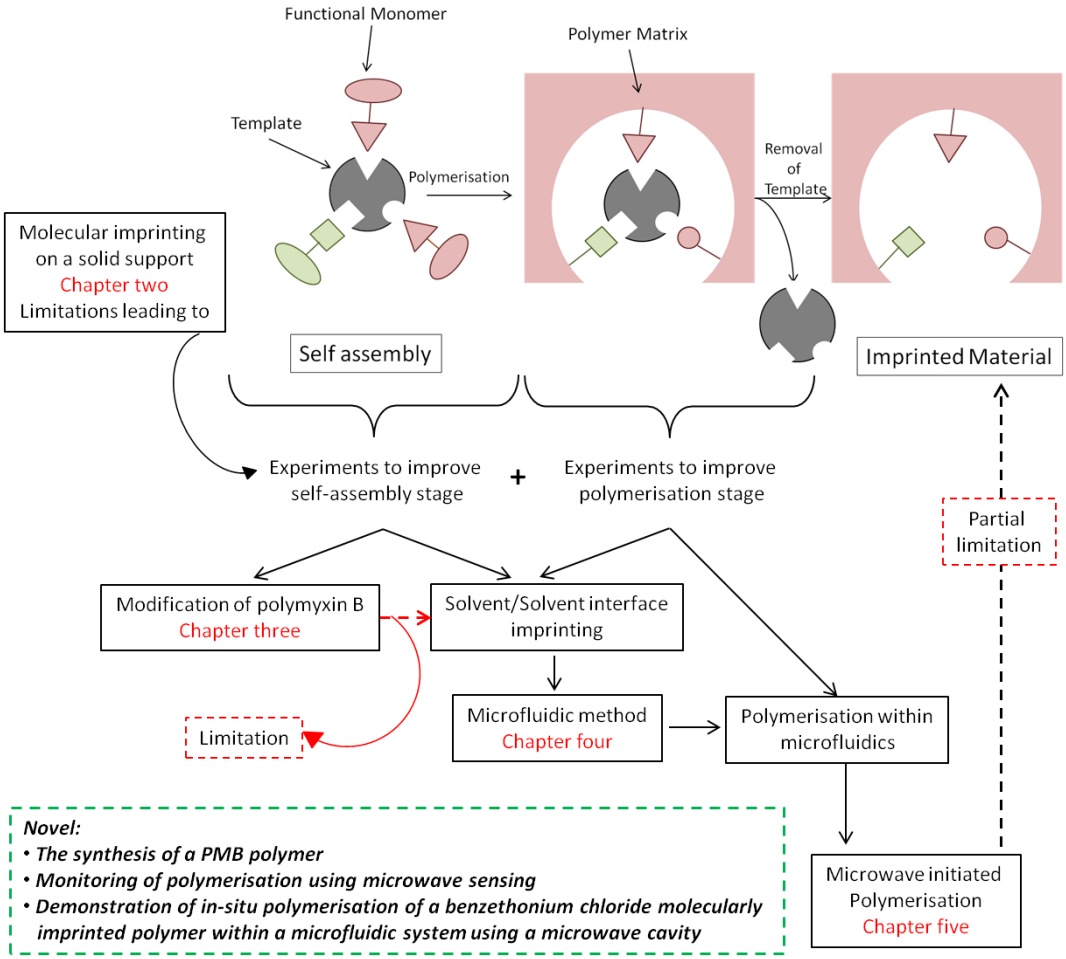

Figure 6.1: Simplified pathway diagram for experimental work

Chapter two described initial molecular imprinting experiments. Using a solid resin support, the immobilisation of polymyxin was a vital stage in this work and the high affinity of polymyxin B for LPS was utilised. Results from this chapter were mixed and overall the successful synthesis of an efficient detection system for LPS using surface imprinting on Merrifield resin was not demonstrated. Part of the problem was using a solid support and therefore the remainder of experimental work moved away from using surface imprinting at a solid/liquid interface.

Without the resin as a backbone, it was desirable that PMB integrated into a polymer therefore producing a standalone molecularly imprinted polymer bead. This process was outlined in chapter three and two main routes for the synthesis of a polymerisable PMB were described. The interaction of PMB and LPS relies on a delicate balance of charges to promote electrostatic interaction of PMB and the lipid A portion of LPS (17,18). Attaching methacrylate moieties to PMB involved the same free amine groups that impart an overall positive charge, therefore some of these free amine groups had to be preserved and one route was more efficient than the other at achieving this. Reasonable binding data were demonstrated using a p-PMB polymer from the glycidyl methacrylate experimental arm.

Table 6.1 compares the main synthesised products from chapters two and three and their respective LPS binding capability.

Table 6.1: Table comparing the major products from chapters two and three and their respective binding ability to LPS.
* azide molar equivalence to chloride (2 mmol/g resin)
** monomer composition: p-PMB_{GMA} 0.74 mmol, acrylamide 3 mmol, N'N- methylenebisacrylamide 0.3 mmol;
***monomer composition: p-PMB_{GMA} 0.74 mmol, acrylamide 2 mmol, N'N- methylenebisacrylamide 0.5 mmol.

Chapter	Product	B_{max} nmol/mg product	K_d µM
Chapter 2: azidomethyl resin plus PMB	0.5 molar equivalent azidomethyl resin*	0.103	0.328
	1 molar equivalent azidomethyl resin*	0.216	0.950
Chapter 3: p-PMB_{GMA} polymer (glycidyl methacrylate route)	p-PMB polymer composition A**	0.069	0.327
	p-PMB polymer composition B***	0.133	0.074

Chapter four described the manufacture of a microfluidic system designed to generate segmented flow of two immiscible fluids at a t-junction. Thereafter, chapter five described microwave-initiated polymerisation via the institution of a microwave delivery protocol. Furthermore, the use of a

microwave resonator cavity allowed the rational choice of organic phase solvent (comparing chloroform and toluene) and also the tracking of polymerisation using microwave sensing.

Chapter five ended with benzethonium chloride experiments. Acting as a LPS surrogate, benzethonium chloride was used as a template in a molecular imprinting process within the integrated microfluidic and microwave system. Subsequent binding experiments demonstrate ability of the produced benzethonium chloride imprinted bead to bind to the original template with a B_{max} of 0.014 nmol per mg product and a K_d of 0.536 μM.

Since completion of experimental work for this thesis, microwave-initiated polymerisation in the process of MIT continues to be exploited by researchers to manufacture MIPs (19,20). Furthermore, in a time when the environmental impact of much human activity is under scrutiny, the use of microwave-assisted organic synthesis offers a more efficient (and therefore energy saving) way of synthesising polymers. This notion of microwave-assisted polymerisation as part of a 'green chemistry' strategy has recently been reviewed (21). This environmental consideration supplements other advantages of using microwave-assisted organic synthesis, strengthening its appeal for use to manufacture MIPS.

Advances in sepsis research continually add potential biomarker candidates to the diverse set already under investigation. For example, in early 2019, Yamamoto *et al.* published work on Presepsin, a biomarker that has previously been the subject of both meta-analysis and laboratory-based work (22,23). Presepsin is the N-terminal fragment of the soluble CD14 glycoprotein that is expressed by certain immune cells and has a central role in LPS recognition. Yamamoto *et al*. showed a potential value of presepsin in the diagnosis of sepsis, demonstrating better diagnostic value than other studies looking at procalcitonin have demonstrated (22). Also in early 2019, Castello *et al.* Published investigative work on the extracellular

matrix protein osteopontin. This reasonably sized (102 patients) single centre study, demonstrated a further complexity of biomarker research. They showed that osteopontin had reasonable *diagnostic* value for patients with sepsis in an emergency medicine setting; however, it had poor *prognostic* value (24).

Sepsis biomarker research therefore continues to re-iterate how increasingly unlikely it is we will discover just one key biomarker to facilitate the early detection of sepsis, and potentially a completely new set of biomarkers will be required to prognosticate.

6.3 Limitations and development

Results from chapter two highlighted issues with Merrifield resin experiments that required aqueous conditions. Despite the addition of a hydrophilic iniferter, the behaviour of Merrifield resin in water was undesirable and, for example, the chapter demonstrated poor iniferter loading onto modified Merrifield resin in aqueous conditions. Experimental findings such as this were the main push towards an alternative approach to imprinting that negated the use of a solid support.

Purchased FITC labelled LPS was used in this work in several binding studies. However, FITC labelled LPS (Sigma Aldrich) has limitations owing to the FTIC labelling efficiency. If the molecular weight of LPS is assumed to be 10,000 g mol^{-1} approximately one in ten LPS molecules are labelled. Alternative labelling techniques have been described including a method for labelling with quantum dots (25) and also labelling with Alexa 488 hydrazide; a described method of which was capable of generating highly fluorescent LPS conjugates (26). Increased detection ability may have been possible by using alterative LPS probes to demonstrate binding with both Merrifield resin composites in chapter two and p-PMB polymers in chapter three.

In chapter three, Merrifield resin experiments had been abandoned and polymyxin was the focus. However, this work was on a small scale. In general, yields of p-PMB product were poor and the purification processes relatively inefficient. Furthermore, detailed characterisation of synthesised polymers was lacking. Possible further desirable steps include FTIR analysis of p-PMB polymers and matched (plain) polymers plus characterisation and analysis of any residual monomers from p-PMB synthesisis reactions. However, this chapter highlighted a potential method for the synthesis of methacrylate polymyxin, it would be interesting to carry out this synthesis on a larger scale and investigate the potential for manufacturing a

polymerisable polymyxin film coating. This would provide an interesting insight into this alternative method of coating extracorporeal circuits for the removal of endotoxin.

Chapters four and five can be thought of as one body of work, with chapter four introducing the system development explored further in chapter five. Both chapters explored the potential for microfluidic/microwave integration in the manufacture of polymer beads and the potential for liquid/liquid interface surface imprinting. However, the suitability of benzethonium chloride use could be seen as an experimental limitation. There are obvious differences in the structure of lipopolysaccharide and benzethonium chloride; however the amphipathic nature of the two molecules is an important similarity. Furthermore, the availability and economic considerations of using a surrogate molecule for fluorescently labelled LPS were important. Considering this background, the proof-of-concept benzethonium chloride studies described in Chapter five have merit in the testing of a novel hybrid microfluidic/ microwave system. Moreover, a significant limitation of this work is the lack of p-PMB polymer utilisation in microfluidic/microwave experiments. The explanation hinges on poor yield and therefore availability of p-PMB polymer in significant quantity for ongoing work. Certainly, if improvements were made to the synthesis process for p-PMB, it would be interesting to see how it behaved in the MF system.

Furthermore, the use of alternative UV transparent material could have been explored. In section the experiment to initiate polymerisation with UV prior to exploring microwave initiated polymerisation is introduced. This method was not successful; however, alternative microfluidic tubing materials could have been used. For example, glass and quartz tubing are UV transparent; however, several attempts were made to use glass tubing (not documented in experimental sections) and difficultly was encountered

in the suitability of connecting components of the fluidic system. COC (cyclic olefin copolymer) tubing is another alternative and has superior optical properties (27). Synthesized from the polymerisation of cyclic olefin monomers and ethene, successful combinational approaches of COC tubing and UV initiated polymerisation have been reported (28). An interesting outcome from working with polymerisation and microwaves was the exploitation of the sensing capability of microwaves to document the polymerisation process. There is potential to explore this further and on a larger scale with the tracking of polymerisation of a more diverse range of polymers and under a variety of conditions. Microwave sensing is an established tool in many engineering and material science disciplines and emerging work is also harnessing the detection abilities of microwaves combined with molecularly imprinted polymers (27). It would be interesting to explore further the benefits of radiofrequency technology in the field of molecular imprinting.

Highlighted in chapter five, section 5.4.4, are the considerations surrounding temperature effects on microwave initiated organic synthesis reactions. Delineation of observed reaction steps between those caused by the electromagnetic radiation and those caused merely by a change in temperature is vitally important. Temperature control is therefore a fundamental consideration in the design of cavity resonators. Materials with high thermal stability can be used and their Coefficient of (linear) Thermal Expansion (CTE) taken into consideration (the degree to which a material expands on heating) and is measured in ppm/$^{\circ}$C. Aluminium, for example, has a CTE of 23 ppm/$^{\circ}$C (30), which is relatively high (titanium 8.5 ppm/$^{\circ}$C; copper 16.8 ppm/$^{\circ}$C (30)). However, aluminium has other derisible characteristics for microwave cavity resonators and therefore compensating for any observed cavity dimension effects at any given temperature due to its known CTE value can be taken into consideration. Furthermore, groups employ methods of microwave irradiation combined

with simultaneous cooling, with specifically designed microwave delivery devices. Such devices (the CEM-Discover-CoolMate® for example) cool the reaction vessel whist the microwave irradiation is applied using compressed air or cooling fluid (31). Reactions can then be observed with temperatures well below those expected during a microwave initiated organic synthesis reaction. Using such devices could be a consideration for future work; moreover, optimisation of temperature measurement (using exclusively fibreoptic and not infrared devices) is also an important consideration.

Moreover, sensitivity analysis and design of experiements (DOE) is an important consideration for chapter five. Detailed in section 5.3.5.1 are the set of experiments that were used to establish a protocol for the successful polymerisation of beads within a microfluidic system via microwave-initiated polymerisation. The general conduct of this experiment could have been improved with consideration of the fundamental experimental design, highlighting a limitation in this chapter. Sensitivity analysis by DOE could have been employed considering the number of parameters under manipulation; this would have provided a framework to establish the parameter with greatest impact on experiment outcomes. Using a sensitivity analysis by DOE model, variables that have little impact on results could have been dropped from ongoing iterations of the microwave-initiated polymerisation protocol (32). Therefore, for any future work looking at the polymerisation of beads within my hybrid microfluidic/microwave system (using different monomers for example), a framework provided by a DOE sensitivity analysis could be employed to improve the robustness of experiments.

6.4 References

1. Singer M, Deutschman CS, Seymour CW, Shankar-Hari M, Annane D, Bauer M, et al. The Third International Consensus Definitions for Sepsis and Septic Shock (Sepsis-3). JAMA. 2016 Feb 23;315(8):801–10.

2. Fleischmann C, Scherag A, Adhikari NKJ, Hartog CS, Tsaganos T, Schlattmann P, et al. Assessment of Global Incidence and Mortality of Hospital-treated Sepsis. Current Estimates and Limitations. Am J Respir Crit Care Med. 2016 Feb 1;193(3):259–72.

3. Vaara M, Vaara T, Jensen M, Helander I, Nurminen M, Rietschel ET, et al. Characterization of the lipopolysaccharide from the polymyxin-resistant pmrA mutants of Salmonella typhimurium. FEBS Lett. 1981 Jun 29;129(1):145–9.

4. Vaara M. Polymyxins and their novel derivatives. Curr Opin Microbiol. 2010 Oct;13(5):574–81.

5. Vaara M. Polymyxin B nonapeptide complexes with lipopolysaccharide. FEMS Microbiol Lett. 1983 Apr;18(1–2):117–21.

6. Alipour M, Halwani M, Omri A, Suntres ZE. Antimicrobial effectiveness of liposomal polymyxin B against resistant Gram-negative bacterial strains. Int J Pharm. 2008 May 1;355(1–2):293–8.

7. Rachoin J-S, Foster D, Dellinger RP. Endotoxin removal: how far from the evidence? From EUPHAS to EUPHRATES. Contrib Nephrol. 2010;167:111–8.

8. Dellinger RP, Bagshaw SM, Antonelli M, Foster DM, Klein DJ, Marshall JC, et al. Effect of Targeted Polymyxin B Hemoperfusion on 28-Day Mortality in Patients With Septic Shock and Elevated Endotoxin Level: The EUPHRATES Randomized Clinical Trial. JAMA. 2018 Oct 9;320(14):1455–63.

9. Klein DJ, Foster D, Schorr CA, Kazempour K, Walker PM, Dellinger RP. The EUPHRATES trial (Evaluating the Use of Polymyxin B Hemoperfusion in a Randomized controlled trial of Adults Treated for Endotoxemia and Septic shock): study protocol for a randomized controlled trial. Trials. 2014;15:218.

10. Klein DJ, Foster D, Walker PM, Bagshaw SM, Mekonnen H, Antonelli M. Polymyxin B hemoperfusion in endotoxemic septic shock patients without extreme endotoxemia: a post hoc analysis of the EUPHRATES trial. Intensive Care Med. 2018 Dec 1;44(12):2205–12.

11. Fair RJ, Tor Y. Antibiotics and Bacterial Resistance in the 21st Century. Perspect Med Chem. 2014 Aug 28;6:25–64.

12. Savard P, Perl TM. Combating the spread of carbapenemases in Enterobacteriaceae: a battle that infection prevention should not lose. Clin Microbiol Infect. 2014 Sep 1;20(9):854–61.

13. Duin D van. Carbapenem-resistant Enterobacteriaceae: What we know and what we need to know. Virulence. 2017 May 19;8(4):379–82.

14. Worse than MRSA: Doctors call for urgent action on deadly superbug threat [Internet]. The Bureau of Investigative Journalism. Available from: https://www.thebureauinvestigates.com/stories/2017-04-21/worse-than-mrsa-experts-call-for-action-on-deadly-new-superbug

15. Gales AC, Jones RN, Sader HS. Global assessment of the antimicrobial activity of polymyxin B against 54 731 clinical isolates of Gram-negative bacilli: report from the SENTRY antimicrobial surveillance programme (2001–2004). Clin Microbiol Infect. 2006 Apr 1;12(4):315–21.

16. WHO | Antimicrobial resistance [Internet]. WHO. Available from: http://www.who.int/mediacentre/factsheets/fs194/en/

17. Velkov T, Thompson PE, Nation RL, Li J. Structure—Activity Relationships of Polymyxin Antibiotics. J Med Chem. 2010 Mar 11;53(5):1898–916.

18. Powers J-PS, Hancock REW. The relationship between peptide structure and antibacterial activity. Peptides. 2003 Nov;24(11):1681–91.

19. Mustafai FA, Balouch A, Abdullah, Jalbani N, Bhanger MI, Jagirani MS, et al. Microwave-assisted synthesis of imprinted polymer for selective removal of arsenic from drinking water by applying Taguchi statistical method. Eur Polym J. 2018 Dec 1;109:133–42.

20. Chen F, Wang J, Chen H, Lu R, Xie X. Microwave-assisted RAFT polymerization of well-constructed magnetic surface molecularly imprinted polymers for specific recognition of benzimidazole residues. Appl Surf Sci. 2018 Mar 30;435(Supplement C):247–55.

21. Viveiros R, Rebocho S, Casimiro T. Green Strategies for Molecularly Imprinted Polymer Development. Polymers. 2018 Mar;10(3):306.

22. Yamamoto T, Nishimura T, Kaga S, Uchida K, Tachibana Y, Esaki M, et al. Diagnostic accuracy of presepsin for sepsis by the new Sepsis-3 definitions. Am J Emerg Med. 2019 Jan 15;0(0).

23. Wu J, Hu L, Zhang G, Wu F, He T. Accuracy of Presepsin in Sepsis Diagnosis: A Systematic Review and Meta-Analysis. PLOS ONE. 2015 Jul 20;10(7):e0133057.

24. Castello LM, Baldrighi M, Molinari L, Salmi L, Cantaluppi V, Vaschetto R, et al. The Role of Osteopontin as a Diagnostic and Prognostic Biomarker in Sepsis and Septic Shock. Cells. 2019 Feb;8(2):174.

25. Morales-Betanzos C, Gonzalez-Moa M, Svarovsky SA. A method for unobtrusive labeling of lipopolysaccharides with quantum dots. Methods Mol Biol Clifton NJ. 2011;739:113–22.

26. Triantafilou K, Triantafilou M, Fernandez N. Lipopolysaccharide (LPS) labeled with Alexa 488 hydrazide as a novel probe for LPS binding studies. Cytometry. 2000 Dec 1;41(4):316–20.

27. Nunes PS, Ohlsson PD, Ordeig O, Kutter JP. Cyclic olefin polymers: emerging materials for lab-on-a-chip applications. Microfluid Nanofluidics. 2010 Aug 1;9(2):145–61.

28. Jena RK, Yue CY. Cyclic olefin copolymer based microfluidic devices for biochip applications: Ultraviolet surface grafting using 2-methacryloyloxyethyl phosphorylcholine. Biomicrofluidics. 2012 Mar 15;6(1):012822-012822–12.

29. Bou-Maroun E, Rossignol J, De Fonseca B, Lafarge C, Gougeon RD, Stuerga D, et al. Feasibility of a microwave liquid sensor based on molecularly imprinted sol-gel polymer for the detection of iprodione fungicide. Sens Actuators B Chem. 2017 Jun;244:24–30.

30. Hui-Wen Yao, Atia AE. Temperature characteristics of combline resonators and filters. In: 2001 IEEE MTT-S International Microwave Sympsoium Digest (Cat No01CH37157). Phoenix, AZ, USA: IEEE; 2001 p. 1475–8.

31. Loupy A. Microwaves in Organic Synthesis (Two Volume Set). Wiley; 2006. 1033 p.

32. Burnside S. The application of design of experiments to RF systems. In: 2018 International Applied Computational Electromagnetics Society Symposium (ACES). 2018. p. 1–2.